RBTH 0203

RARE BOOKS LIB.

The University of Sydney

Copyright and use of this thesis

This thesis must be used in accordance with the provisions of the Copyright Act 1968.

Reproduction of material protected by copyright may be an infringement of copyright and copyright owners may be entitled to take legal action against persons who infringe their copyright.

Section 51(2) of the Copyright Act permits an authorized officer of a university library or archives to provide a copy (by communication or otherwise) of an unpublished thesis kept in the library or archives, to a person who satisfies the authorized officer that he or she requires the reproduction for the purposes of research or study.

The Copyright Act grants the creator of a work a number of moral rights, specifically the right of attribution, the right against false attribution and the right of integrity.

You may infringe the author's moral rights if you:

- fail to acknowledge the author of this thesis if you quote sections from the work
- attribute this thesis to another author
- subject this thesis to derogatory treatment which may prejudice the author's reputation

For further information contact the University's **Director of Copyright Services**

Telephone: 02 9351 2991
e-mail: copyright@usyd.edu.au

THIS THESIS HAS BEEN ACCEPTED FOR
THE AWARD OF THE DEGREE IN THE
FACULTY OF ENGINEERING AND
INFORMATION TECHNOLOGIES

THE UNIVERSITY OF SYDNEY
SCHOOL OF CIVIL ENGINEERING

Time Dependent Analysis of Tunnel in Creeping Rock

by
Ran Chen

A thesis submitted for the degree of Doctor of Philosophy
May, 2009

SYNOPSIS

In this thesis, a viscoelastic creep model of material has been developed to investigate the long-term behaviour of tunnel structures due to the creep performance of the ground and the shotcrete lining. The finite element method was used in the research to calculate the time-dependent deformation and stress in the tunnel and its support structure. The research was concerned with the following aspects:

1. It is assumed that the material properties of the soil or rock surrounding a tunnel, and the shotcrete lining are time-dependent. Although the time-dependent functions can have many forms, here it is assumed that the bulk modulus and the shear modulus are logarithmic functions of time.

2. The analysis was carried out by the application of the finite element method, and a program named SAFEA (Semi Analytic Finite Element Analysis) has been developed to simulate tunnel excavation and to calculate time-dependent deformation and stress in a tunnel structure due to creep behaviour. The governing finite element equations can be established in terms of time *t* and transformed by using a Laplace transform, then solved in terms of the Laplace transform parameter. Finally the transforms are numerically inverted to give the solutions in real time.

3. A commercial finite element program ABAQUS has also been used in the research, which uses a power time hardening law to describe the visco-elastic creep properties of materials.

4. Creep parameters for different materials can be extrapolated through either laboratory creep tests or back analysis of time-dependent field data from tunnel projects. Both approaches have been used in the present research, and the obtained parameters were employed in the finite element model to predict the time-dependent performance of underground structures.

5. Different shaped tunnel sections were modelled in parametric studies and practical tunnel projects were modelled in the research to verify the applicability of the method and to investigate the long-term performance of a tunnel and its support system due to creep behaviour.

6. From the analysis carried out it is deduced that in some cases, the creep properties of the materials should be taken into consideration in the tunnel design to satisfy the long term performance of the tunnel and its support.

7. More laboratory creep tests and field data from full scale projects are required to better understand the creep performance of a tunnel structure and predict the time-dependent convergence of a tunnel section.

PREFACE

The work described in this thesis was carried out in the School of Civil Engineering at the University of Sydney during the period from 2005 to 2009. It has been supported by an Australian Postgraduate Awards Industry Scholarship, under the supervision of Professor John. C. Small.

The By-Laws of the University of Sydney require a candidate for the degree of Doctor of Philosophy to indicate which sections of this thesis are original. In accordance with these By-Laws, any material derived from other sources has been acknowledged in the text in this thesis, and the author claims the following work as original:

1. In Chapter 3, the application of the Laplace transform and the use of complex arithmetic to perform a numerical Talbot inversion in solving the material's creep deformation under three-dimensional conditions by use of a convolution integral, is claimed as original.

2. In Chapter 4, the numerical simulation of laboratory creep tests, and obtaining creep parameters for fibre reinforced shotcrete, sandstone and shale, are claimed as original.

3. In Chapter 5, the development of a finite element program named SAFEA and the application of SAFEA in tunnel excavation, support and creep analysis are claimed as original work.

4. In Chapters 6 & 7, the numerical modelling of circular and flat roof tunnels, and the time-dependent creep analysis of the tunnel and its support are claimed as original.

5. In Chapter 8, the numerical modelling of the Frejus tunnel, the Middle Marsyangdi Hydropower Tunnel and the Lane Cove tunnel, performing creep

analysis of the tunnel and its support, verifying the numerical results against field data, are claimed as original.

Three papers were published and one paper was finished by the author in conjunction with others during the period of candidature. They are presented in support this thesis:

1. Chen, R. and Small, J. C., (2008), 'Analysis of the Creep Behaviour of Tunnels in Sandstone/Shale', Proceedings of the 13th Australian Tunnelling Conference, Melbourne, 4-7 May, pp.197-202.

2. Chen, R. and Small, J. C., 'Numerical Analysis of Time Dependent Creep Behaviour of Tunnel Support Systems', Proceedings of the 2008 North American Tunneling Conference, San Francisco, 7-11 June, pp.399-404.

3. Chen, R. and Small, J. C., (2008), 'Time-dependent behaviour of tunnels in sandstone', Proceedings of the fourth Int. Symp. on Deformation Characteristics of Geo-materials, 22-24 Sep, Atlanta, Eds Susan E. Burns etc. Vol.1, pp.483-488.

4. Chen, R. and Small, J. C., (2008), 'Numerical analysis of Time-dependent behaviour of tunnels'. (draft)

ACKNOWLEDGMENTS

I started my Ph.D. project in July, 2005. During the years of my candidature, I was privileged to receive the support and help from both inside and outside of the university.

I should give my deep gratitude to my supervisor, Professor John. C. Small, for his valuable support, encouragement and assistance during the whole of my candidature period. My special thanks are due to John for all the kind help he provided not only in the academic field, but for helping with financial arrangements, career support and friendship.

I would also like give my thanks to the other academic staff who provided advice on my research, particularly Dr. Hongyuan Liu, who gave me a lot of valuable advice and support when using the finite element code ABAQUS on this tunnel project. I would also like to express my appreciation to Dr. Nigel Balaam for his kind support in modifying the Finite Element mesh generation program GENTOP for the present research.

Acknowledgments are also due to other academics and engineers outside the university. I would like to thank Mr. Gregory W Won from the Road and Traffic Authority for providing valuable field measurement data from the Lane Cove tunnel and other projects; Dr. Stefan Bernard and Dr. Geoff Xu from Elasto-Plastic Concrete Pty Ltd (EPC) for providing laboratory creep test results for fibre reinforced shotcrete and shale specimens and valuable advice for the research.

I have greatly enjoyed the time at the University of Sydney and I should extent my thanks to my postgraduate friends, Helen Chow, David Cao, Derrick Yap, Frank Zhu, Benoit Gilbert, Jurgen Becque, Niphan Yaiaroon, Korn Chandrangsu, Cao Hung Pham, Eric Yao, Yue Gen, and Ezzat William. Friendship is another valued treasure I received at the University of Sydney.

Finally, I would like to thank my wife Shu Wang for giving me a lot of support and encouragement during the whole candidature period.

R.Chen

TABLE OF CONTENTS

NOTATION

Some of the abbreviations more commonly used in this thesis are presented below. All abbreviations and symbols have been defined at the first point they are used in the text, ad they are assumed to apply throughout this thesis unless otherwise stated.

A, B, α	Creep parameters of logarithmic model in SAFEA
C_{ijkl}	Elastic tensor coefficients
$\{d\}$	Nodal displacement vector
E	Young's modulus
$E(t)$	time-dependent function of Young's modulus
F	creep multiplier factor of power law model in ABAQUS
m	creep stress order factor of power law model in ABAQUS
n	creep time order factor of power law model in ABAQUS
$[N]$	shape function matrix for an individual finite element
G	shear modulus
$G(t)$	time-dependent function of shear modulus
H	overburden depth
I_y, I_z	second moments of area
J	torsion constant
$J(t)$	creep function
$[J]$	Jacobian matrix
K	bulk modulus
$K(t)$	time-dependent function of bulk modulus
$[K]$	element stiffness matrix
£	Laplace transform
v	Poisson's ratio
$R(t)$	relaxation modulus
t	time
ε	strain

$\varepsilon(t)$	time-dependent strain variable
σ	normal stress
$\sigma(t)$	time-dependent stress variable
σ_v	vertical stress
σ_{WE} , σ_{NS}	horizontal stress in west-east and north-south directions respectively
τ	shear stress
ϕ	creep factor used to define the magnitude of creep deformation
$\delta U^{(e)}$	element virtual work due to internal forces
$\delta W^{(e)}$	element virtual work due to external forces
U	total internal virtual work
W	total external virtual work

CHAPTER 1 - INTRODUCTION

1.1 INTRODUCTION

Most tunnels built in Sydney recently as well as in other places all around the world are supported by a combined shotcrete lining and rockbolt system. The geo-materials such as shotcrete and rock undergo a time-dependent deformation when under a constant load and this 'creep' deformation may continue for a very long period causing changes in load in the tunnel structure. If the closure deformation increases too much with time, it will influence the service function of a tunnel; it may even cause collapse of a tunnel after a long period. In general, soft rock or soil has a lower strength and modulus and will undergo a higher creep deformation as time goes by, while hard rock do not deform much under load and its creep deformation is usually not significant in the long term. This thesis presents a study of the creep behaviour of the rock and shotcrete surrounding a tunnel, and how the creep performance of these materials influences the behaviour of the tunnel structure over a long period of time. The effect of the creep in the surrounding rock and shotcrete lining on the rockbolts is also examined.

The mechanical behaviour of geo-materials is time-dependent and the creep performance can be modelled by the use of visco-elastic or visco-plastic theory. The finite element method was used in this thesis to model the behaviour of tunnels and their support systems and a program called SAFEA was developed. The properties of the materials are represented by functions in time. A Laplace transform is then applied to the material variables and the solution of the equations is found from a three-dimensional finite element analysis code based on the transformed variables. Finally the solution in real time is obtained through a numerical inversion of the solution (Talbot's inversion). The commercial finite element software ABAQUS which uses a power law model for creep behaviour was also used to model the tunnel projects in the thesis.

Creep phenomena can be observed in many engineering projects, such as the continuous closure of underground tunnel sections, the increasing settlement of buildings, and also in laboratory tests. It may undergo three stages: primary, steady, and tertiary state creep. The creep deformation increases quickly in the first primary stage, which is then followed by a long steady stage where displacement increases slowly with time, and then finally in the tertiary creep stage the deformation increases rapidly and which leads to damage of the material. The tertiary creep stage only happens when the material is under a relatively high stress level. In this research, it is assumed that the properties of the material change with time and this results in the creep deformation. Here, the bulk modulus K and shear modulus G which control the volumetric and deviatoric behaviour of materials are represented by a time-dependent numerical model. The creep parameters of a material can be estimated from a time-dependent laboratory test which may last for several months or even longer. With back analysis of the time-dependent closure records of a tunnel project, it is also possible to estimate the creep parameters of the rock surrounding the tunnel.

Some laboratory tests were carried out to define the properties of different kinds of rock and fibre reinforced shotcrete. Uniaxial creep laboratory tests were carried out to record the time-dependent deformation of rock samples under compression; and ASTM C-1550 round determinate panel tests were used to examine the creep performance of fibre reinforced shotcrete under flexure. In the uniaxial creep tests, the specimens were fixed at the bottom, a constant pressure load was applied on the top surface of the specimens, and the uniaxial deformation was recorded over time, while in the ASTM C-1550 tests, the round panels were supported by three symmetric pivots on the edge, a constant load was applied to the centre of the panel, and the deflection was recorded over a few months. The different creep tests were simulated by finite element models, and numerical creep parameters were selected to fit the experimental curve and then employed in the tunnel models to examine the creep performance of a tunnel structure.

A finite element code called SAFEA (Semi Analytic Finite Element Analysis) has been developed and a logarithmic function was employed in the program to represent the time-dependent properties of the materials. The purpose of the program is to predict the long term closure of a tunnel section, and examine the stress changes in the surrounding rock, shotcrete lining and rock bolts. To testify to the accuracy of the code, another commercial finite element program ABAQUS was used and the results of the two programs were compared. First, a normal circular tunnel was modelled, the shotcrete lining was applied to the whole circumference of the tunnel section and rock bolts were not used. Then a flat roof tunnel section was modelled which was supported by a shotcrete lining and rock bolts on the crest of the tunnel section. A parametric study was carried out based on the different rock types, types of fibre reinforced shotcrete and tunnel depth. Finally, back analysis of some real tunnel projects was carried out, which included the Lane Cove tunnel in Sydney, the Frejus tunnel in Europe, and the Middle Marsyangdi Hydropower tunnel in Nepal. The study showed that the predictions made by the program are of an acceptable degree of accuracy, and also highlighted some important points that we should pay attention to in designing and constructing tunnels with respect to their long term performance.

The thesis shows that it is necessary in some cases to take the creep deformation into consideration to satisfy the long term serviceability and strength requirement of a tunnel structure. The current analysis and design of tunnel projects is mainly based on the material's elastic properties which satisfy the short term performance of a tunnel quite well. A more rational model such as the one presented in the present thesis which considers the creep properties of the materials should be used to get a better understanding of the behaviour of a practical tunnel structure over a long term period.

CHAPTER 2 - LITERATURE REVIEW

2.1 INTRODUCTION

Creep is a complex and important mode of behaviour of soil/rock in many geo-engineering problems and scientists have always sought a better understanding of this phenomena and how it affects an underground structure's long term behaviour. An overview of previous work is presented in this chapter, which includes historic observations of creep phenomena both for in situ projects and laboratory tests, the previous theoretical analytic and numerical models for modelling the creep characteristics of rock and soil, and the investigation and prediction of time-dependent creep deformation in tunnel projects using empirical methods, and analytical methods as well as numerical methods.

2.2 HISTORIC OBSERVATION OF CREEP PHENOMENA

Since the early nineteenth century, creep behaviour has been observed and studied by scientists, and much work has been done by researchers both experimentally and theoretically to investigate this phenomenon. Here some important aspects of creep behaviour are presented.

2.2.1 FIELD OBSERVATION OF CREEP IN TUNNELS

In the tunnelling industry, creep deformation has already caused serious problems in many projects and has been investigated by many researchers, e.g. Stillwater Tunnel (Phien-Wej and Cording, 1991), Lam Ta Khong tunnel (Gurung and Iwao, 1998), Tymfristos tunnel (Kontogianni et al. 2004), and Taloun Tunnel (Yassaghi and Salari-Rad, 2005). The creep properties of the rock mass have a significant effect on the tunnel structure, especially when the tunnel is excavated in soft rock or is under high in-situ stress (Chen et al., 2004). After excavation of a tunnel section, the closure displacement of the section will increase with time; it may last for a vey long period and make the tunnel lose serviceability or even collapse. For example, the Tymfristos tunnel in Greece experienced a convergence of up to 20% and this was followed by failure of the tunnel within about one year of its excavation (Kontogianni et al, 2004), and the Laerdal tunnel in Norway experienced a continuing increase in closure deformation and finally collapsed within four years of its excavation (Grimstad 2001). The time-dependent convergence measurement records of the Frejus tunnel clearly show the evidence of creep deformation in a tunnel structure. Sulem et al. (1987a) deemed that the wall displacement and pressure on the lining of a tunnel will increase with time and they proposed a convergence law to predict this closure with time. On the other hand, the pressure in the lining of a tunnel may not increase but decrease as found in the present investigation. Figure 2.1 shows the measured and calculated convergence displacement on a station in the Frejus tunnel, and it shows that the analytical result of Sulem et al. fits the actual measured convergence well.

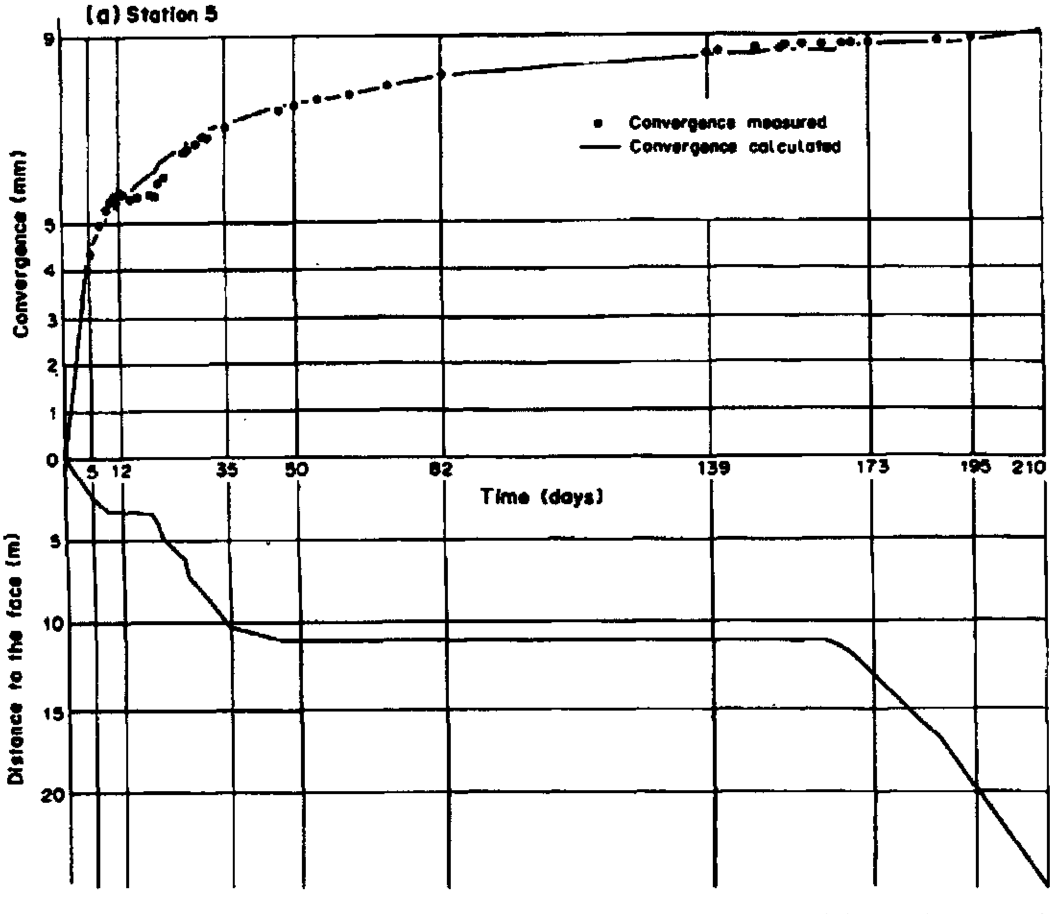

Figure 2.1: Measured and calculated convergence at a station of the Frejus tunnel (after Sulem et al. 1987a)

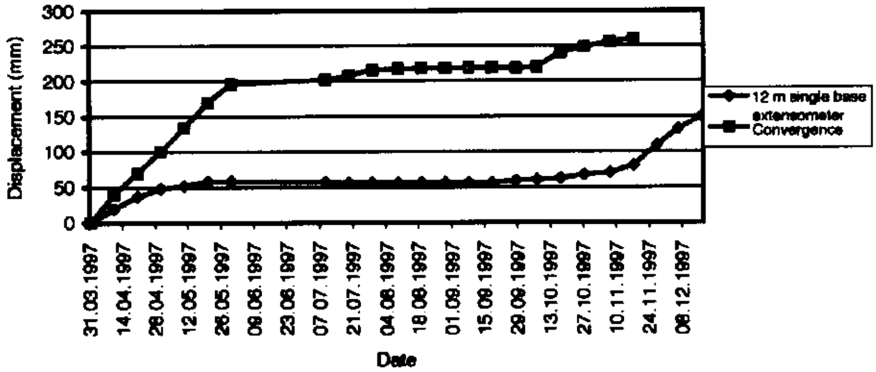

Figure 2.2: Relationship between time and deformation in the Bolu tunnel (after Dalgic, 2002)

Another example is the Bolu tunnel in Turkey (Dalgic, 2002). The tunnel suffered considerable deformation due to the squeezing of the rock and resulted in a serious geotechnical problem. Figure 2.2 clearly records the creep deformation of the tunnel which experienced three stages: the deformation increased quickly in the first primary stage, which was then followed by a long steady stage where displacement did not increase much, and then finally the deformation increased rapidly in the tertiary creep stage causing collapse of the tunnel.

Besides the tunnel deformation, the field load on the supports was also monitored, recorded and used to explain the phenomena of squeezing pressures in the tunnel excavation (Dube et al. 1977). In the analysis of a rock-burst problem in a deep mining project, Roux and Denkhaus (1954) found that the time-dependent strength of rocks satisfactorily explained the occurrence of rock-burst after the mining operations. On the other hand, creep deformation may lead to a gradual non-violent release of stress in the surrounding rock and decrease the risk of rock-burst.

2.2.2 LABORATORY DATA FOR CREEP/SECONDARY SETTLEMENT

Creep deformation has been investigated for both soil and rock through the use of different types of laboratory tests. Different tests have been used by researchers to investigate the creep properties of different materials under different situations. One-dimensional compression tests have been used by many researchers to investigate the secondary consolidation and time-dependent behaviour of soil (Taylor, 1942; Barden, 1969; Sekiguchi & Toriihara, 1976; Ter-Martirosyan, 1979; Busch & Keller, 1982).

Terzaghi (1925) introduced a logarithmic stress dependency for both the primary strain and the secondary strain; he proposed that the Young's modulus has a linear relationship with the stress.

Buisman's (1936) experimental curve as shown in Figure 2.3 indicated that the settlement will not stop after the primary consolidation when all excess pore pressure has dissipated, and a further increase of the settlement occurs that is called the secondary (creep) deformation of the material.

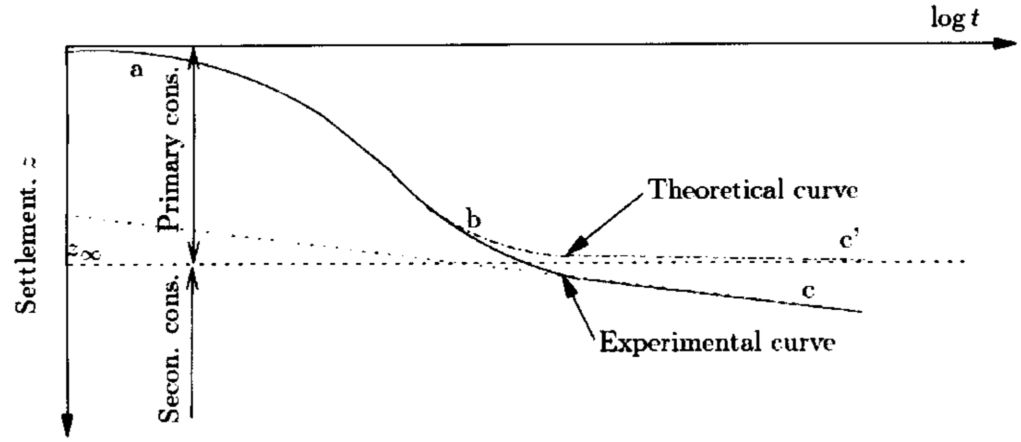

Figure 2.3: Theoretical and experimental settlement curve during consolidation.
(after Buisman 1936).

He was possibly the first to propose that the secondary settlement has a linear relationship with the logarithm of time when the soil is under a constant load. He gave the following relationship and proposed an intrinsic coefficient of secondary settlement $C_{\alpha s}$ to describe the magnitude of the creep settlement.

$$\frac{\Delta h_s}{h_1} = C_{\alpha s} \cdot \log \frac{t}{t_1} \qquad (2.1)$$

where h_1 is the original thickness of the compressible soil layer at time t_1, Δh_s is the change of thickness due to the secondary settlement over time t.

This linear relationship for the secondary consolidation and log-time is only valid for some log cycles of time, but the strain-log time behaviour is nonlinear in general for the whole period of creep (Bjerrum, 1967; Berre and Iversen, 1972).

A formula was later developed by combining the Terzaghi (1925) load compression relationship and the Buisman (1936) secular time effect together to predict the soil settlement ε under stress over time as shown below (Koppejan, 1948).

$$\varepsilon = \left(\frac{U}{C'_p} + \frac{1}{C'_s} \log(t) \right) \ln\left(\frac{\sigma'_v}{\sigma'_{vi}} \right) \tag{2.2}$$

where U is the consolidation ratio,

σ'_v is the final vertical effective stress,

σ'_{vi} is the initial vertical effective stress.

C'_p and C'_s are constants dependent on the units of time, but are independent of the stress. For clay, C'_p is 10 to 25 and C'_s is 50 to 250 with time in days.

To evaluate the magnitude of creep in a soil, it is important to define the end of primary consolidation, which is to know when creep happens, or the so called reference time problem. Two philosophies have been adopted to answer this question, which are called hypothesis A & B. Hypothesis A assumes that the creep occurs only after the primary consolidation is complete and the sample thickness has no effect on the reference time (Ladd et al., 1977; Jamiolkowski et al., 1985), while Hypothesis B assumes that creep occurs during the whole consolidation process and the strain-stress relationship at the end of primary consolidation is not unique, but depends on the thickness of the clay (Wahls, 1962; Bjerrum, 1967; Yin and Graham, 1996). Figure 2.4 shows the strain-log time relationship based on hypothesis A & B with different sample thickness.

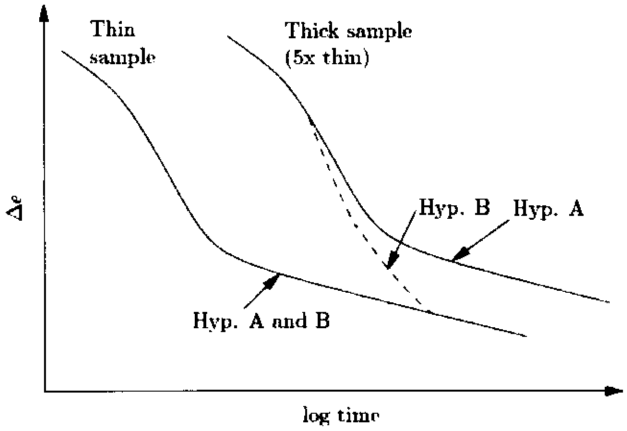

Figure 2.4: Strain-log time curve for hypothesis A & B.
(after Jamiolkowski et al., 1985).

Singh and Mitchell (1968) pointed out that creep happens when the stress level is about 30% to 90% of initial soil strength and the logarithm of strain rate is linear with the logarithm of time for a given stress. An equation with three parameters for the creep strain rate $\dot{\varepsilon}$ was provided as

$$\dot{\varepsilon} = A \cdot \exp(\overline{aq})(t_1 / t)^m \tag{2.3}$$

where A is the soil property that reflects composition, structure, and stress history,

$\overline{a} = aq_{\max}$ and $\overline{q} = q / q_{\max}$,

q is the deviator stress, $q_{\max}$ is the strength,

a indicates the stress effect on the creep rate,

m controls the rate at which the axial strain rate decreases with time.

The parameters A, a and m can be determined by normal creep tests for a given soil, and further laboratory results reported by Augustesen et al. (2004) indicated that the value of m is between 0.7 and 1.3 for most geo-materials.

Taylor (1942) described the secondary consolidation as a 'plastic resistance' which is assumed to be based on bond resistance and viscous structural resistance. He believed that the secondary consolidation is due to a remoulding of the soil structure which is independent of the soil permeability and thus he defined the material as a quasi-plastic material. The relationship of the void ratio, stress and time was given as shown in Figure 2.5.

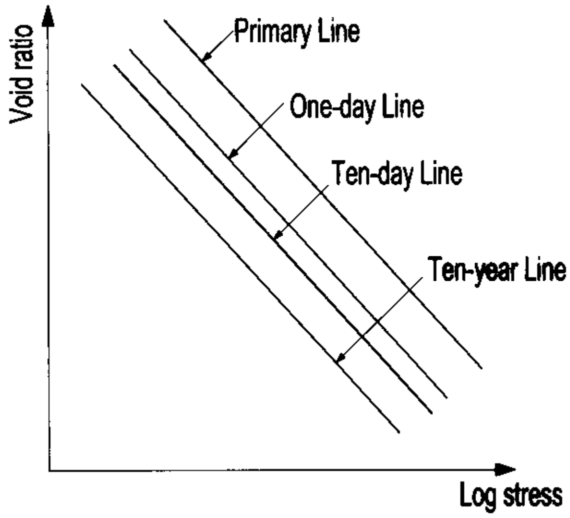

Figure 2.5: Void ratio-stress relationships for different times. (after Taylor 1942).

The coefficient of secondary settlement C_α is a commonly used parameter for describing secondary consolidation. Based on a series of reported data, Mesri (1973) concluded that soils which show high compressibility in the primary stage are also highly compressible in the secondary phase, and he classified the clay according to its value of C_α as shown in Table 2.1.

C_α	Secondary Consolidation
<0.002	Very low
0.004	Low
0.008	Medium
0.016	High
0.032	Very high
0.064	Extremely high

Table 2.1. Classification of clay based on C_α (Mesri, 1973)

A unique relationship between the secondary compression index C_α and compression index C_c was defined by Mesri & Godlewski (1977) as ' C_α / C_c ' to analyse the secondary consolidation. It was found that the value of C_α / C_c for geotechnical materials is normally less than 0.07 (Terzaghi et al. 1996). Tables 2.2 and 2.3 show some collections of the properties of soil from all around the world, where the maximum C_α / C_c value is 0.055 for the Vasby soft clay deposit in Sweden (Mesri et al, 1999). Mesri and Castro (1987) reached the conclusion that the C_α / C_c value for inorganic soft clays and highly organic plastic clays is about 0.04±0.01 and 0.05±0.01, respectively.

In one-dimensional tests, the vertical stress and strain dominate the creep behaviour, while under three-dimensional conditions, the deviator stress level may significantly affect the creep rate of clay under three-dimensional stresses. Triaxial tests were also carried out to study the materials' creep performance under three-dimensional conditions (Akai, 1963; Barden, 1968; Yamada, 1968; Baek & Moriwaki, 2004).

Soft clay deposits (1)	Location (2)	Wn (%) (3)	Wl (%) (4)	Wp (%) (5)	CF (%) (6)	σ'_p/σ'_{v0} (7)	C_α/C_c (8)
Batiscan	Quebec, Canada	71–88	49	22	80	1.6–1.7	0.03
Berthierville	Quebec, Canada	57–63	46	24	36	1.3–1.4	0.044
Boston Blue	Boston, USA	24–29	33	18	40	3.2	0.026
Broadback	Quebec, Canada	42–48	36	25	67	2.6–3.2	0.04
Brown Mexico City	Mexico City, Mexico	311–340	361	91	15	1.4	0.046
Chicago Blue	Chicago, USA	23	24	16	20	—	0.033
La Grande	Quebec, Canada	55–58	64	26	52	1.8–2	0.052
Ottawa	Quebec, Canada	80–91	68	29	75	1.7	0.03
Louiseville	Quebec, Canada	64–71	65	28	72	2.6–2.9	0.03
Olga	Quebec, Canada	85–94	67	29	67	2.2–2.5	0.033
Organic Poulding	Ohio, USA	84	70	45	53	—	0.048
Pancone (Pisa)	Pisa, Italy	55–65	75–90	34–36	73	1.65–2.02	0.034
San Francisco Bay Mud	San Francisco, USA	86–97	89	37	42	1.2	0.05
Singapore Marine	Singapore	38–79	54–86	19–32	54	1.4	0.032
St. Alban	Quebec, Canada	48–74	31–42	18–22	42	2.1–3.0	0.024
St. Espirit	Quebec, Canada	74–91	75	27	76	3.4–3.7	0.038
St. Hilaire	Quebec, Canada	62–71	55	23	76	1.4–1.5	0.031
Vasby	Vasby, Sweden	114–122	122	41	67	1.5–1.9	0.055

Table 2.2. Properties of soft clay deposits (Mesri et al, 1999).

Shale deposits (1)	Location (2)	Wn (%) (3)	Wl (%) (4)	Wp (%) (5)	Ws (%) (6)	CF (%) (7)	C_α / C_c (8)
Bearpaw	Ft. Peck Dam, Montana	15.8	288	44	10	88	0.029
Claggett	Benton, Montana	11.7	157	31	11	71	0.024
Comanche	Proctor Dam, Texas	11.5	62	32	22	68	0.023
Cucaracha	Panama Canal, Panama	18.4	111	42	11	63	0.022
Denver	Denver, Colorado	30.5	121	37	11	67	0.022
Patapsco	Washington, D.C.	21.6	77	25	11	59	0.017
Pierre	Limon, Colorado	24.3	82	30	13	42	0.030

Table 2.3. Properties of clay shales (Mesri et al, 1999).

Murayama and Shibata (1958) proposed an "upper yield value" which is the stress corresponding to the first inflection point of a log stress versus log axial strain plot, and indicated that hypothesised stress level above this "upper yield value" will lead to tertiary creep. They carried out laboratory drained triaxial creep tests on Umeda Clay, and the results are presented in Figure 2.6 in the form of log strain rate versus normalised strain (strain/strain at peak stress). Later, Hunter and Khalili (2000) proposed a simple creep criterion where the level of shear strain at which the onset of failure due to creep occurs is equivalent to the shear strain at peak stress ε_{peak} in the equivalent conventional strength test. The onset of failure is defined as the point of minimum strain rate, the change from primary to tertiary creep behaviour. The results indicate good correlation with the creep strain criterion.

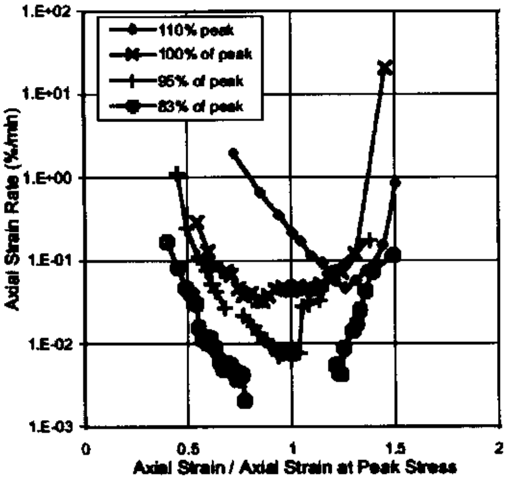

Figure 2.6: Drained creep tests on Umeda clay (Murayama and Shibata, 1958).

Based on the drained and undrained triaxial creep tests on diverse clays, Singh and Mitchell (1968) pointed out that creep rate increases with the deviator stress level and proposed a parameter m for the relationship between $\log\dot{\varepsilon} - \log t$ (Equation 2.4). It was suggested that m is mostly between 0.75 and 1.0 and it is independent of the deviator stress level for a given soil. But, the opinion that the m value is independent of the deviator stress level was challenged by Feda (1992) and Tian et al. (1994), as their observation of triaxial test data showed that the value of m changed with the deviator stress level, and that the value of m is different for axial and volumetric creep deformation.

$$m = -\frac{\Delta \log \dot{\varepsilon}}{\Delta \log t} \tag{2.4}$$

Creep tests on rock are rather rarer then tests on soils, however some methods have been reported in the literature. Li and Xia (2000) used an electronic hydraulic servo-controlled stiff testing machine to carry out multi-level loading and unloading cyclic uniaxial compression creep tests on four types of rock, and some rheological model parameters were derived for the different rocks. Different strain rates were applied in the tests, the effects of strain rates on rock strength and limit strain were discussed and evaluated using empirical equations. It was shown that an increase of applied strain rate leads to higher peak strength and peak limit strain, and the peak strain has a linear relationship to the logarithm of strain rate.

A laboratory creep test was carried out under a constant temperature on Sicilian marble specimens, and both axial and lateral deformation of the samples was measured by dial gauges and shown in Figure 2.7 (Singh, 1975). It was seen that the creep curves in both directions display three idealized stages, and the lateral creep rate is much greater than in the axial direction. An empirical power law curve was then used to fit the laboratory results up to the end of the steady stage of creep under a sustained stress.

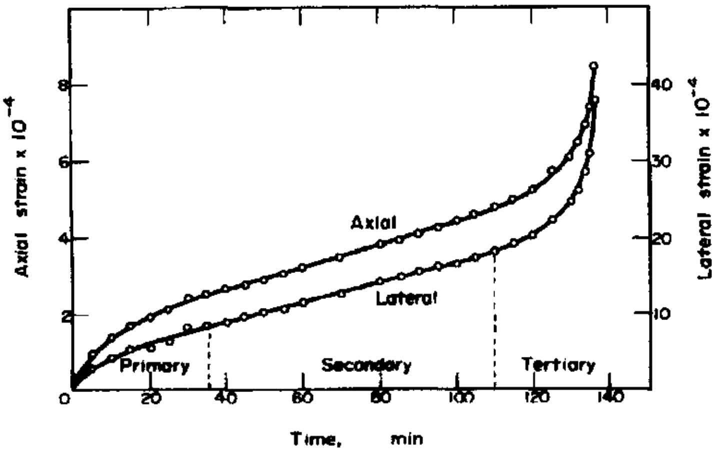

Figure 2.7: Axial- and lateral-creep curves for Sicilian marble (Singh, 1975).

2.2.3 CREEP TESTS ON SHOTCRETE

Like clay and rock, concrete and shotcrete materials also display time-dependent creep deformation under sustained load. Oedometer tests and triaxial texts have also been applied to creep tests on concrete and shotcrete samples. Persson (1998) studied the quasi-instantaneous, short-term and long-term deformations of high performance concrete with sealed curing. More than 100 cylinders and 400 cubes made of eight different types of concrete were studied in relation to creep and shrinkage, hydration, internal relative humidity, and compressive strength. The specimens were sealed-cured at constant temperature 20°C, and one heat-cured concrete was studied at temperatures other than 20°C varying between -20°C and 60°C. His results indicated that the creep rate was dependent on both the duration of loading and the maturity of the High Performance Concrete (HPC), and the specific creep was reduced with an increase in the silica fume content. An example result of long-term creep deformation of high performance concrete is presented in Figure 2.8a. The ratio of testing stress to cube compressive strength was either 0.3 or 0.6. The loading was performed on concrete 1 or 2 days old for high stress level (0.6), and 2 or 28 days old for low stress level (0.3). Figure 2.8b indicates the relationship of creep rate vs. temperature of the specimen and it shows that the creep rate of HPC at -1°C was significantly larger than at other temperatures. It may be due to the formation of salts only stable at this temperature, since at -1°C no freezeable water exists in HPC owing to self-desiccation.

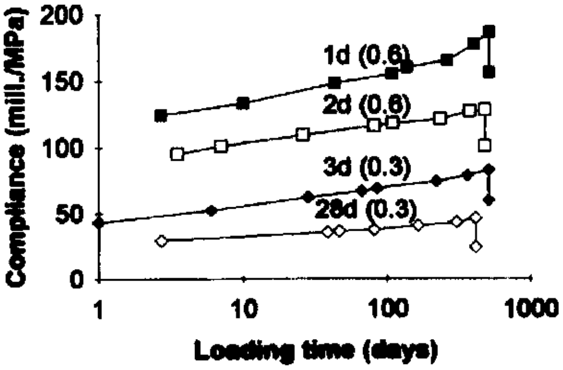

Figure 2.8a: Long-term creep of high performance concrete (HPC) (Persson, 1998).

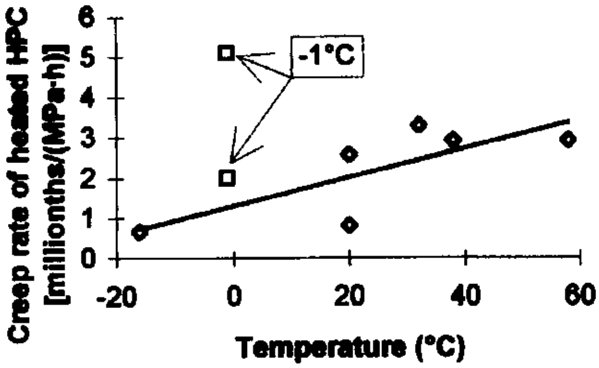

Figure 2.8b: Long-term creep of high performance concrete (HPC) (Persson, 1998).

The creep behaviour of fibre reinforced shotcrete under flexural action has been studied by many researchers using round determinate panel tests recently (Bernard, 2004; Tran et al., 2005). In a flat roof tunnel, the shotcrete lining on the crown of the tunnel is normally under bending. The creep behaviour of shotcrete under flexure is quite different to when the material is under compression. The tension strength of concrete is not taken into account while the fibre carries the load in the tension region and dominates the creep performance of shotcrete when it is under bending. Bernard (2004) carried out time-dependent Round Determinate Panel (ASTM C-1550) tests on different types of shotcrete reinforced with macro-synthetic fibres and steel fibres. The deflection curves of circular panel samples containing three different fibres are presented below (Figure 2.9).

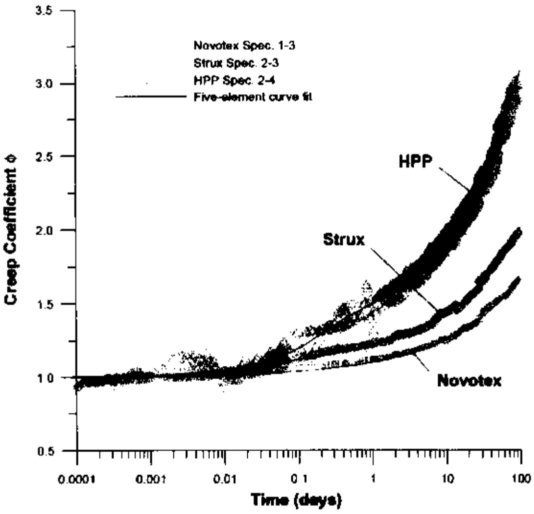

Figure 2.9: Creep curves of three different types of fibre reinforced shotcrete (Bernard 2004).

2.2.4 LABORATORY DATA FOR STRESS RELAXATION

Besides creep phenomena, stress relaxation is another manifestation of the time-dependent effects of a soil. When under a constant strain, the stress in a soil or rock will decrease gradually over time and this phenomenon is defined as the stress relaxation. Since in most geotechnical cases, the projects are under a constant load rather than a constant strain, most research interest has been devoted to creep tests. However, stress relaxation tests have also been used by many researchers to study the stress-strain-time relationship of soil (Kondner and Ho, 1965; Murayama, 1969; Ladanyi and Melouki, 1993).

Silvestri et al. (1988) carried out consolidated undrained triaxial relaxation tests on a soft overconsolidated clay and found that the pore water pressure remained nearly constant during the relaxation process, which was in accord with observations reported by Murayama and Shibata (1964) and Lacerda and Houston (1973). Murayama and Shibata (1964) also reported that the stress rate is linearly related to log time after the first time period. Lacerda and Houston (1973) provided an equation for the stress variation rate:

$$\frac{q}{q_0} = \frac{\bar{q}}{\bar{q}_0} = 1 - s\log\left(\frac{t}{t_0}\right) \qquad (2.5)$$

where q is the observed deviatoric stress with time,

q_0 is the initial deviatoric stress,

$\overline{q}$ is the deviator stress level,

$\overline{q}_0$ is the deviator stress level at time t_0,

t is the time since beginning of relaxation,

t_0 is the initial time period at the beginning of relaxation,

s is the slope of the relaxation curve as shown in Figure 2.10.

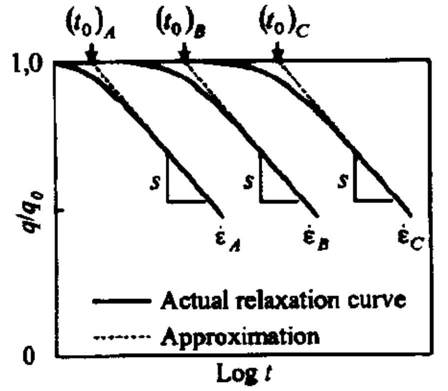

Figure 2.10: q/q_0 - $\log(t)$ relationship in relaxation tests (Lacerda and Houston, 1973)

Oda and Mitachi (1988) performed undrained triaxial stress relaxation tests to investigate saturated remoulded clays under isotropic stress. Their results showed that the principal stress changed linearly with logarithm of time by two straight lines independent of strain level, strain rate and mode of stress application in the preceding undrained shear process, and the intersection point of the two stress straight lines is close to the effective stress path calculated by the Cam-clay model proposed by Roscoe et al. (1963).

2.2.5 FACTORS INFLUENCING THE CREEP PERFORMANCE

An idealized creep curve will undergo three stages: primary, steady, and tertiary state creep (Figure 2.11, Singh & Verma, 2005). The primary creep strain is usually small and governed by initial dislocations in the material (Okubo et al. 1991). The steady creep will last for a long time period and is the most important region in the creep period. When the stress level is relatively high, the creep curve may enter the tertiary stage, and the strain will accelerate and lead to the fracture of the material.

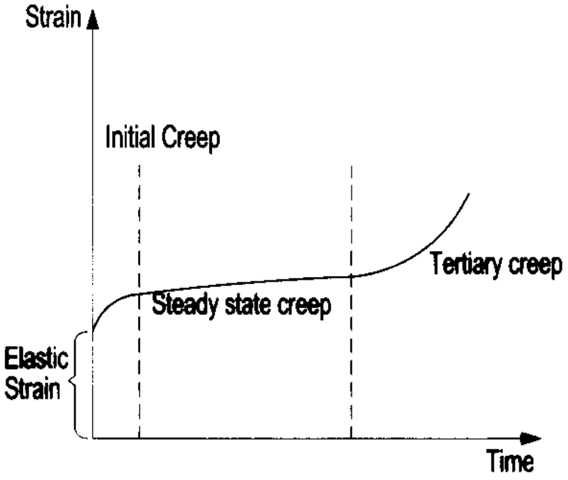

Figure 2.11: Idealized creep curve (Singh & Verma, 2005).

The creep behaviour is complex and determined by many factors. Kranz (1979) investigated the sub critical crack growth of crystalline rock and pointed out that the stress level, chemical environment, temperature, and the microstructure of the rock are the most important factors affecting the creep rate of the material.

The rock type itself is a main factor affecting the creep rate. Different rocks display different time-dependent strain, hard rocks such as gabbro and granite normally show little creep deformation, while other rocks such as salt, potash, trona, coal, and alabaster display significant creep deformation with time when under a constant load (Singh, 1975).

It was also observed that clay and sand both display creep deformation but have different basic time mechanisms. Leroueil and Marques (1996) indicated that the creep, or relaxation behaviour of a given clay is governed by the "isotach" behaviour. The observed laboratory measurements of clay match this isotach behaviour to some extent. This means that creep and relaxation properties can be obtained by means of constant rate of strain tests and vice versa. The tests on sand carried out by Matsushita et al. (1999) exhibited clear creep and relaxation but no strain rate effects. This means that the sand does not exhibit the isotach behaviour as does clay. This different behaviour of clay and sand are compared in Figure 2.12, where q is the deviatoric stress, ε_1 is the axial strain.

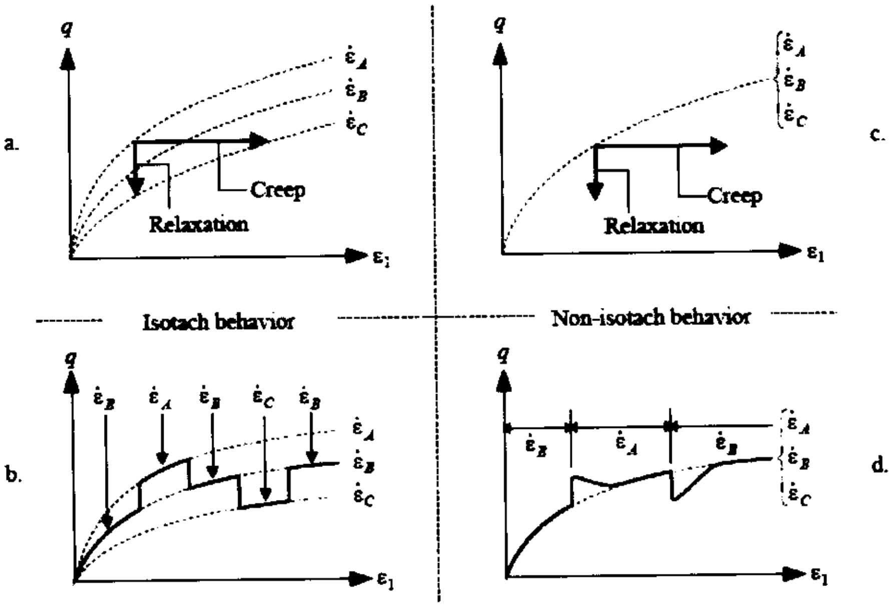

Figure 2.12: Isotach behaviour of clay for a) creep and relaxation and b) stepwise change in rate, Non-isotach observed behaviour of sand for c) creep and relaxation and d) stepwise change in rate (Liingaard et al. 2002).

The nature of pore water and consolidation rate also influences the creep performance of rock. Schiffman (1964) used a model with a series of Kelvin elements to represent the viscoelastic influence of time-dependent secondary deformation. Several laboratory tests were carried out on the normally consolidated and over consolidated clay samples, and the results showed that the creep rates are similar for isotropically consolidated triaxial tests, and that over-consolidated samples have lower creep rates.

Temperature and stress affect the creep rate of a soil significantly. Generally speaking, an increase of stress and temperature will lead to an increasing rate of creep deformation as shown in Figure 2.13 (Singh & Verma, 2005). Leroueil and Marques (1996) suggested a unique stress-strain-strain rate-temperature relationship for a given soil and explained the activation energy at the level of molecules, atoms or particles by the rate process theory. They reached the conclusion that viscous effects on the limit state curve, the undrained shear strength and the preconsolidation pressure of clays are significant, of the order of

10% per logarithmic cycle of strain rate or a temperature change of about 12 °C. Mott (1956a, 1956b) studied the creep performance of metals and crystals at high and low temperature. He indicated that the creep mechanism is dislocation climb when the temperature is between 0.3℃ and 0.7℃ of a material's melting temperature, while the creep is independent of temperature below $10^o K$ in cadmium. An equation that can be used to calculate the dislocation climb was provided by Mott (1956a) as:

$$\frac{\dot{\varepsilon}_{ss}}{\dot{\varepsilon}_0} = A\left(\frac{\sigma}{\sigma_0}\right)^m e^{-HkT} \tag{2.6}$$

where A is constant parameter,

H is the activation energy for the diffusion,

σ and σ_0 are the applied stresses.

T is temperature.

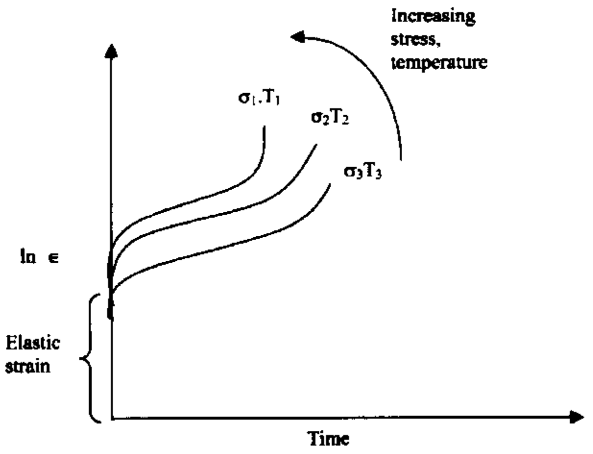

Figure 2.13: Strain versus time creep behaviour effect of temperature and stress (Singh & Verma, 2005).

2.3 THEORETICAL INVESTIGATION OF CREEP PHENOMENA

Historical field observations and laboratory tests have allowed accumulation of a great deal of data for the qualitative and quantitive investigation of creep behaviour. Many analytical hypotheses and different viscoelastic or viscoplastic constitutive creep laws have been proposed to describe the relationship between stress, strain, and time, as well as temperature (Hoefer and Knoll, 1971; Zakhariev et al., 1971; Starfield and McClain, 1973; Bridge, 1979). The creep models were developed based on the change of micro-structure of the material and/or thermal effect processes, and some important models are presented below.

2.3.1 RHEOLOGICAL METHODS

The mechanical properties of soil can be represented by models composed of springs, dashpots and sliders. The characteristics of the three idealized elementary models are given below:

Spring: $\sigma^e = E \cdot \varepsilon^e$

Dashpot: $\sigma^v = \eta \cdot \dot{\varepsilon}^v$

Slider: $\sigma - \sigma_y = \begin{cases} \sigma - \sigma_y & for \ \ \sigma > \sigma_y \\ 0 & for \ \ \sigma \leq \sigma_y \end{cases}$

where E is the spring elastic constant, η is the viscosity constant, σ_y is the threshold stress.

Several rheological models were developed and the two most well known basic models are the Maxwell model and Kelvin/Voigt model as shown in Figure 2.14. Maxwell (1867) assumed that the observable macroscopic properties of a material can be expressed by a combination of microscopic elasticity and viscosity elements. A classic Maxwell model is composed by a spring and a dashpot in series, while the Kelvin/Voigt model connects the two elements in parallel.

In the Maxwell model, the stress is equal in the spring and dashpot and the rate of strain is written as:

$$\dot{\varepsilon}_{total} = \frac{d\varepsilon_D}{dt} + \frac{d\varepsilon_S}{dt} = \frac{\sigma}{\eta} + \frac{\dot{\sigma}}{E}$$

In the Kelvin/Voigt model, the spring and dashpot have the same deformation and the stress-strain-time behaviour is governed by:

$$\sigma(t) = E \cdot \varepsilon(t) + \eta \cdot \frac{d\varepsilon(t)}{dt}$$

In the Maxwell model, when a load is applied, the spring is compressed under load immediately and the dashpot represents the viscous displacement with time at a constant rate. In the Kelvin/Voigt model, the strain will increase at a decreased rate and asymptotically reach a strain of σ_0 / E. Thus the Kelvin/Voigt model is more suitable for the analysis of creep behaviour of a soil, since in the Maxwell model, the strain is linear with time, which is not the case for the creep performance of most materials. Another model often used in geotechnical problems is the Bingham model which consists of a dashpot and a slider in parallel to define the yield strength value and the viscosity coefficient respectively.

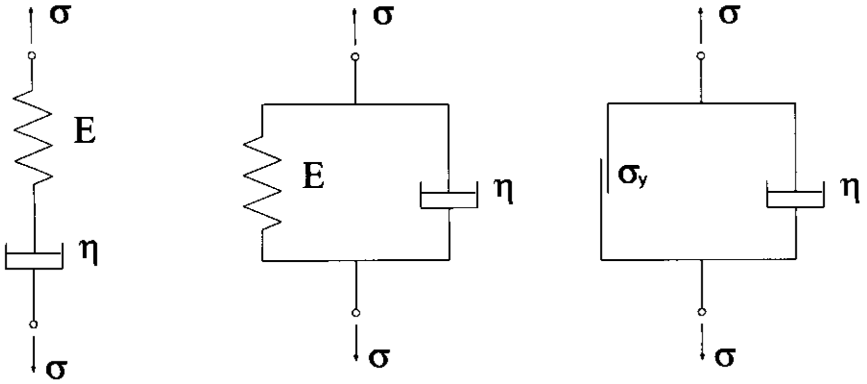

Maxwell model Kelvin/Voigt model Bingham model

Figure 2.14: Common rheological models

Different rheological models making use of linear springs, linear/nonlinear dashpots and sliders have been developed to represent the stress-strain-time relationship of different soils (George, 1969; Komamura and Huang, 1974; Ter-Stepanian, 1975; Gioda and Cividini, 1979; Akagi, 1985). These mechanical models consist of the Maxwell model, Voigt model and/or Bingham model to give a description of some visco-elastic-plastic property of a given soil under certain load conditions. For instance, Lopes et al. (1994) developed a creep model based on a series of Kelvin models; a creep function was derived as:

$$J(t,x) = \sum_{\mu=1}^{k} \frac{\tau_\mu}{\eta_\mu(x)} \left(1 - e^{-\frac{t-x}{\tau_\mu}} \right) \tag{2.7}$$

where τ_μ is the retardation coefficient depending on the Kelvin element's elastic modulus E_μ and viscosity coefficient η_μ, x is the time when the loading starts. The strain at a given time can then be calculated by using the following equation:

$$\varepsilon(t) = \int_{t_0}^{t} J(t,x)\frac{\partial\sigma}{\partial x}dx = \sum_{\mu=1}^{k}\int_{t_0}^{t}\frac{\tau_\mu}{\eta_\mu(x)}\left(1-e^{-\frac{t-x}{\tau_\mu}}\right)\frac{\partial\sigma}{\partial x}dx \tag{2.8}$$

Oida (1984) used a three-element rheological model to analyse the linear time-dependent viscoelastic behaviour of a soil. The model was composed of a spring connected with a Voigt model in series as shown in Figure 2.15. The stress-strain relationship of the element is written as:

$$(E+E_1)\sigma + \eta_1\dot{\sigma} = EE_1\varepsilon + E\eta_1\dot{\varepsilon} \tag{2.9}$$

Both stress relaxation and time-dependent creep tests for soil were simulated by the numerical method using this three-element model, and the results showed a good fit with the experiment data.

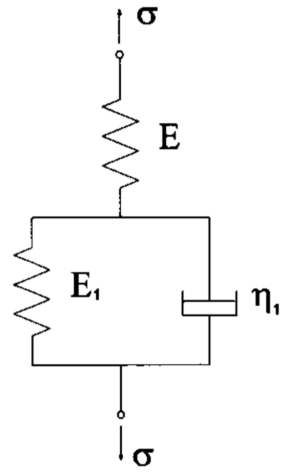

Figure 2.15: Oida's model

Pan (1986) used a Burger's model as shown in Figure 2.16 to analyse the paddy soil in South China. He indicated that the deformation of soil under a load consisted of three parts: elastic deformation μ_e, viscous deformation μ_v and delayed deformation μ_d, the total deformation is calculated by:

$$\mu_{total} = \mu_e + \mu_v + \mu_d = \frac{\alpha P}{\sqrt{A}}\left[\frac{1}{E_M} + \frac{t}{\lambda_M} + \frac{1}{E_K}(1-e^{-E_K t/\lambda_K})\right] \tag{2.10}$$

where t is time,

α is the shape factor,

P is the load,

A is the area of an experimental round plate,

$E_M, E_K, \lambda_M, \lambda_K$ are rheological parameters, here $\lambda_M = 4\eta^*$, $E_K = 4K$, $E_M = \frac{4}{3}E$, and $\lambda_K = \frac{4}{3}(3\xi + \eta^*)$,

η^* is the apparent plastic viscosity,

ξ is the viscosity,

K is the bulk modulus,

E is the elastic modulus.

Later, Pan et al. (1990) modified his model for remoulded paddy soils. He observed that after the soil sample is disturbed, the instantaneous deformation increases, followed by rebounding within a very short time. He also indicated that the deformation is linear to a time less than the time of rebounding, and then the Burger's model is used after the rebound time.

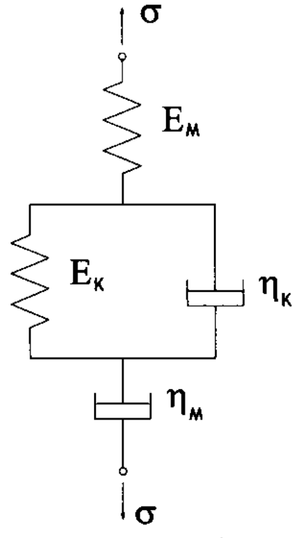

Figure 2.16: Burger's model

Murayama & Shibata (1959) and Wu et al. (1964) employed rate process theory to analyse the consolidation deformation of clay and a model as shown in Figure 2.17 was proposed. The friction slider represents the "resistance stress" and they assumed that the material will not creep if the stress level is below the "resistance stress". This was because it is commonly observed in laboratory tests that when the load is relatively low, creep deformation is very small or negligible.

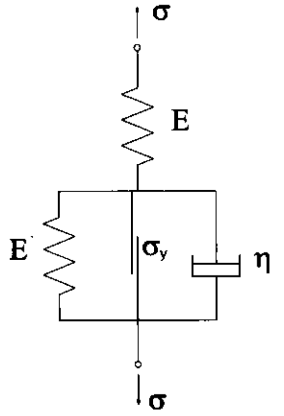

Figure 2.17: The Murayama & Shibata (1959) model

Poulos et al. (1976) separated the volumetric and deviatoric creep behaviour. A Maxwell model with a linear spring and dashpot was used to represent the volumetric and deviatoric components separately. Carter and Booker (1983) also used rheological models as shown in Figure 2.18 to represent the volumetric and deviatoric creep behaviour respectively, and the creep functions are presented below:

$J_V(t) = A_V - B_V \exp(-\alpha_V t)$

$J_D(t) = A_D - B_D \exp(-\alpha_D t)$

where J_V is the volumetric creep function and J_D is the deviatoric creep function.

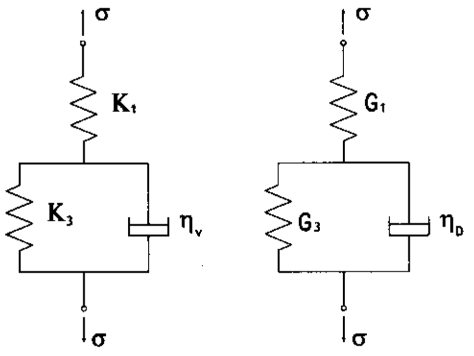

volumetric creep model deviatoric creep model

Figure 2.18: Carter and Booker's model (1983)

proposed. The friction slider represents the "resistance stress" and they assumed that the material will not creep if the stress level is below the "resistance stress". This was because it is commonly observed in laboratory tests that when the load is relatively low, creep deformation is very small or negligible.

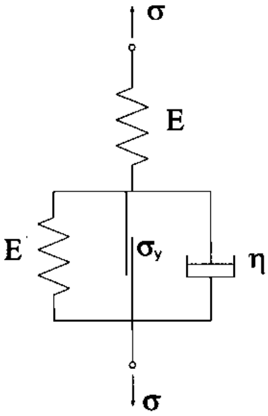

Figure 2.17: The Murayama & Shibata (1959) model

Poulos et al. (1976) separated the volumetric and deviatoric creep behaviour. A Maxwell model with a linear spring and dashpot was used to represent the volumetric and deviatoric components separately. Carter and Booker (1983) also used rheological models as shown in Figure 2.18 to represent the volumetric and deviatoric creep behaviour respectively, and the creep functions are presented below:

$$J_V(t) = A_V - B_V \exp(-\alpha_V t)$$

$$J_D(t) = A_D - B_D \exp(-\alpha_D t)$$

where J_V is the volumetric creep function and J_D is the deviatoric creep function.

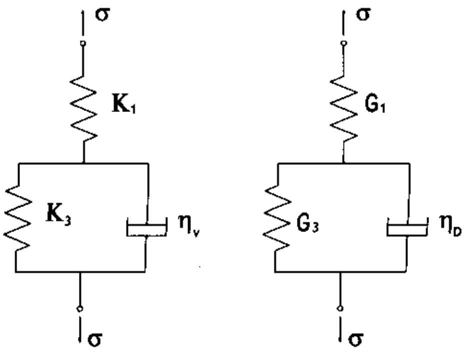

volumetric creep model deviatoric creep model

Figure 2.18: Carter and Booker's model (1983)

All of these different rheological models have been used to predict time effects of soil under a certain stress, but the parameters used in the rheological models are not stress dependent, thus different values of parameters need to be selected for different stress levels. For a geotechnical project where the soil or rock is under a known stress range, the parameters of the rheological models can be obtained from laboratory or in situ tests under the same stress level and the creep deformation can then be predicted over time. However if the stress range changes (i.e. the bulk or deviator stress changes) then more advanced models are needed.

2.3.2 GENERAL TIME-STRESS-STRAIN MODELS

To describe the mechanical behaviour of a material under any possible load level, general time-stress-strain constitutive laws have been developed. These models are not limited to the stress paths from which the samples are calibrated and can be implemented in a finite element program.

Yin and Graham (1989) developed a one-dimensional model and introduced a new concept 'equivalent times' t_e, which is defined as the time needed to creep from a reference time line where $t_e = 0$ to the current vertical strain ε_z and vertical stress σ_z. Three parameters λ (elastic-plastic parameter), κ (elastic stiffness of soil) and ψ (constant creep parameter) were used in the model to define the elastic-viscoplastic property of a soil, and conventional oedometer tests were utilized to acquire the value of these parameters for a certain soil. The model can be used to represent the creep tests, relaxation tests, and constant rate of strain tests, as well as constant rate of stress tests. A general constitutive equation for stress-strain behaviour under any loading condition was provided by Yin and Graham (1994) as follows:

$$\dot{\varepsilon}_z = \frac{\kappa}{v}\cdot\frac{1}{\sigma_z'}\dot{\sigma}_z' + \frac{\psi}{v t_0}\cdot\exp\left[-(\varepsilon_z-\varepsilon_{z0})\frac{v}{\psi}\right]\left(\frac{\sigma_z'}{\sigma_{z0}'}\right)^{\lambda/\psi} \tag{2.11}$$

where ε_{z0} is the initial strain under initial stress σ_{z0}',

v is the specific volume,

κ is the elastic stiffness material parameter of the soil,

λ is the elastic–plastic material parameter,

ψ is the creep parameter for a given soil;

t_0 is the intrinsic creep parameter in units of time.

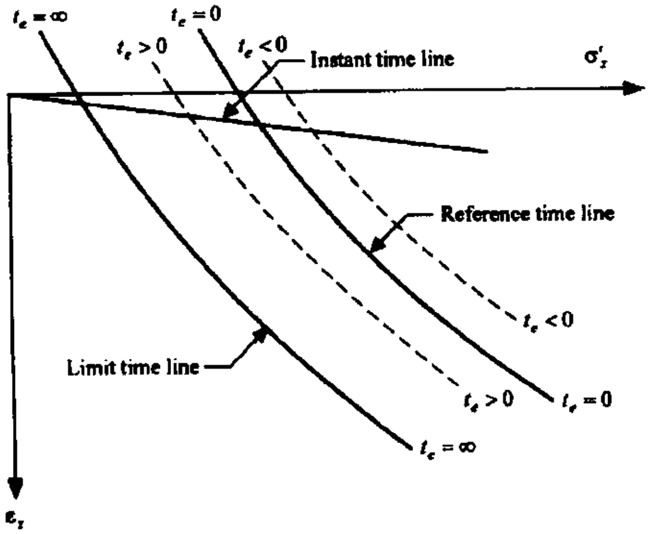

Figure 2.19: Yin and Graham's model (1989)

This one-dimensional model was then developed by Yin and Graham (1999) into a three-dimensional model based on Modified Cam-Clay and viscoplasticity. The constitutive law for the soil under triaxial stress states was given by:

$$\dot{\varepsilon}_{ij} = \dot{\varepsilon}^{e}_{ij} + \dot{\varepsilon}^{vp}_{ij} = \left(\frac{1}{2G}\dot{s}_{ij} + \frac{\kappa}{3\mathrm{v}}\frac{\dot{p}'}{p'}\delta_{ij}\right) + \frac{\psi}{\mathrm{v}t_0}\cdot\exp\left[\left(\varepsilon^{r}_{vm0} + \frac{\lambda}{\mathrm{v}}\ln\frac{p'_m}{p'_{m0}} - \varepsilon_{vm}\right)\frac{\mathrm{v}}{\psi}\right]\frac{1}{2p' - p'_m}\frac{\partial F}{\partial \sigma'_{ij}} \tag{2.12}$$

where $\dot{\varepsilon}_{ij}$ is the total strain rate,

$\dot{\varepsilon}^{e}_{ij}$ and $\dot{\varepsilon}^{vp}_{ij}$ are the elastic and visco plastic strain rate,

p' is the mean effective stress,

σ'_{ij} is the effective stress,

$\dot{s}_{ij}$ is the deviator stress rate,

κ/v is a constant for elastic behaviour (v is specific volume),

λ/v is a constant for the slope of a 'reference time' line,

ψ / v is a creep parameter,

t_0 is a creep parameter in unit of time,

ε^r_{vm0} and p'_{m0} are model parameters.

Skrzypek (1993) introduced the concept of hardening into engineering creep theories, which were mainly based on laboratory observation and phenomenological laws. There are three main basic engineering models for the creep phenomenon: the total stain model, the time-hardening model and the strain-hardening model.

In the total strain model, the total strain consists of two parts: the elastic strain ε^e plus the visco plastic component ε^c. The creep strain is often represented as a function of stress and time as given below:

$$\varepsilon^c = f(\sigma)g(t)$$

The relation between the creep strains and the stress is often modelled by a power function in the total strain model, and it was recommended that the theory should be used for the constant stress condition or for the case where stress is changing at a very low rate (Rabotnov, 1969).

In the time-hardening model, the strain rate is used instead of strain in the equation and the hardening is governed by time.

$$\dot{\varepsilon}^c = f(\sigma)g(t)$$

In the strain-hardening model, the strain is used as the hardening parameter

$$\dot{\varepsilon}^c = f(\sigma)g(\varepsilon^c)$$

Some widely used rate-dependent viscoplastic models were developed based on the overstress concept (Malvern, 1951, 1984; Perzyna, 1963, 1966; Adachi and Oka, 1982). Perzyna (1966) assumed that the elastic strains are time-independent and the viscoelastic strains are insignificant in the elastic region. The visco-plastic strains in the overstress model are independent of the stress history and determined by the current stress only. An equation to calculate the viscoplastic strain rate was proposed as:

$$\dot{\varepsilon}^{vp}_{ij} = \gamma\phi(F)\frac{\partial g}{\partial \sigma'_{ij}} \tag{2.13}$$

where γ is the fluidity parameter, ϕ is the viscous factor, F is the overstress function, g is the potential function, and $\sigma_{ij}^{'}$ is effective stress. The value of overstress parameter $\phi(F)$ can be determined by laboratory tests (Oka, 1994).

2.3.3 CREEP MODELS FOR SHOTCRETE

Fibre reinforced shotcrete is used in the tunnel structure as a support lining and it displays similar creep and relaxation performance as does soil/rock. Different creep models which represent the mechanical behaviour of soil/rock were also used to fit the creep deformation of shotcrete.

Mangat and Motamedi (1985) proposed a theoretical model to predict the creep of steel fibre reinforced cement matrices. The model represented the cement matrices by an aligned steel fibre which is surrounded by a thick cylinder of the cement matrix. They indicated that the steel fibre does not affect the delayed elastic component of creep, but provides restraint to the flow component of creep of the matrix. A simple empirical equation was derived to predict the creep deformation of steel fibre reinforced concrete under a sustained stress/strength ratio of 0.3:

$$\varepsilon_{fc} = \varepsilon_{oc}(1 - 1.96\mu\upsilon_f l / d) \tag{2.14}$$

where ε_{fc} is the creep strain of steel fibre reinforced concrete,

ε_{oc} is the corresponding creep of cement matrices,

μ is the coefficient of friction at the steel fibre and cement matrix interface,

υ_f is the fibre content of the matrix,

l and d are length and diameter of the fibre.

Based on the assumption that shear stress is produced between the fibre and surrounding matrix as the matrix deforms, Zhang (2003) developed an analytical method to model the fibre influence on creep of fibre reinforced cementitious composite. The creep strain was calculated by multiplying the matrix creep strain by a fibre influence factor:

$$\varepsilon_c = \varepsilon_{cm} \cdot \varphi = \varepsilon_{cm} \cdot \left[1 - \eta \frac{kV_f}{1 - kV_f(1 + 1/\gamma_1)} \left(1 - \frac{1}{\beta\gamma} \tan \mathrm{h} \beta\gamma \right) \right] \qquad (2.15)$$

where ε_c and ε_{cm} are the creep strains of composite and pure matrix, respectively,

φ is the fibre influence factor,

V_f is the fibre content,

k is the fibre orientation factor,

$\eta = \frac{E_f}{E_m}$, $\gamma = \frac{kl_f}{2r_f}$, $\gamma_1 = \frac{kl_f}{2R}$ and $\beta = \sqrt{\frac{E_m}{(1+v_m)E_f \log(R/r_f)}}$,

E_f is the elastic modulus of the fibre,

E_m is the elastic modulus of the matrix,

l_f is the length of fibre,

r_f is the radius of fibre,

$R = r_f/(kV_f)^{1/2}$.

A parametric study of the model indicated that the creep performance is significantly influenced by the elastic modulus of the fibre, fibre length and diameter. It was shown that the higher the elastic modulus of the fibres and the higher the fibre content, the lower the creep rate.

Sercombe et al. (2000) modelled the creep of shotcrete by two mechanisms: a stress-induced water movement for the short-term creep and a relaxation in the micropores of the cement for the long-term creep, and the creep was considered within the framework of closed reactive porous media. The creep parameters were based on a standard compression creep test loading at 28 days. The model was then applied in the tunnel structure by Hellmich et al. (2000) to analyse a tunnel excavation using the new Austrian tunneling method. The study showed the significance of shotcrete creep for the long-term behaviour of the combined soil-shotcrete structure.

2.4 ANALYSIS OF TIME-DEPENDENT TUNNEL CLOSURE

Many methods using creep analysis have been utilized to predict the time-dependent performance of structures in geotechnical engineering projects. Saito (1965) described a method of predicting time-related landslide movement by employing a steady-state creep model, and later a creep model based on the tertiary stage creep was used to predict the time of slope failure (Saito, 1969). Lopes et al. (1994) employed a rheological creep function to predict the behaviour of a sloped reinforced soil wall. Different creep methods and models were used to investigate the time-dependent behaviour of a tunnel structure by several researchers (Semple et al., 1973; Ghaboussi and Gioda, 1977; Kaiser and Morgenstern, 1981; Carter and Booker, 1982, 1983). Empirical methods and analytical methods were mainly employed before the 1980's. With the development of computer technology, finite element methods have now become the most powerful tools for solving the time-dependent problems associated with tunnel support structures.

2.4.1 EMPIRICAL METHODS

Empirical creep models were directly derived from measured laboratory relationships between stress, strain and time. Some commonly used models are power laws, exponential laws and hyperbolic law models. These models can simply fit the observed test data and successfully predict the creep performance of materials in specific cases.

Peck (1969) introduced an empirical method to investigate the short term surface settlement due to tunnel excavation. He concluded that the settlements above the tunnel opening are symmetrical above the vertical axis of the tunnel and can be described by a Gaussian error function (Figure 2.20). This method provided an estimate of surface settlement at various distances from the centreline of the tunnel, and the vertical settlement was calculated by:

$$S_v(x) = S_{v,\max} \cdot e^{-\frac{x^2}{2i^2}} \tag{2.16}$$

where $S_{v,\max}$ is the maximum settlement above the tunnel axis; i represents the standard deviation in the original Gaussian equation.

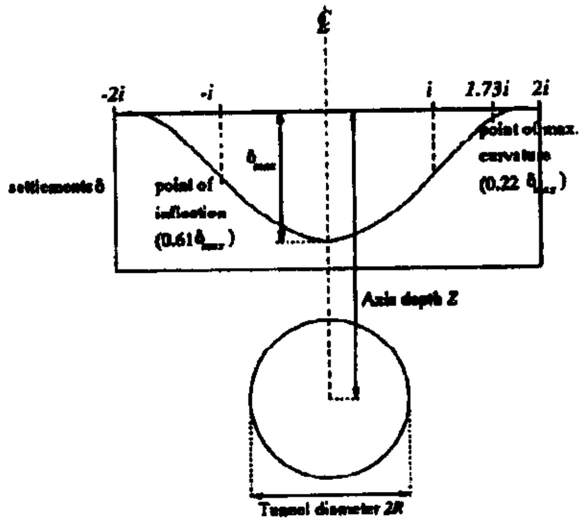

Figure 2.20: Surface settlements above tunnel (Peck, 1969)

Gurung and Iwao (1998) presented the engineering geological observations, rock mass classification and deformation data for Lam Ta Khong tunnel, Thailand. The convergence of the tunnel was found mainly to depend upon rock mass class, face advance and time. A simple empirical deformation equation which is generally valid for face advance within one to five tunnel diameters and time elapsed over a day was proposed as:

$$d = a + b\ln t \tag{2.17}$$

where d is deformation in mm; a =0.8–0.9 and b =f(RMR)=0.98–1.0 are rock mass parameters; t is elapsed time in days.

Hoek (2001) pointed out that the instability of a tunnel face can be ignored in small tunnels, while it should be considered in big tunnels excavated in poor ground conditions when the ratio of rock mass strength to in situ stress falls below 0.2. Simple approximate solutions to predict the strain of the tunnel ε_t and surface ε_f were proposed:

$$\varepsilon_t\,\% = 0.15(1-((p_i/p_0))\frac{\sigma_{cm}}{p_0}^{-(3(p_i/p_0)+1)/(3.8(p_i/p_0)+0.54)} \tag{2.18a}$$

$$\varepsilon_f\,\% = 0.1(1-((p_i/p_0))\frac{\sigma_{cm}}{p_0}^{-(3(p_i/p_0)+1)/(3.8(p_i/p_0)+0.54)} \tag{2.18b}$$

where ε_t is the radial strain of tunnel wall,

ε_f is axial strain at the centre of the tunnel face,

p_i is the internal support pressure upon the tunnel,

p_0 is the in situ stress upon the tunnel,

σ_{cm} is the rock mass strength.

Various practical solutions to reinforcing the tunnel surface and supporting the tunnel were also discussed in the paper.

Phienwej et al. (2007) used the hyperbolic and power creep laws to predict the time-dependent closure of circular tunnels. Several tunnels were modelled and it was indicated that the hyperbolic creep law is more practical for modelling the closure due to the creep behaviour than the power law model since it has the ability to model the yielding around the tunnel when the R_f value is close to 1.0, where R_f is the hardening parameter controlling the nonlinearity of the stress–strain relationship. The deformation and stress in the surrounding rock and soil were both analyzed and compared with the field data. The values of the creep parameters derived from back analysis of tunnel field data matched well with the values gained from the laboratory tests.

2.4.2 ANALYTICAL METHODS

Analytical methods have been widely used in the creep analysis of tunnel structures. The different types of ground conditions significantly affect the creep deformation of a tunnel, and so different rheological models were applied in the models to represent the surrounding rock as well as the shotcrete linings.

Lo and Yuen (1981) developed analytical closed form solutions for circular tunnel structures. The input parameters for their model are the initial stresses, the time-dependent properties of the lining as well as the rock, and the time lapse between excavation and lining. Rheological models were used to represent the rock and concrete separately (Figure 2.21) and expressions for lining pressures, stresses, thrusts and moments were calculated for both ‘no slip’ and ‘full slip’ interface conditions. The results showed that the maximum stresses at the springline and crown-invert decrease significantly with the increase of flexibility ratios G_r / G_l and G_{rt} / G_{lt} (where G_r and G_l are the shear modulus of rock and lining, respectively; G_{lt} and G_{rt} are the rheological parameters of the rock and lining, respectively); the critical tensile stress in the lining increases with the initial stress ratio and decreases with time; the method gave an acceptable fit with the 5 years’ field observations for the Heart Lake tunnel.

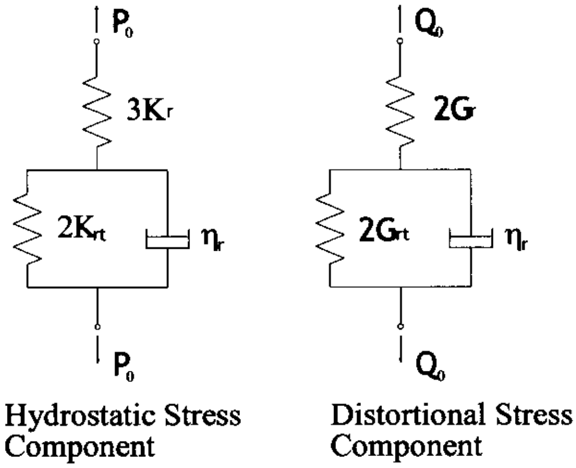

Figure 2.21: Rheological models of rock and concrete, Lo and Yuen (1981)

Sulem et al. (1987b) developed an analytical solution which takes into account the face advance effect to study the time-dependent wall displacement and lining pressure of a circular tunnel. They proposed a generalization of the ‘convergence confinement method’ which includes time effects in the analysis of in situ measurements. The radial displacement u_r at $\rho = r$ is calculated from:

$$\frac{u_r}{r} = \underbrace{\lambda_e \frac{\sigma^0}{2G_0} \frac{r_p^2}{r^2}}_{\text{depends only on face advance effect}} \underbrace{\left[1 + \frac{G_0}{G_f} f(t)\right]}_{\text{depends only on creep effect}} \qquad (2.19)$$

where λ_e is the value of face advance parameter λ when the yield criterion is reached at the tunnel wall,

σ^0 is the initial total stress,

r_p is the radius of the zone of damaged rock,

r is the radius of the tunnel,

G_f is the creep modulus,

G_0 is the shear modulus,

$f(t)$ is the creep function, $0 < f(t) < 1$.

This simple solution only worked for circular shaped tunnels in homogeneous and isotropic ground conditions and could give a reasonable estimate of the convergence of the tunnel and pressure in the lining.

Pan and Dong (1991) indicated that tunnel convergence is mainly affected by the initial in situ stress level, properties of the surrounding rock, properties of the tunnel support, and excavation and construction procedure. A time-dependent tunnel convergence model was proposed by them which considered creep effects, tunnel advance effects and support effects. The radial displacement was calculated from:

$$\frac{U_r(t)}{a} = g_{ve}[h_c(t) \times F_c(t)] - g_{ve} K_s H_s(t - t_s)[D(t) \times F_c(t)] \tag{2.20}$$

where $U_r(t)$ is the radial displacement of tunnel wall at time *t*,

$F_c(t)$ is the 'creep function',

g_{ve} is the compliance function,

K_s is the support stiffness,

t_s is the time of support installation,

$h_c(t)$ is the changing rate of the pressure,

$H_s(t - t_s)$ is the unit step function (or Heaviside function),

$D(t)$ is the changing rate of the radial displacement, $D(t) = \frac{d[U_r(t) - U_r(t_s)]}{dt}$.

Their research concluded that the tunnel advance rate does not influence the final tunnel convergence; a stiffer tunnel support can reduce the tunnel convergence; early tunnel support can reduce the final tunnel convergence; and tunnel-support interaction and the time of tunnel installation should be considered. A comparison of the analytical results and field measured data was carried out as shown in Figure 2.22.

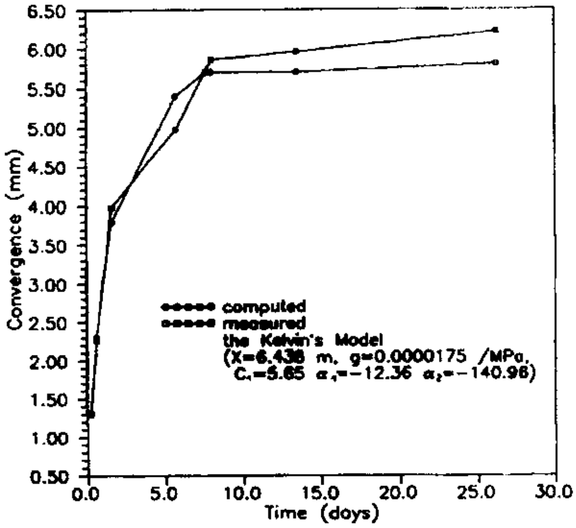

Figure 2.22: Comparison of the calculated and measured time histories of tunnel convergence (Pan and Dong, 1991).

Pells (2002) provided a concise description of the engineering geology of the horizontally bedded Hawkesbury sandstones in the Sydney region. Due to weaknesses such as bedding discontinuities, jointing and faulting, field scale strength of the Hawkesbury sandstone at the 'tunnel scale' was proposed to be about 20 MPa. He provided the following equations for the natural regional stress field for tunnels constructed to a depth of 150m:

$$\begin{aligned} \sigma_1 &= \sigma_{NS} = 1.5 + 1.2\sigma_v \quad to \quad 2.0\sigma_v \quad MPa \\ \sigma_2 &= \sigma_{WE} = 0.5\sigma_1 \quad to \quad 0.7\sigma_1 \quad MPa \\ \sigma_3 &= \sigma_v = 0.024H \quad MPa \end{aligned} \tag{2.21}$$

where H is the depth, σ_v is the vertical stress, σ_{WE} and σ_{NS} are horizontal stress in the west-east and north-south directions respectively. Analytical methods were used to design rockbolt and shotcrete support for tunnels and large span caverns. The maximum compressive crown stresses can be calculated as:

$$\sigma_0 = (S_f K_0 - 1)\gamma d \tag{2.22}$$

where S_f is a constant depending on the tunnel shape and the anisotropy of the rock, K_0 is the natural stress parameter, γ is the unit weight, d is the overburden depth.

To clarify the effects of steel fibre reinforced high-strength shotcrete (SFRS) applied to a squeezing tunnel, Hisatake (2003) used analytical methods to analyze the stress–strain–time constitutive relationships of SFRS and the time-dependent movement of the surrounding ground in a tunnel structure. The field measurement and analytical results showed that if both SFRS and steel-pipe supports are used for the primary lining, it provided an effective support for the construction of a tunnel excavated in ground with severe geological conditions (Figure 2.23).

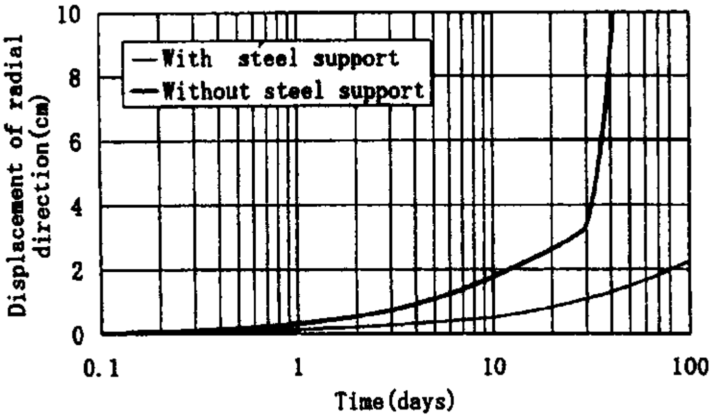

Figure 2.23: Displacement of SFRS with and without steel-pipe supports (Hisatake, 2003).

Kontogianni et al. (2006) indicated that the convergence of a tunnel after excavation was mainly affected by the strain resulting from the face advance effect and the time-dependent properties of the surrounding rock. A solution that took into account these two effects was proposed:

$$d_i = d_{xi} + d_{ti} = d_x^* \cdot \left[1 - \left(\frac{X}{x_i + X}\right)^2\right] + d_t^* \cdot (1 - e^{\left(\frac{-t_i}{T}\right)}) \tag{2.23}$$

where d_{xi} is the displacement caused by face advance,

d_{ti} is time-dependent creep deformation which is computed based on the rheological Kelvin/Voigt model,

d_x^* is the total displacement due to face advance x,

d_t^* is the total time-dependent displacement,

x_i is the advancing excavation distance,

X is the ground characteristic length parameter,

t_i is the time after excavation,

T is the ground characteristic time parameter.

The analysis revealed that the major proportion of the total tunnel deformation is due to the time-dependent property of the ground conditions not the face advance effect. This explained the phenomena that some tunnels experienced large deformation and failure a long time after excavation and far from the excavation face.

2.4.3 FINITE ELEMENT METHODS

Making use of highly developed computer hardware and software, researchers have employed finite element tools in the analysis of tunnel projects. It has given researchers a powerful tool to perform a detailed analysis of a tunnel support system and the behaviour of each component in the structure.

Campos de Orellana (1999) investigated a potash mine rock mechanics project. The long-term creep deformations were obtained from several control stations under different opening geometries and geological conditions. Properties of different layers of the saline rocks were tested in laboratories with over 300 samples, and a power law creep model was implemented in the numerical analysis code ANSYS to analyze the in situ mechanical behaviour of fine-grained salt rocks opening under actual mining conditions, that is, under equivalent stresses, temperatures and strain rates, below 25 MPa, 100°C and, 10^{-11}sec^{-1} respectively. The magnitude of roof sags, floor heaves and horizontal convergences of each control section were predicted and a good match was achieved between the measured and calculated deformations around mine openings, with differences in the steady state regime of 10^{-3} mm. The comparison of the calculated deformation and measured data in a typical section is shown in Figure 2.24.

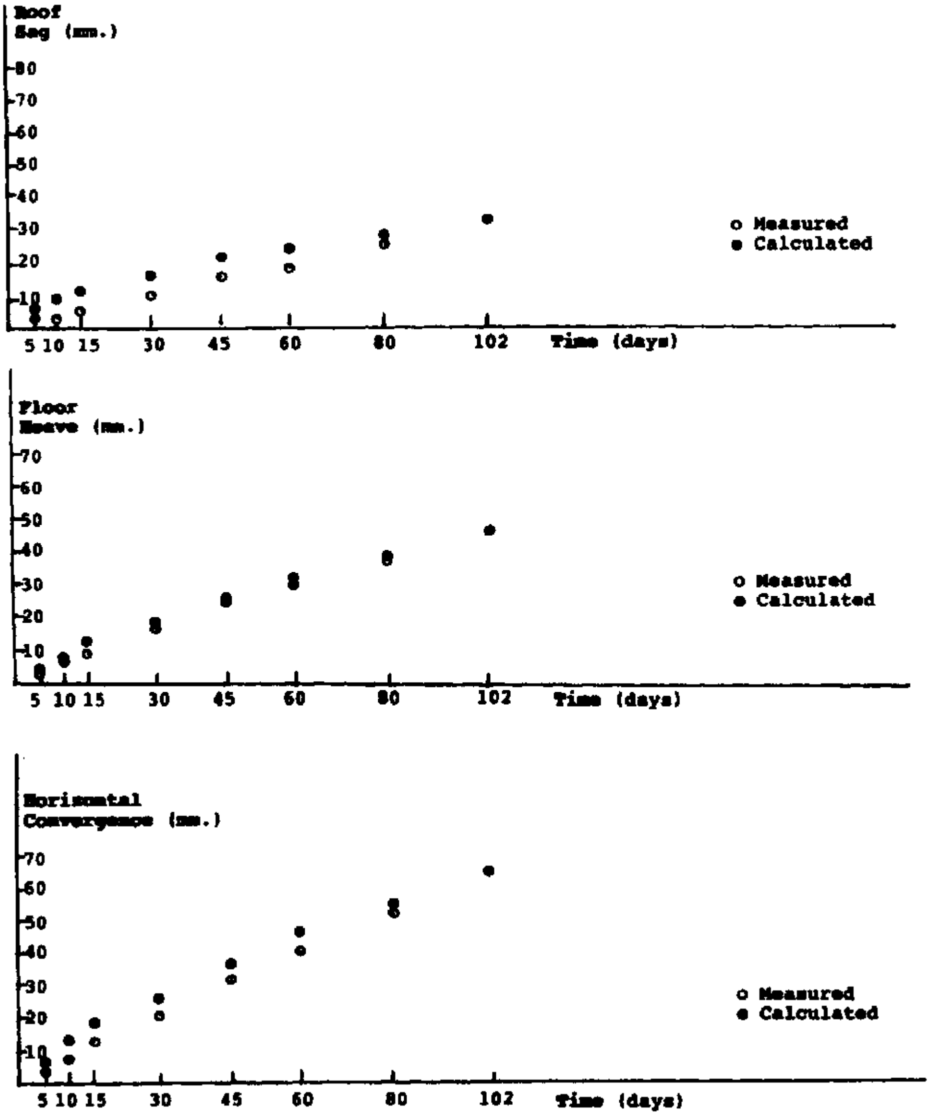

Figure 2.24: Control Station 27 creep curves (Campos de Orellana, 1999).

Pellet et al. (2000) implemented a new viscoplastic model in a two-dimensional explicit finite-difference program FLAC. Several creep and relaxation tests were carried out on the dry homogenous sandstone samples and numerical simulations were used to fit the laboratory curve. The creep parameters extrapolated from experimental results were applied in a circular tunnel model and the creep deformation of the tunnel was predicted. The method was also used by Sahli et al. (2001) to investigate the creep deformation and stress relaxation behaviour of a deep circular tunnel excavated in both sandstone and shale. Only a simple circular tunnel was modelled and the shotcrete lining and rock bolts were not taken into consideration in their models. The numerical creep and relaxation curve calculated by this finite element program is shown in Figure 2.25.

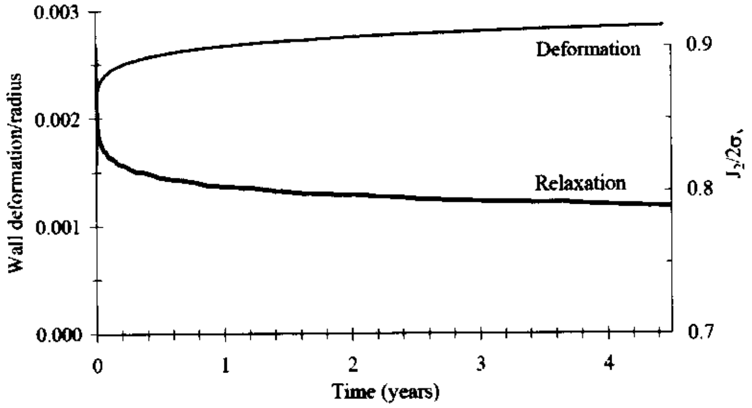

Figure 2.25: Time-dependent closure and stress relaxation for tunnel (Sahli et al. 2001)

Boidy et al. (2002) carried out a back analysis of the time-dependent behaviour of a tunnel in Switzerland with a numerical code FLAC 2D. Lemaitre's viscoplastic model which was implemented in FLAC 2D was used to fit the creep tests and then in situ convergence measurements. The deformation over a period of approximately 10 years was extrapolated using the numerical simulation. The numerical results for the Mont Terri gallery were compared with the measured data and they showed good agreement on an engineering scale. The discrepancies between creep of small samples and monitored excavation data could be explained by the scale effects on the viscosity parameter, and the results of the research were satisfactory prediction capabilities of the model. The calculated strain in the lining had a reasonable match with the measured data as shown in Figure 2.26.

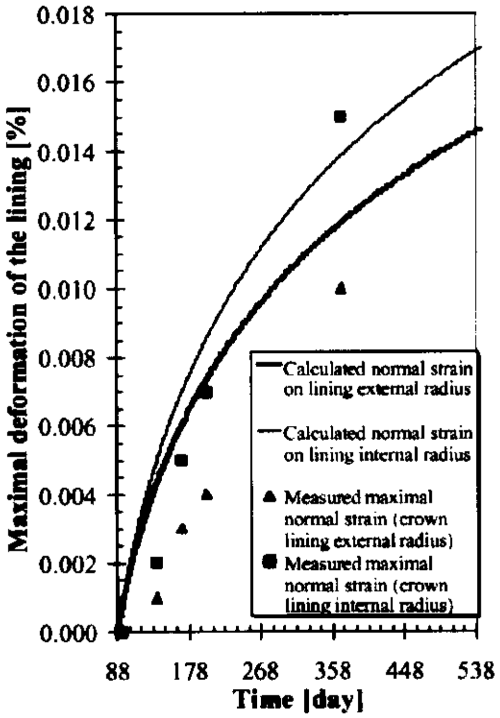

Figure 2.26: Comparison of measured and computed strains in the lining (Boidy et al. 2002).

Lackner et al. (2002) pointed out that large deformations occurring when excavating tunnels under squeezing rock conditions lead to the destruction of a conventional shotcrete lining. As a remedy, segmented shotcrete linings characterized by an increased compliance have successfully been installed. They combined the in situ measurements with a thermo-chemo-mechanical material law to establish a model of segmented shotcrete linings. They developed a hybrid method which considers the longitudinal gaps in the shotcrete lining adjusted with lining stress controllers (LSCs), and the method was used to model the Semmering pilot tunnel. The numerical results showed that the longitudinal gaps left in the tunnel shell prevent the destruction of the conventional shotcrete lining under squeezing rock conditions, and the LSCs provide a controlled transfer of axial forces across the longitudinal gaps.

Ground deformation and pressures in the lining of Stillwater Tunnel were investigated by Shalabi (2005) with different creep models. Axisymmetric finite element analysis using the commercial code ABAQUS was used in the research. A hyperbolic creep model and a power law creep model were applied separately to evaluate the time-dependent lining pressure and ground convergence of a circular tunnel with a circumferential shotcrete lining. In the analysis, the lining and ground deformation, radial ground movement above the crown, and lining-ground contact pressure were predicted and compared with field measured data. The results showed that the power law and hyperbolic creep models both predicted the crown displacement well, but the power law model gave more consistent results, and the power law model gave a good prediction of the lining pressure and deformation when taking into account the delay time before lining erection. Shalabi did not take into consideration rockbolts in the model and the research was based on the assumption that the rock and the shotcrete lining creep at the same rate. The calculated lining deformation was compared with the measured deformation as shown in Figure 2.27. The gap between the measurement curve A and the curves of the two creep models was explained due to the delay of the in situ measurement. A calibrated deformation curve B gave a reasonable fit with the power law model creep curve.

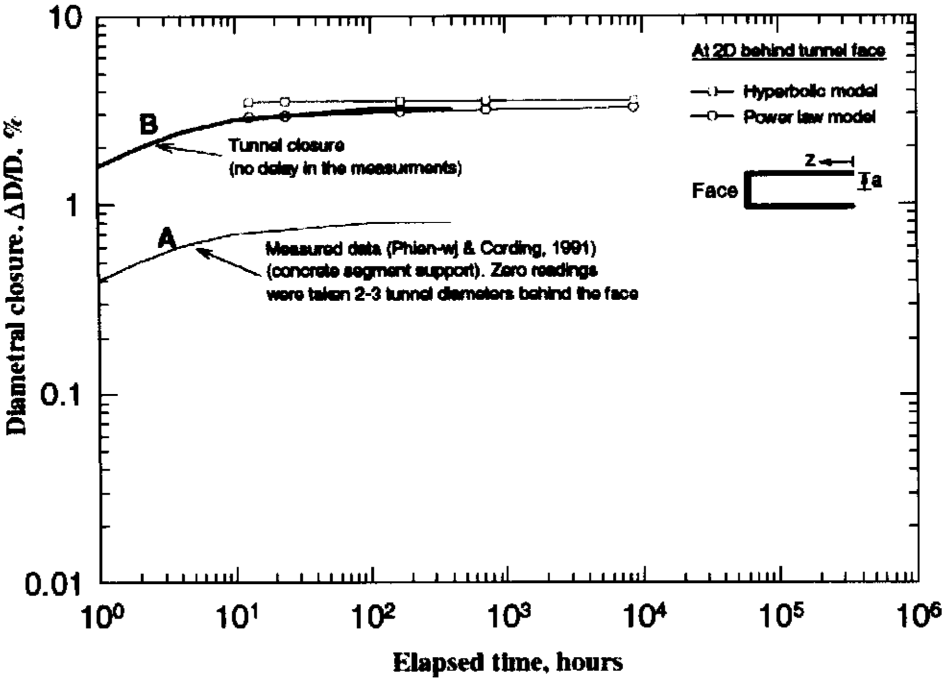

Figure 2.27: Predicted and measured diametral tunnel closure vs. time (Shalabi, 2005).

2.5 CONCLUSIONS

A literature review of creep and creep in tunnel linings has been conducted and reported in this chapter. It can be seen that creep is a significant and complex property of geo-materials such as clay, rock, concrete and shotcrete. Creep has an important influence on the time-dependent behaviour of infrastructure and should be taken into consideration in the analysis of the long-term strength and serviceability of a tunnel structure. There has been a great deal of research, including field measurements, laboratory tests and theoretical studies, on the creep behaviour of materials, but we still have not accumulated enough knowledge about this phenomenon. Different models have been proposed to model the creep, but no agreement has been reached and there is no single 'best' solution for this problem. The time-dependent creep behaviour of tunnel structures has been studied by many researchers with different methods, such as empirical methods, analytical methods and finite element analyses. The finite element method has undergone great improvement with the development of computer technology and now it is arguably the most powerful scientific and engineering tool in solving these geotechnical problems.

The aim of this research is to get a better understanding of the creep behaviour of geo-materials, especially sandstone in Sydney and fibre reinforced shotcrete used in Sydney tunnels. Laboratory tests were carried out and a new logarithmic model was proposed to represent the creep performance.

A three-dimensional finite element analysis program using the logarithmic creep model was developed to represent the laboratory creep tests and to analyze the tunnel excavation and time-dependent creep performance. A commercial finite element program ABAQUS, which uses a power law creep model, was also used in the analysis.

The combined shotcrete lining and rock bolts supporting tunnels with different shapes were modelled. The creep deformations and stress changes in the different components of a tunnel structure over time were investigated. Numerical solutions were compared with field data.

CHAPTER 3 - CREEP PROPERTIES OF MATERIALS

3.1 INTRODUCTION

To model the time-dependent deformation of a tunnel structure, it is important to understand the time-related properties of the materials which compose the tunnel structure. The rock and shotcrete are treated as viscoelastic materials in the present research and they exhibit an instantaneous deformation and a time-dependent creep deformation under a constant load. A constitutive mechanical law which can represent the stress-strain-time relationship of the material was developed in the research.

A three-dimensional finite element code was developed to model the tunnel and its support system. The constitutive law is then implemented in the finite element code to represent the behaviour of the materials in time. The code is aimed at predicting the deformation of the tunnel section, as well as the stress in the surrounding rock, shotcrete lining and rock bolts for a required time.

There are three different materials in the tunnel structure, the rock, the shotcrete lining and the steel rock bolts. The rock and shotcrete are treated as viscoelastic materials, while the steel bolts are assumed to be linear elastic and do not 'creep' with time. The basic mechanical properties of these materials are discussed and defined in this chapter; 'time' is introduced into the material properties such as bulk and shear modulus through a logarithmic function in time to represent the long-term behaviour of the materials. A convolution integral is used to evaluate the creep in real time, and the mathematical tools of a Laplace transform and Talbot inversion are applied to solve the resulting finite element equations.

A simple two-dimensional one element case study is carried out to verify the efficiency and accuracy of the constitutive law.

3.2 FORMULATION

The mechanical properties of materials are represented by the relationship between stress and strain in the classical theory of elasticity. The stress at a given point of a material is represented by six components that are $\{\sigma_x, \sigma_y, \sigma_z, \tau_{yz}, \tau_{zx}, \tau_{xy}\}$, while the strain is represented by $\{\varepsilon_x, \varepsilon_y, \varepsilon_y, \gamma_{yz}, \gamma_{zx}, \gamma_{xy}\}$ under general three-dimensional conditions. With the above components, the stress and strain status of a material at a given point can be quantified. In the classic Hooke's law for elastic materials, the stress is linearly proportional to the strain based on the small deformation assumption. If we take the material as visco-elastic, a new variable 'time' is introduced into the equations, and the relationship between time, stress and strain should also be included in the equations.

3.2.1 BASIC ASSUMPTIONS

Rock and shotcrete are both composite materials, and their interior make up is very complicated. Rock may be an aggregate of minerals, organic matter, and/or chemical precipitates; shotcrete is a man-made material which is composed of fibre, cement, aggregates, chemical admixtures, sand and water. Both materials consist of three state phases: solid, liquid and gas. Some research has been carried out based on the micro-mechanical behaviour of these materials, but this study is focused on the 'engineering scale' and macro-mechanical behaviour of the material, thus some simplified assumptions are made here:

1. The material is treated as continuous and isotropic. That is to say, the physical variables such as stresses, strains and displacements in the material are continuous and thus we can use a continuous function to represent them; the elastic constants of the material do not change with direction, since the micro-components in the body are arranged randomly so the macro-mechanical behaviour can be treated as being the same in all directions. The material is also treated as homogeneous during the instantaneous deformation stage, when it is assumed to be one uniform material and every part of the material has the same mechanical properties.

However, due to the creep behaviour, the mechanical properties of material will change at different rates under different stress levels with time.

2. The displacements and deformations are small. The instantaneous deformation is assumed to obey the classic elasticity theory, the deformation is linearly related to the applied load and does not depend on the load history; while the time-dependent deformation is assumed to obey some visco-elastic laws; here two different constitutive laws are used, that is a logarithmic law used in SAFEA and a power law used in ABAQUS.

3. The creep curve is modelled to fit to the steady stage, while the tertiary stage creep is not considered in the present model.

4. Temperature factors are not taken into account in the present research, and the experiments carried out are considered to take place under constant temperature conditions.

It is too complicated and technically impossible to consider the material from the micro-structure scale in the present research. The assumptions defined here can simplify the analysis and get rid of unnecessary factors such as the different mineral and/or mineraloid components in a rock element at a micro-scale view. They give a good representation of the materials' mechanical behaviour in the 'engineering scale' without the loss of much precision.

3.2.2 THEORY OF ELASTICITY

Hooke's law is named after British physicist Robert Hooke, who proposed his famous law in 1678 as *"Ut tension, sic vis"*, which means "as the tension, so the force". Under one-dimensional conditions, it means the stress σ change is related linearly to the strain ε through the Young's Modulus E, and Hooke's law can be expressed as:

$$\sigma = E\varepsilon \tag{3.1}$$

When the material is under three-dimensional stress state, the relationship between stress tensor and strain tensor is defined as

$$\sigma_{ij} = C_{ijkl}\varepsilon_{kl} \tag{3.2}$$

where C_{ijkl} is a tensor consisting of elastic coefficients.

In matrix form, we can write

$$[\sigma] = [D][\varepsilon] \tag{3.3}$$

That is

$$\begin{bmatrix} \sigma_{xx} \\ \sigma_{yy} \\ \sigma_{zz} \\ \tau_{yz} \\ \tau_{zx} \\ \tau_{xy} \end{bmatrix} = \begin{bmatrix} D_{11} & D_{12} & D_{13} & D_{14} & D_{15} & D_{16} \\ D_{21} & D_{22} & D_{23} & D_{24} & D_{25} & D_{26} \\ D_{31} & D_{32} & D_{33} & D_{34} & D_{35} & D_{36} \\ D_{41} & D_{42} & D_{43} & D_{44} & D_{45} & D_{46} \\ D_{51} & D_{52} & D_{53} & D_{54} & D_{55} & D_{56} \\ D_{61} & D_{62} & D_{63} & D_{64} & D_{65} & D_{66} \end{bmatrix} \begin{bmatrix} \varepsilon_{xx} \\ \varepsilon_{yy} \\ \varepsilon_{zz} \\ \gamma_{yz} \\ \gamma_{zx} \\ \gamma_{xy} \end{bmatrix} \tag{3.4}$$

For a homogeneous, isotropic material, the equation can be simplified to:

$$\begin{bmatrix} \sigma_{xx} \\ \sigma_{yy} \\ \sigma_{zz} \\ \tau_{yz} \\ \tau_{zx} \\ \tau_{xy} \end{bmatrix} = \begin{bmatrix} D_1 & D_2 & D_2 & 0 & 0 & 0 \\ D_2 & D_1 & D_2 & 0 & 0 & 0 \\ D_2 & D_2 & D_1 & 0 & 0 & 0 \\ 0 & 0 & 0 & D_3 & 0 & 0 \\ 0 & 0 & 0 & 0 & D_3 & 0 \\ 0 & 0 & 0 & 0 & 0 & D_3 \end{bmatrix} \begin{bmatrix} \varepsilon_{xx} \\ \varepsilon_{yy} \\ \varepsilon_{zz} \\ \gamma_{yz} \\ \gamma_{zx} \\ \gamma_{xy} \end{bmatrix} \tag{3.5}$$

If the material is under a three-dimensional stress state as shown in Figure 3.1, we can calculate the strain in the x-direction under σ_x, σ_y and σ_z separately and then sum the algebraic value of each of the components.

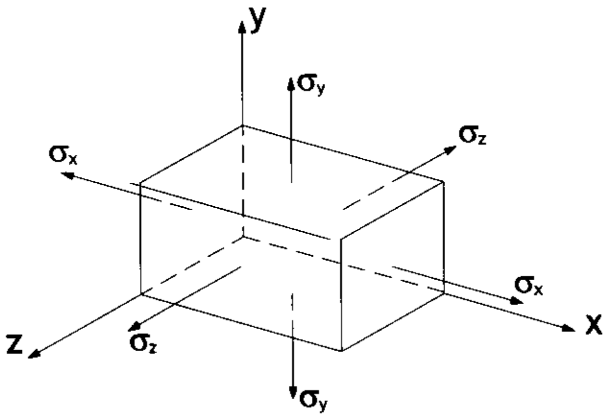

Figure 3.1: Element under three-dimensional stress state.

For strain in the x-direction under σ_x,

$$\varepsilon_x' = \frac{\sigma_x}{E} \tag{3.6}$$

For strain in the x-direction under σ_y and σ_z, due to the Poisson effect, the strain is negative and is calculated by

$$\varepsilon_x'' = -\frac{\nu\sigma_y}{E} \tag{3.7}$$

$$\varepsilon_x''' = -\frac{\nu\sigma_z}{E} \tag{3.8}$$

where ν is Poisson's ratio.

Summing the strains in (3.6) ~ (3.8), we get

$$\varepsilon_x = \frac{\sigma_x}{E} - \nu\frac{\sigma_y}{E} - \nu\frac{\sigma_z}{E} \tag{3.9}$$

Similarly, the strain in the y and z-directions can also be calculated

$$\varepsilon_y = -\nu\frac{\sigma_x}{E} + \frac{\sigma_y}{E} - \nu\frac{\sigma_z}{E} \tag{3.10}$$

$$\varepsilon_z = -\nu\frac{\sigma_x}{E} - \nu\frac{\sigma_y}{E} + \frac{\sigma_z}{E} \tag{3.11}$$

Solving equations (3.9) ~ (3.11), for the stress we obtain

$$\begin{aligned}
\sigma_x &= \frac{E}{(1+v)(1-2v)}\left[\varepsilon_x(1-v)+v\varepsilon_y+v\varepsilon_z\right]\\
\sigma_y &= \frac{E}{(1+v)(1-2v)}\left[v\varepsilon_x+(1-v)\varepsilon_y+v\varepsilon_z\right]\\
\sigma_z &= \frac{E}{(1+v)(1-2v)}\left[v\varepsilon_x+v\varepsilon_y+(1-v)\varepsilon_z\right]
\end{aligned} \tag{3.12}$$

The shear stress and strain can be calculated by

$$\tau_{xy} = G\gamma_{xy} \qquad \tau_{yz} = G\gamma_{yz} \qquad \tau_{zx} = G\gamma_{zx} \tag{3.13}$$

In matrix form, this can be written as

$$\begin{bmatrix}\sigma_x\\ \sigma_y\\ \sigma_z\\ \tau_{yz}\\ \tau_{zx}\\ \tau_{xy}\end{bmatrix} = \frac{E}{(1+v)(1-2v)}\begin{bmatrix}1-v & v & v & 0 & 0 & 0\\ & 1-v & v & 0 & 0 & 0\\ & & 1-v & 0 & 0 & 0\\ & & & \frac{(1-2v)}{2} & 0 & 0\\ & \text{Symmetric} & & & \frac{(1-2v)}{2} & 0\\ & & & & & \frac{(1-2v)}{2}\end{bmatrix}\begin{bmatrix}\varepsilon_x\\ \varepsilon_y\\ \varepsilon_z\\ \gamma_{yz}\\ \gamma_{zx}\\ \gamma_{xy}\end{bmatrix} \tag{3.14}$$

In the equation, shear modulus G is represented by $G = E/2(1+v)$, and if we introduce the bulk modulus K as $K = E/3(1-2v)$, the matrix can be rewritten as:

$$\begin{bmatrix}\sigma_x\\ \sigma_y\\ \sigma_z\\ \tau_{yz}\\ \tau_{zx}\\ \tau_{xy}\end{bmatrix} = \begin{bmatrix}K+4G/3 & K-2G/3 & K-2G/3 & 0 & 0 & 0\\ & K+4G/3 & K-2G/3 & 0 & 0 & 0\\ & & K+4G/3 & 0 & 0 & 0\\ & & & G & 0 & 0\\ & \text{Symmetric} & & & G & 0\\ & & & & & G\end{bmatrix}\begin{bmatrix}\varepsilon_x\\ \varepsilon_y\\ \varepsilon_z\\ \gamma_{yz}\\ \gamma_{zx}\\ \gamma_{xy}\end{bmatrix} \tag{3.15}$$

3.2.3 CREEP THEORY

For an elastic material under a constant stress, the strain is independent of time (Figure 3.2a). However, for a viscoelastic material under a constant stress, the strain will increase with time, and conversely when it is under a constant strain, the stress will decrease with time (Figures 3.2b&c).

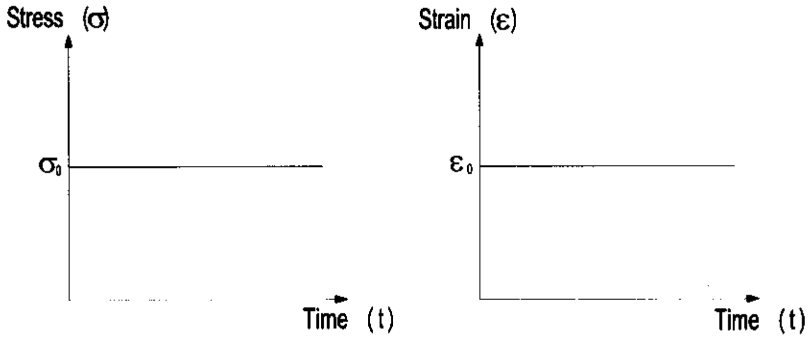

3.2a Elasticity

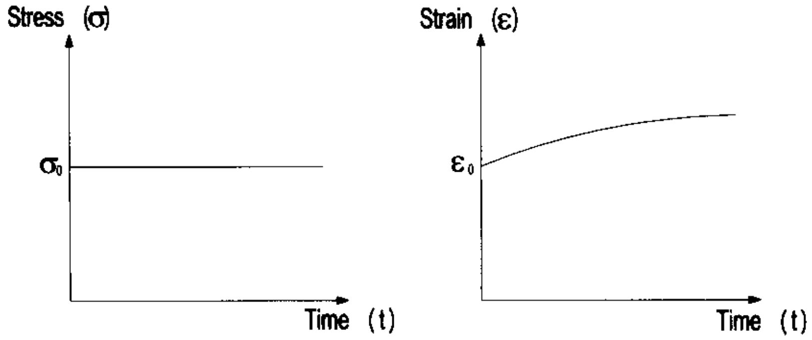

3.2b Creep

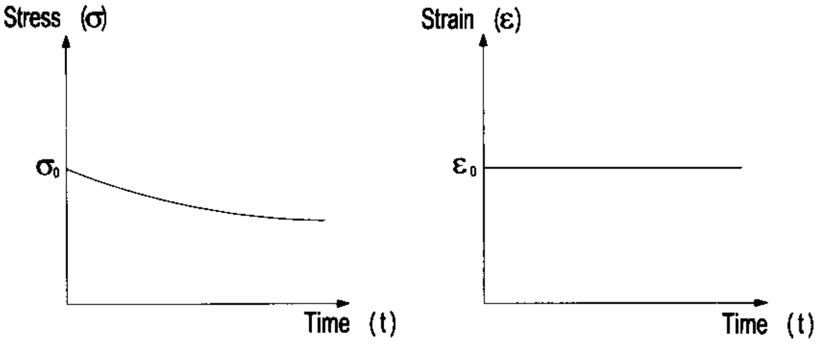

3.2c Relaxation

Figure 3.2: response of elastic and viscoelastic material with time.

To model the time-dependent behaviour of a material, a new variable 'time' can be introduced into the equation relating strain to stress. In the present research, 'days' are generally used as the units of time. We can use

$$\varepsilon(t) = J(t)\sigma_0 \tag{3.16}$$

where $\varepsilon(t)$ is the strain at any time, σ_0 is the instantaneous stress at time t=0, and $J(t)$ is a creep function.

Alteratively we can write

$$\sigma(t) = R(t)\varepsilon_0 \tag{3.17}$$

where $\sigma(t)$ is the stress at any time, ε_0 is the instantaneous strain at time t=0, and $R(t)$ is a relaxation function.

For a one-dimensional constant stress state,

at time $t = 0$, $\varepsilon(0) = \frac{\sigma_0}{E_0}$, and when $t = \infty$, $\varepsilon(\infty) = \frac{\sigma_0}{E_\infty}$

here, $\varepsilon(\infty) > \varepsilon(0)$, $E_\infty < E_0$

For a one-dimensional constant strain state,

at time $t = 0$, $\sigma(0) = E_0\varepsilon_0$, and when $t = \infty$, $\sigma(\infty) = E_\infty\varepsilon_0$

here, $\sigma(\infty) < \sigma(0)$, $E_\infty < E_0$

Thus we can see that $E(t) = R(t) = \frac{1}{J(t)}$ in this simple one-dimensional case and $E(t)$ decreases with time during the creep (relaxation) process.

The constant stress/strain condition is usually only found under laboratory conditions, while in practical situations, the applied stress/strain normally also changes with time. This makes the problem even more complicated, but the process can be explained by considering a stepped change of strain as shown in Figure 3.3.

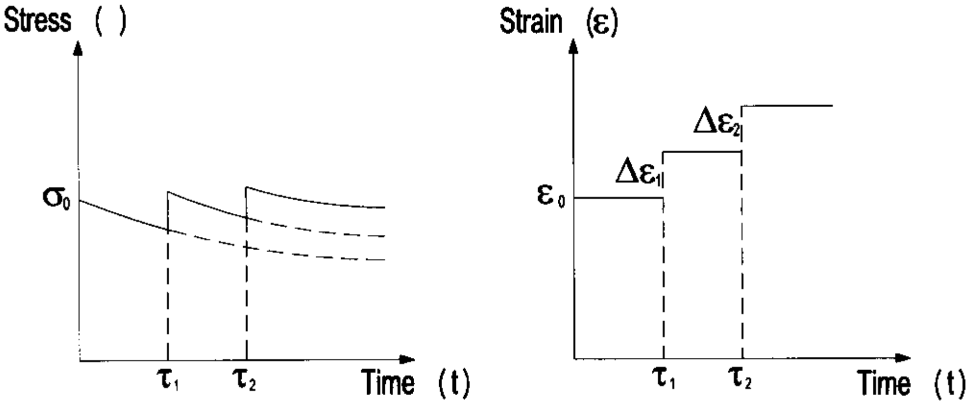

Figure 3.3: Responses to changed strain.

It can be seen that the initial strain is ε_0 and initial stress is σ_0 at $t = 0$, and an increment strain $\Delta\varepsilon_1$ is applied at $t = \tau_1$, then a further increase in strain $\Delta\varepsilon_2$ is applied at $t = \tau_2$. The stress in each time period can be calculated as

$$\begin{aligned} &\sigma(t) = R(t)\varepsilon_0 && \textit{for} \quad 0 < t < \tau_1 \\ &\sigma(t) = R(t)\varepsilon_0 + R(t-\tau_1)\Delta\varepsilon_1 && \textit{for} \quad \tau_1 < t < \tau_2 \\ &\sigma(t) = R(t)\varepsilon_0 + R(t-\tau_1)\Delta\varepsilon_1 + R(t-\tau_2)\Delta\varepsilon_2 && \textit{for} \quad \tau_2 < t \end{aligned} \tag{3.18}$$

So the time-dependent stress due to an increase in strain is calculated from the sum of stresses due to individual strain increments which cause a stress relaxation from the time of application. So for a large number of time steps (n), we can calculate the stress at $t > \tau_n$ when we know the history of the strain increments.

$$\sigma(t) = R(t)\varepsilon_0 + R(t-\tau_1)\Delta\varepsilon_1 + \ldots\ldots + R(t-\tau_n)\Delta\varepsilon_n \qquad \textit{for} \quad \tau_n < t \tag{3.19}$$

For a continuous strain variation, we can set very small time steps to represent the strain increment approximately as shown in Figure 3.4.

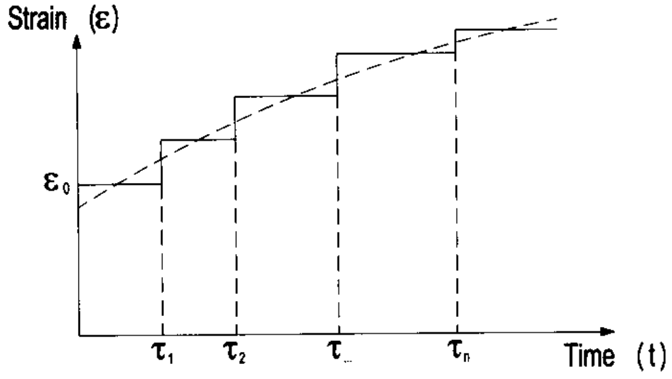

Figure 3.4: continuous increased strain.

So when the strain is time-dependent, we need evaluate a convolution integral to calculate the stress at a required time.

$$\sigma(t) = R(t)\varepsilon_0 + \int_0^t R(t-\tau)\frac{\partial\varepsilon(\tau)}{\partial\tau}d\tau \tag{3.20}$$

The material's time-stress-strain relationship is defined by equation (3.20) through a relaxation function. Alternatively, we can rewrite the convolution integral in terms of the creep function $J(t)$, that is

$$\varepsilon(t) = J(t)\sigma_0 + \int_0^t J(t-\tau)\frac{\partial\sigma(\tau)}{\partial\tau}d\tau \tag{3.21}$$

In the present research, the relaxation (creep) function is represented by a logarithmic function

$$R(t) = A + B\ln(1+\alpha\cdot t) \tag{3.22}$$

where A, B are α are the creep parameters, t represents the 'time' variable. The value of α is positive and B is negative in the equation since the material's modulus decreases with time.

For one-dimensional conditions, at time $t = 0$, $R(0) = E_0 = A$, and when $t = \frac{e^{-\frac{A}{B}}-1}{\alpha}$, $R(t) = E(t) = 0$, which means that the material's elastic modulus drops to zero, and the material loses all its stiffness theoretically. However, with the selected parameters for the practical material in the 'engineering scale', the relaxation function was only used to fit the material's creep curve to the steady stage and the tertiary creep stage which leads to the damage of the material is not considered in the present research. Thus it is assumed that $t << \frac{e^{-\frac{A}{B}}-1}{\alpha}$ in this study.

To model the creep under a three-dimensional stress state, we assume the bulk modulus K and shear modulus G of the materials vary with time, (or 'relax') according to the logarithmic functions in time,

$$\begin{aligned} K(t) &= K_0(A + B\ln(1+\alpha\cdot t)) \\ G(t) &= G_0(A + B\ln(1+\alpha\cdot t)) \end{aligned} \tag{3.23}$$

or in the one-dimensional model, $E(t) = E_0(A + B\ln(1+\alpha\cdot t))$.

So the 'time' variable is introduced in the D matrix as

$$[D(t)] = \begin{bmatrix} K(t)+4G(t)/3 & K(t)-2G(t)/3 & K(t)-2G(t)/3 & 0 & 0 & 0 \\ & K(t)+4G(t)/3 & K(t)-2G(t)/3 & 0 & 0 & 0 \\ & & K(t)+4G(t)/3 & 0 & 0 & 0 \\ & & & G(t) & 0 & 0 \\ & \text{Symmetry} & & & G(t) & 0 \\ & & & & & G(t) \end{bmatrix} \tag{3.24}$$

3.3 FINITE ELEMENT FORMULATION

In the preceding section, the constitutive law for a general visco-elastic material has been proposed. The time-stress-strain relationship is then implemented in a three-dimensional finite element code to solve the complex structural problem. The Finite Element Method (FEM) is a powerful numerical technique used for solving complex structural problems. The body under consideration is divided into a set of finite elements which are interconnected at nodes. The method is well established and can be found in references such as Zienkiewicz (1983). The employment of FEM in structural continuum analysis is usually based on the traditional methodology using the virtual work principle.

3.3.1 VIRTUAL WORK PRINCIPLE

Virtual work is defined as the work resulting from either a real force acting at a virtual displacement or a virtual force acting at a real displacement. It was first proposed by the Swiss mathematician Johann Bernoulli (1667-1748) in 1715 as the principle of virtual velocities, and later developed into the principle of virtual work today. For a rigid body, it may be stated as follows: *If a body is in equilibrium, the total virtual work of the external force system acting on its free body during any compatible virtual displacement of its free body is equal to zero, and conversely* (Jong, 2005), while for a deformable body, it can be written as: *External virtual work is equal to internal virtual work when equilibriated forces and stresses undergo unrelated but consistent displacements and strains.*

In the FEM, the principle of virtual work can be written as:

$$\delta U^{(e)} = \delta W^{(e)} \tag{3.25}$$

where $\delta U^{(e)}$ is the virtual work done by internal forces, $\delta W^{(e)}$ is the virtual work done by external forces.

The internal virtual work on a typical element can be expressed as

$$\delta U^{(e)} = \int_{V_e} \delta \underline{\varepsilon}^T \underline{\sigma} dV \tag{3.26}$$

where $\delta \underline{\varepsilon}$ is the vector of virtual strain components, $\underline{\sigma}$ is the stress components.

The external virtual work on a typical element can be expressed as

$$\delta W^{(e)} = \delta \underline{d}^T \underline{P} + \int_{S_e} \delta \psi_s{}^T T dS + \int_{V_e} \delta \psi^T \underline{F} dV \tag{3.27}$$

where $\delta \underline{d}$ is the vector of virtual nodal displacement components,

$\underline{P}$ is the vector of point load components,

$\delta \psi_s$ is the vector of surface virtual displacement components,

T is the surface pressure vector components,

$\delta \psi$ is the vector of virtual displacements, $\delta u, \delta v, \delta w$ in the x, y, z directions respectively,

$\underline{F}$ is the body force vector.

We can see from equations (3.26) & (3.27) that the internal virtual work is derived from the internal stresses, while the external virtual work is derived from the point loads, surface force and body force. Put equations (3.26) & (3.27) into equation (3.25), we can get

$$\int_{V_e} \delta \underline{\varepsilon}^T \underline{\sigma} dV = \delta \underline{d}^T \underline{P} + \int_{S_e} \delta \psi_s{}^T T dS + \int_{V_e} \delta \psi^T \underline{F} dV \tag{3.28}$$

For the whole structural system, summing the internal virtual work and the external virtual work for all elements, we can get

$$\begin{aligned} U &= \sum \delta U^{(e)} = \sum_e \int_{V_e} \delta \underline{\varepsilon}^T \underline{\sigma} dV \\ W &= \sum \delta W^{(e)} = \sum_e (\delta \underline{d}^T \underline{P} + \int_{S_e} \delta \psi_s{}^T T dS + \int_{V_e} \delta \psi^T \underline{F} dV) \end{aligned} \tag{3.29}$$

where U is the total internal virtual work, W is the total external virtual work.

3.3.2 FINITE ELEMENT FORMULATION

The FEM uses different types of elements in the structural analysis, from the simplest one-dimensional spring element to the three-dimensional solid elements. There is no single 'best' element for all problems, and we need select the appropriate elements for different issues. In the present research, the rock is represented by a solid 20-noded element, the shotcrete lining is represented by an 8-noded shell element and the rockbolt is modelled by a 2-noded beam element. Despite the different types of elements, the basic constitutive rules for every element are the same.

Generally speaking, the forces and displacements of the n-node three-dimensional element can be defined as

$$\{F\}=\begin{Bmatrix} F_{1x} \\ F_{1y} \\ F_{1z} \\ \vdots \\ F_{nx} \\ F_{ny} \\ F_{nz} \end{Bmatrix}, \quad \{d\}=\begin{Bmatrix} u_1 \\ v_1 \\ w_1 \\ \vdots \\ u_n \\ v_n \\ w_n \end{Bmatrix} \tag{3.30}$$

In a three-dimensional coordinate system, the displacement of an element can be written as

$$\{\psi\}=\begin{Bmatrix} u \\ v \\ w \end{Bmatrix}=\begin{bmatrix} N_1 & 0 & 0 & & N_n & 0 & 0 \\ 0 & N_1 & 0 & \cdots & 0 & N_n & 0 \\ 0 & 0 & N_1 & & 0 & 0 & N_n \end{bmatrix}\cdot\begin{Bmatrix} u_1 \\ v_1 \\ w_1 \\ \vdots \\ u_n \\ v_n \\ w_n \end{Bmatrix}=[N]\cdot\{d\} \tag{3.31}$$

where $[N]$ is the shape function matrix which is used to calculate values within an element by interpolating the values at nodes.

The shape functions are normally polynomials. They are continuous both inside the element and between the elements, so that the displacements inside the element and between the elements are also continuous. With the shape functions, the displacement vector in an element can be expressed by the nodal displacements. It is also observed that $N_1 + N_2 + \cdots + N_n = 1$, which can be used to check the validity of the shape functions.

The n-node element strain under a three-dimensional stress state is given by

$$\{\varepsilon\} = \begin{Bmatrix} \varepsilon_x \\ \varepsilon_y \\ \varepsilon_z \\ \gamma_{yz} \\ \gamma_{zx} \\ \gamma_{xy} \end{Bmatrix} = \begin{Bmatrix} \dfrac{\partial u}{\partial x} \\ \dfrac{\partial v}{\partial y} \\ \dfrac{\partial w}{\partial z} \\ \dfrac{\partial v}{\partial z} + \dfrac{\partial w}{\partial y} \\ \dfrac{\partial w}{\partial x} + \dfrac{\partial u}{\partial z} \\ \dfrac{\partial u}{\partial y} + \dfrac{\partial v}{\partial x} \end{Bmatrix} \tag{3.32}$$

Substituting equation (3.31) into (3.32), we obtain

$$\{\varepsilon\} = [B] \cdot \{d\} \tag{3.33}$$

where

$$[B] = [B_1 \quad B_2 \quad \cdots \quad B_n] = \begin{bmatrix} N_{1,x} & 0 & 0 & \cdots & N_{n,x} & 0 & 0 \\ 0 & N_{1,y} & 0 & \cdots & 0 & N_{n,y} & 0 \\ 0 & 0 & N_{1,z} & \cdots & 0 & 0 & N_{n,z} \\ 0 & N_{1,z} & N_{1,y} & \cdots & 0 & N_{n,z} & N_{n,y} \\ N_{1,z} & 0 & N_{1,x} & \cdots & N_{n,z} & 0 & N_{n,x} \\ N_{1,y} & N_{1,x} & 0 & \cdots & N_{n,y} & N_{n,x} & 0 \end{bmatrix}$$

with

$$N_{i,x} = \frac{\partial N_i}{\partial x} \qquad i = 1 \ldots n$$

$$N_{i,y} = \frac{\partial N_i}{\partial y} \qquad i = 1 \ldots n$$

$$N_{i,z} = \frac{\partial N_i}{\partial z} \qquad i = 1 \ldots n$$

The stress-strain relationship is given as

$$\{\sigma\} = [D] \cdot \{\varepsilon\} \tag{3.34}$$

or

$$\{\sigma\} = [D] \cdot [B] \cdot \{d\} \tag{3.35}$$

using the virtual work principle (3.28), and taking the total force system as

$$\{f\} = \{P\} + \int_{S_e} [N_s]^T \{T\} dS + \int_{V_e} [N]^T \{F\} dV \tag{3.36}$$

we can get

$$\{f\} = \int_V [B]^T [D][B] dV \cdot \{d\} = [K] \cdot \{d\} \tag{3.37}$$

here $[K] = \int_V [B]^T [D][B] dV$ is the element stiffness matrix.

The stiffness matrix provides a relationship between the nodal displacement and total nodal force in the element. It is a basic and key step in the finite element analysis, and it can be used to provide an approximate solution for the problem considered.

3.4 SOLUTION OF EQUATIONS

To model the material's time-dependent mechanical behaviour, the $[D]$ matrix must contain viscoelastic terms to introduce the 'time' variable as in equation (3.24), and a convolution integral as in equation (3.20) should be used to calculate the stress or strain after a required time interval.

It is practically difficult to solve the convolution integral because of the limitation of storing all the continuously changing time history. This difficulty was overcome by Cater and Booker (1982) by using a Fourier or Hankel transform in conjunction with a Laplace transform. In the present research, a Laplace Transform is also used to simplify the integral equation to an easily solvable algebraic equation. A three-dimensional finite element formulation is then used to solve the equation based on the transformed field variables. Finally, a direct numerical inversion of the Laplace Transform is used to invert the complex result to get the solution in real time. This simplified process can save a lot of storage space and computing time, and get an approximate result of the convolution integral equation without losing much precision.

3.4.1 LAPLACE TRANSFORM

The Laplace transform can be written as

$$£\{f(t)\} = F(s)$$

where $f(t)$ is the original function of time t, $F(s)$ is the image function with an argument s.

The Laplace transform of a differentiation with respect to time is

$$£\left\{\frac{df(t)}{dt}\right\} = s\cdot £\{f(t)\} - f(0) = s\cdot F(s) - f(0)$$

The Laplace transform of a convolution integral is

$$£\{\int_0^t f(t-\tau)\cdot g(t)d\tau\} = F(s)\cdot G(s)$$

Thus the Laplace transform of the stress-strain-time equation (3.20) can be written as

$$£\{\sigma(t)\} = £\{\sigma_1\} + £\{\sigma_2\} = £\{R(t)\varepsilon_0\} + £\left\{\int_0^t R(t-\tau)\frac{\partial\varepsilon(\tau)}{\partial\tau}d\tau\right\} \tag{3.38}$$

where $£\{\sigma_1\} = £\{R(t)\varepsilon_0\} = \overline{R}\cdot\varepsilon_0$

$$£\{\sigma_2\} = £\left\{\int_0^t R(t-\tau)\frac{\partial\varepsilon(\tau)}{\partial\tau}d\tau\right\} = \overline{R}\cdot(s\cdot\overline{\varepsilon} - \varepsilon_0)$$

here the bar denotes a Laplace transform.

So the equation (3.38) can be written as

$$\begin{aligned} £\{\sigma(t)\} = £\{\sigma_1\} + £\{\sigma_2\} &= \overline{R}\cdot\varepsilon_0 + \overline{R}\cdot(s\cdot\overline{\varepsilon} - \varepsilon_0) \\ &= \overline{R}\cdot s\cdot\overline{\varepsilon} \end{aligned} \tag{3.39}$$

or we can write $\overline{\sigma} = s\overline{R}\cdot\overline{\varepsilon}$ if the initial strain is zero. (3.40)

In the three-dimensional stress state, if we apply the Laplace transform to the equation (3.34), the stress-strain law in matrix form is given by

$$\overline{\sigma} = s\overline{D}\cdot\overline{\varepsilon} \tag{3.41}$$

where the $\overline{D}$ is the Laplace transform of the D matrix, which can be written as

$$\overline{D} = \begin{bmatrix} \overline{K}+4\overline{G}/3 & \overline{K}-2\overline{G}/3 & \overline{K}-2\overline{G}/3 & 0 & 0 & 0 \\ & \overline{K}+4\overline{G}/3 & \overline{K}-2\overline{G}/3 & 0 & 0 & 0 \\ & & \overline{K}+4\overline{G}/3 & 0 & 0 & 0 \\ & & & \overline{G} & 0 & 0 \\ & \text{Symmetry} & & & \overline{G} & 0 \\ & & & & & \overline{G} \end{bmatrix} \tag{3.42}$$

Where $\overline{K} = \pounds\{K(t)\}$, $\overline{G} = \pounds\{G(t)\}$.

Thus in the finite element method, if we apply a Laplace transform to equation (3.33), we can get

$$\overline{\varepsilon} = B\cdot\overline{d} \tag{3.43}$$

And the stiffness matrix is formed by using the transformed D matrix, i.e. $\overline{K} = \int B^T\overline{D}BdV$. So the equation (3.37) may be written as

$$\overline{f} = s\overline{K}\cdot\overline{d} \tag{3.44}$$

3.4.2 TALBOT INVERSION

A three-dimensional finite element solver is used to solve the equation (3.44) based on the Laplace transformed variables s. This yields the transformed displacement $\overline{d}$ for the finite element mesh. Talbot's method is finally used to invert the complex result to get the solution at any required real time.

Talbot (1979) indicated that the inversion of Laplace transforms is a topic of primary importance in many areas of applied mathematics. Most standard applications of the inversion can be achieved by the use of a dictionary of transforms, or in the case of rational function transforms by partial fraction decomposition. However, these methods may lead to an intractable integral, or to an infinite series. He proposed a numerical method to obtain an accurate numerical value of the inverse for a specified value of the argument t.

The standard inversion formula of $F(s)$ is

$$f(t) = \text{£}^{-1} F(s) = \frac{1}{2\pi i} \int_B e^{st} F(s) ds, \qquad t > 0 \tag{3.45}$$

where B is the "Bromwich contour" from $\gamma - i\infty$ to $\gamma + i\infty$, where $\gamma > \gamma_0$, so that B is to the right of all singularities of $F(s)$. Direct numerical integration along B is impractical on account of the oscillations of e^{st} as Im $s \to \pm\infty$. Talbot overcame this difficulty by replacing B by an equivalent contour L starting and ending in the left half-plane, so that Re $s \to -\infty$ at each end. The equation (3.45) is then written as a trapezoidal approximation

$$\overline{f}(t) = \frac{2}{n} \sum_{k=0}^{n-1} \operatorname{Re} Q(z_k), \qquad z_k = 2k\pi i / n \tag{3.46}$$

where $Q(z) = \lambda e^{(\lambda S + \sigma)t} F(\lambda S + \sigma) S'(z)$,

λ is the scaling parameter,

σ is the shift parameter,

$z = x + iy$ is a complex variable,

and $s = S(z)$ is a real uniform analytic function of z.

The final formula to invert the Laplace transform of function *f(t)* derived by Talbot (1979) was as given in (3.47)

$$\overline{f}(t) = \frac{\lambda e^{\sigma t}}{n} \sum_{k=0}^{n-1} \left[e^{\alpha\tau} \left\{ (\nu G - \beta H) \cos \nu\theta\tau - (\nu H + \beta G) \sin \nu\theta\tau \right\} \right]_{\theta = \theta_k} \tag{3.47}$$

where λ, σ, ν are "geometrical" parameters selected for a given *F(s), t,* and computer precision,

n is a parameter selected for prescribed accuracy,

$\beta = \beta(\theta) = \theta + \alpha(\alpha - 1) / \theta$

$\theta_k = k\pi / n, \qquad k = 0, 1, \ldots, n-1.$

$\tau = \lambda t$

In the present research, to solve the convolution integral equation for the model of time-dependent elastic material with a relaxation function of $R(t) = A + B\ln(1+\alpha \cdot t)$, the following parameters are selected:

$$\begin{aligned} \tau &= 6, \\ \sigma &= 0, \\ \nu &= 1, \\ n &= 20 \end{aligned} \tag{3.48}$$

The FORTRAN code of the Talbot inversion routine which can invert $R(t) = A + B\ln(1+\alpha \cdot t)$ is given in Appendix 3A. It gave an accurate numerical result for the present problem with the selected Talbot parameters.

3.5 SIMPLE CASE

If we assume that the material's relaxation function obeys a function of the type $R(t) = A + B\ln(1+\alpha \cdot t)$, then the elastic modulus of the material can be written as

$$E(t) = E_0(A + B\ln(1+\alpha \cdot t))$$

The Laplace transform of such a function is

$$\overline{E} = \frac{E_0 A}{s} + \frac{E_0 B}{s} e^{s/\alpha} E_1(s/\alpha) \tag{3.49}$$

where E_1 is the exponential integral defined as

$$E_1(\varsigma) = \int_{\varsigma}^{\infty} \frac{e^u}{u} du \tag{3.50}$$

For selected parameters $A = 1.0,\ B = -0.015,\ \alpha = 100$, we can calculate $R(t)$ by hand and by the FORTRAN code for the Talbot inversion of Equation 3.49 given in Appendix 3A. The results are shown in Table 3.1 & Figure 3.5.

t	$R(t)$ by hand	$R(t)$ by Tablot	Difference
0.0001	0.99985075	0.999852	-1.2552E-06
0.001	0.99857035	0.998572	-1.6551E-06
0.01	0.98960279	0.989602	8.0062E-07
0.1	0.96403157	0.964031	5.9220E-07
1	0.93077319	0.930775	-1.9423E-06
10	0.89636868	0.896371	-2.5901E-06
100	0.86184339	0.861843	4.5774E-07

Table 3.1: results of $R(t)$ by hand and by FORTRAN.

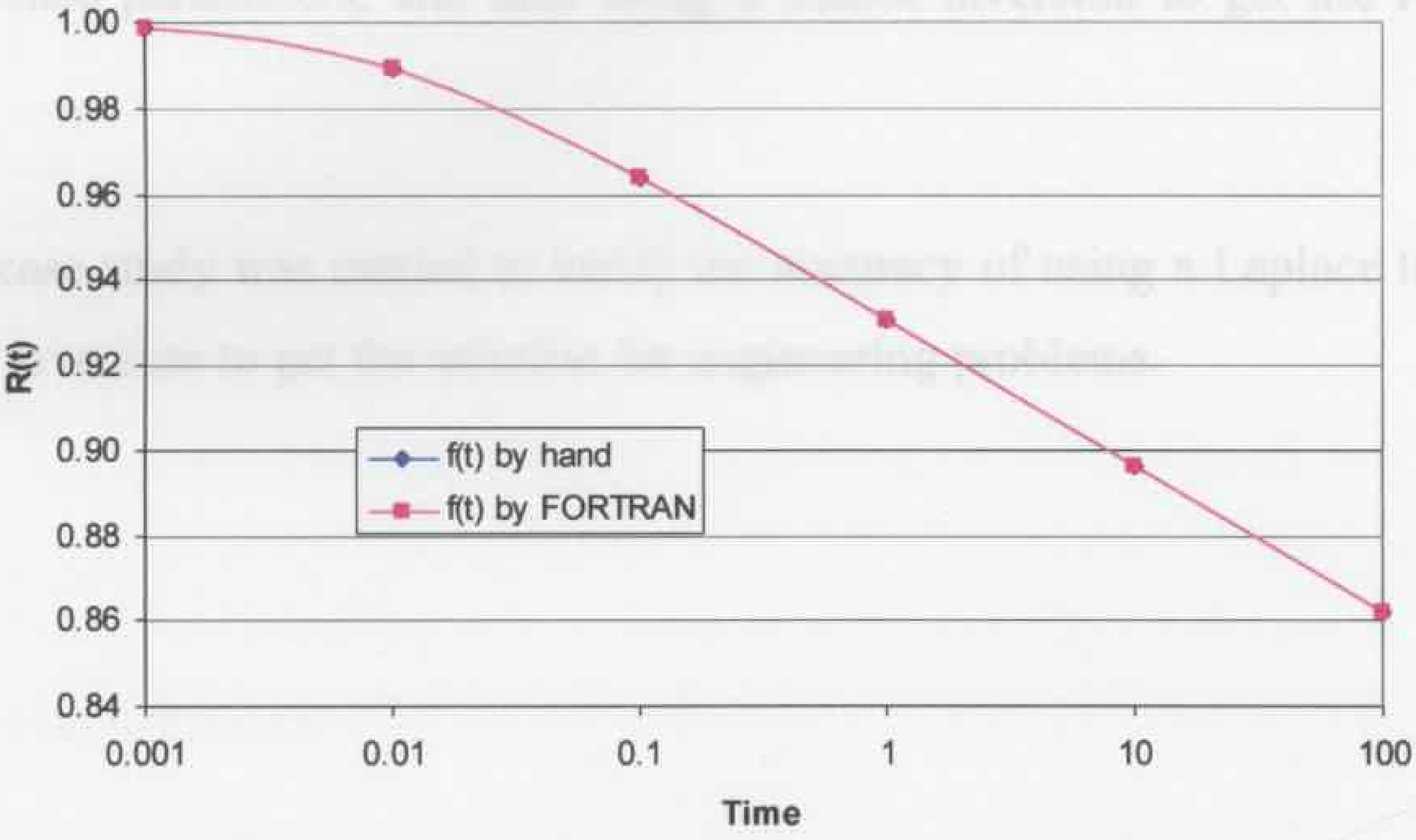

Figure 3.5: results of $R(t)$ by hand and by Talbot inversion.

The results show that the Talbot inversion of the Laplace transform gives an accurate numerical result compared with the results from a hand calculation. This approximate process can be used to solve the finite element equations to a satisfactory precision in the 'tunnel engineering structure scale'.

3.6 CONCLUSIONS

In this chapter, some basic assumptions for modelling the mechanical behaviour of the material was presented; the instantaneous elastic deformation and time-dependent creep deformation of rock/shotcrete was modelled by using a logarithmic function to represent the shear modulus and bulk modulus of the materials.

The Finite Element Method based on the traditional virtual work principle was described; the stiffness matrix of an element was based on the bulk and shear modulus that were functions of time. The convolution integral equation that is involved in the solution was simplified by employing a Laplace transform solving the finite element equation in terms of transformed parameters, and then using a Talbot inversion to get the results in real time.

A simple case study was carried to verify the accuracy of using a Laplace transform and numerical inversion to get the solution for engineering problems.

APPENDIX 3A FORTRAN Code for Talbot Inversion

This code is used to invert the function of $R(t) = A + B\ln(1+\alpha \cdot t)$.

```
C===========================================================
C MODIFIED VERSION OF TALBOT INVERSION ROUTINE WHICH CAN
C INVERT   A+B*LN(1.+ALPHA*T)
C===========================================================
      COMMON/INTEGP/TAU,SIG,RNU,N,NUMT
      COMMON /UNITS/ LU2
      CHARACTER*20 IOUT
      DIMENSION T(2000),F(2000)

      LU2 = 8

      read (0,*) Iout
      open (lu2,FILE=Iout,status='unknown')

      NUMT=7
      T(1) = 0.0001
      T(2) = 0.001
      T(3) = 0.01
      T(4) = 0.1
      T(5) = 1
      T(6) = 10
      T(7) = 100

      TAU=6.
      SIG=0.
      RNU=1.
      N=20
      CALL TALBOT(F,T,G,H)


      WRITE(lu2,2001) (I, T(I), F(I), I = 1, NUMT)
c     WRITE(6,2001) (T(I),F(I),I=1,NUMT)
 2001 FORMAT (I5,2E15.6)
c     FORMAT(1X,2E15.6)
      STOP
      END
C==============================================================
      SUBROUTINE TALBOT(F,T,G,H)
      COMMON/INTEGP/TAU,SIG,RNU,N,NUMT
      DIMENSION T(2000),F(2000)
      PI=3.14159265
      DO 10 I=1,NUMT
      RL=TAU/T(I)
      SUM=0.0
      DO 11 K=1,N
      TH=(K-1)*PI/N
      A=1.
      B=0.
      IF(K.EQ.1) GO TO 100
```

```
      A=TH*COS(TH)/SIN(TH)
      B=TH+A*(A-1.)/TH
  100 SX=A*RL+SIG
      SY=RNU*TH*RL
      TNT=TH*RNU*TAU
      CALL CIGRAN(SX,SY,G,H)
      SUM=SUM+EXP(A*TAU)*((RNU*G-B*H)*COS(TNT)-
     *   (RNU*H+B*G)*SIN(TNT))

      IF(K.EQ.1) SUM=SUM/2.
   11 CONTINUE

   10 F(I)=SUM*RL*EXP(SIG*T(I))/N

      RETURN
      END
C=================================================================
      SUBROUTINE CIGRAN(XX,YY,GG,HH)
      COMPLEX*16 Z,FF,CR,RLX
C=== SET PARAMETERS
      ALPHA=100
      A=1.0
      B=-0.015
C=== EVALUATE CREEP FUNCTION
C=== ROUTINE TO CALCULATE EXP(Z)*EI(Z)/Z
      X=XX/ALPHA
      Y=YY/ALPHA
      Z=CMPLX(X,Y)

      TEST1=ABS(X-Y+17)+ABS(X+Y+11)-6
      TEST2=ABS(X-Y+11)+ABS(X+Y+5)-6
      TEST3=ABS(X-Y+5)+ABS(X+Y-1)-6
      K=4
      IF(TEST1.LE.0) K=1
      IF(TEST2.LE.0) K=2
      IF(TEST3.LE.0) K=3
      IF(K.LE.3) CALL SER(Z,K,FF,N)
      IF(K.EQ.4) CALL CF(Z,FF,N)
      CR = (A/Z + B*FF) / ALPHA

      GG=REAL(CR)
      HH=AIMAG(CR)
      RETURN
      END
C==========================================================
      SUBROUTINE SER(Z,K,FF,I)
      COMPLEX*16 AC(3),PC(3)
      COMPLEX*16 C(2000),PHI(2000)
      COMPLEX*16 A,T,Z,TI,TERM,SUM,FF,PSI,ARG

      AC(1)=CMPLX(-14.,3.)
      PC(1)=CMPLX(1.079313,0.020604)
      AC(2)=CMPLX(-8.,3.)
      PC(2)=CMPLX(1.131255,0.074701)
      AC(3)=CMPLX(-2.,3.)
      PC(3)=CMPLX(1.013205,0.289366)
```

```
      A=AC(K)
      EPS=0.000001
      C(2)=EXP(A)
      C(1)=C(2)-1.0
      PSI=PC(K)

      PHI(1)=PSI/A+EXP(A)*LOG(A)
      PHI(2)=PHI(1)+C(1)/A
      T=z-A

      RADT=ABS(T)
      SUM=PHI(1)+PHI(2)*T
      TI=T
      I=1
   12 I=I+1
      PHI(I+1)=(C(I)+PHI(I-1)+(A+1-I)*PHI(I))/A/I
      TI=TI*T
      TERM=TI*PHI(I+1)
      SUM=SUM+TERM
      TEST=ABS(TERM/SUM)
      C(I+1)=C(I)/I
      IF(I.GT.199) WRITE(0,*) 'I term is too big!'
      IF(I.GT.199) STOP
      IF(TEST.GT.EPS) GO TO 12
      z=T+A

      FF=(SUM-EXP(z)*LOG(z))/z
      RETURN
      END
C=======================================================================
      SUBROUTINE CF(Z,FF,N)
      COMPLEX*16 A(2000),B(2000),F(2000)
      COMPLEX*16 Z,AL,BL,ARG,FF
      EPS=0.000001
      BIG=1.0/EPS
      A(1)=1.0
      B(1)=0.0
      A(2)=0.0
      B(2)=1.0
      N=2
      ISWIT=1
   12 N=N+1
      ISWIT=-ISWIT
      BL=Z
      IF(ISWIT.EQ.1) BL=1.
      IF(ISWIT.EQ.1) AL=AL+1.
      IF(N.LE.5) AL=1.
      A(N)=BL*A(N-1)+AL*A(N-2)
      B(N)=BL*B(N-1)+AL*B(N-2)
      TEST=ABS(A(N)*A(N)+B(N)*B(N))
      TEST=SQRT(TEST)
      IF(TEST.LT.BIG) GO TO 53
      A(N)=A(N)/TEST
      B(N)=B(N)/TEST
      A(N-1)=A(N-1)/TEST
      B(N-1)=B(N-1)/TEST
```

```
 53 CONTINUE
  F(N)=A(N)/B(N)
  ARG=(1.-F(N-1)/F(N))
  TEST=ABS(ARG)
  IF(TEST.GT.EPS) GO TO 12
  FF=F(N)/Z
  RETURN
  END
```

CHAPTER 4 - CREEP PARAMETERS FROM LABORATORY TESTS

4.1 INTRODUCTION

In the previous chapters, literature reviews have been performed and the creep properties of the materials have been discussed. Two different creep tests have been carried out to investigate the time-dependent mechanical properties of shotcrete, sandstone and shale in the present research.

When a shotcrete lining is subjected to bending, the fibres in the tension region are assumed to carry the tension load while the concrete is assumed to have no tensile strength. When under compression, the concrete and fibres are assumed to work together to carry the compression stress, thus the fibre reinforced shotcrete (FRS) is assumed to creep at a different rate when under bending than when it is under compression. The ASTM C-1550 round determinate panel tests were used to investigate the creep deformation of FRS samples under bending.

The uniaxial compressive test is the most commonly used test in geotechnical engineering, the deformation of test samples over time under a constant load were obtained in the present research to investigate the creep properties of sandstone and shale. Similar results were obtained for shotcrete under direct compression.

Both experiments were simulated by numerical methods, and appropriate creep parameters were selected to fit the experimental deformation curve and later employed in the numerical tunnel models.

4.2 CREEP TESTS FOR SHOTCRETE UNDER BENDING

Reinforced shotcrete has been widely applied in constructing ground support linings in the tunnelling and mining industry. Round determinate panel samples composed of three different types of FRS were tested to investigate creep behaviour of the materials. One steel fibre (Novotex) and two new kinds of macro-synthetic fibre (Strux and HPP) were used in the present research. The tests were carried out by E.S. Bernard of the TES Pty Ltd Company, Penrith, Australia.

4.2.1 SHOTCRETE SPECIMENS

The ASTM C1550 panels used in the tests are 750mm in diameter and 75mm in thickness, and made by shotcrete reinforced with either NOVO steel fibre or HPP/STRUX macro-synthetic fibre. The specimens were made by casting shotcrete into round forms, and then curing them for 180 days in water before they are cured in air for a further 180 days. This process is to minimise the differences in properties of the first and last specimens cast. The dosages of three different fibres are given in Table 4.1. It shows that the usage of the macro-synthetic fibre in the specimens is less than 20% of the usage of the steel fibre in weight. The mix designs of the shotcrete are the same for the three sets of specimens and their nominal 28 day ultimate compressive strengths are 32MPa. Details of the mix components of the shotcrete are given in Table 4.2.

Mix	Fibre type	Dosage (kg/m^3)
1	Novotex 0730 flattened-end steel	50
2	HPP 50 mm corrugated macro-synthetic	8.8
3	Strux 85/50 straight macro-synthetic	9.2

Table 4.1: Fibres used in three sets of specimens (Bernard, 2004).

Component	Quantity (kg/m^3)
Coarse aggregate (10/7 mm CRG)	620
Coarse sand (2 mm)	600
Fine sand	400
Cement	360
Fly ash	40
Silica fume	20
Water reducer (L/m^3)	0.42

Table 4.2: Mix design for shotcrete (Bernard, 2004).

4.2.2 ASTM C1550 TESTS

When a shotcrete lining is under bending, which is common in a flat roof tunnel, the tension region will have some small cracks and the fibre in these small cracks is assumed to carry the tensile load and the concrete is assumed not to contribute to the tensile strength in this region. Thus, the creep behaviour of the cracked shotcrete under bending is quite different to when the material is under compression.

The objective of the tests is to determine the creep performance of steel and macro-synthetic FRS under bending after cracking. An initial cracking test was carried out on a servo-controlled test machine, and the specimens were then transferred to a gravity-load device for the creep test over a couple of months.

The creep tests were performed by devices such as the one shown in Figure 4.1. The panel specimens were supported by three symmetrical pivots at the edge of the panel. A constant dead load was applied at the centre of the panel, and a different gravity load assembly can be applied on the specimens to determine the creep behaviour of the material under different stress levels. A linear variable differential transducer (LVDT) was positioned above the panel to measure the displacement over a few months. The LVDT was not positioned under the specimens as in a conventional ASTM C1550 test, so as to avoid the risk of damaging the device due to the collapse of the specimens. The tests were carried out in a constant climate room where the temperature was maintained at 22.9±0.5°C and relative humidity was kept at 50±2%.

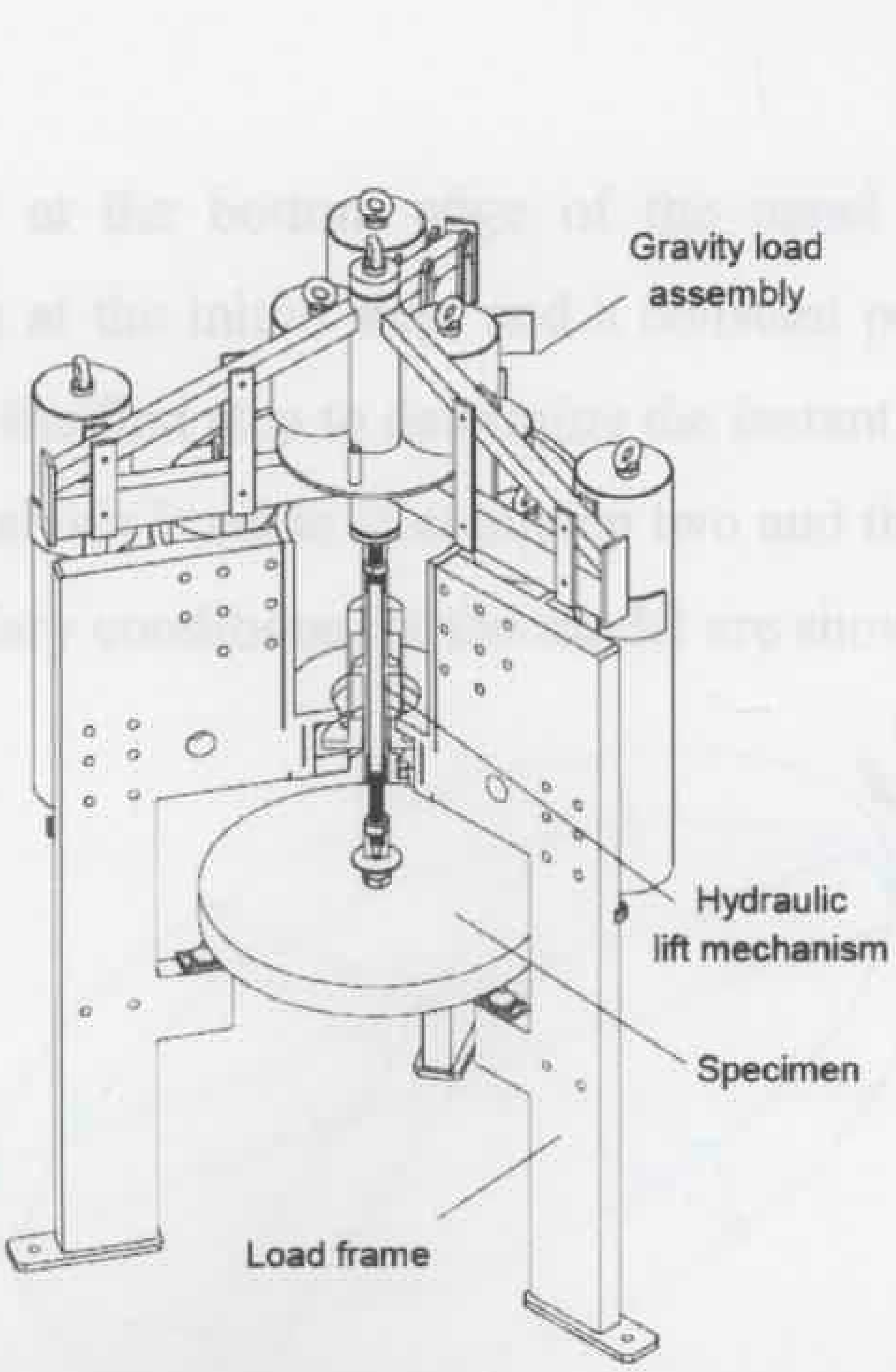

Figure 4.1: Creep test device (Bernard, 2004).

4.2.3 NUMERICAL MODELS

The ASTM C1550 circular panels were modelled by the finite element code ABAQUS. The right choice of element is important for the finite element analysis to get accurate results at a reasonable cost. The test specimens have a standard simple circular shape and the creep strain is relatively small during the test, thus a 20-node quadratic brick, reduced integration solid element C3D20R was selected for the simulation. The circular panel model is 750mm in diameter and 75mm in thickness and the mesh division of the model is shown in Figure 4.2.

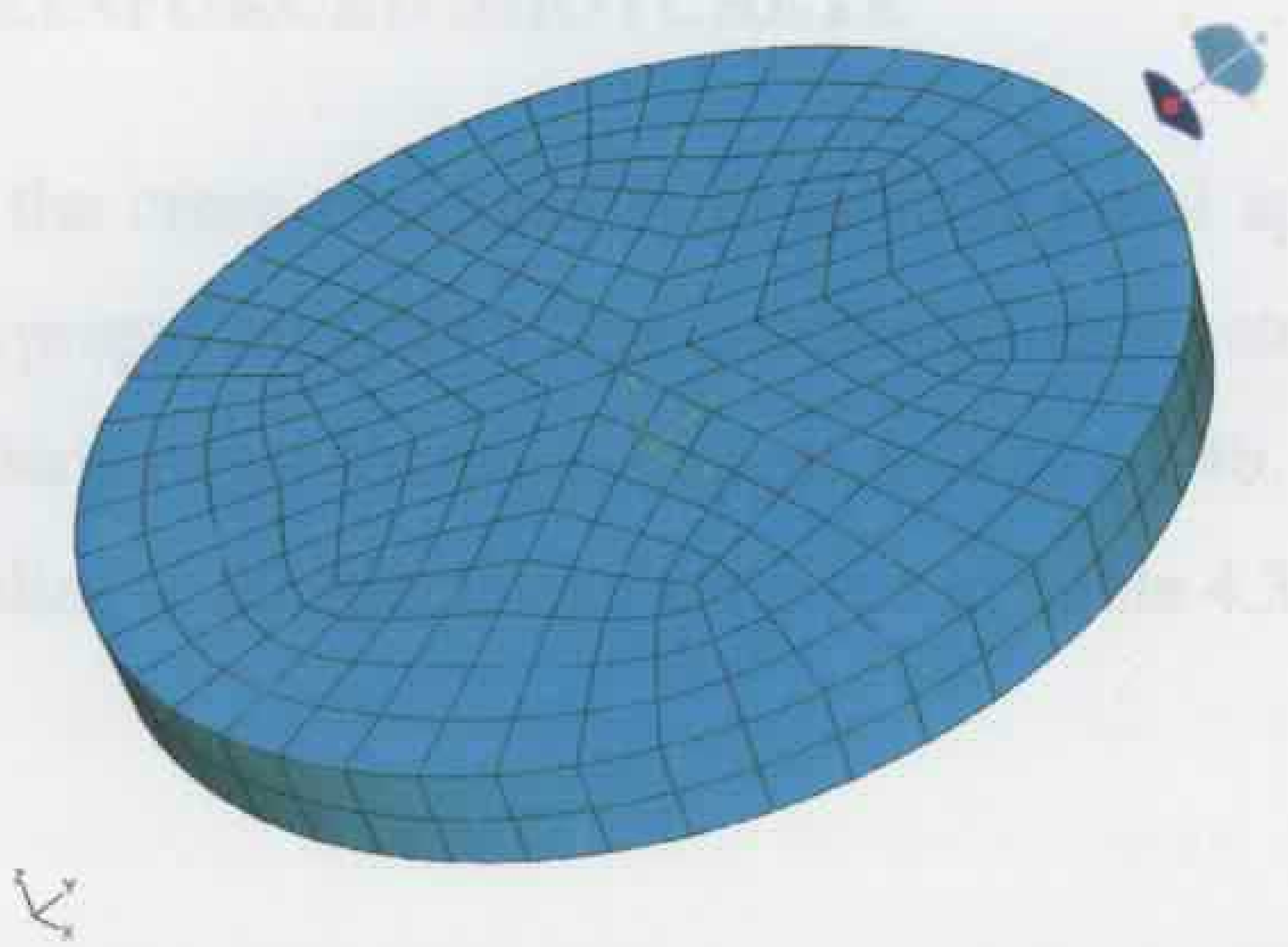

Figure 4.2: Mesh division of the ASTM C1550 panel specimen.

Three symmetrical pivots at the bottom edge of the panel model are fixed against movement in all directions at the initial step, and a constant point load is applied at the centre of the top surface at the first step to determine the instant elastic deformation of the specimen. Visco-elastic analysis is set to start at step two and the calculated time range is set as 200 days. The boundary conditions for the model are shown in Figure 4.3.

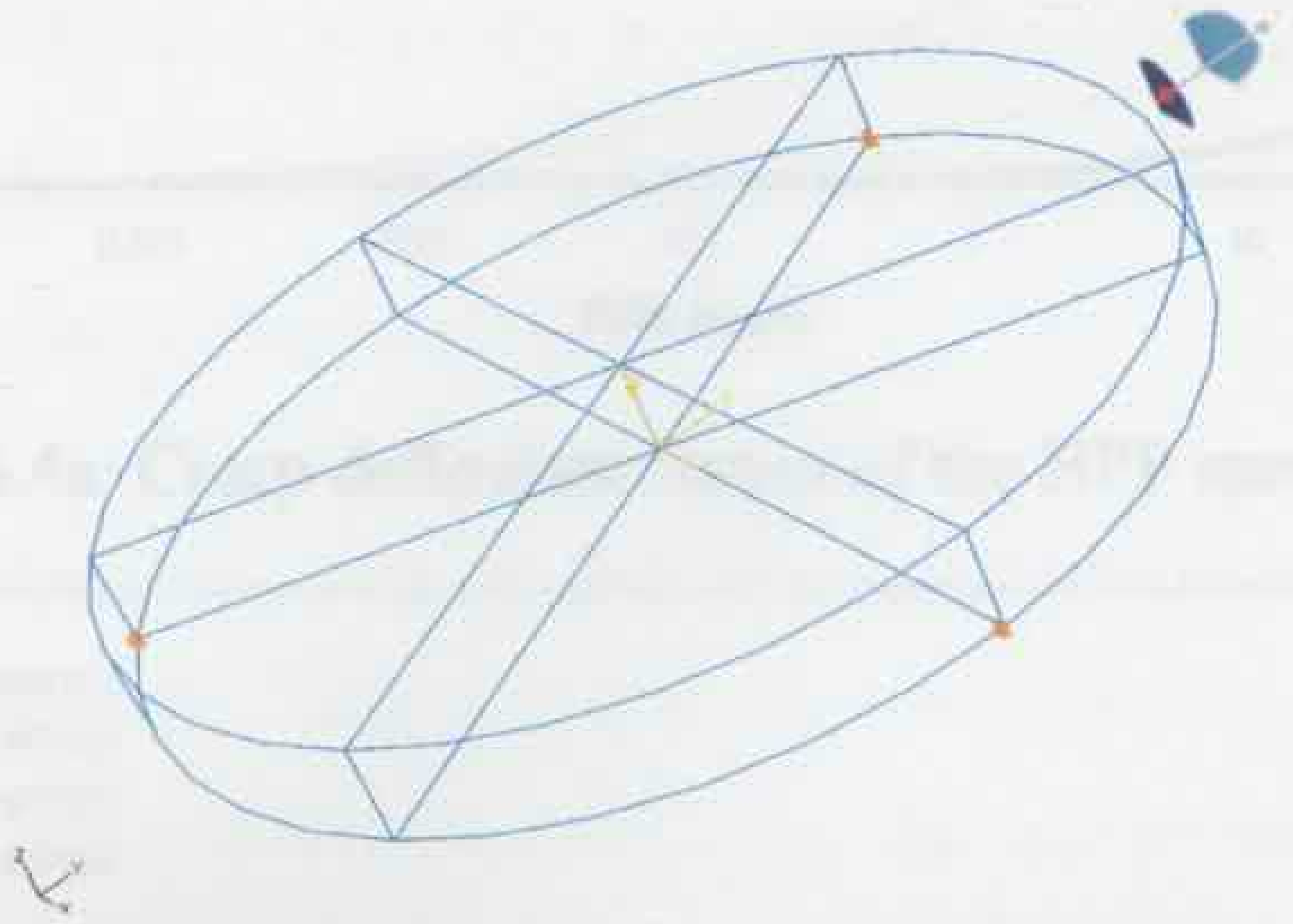

Figure 4.3: Boundary conditions of the test specimen.

The elastic properties of the shotcrete material are defined as isotropic and by two parameters, Young's modulus and Poisson ratio, while the visco-elastic creep behaviour of the material is represented by a time-hardening power law model with three parameters, power law multiplier factor *F*, stress order factor *m* and time order factor *n*. Different material properties and creep parameters are selected for fitting the experiment curves of different types of FRS specimens under different load conditions.

4.2.4 HPP FIBRE REINFORCED SHOTCRETE

A series of results for the creep deformation of circular panel specimens composed of High Performance Polypropylene (HPP) fibre reinforced shotcrete and the experimental results as provided by Bernard are shown in Figures 4.4a and 4.4b. The magnitudes of the constant dead loads applied to the specimens are given in Table 4.3.

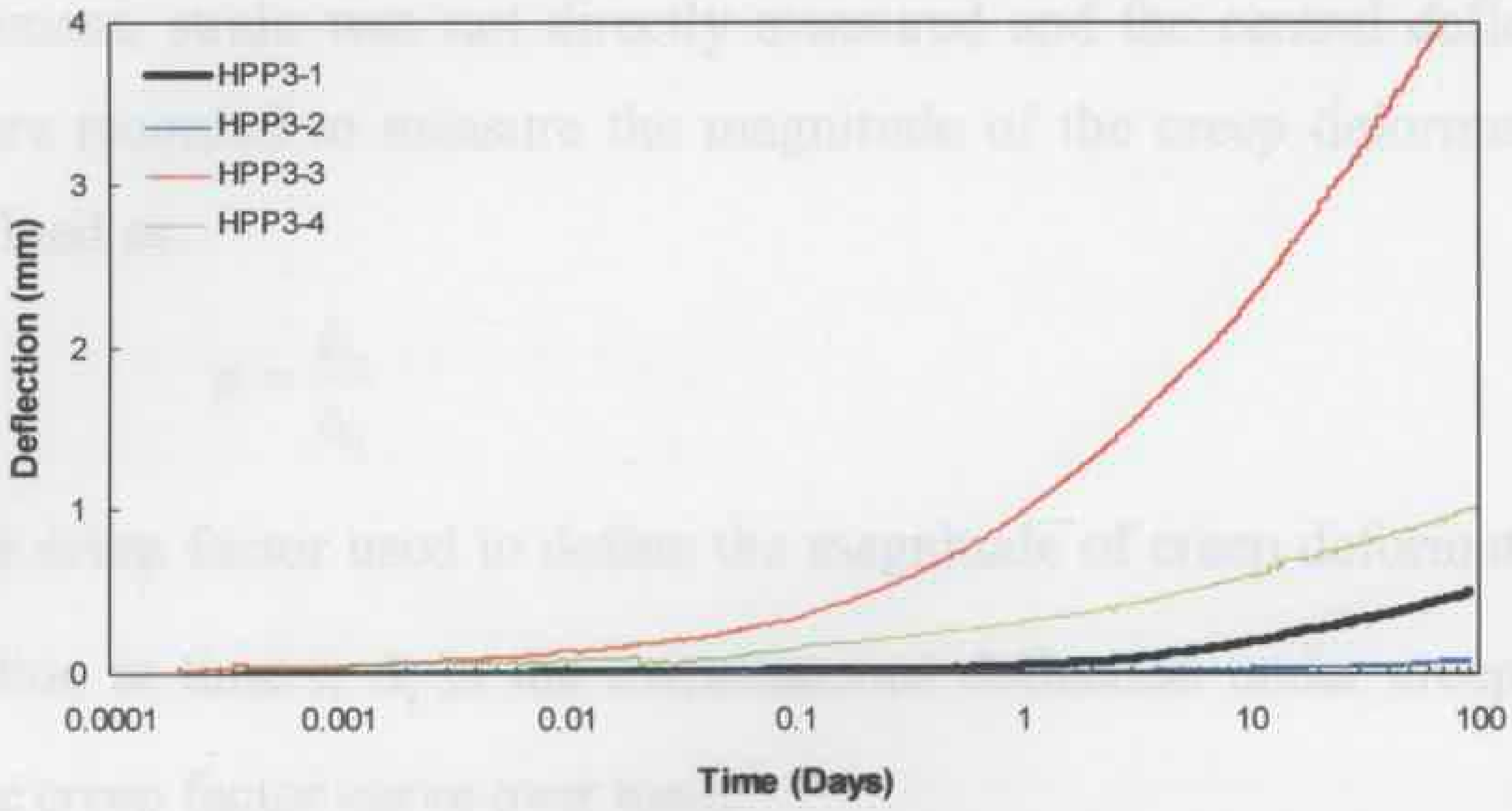

Figure 4.4a: Creep deflection curves of the HPP specimens.

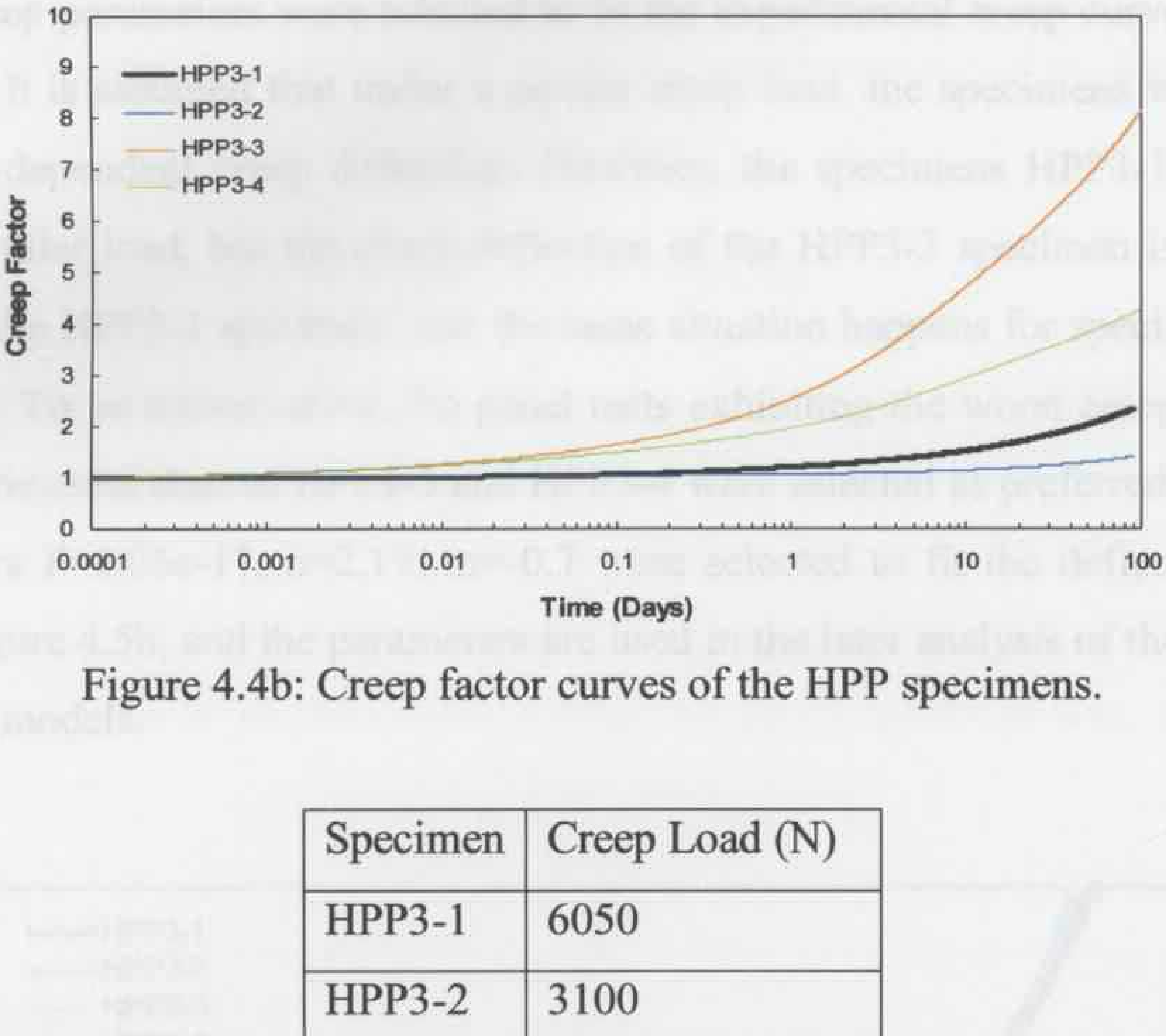

Figure 4.4b: Creep factor curves of the HPP specimens.

Specimen	Creep Load (N)
HPP3-1	6050
HPP3-2	3100
HPP3-3	6080
HPP3-4	3050

Table 4.3: Creep loads applied on the HPP specimens.

In Figure 4.4a, the deflection records start from zero, and the time-dependent creep deflection was seen to increase with time. The time-dependent creep behaviour of the material was normally defined by time-strain or time-strain rate relationship. In the present experiment, strain was not directly measured and the central deflections of the specimens were recorded to measure the magnitude of the creep deformation. A creep factor was defined as

$$\phi = \frac{\Delta_t}{\Delta_i} \tag{4.1}$$

where ϕ is the creep factor used to define the magnitude of creep deformation, Δ_t is the central deflection at time *t*, Δ_i is the instantaneous deflection under creep load. Figure 4.4b shows the creep factor curve over time.

Different creep parameters were selected to fit the experimental creep curve as shown in Figure 4.5a. It is assumed that under a certain creep load, the specimens will undergo a certain time-dependent creep deflection. However, the specimens HPP3-1 and HPP3-3 are under similar load, but the creep deflection of the HPP3-3 specimen is much larger than that of the HPP3-1 specimen, and the same situation happens for specimens HPP3-2 and HPP3-4. To be conservative, the panel tests exhibiting the worst creep deformation i.e. the experimental data of HPP3-3 and HPP3-4 were selected as preferred results. A set of parameters F=1.05e-17, n=2.19, m=-0.7 were selected to fit the deflection curve as shown in Figure 4.5b, and the parameters are used in the later analysis of the tunnel creep deformation models.

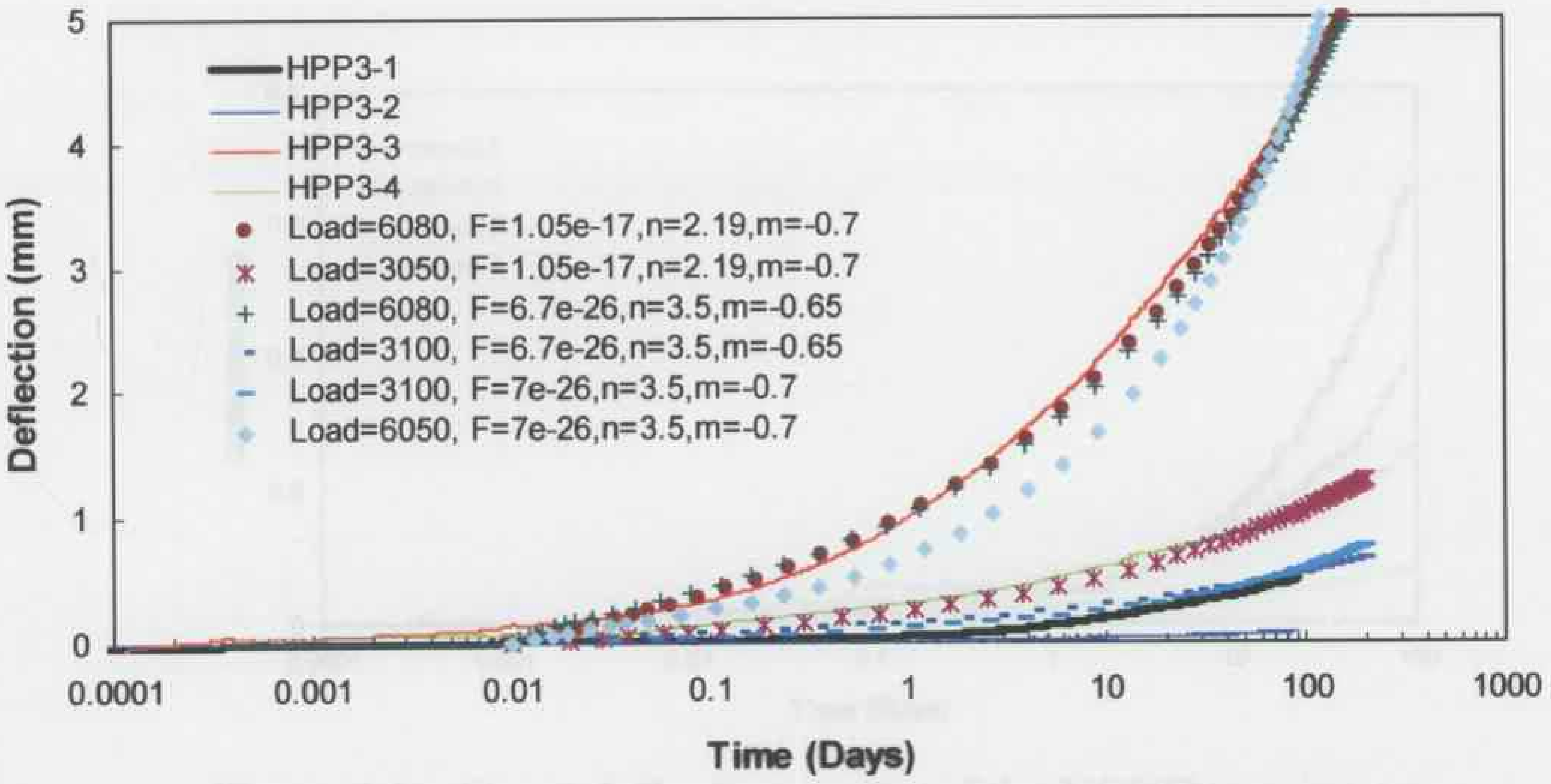

Figure 4.5a: Numerical fits of creep curves of the HPP specimens.

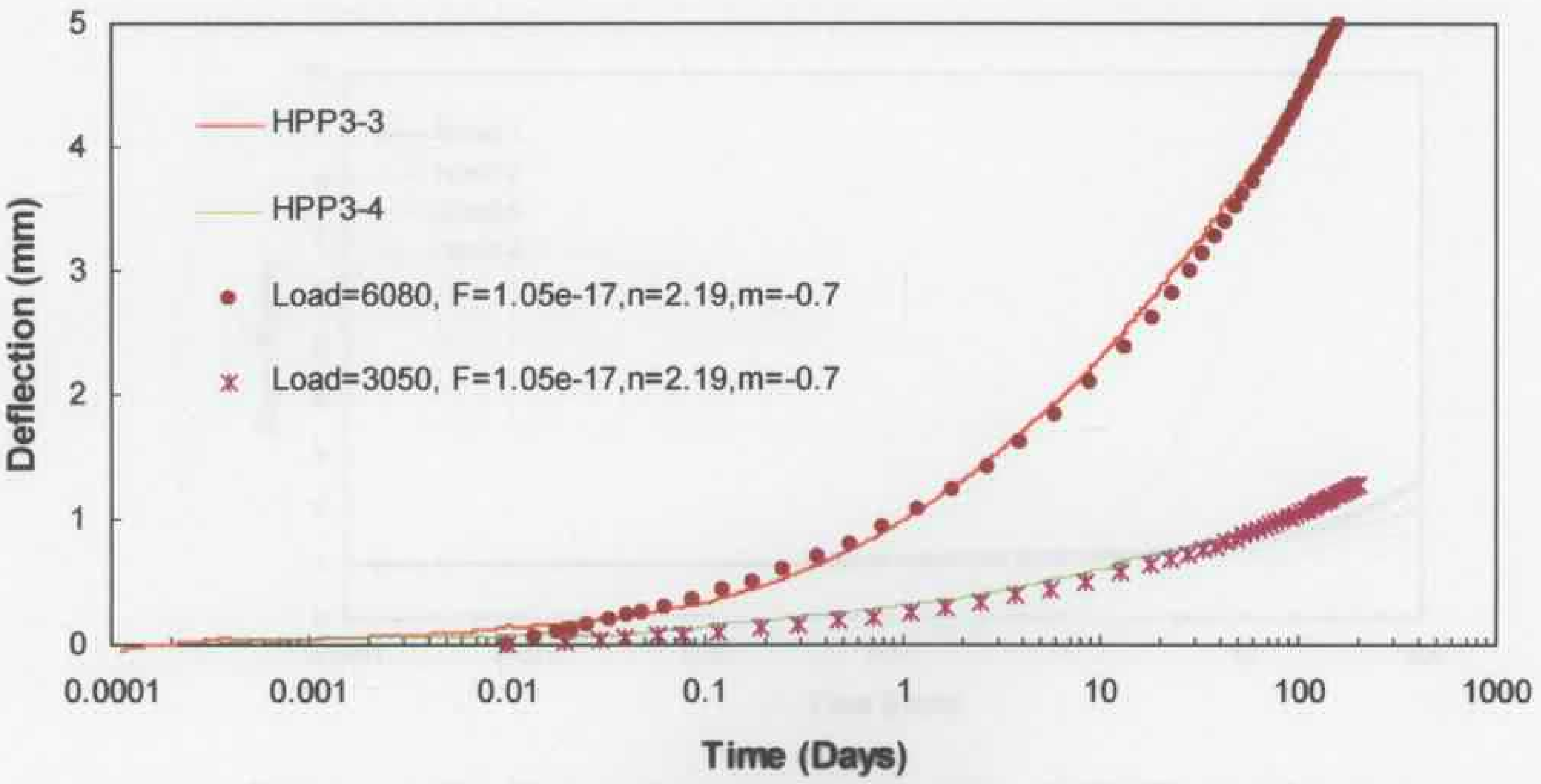

Figure 4.5b: Numerical curves with the selected creep parameters of the HPP specimens.

4.2.5 NOVO FIBRE REINFORCED SHOTCRETE

The experimental creep deflection and the creep factor curve of NOVO FRS specimens were provided by Bernard as shown in Figure 4.6a and 4.6b, respectively. The creep loads are given in Table 4.4. The creep load on the specimen NOVO2-1 was a little smaller than that on the specimen NOVO2-3, but creep deflection increased faster for the NOVO2-1 specimen. A similar situation happened in the results of tests NOVO2-2 and NOVO2-4.

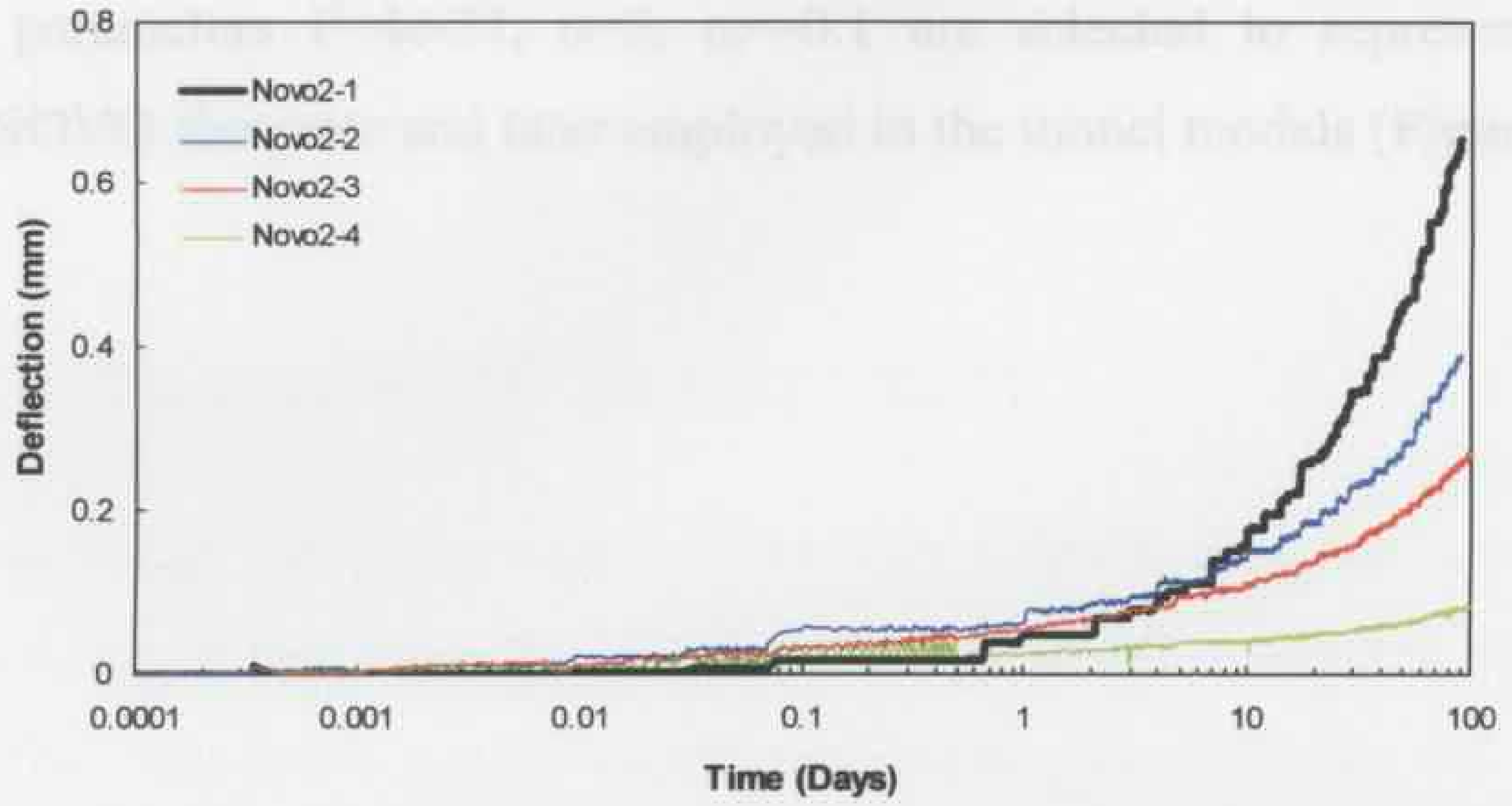

Figure 4.6a: Creep deflection curves of the NOVO specimens.

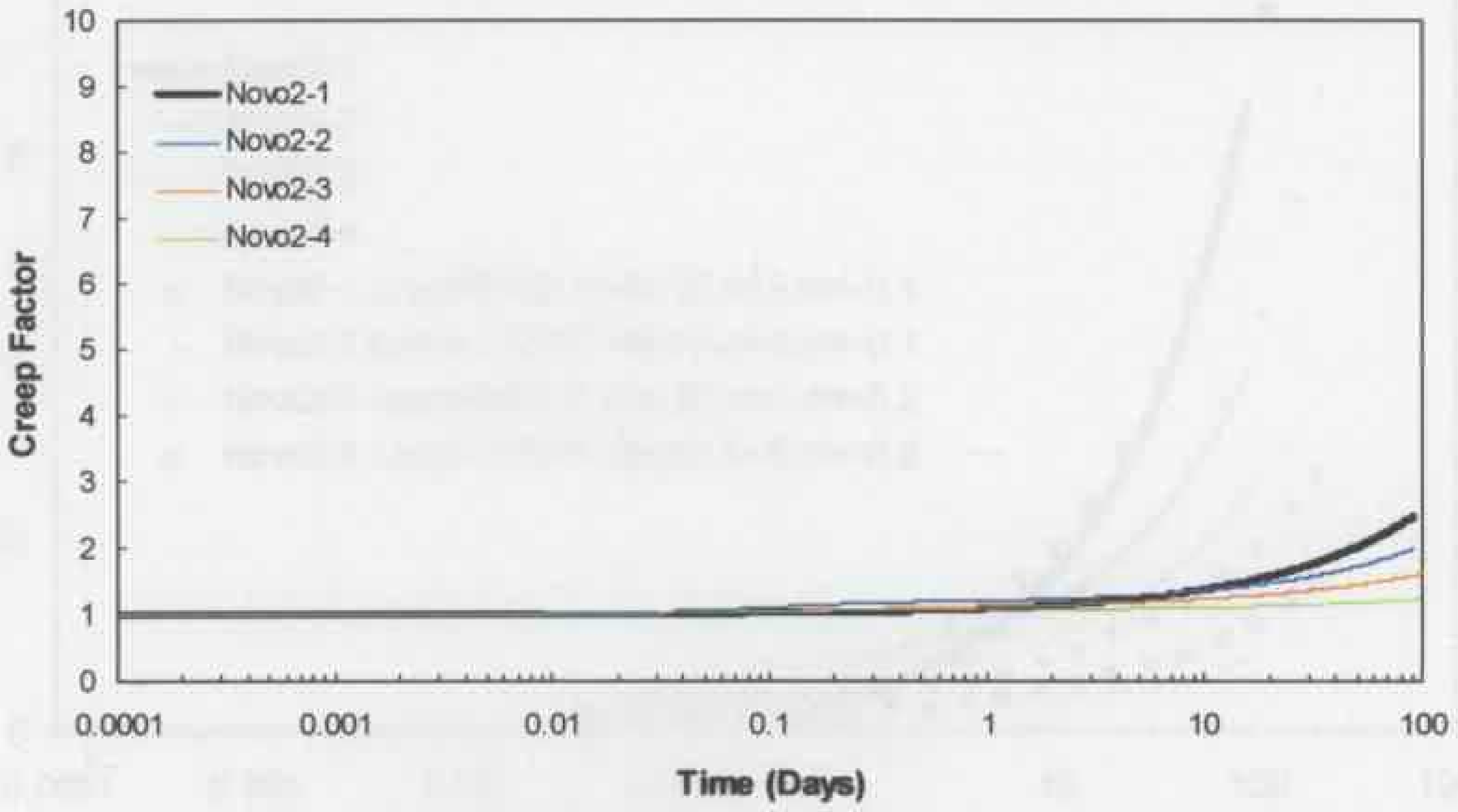

Figure 4.6b: Creep factor curves of the NOVO specimens.

Specimen	Creep Load (N)
NOVO2-1	8100
NOVO2-2	7120
NOVO2-3	8620
NOVO2-4	7190

Table 4.4: Creep loads applied on the NOVO specimens.

Different creep parameters were selected to fit the creep deflection curves as in Figure 4.7a. The experimental data of tests on the NOVO2-1 and NOVO2-2 specimens are selected as the preferred results based on the same criteria used for the HPP specimens. A set of creep parameters F=4e-37, n=5, m=-0.1 are selected to represent the creep behaviour of NOVO shotcrete and later employed in the tunnel models (Figure 4.7b).

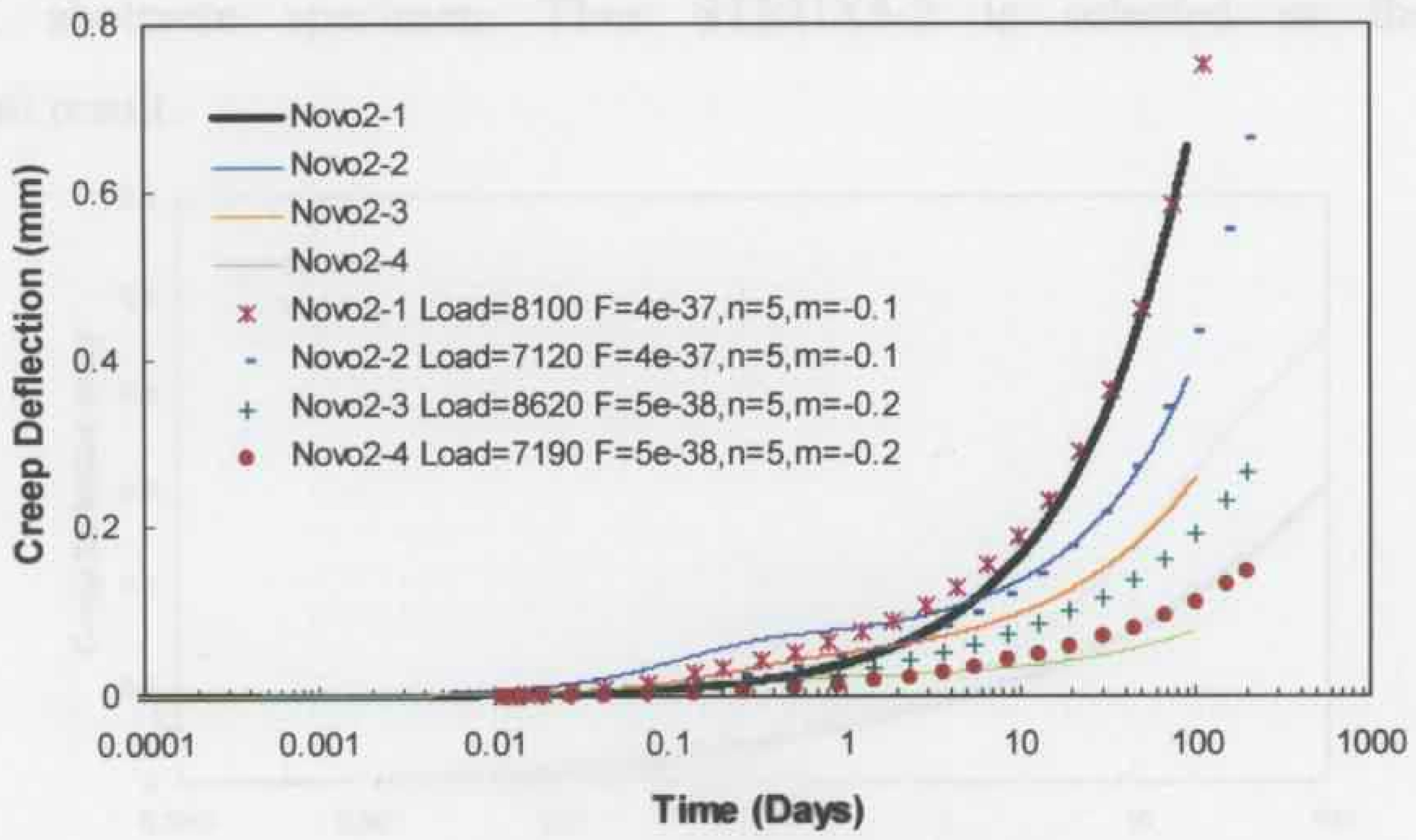

Figure 4.7a: Numerical fits of creep curves of the NOVO specimens.

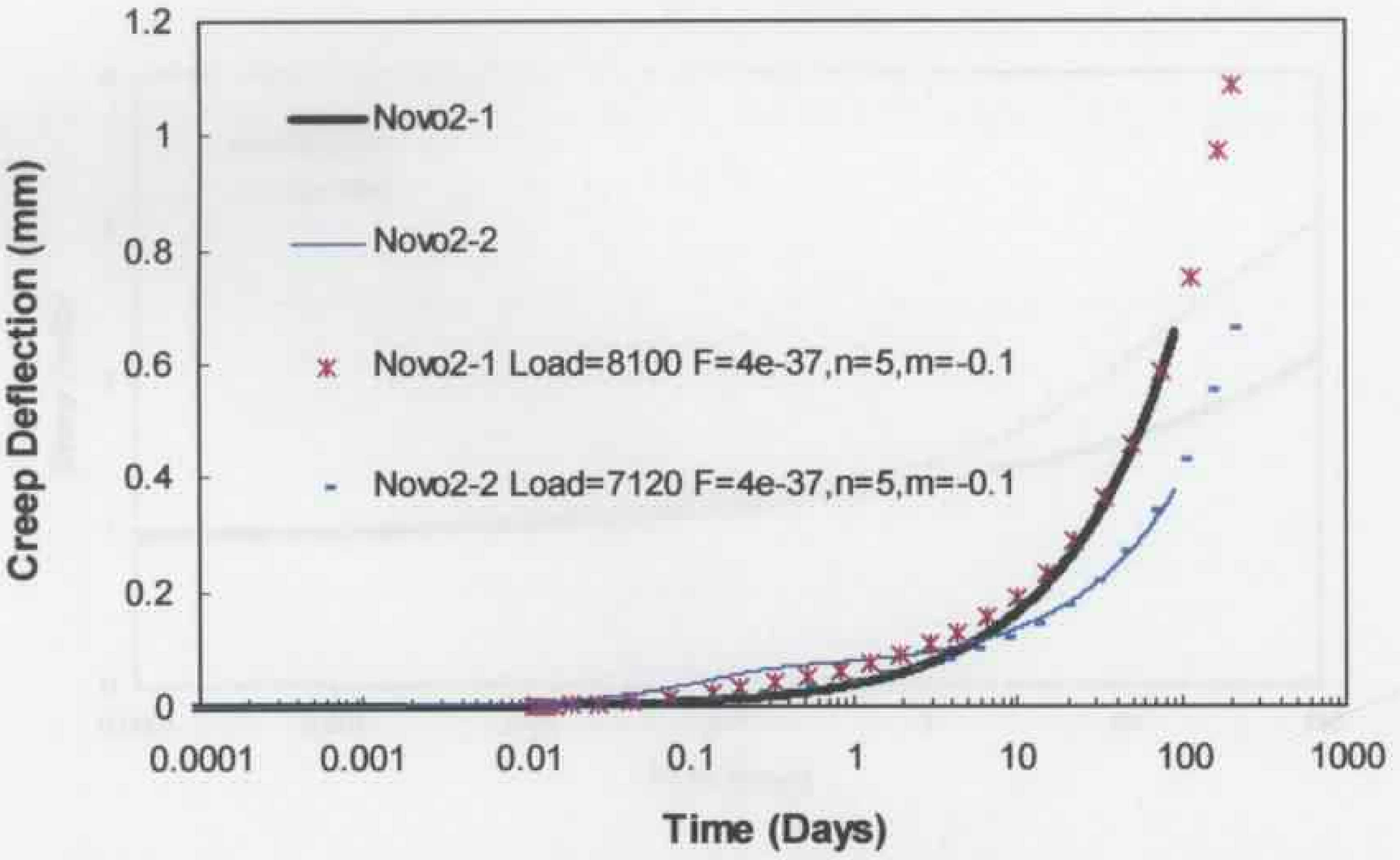

Figure 4.7b: Numerical curves for the selected creep parameters of the NOVO specimens.

4.2.6 STRUX FIBRE REINFORCED SHOTCRETE

Bernard also provided the experiment data for two STRUX shotcrete specimens. The creep deflection curves and creep factor curves are presented in Figures 4.8a and 4.8b, respectively. The creep loads applied on the specimens given in Table 4.5 indicate that the load on specimen STRUX5-1 is larger than that on specimen STRUX5-2. However, the creep deflection of the STRUX5-2 shotcrete specimen increases faster than that of the

STRUX5-1 shotcrete specimen. Thus STRUX5-2 is selected as the preferred experimental result.

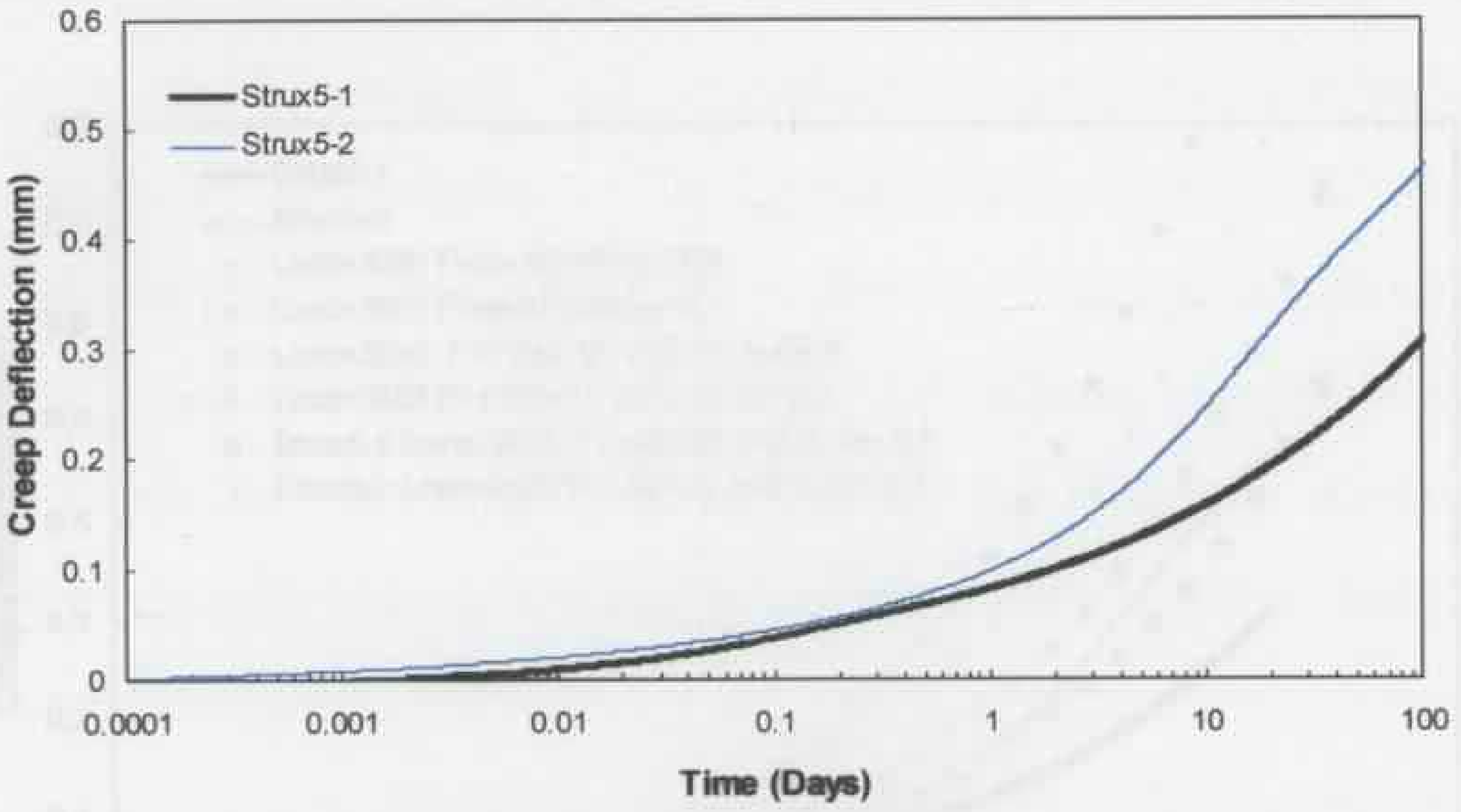

Figure 4.8a: Creep deflection curves of the STRUX specimens.

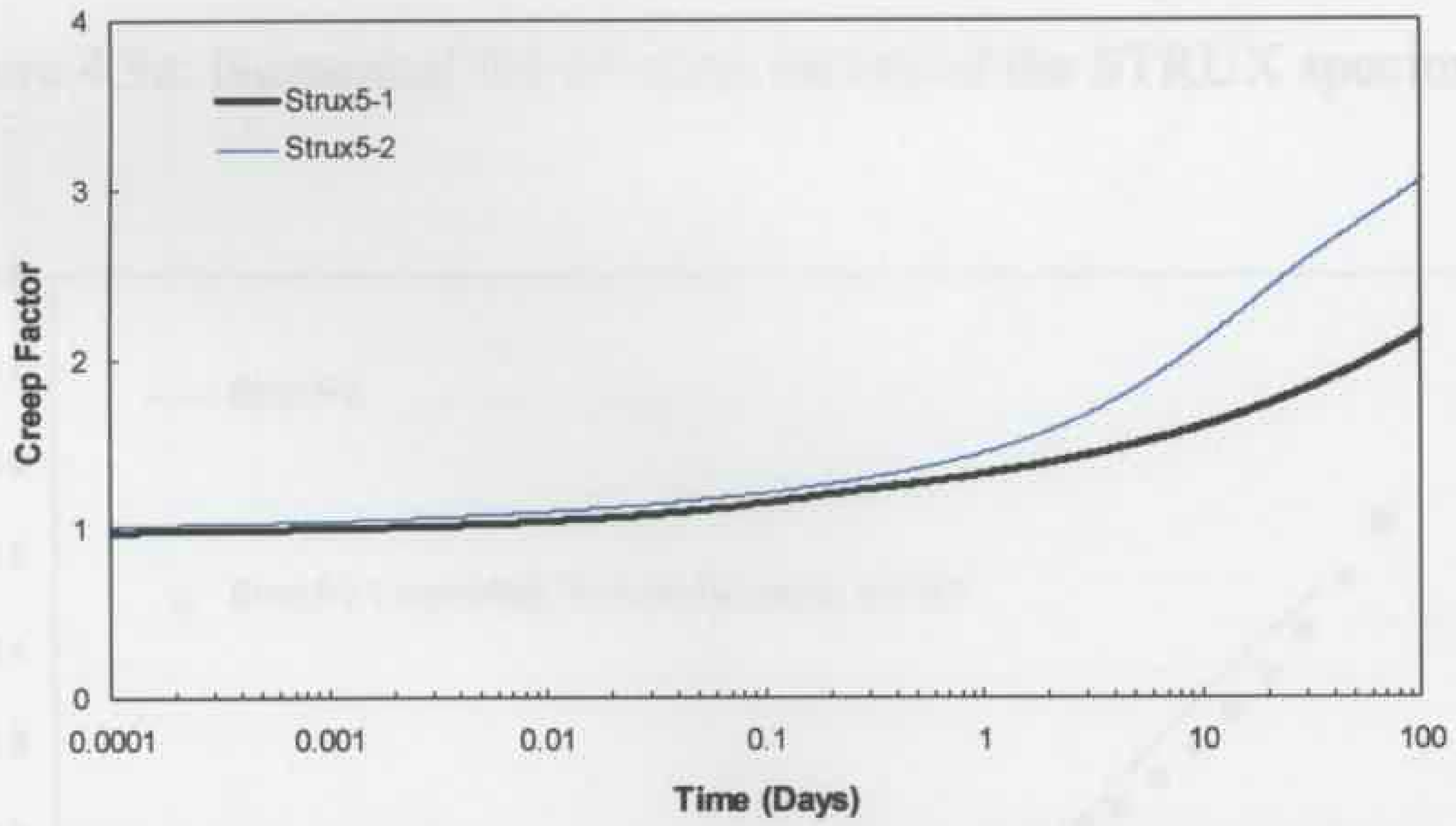

Figure 4.8b: Creep factor curves of the STRUX specimens.

Specimen	Creep Load (N)
STRUX5-1	3885
STRUX5-2	3030

Table 4.5: Creep loads applied on the STRUX specimens.

Different creep parameters are chosen in the numerical models as shown in Figure 4.9a and A set of creep parameters F=1.2e-19, n=2.5, m=-0.7 are finally selected to represent the creep behaviour of STRUX shotcrete (Figure 4.9b) and later used for simulate the creep behaviour of a tunnel composed of STRUX shotcrete lining.

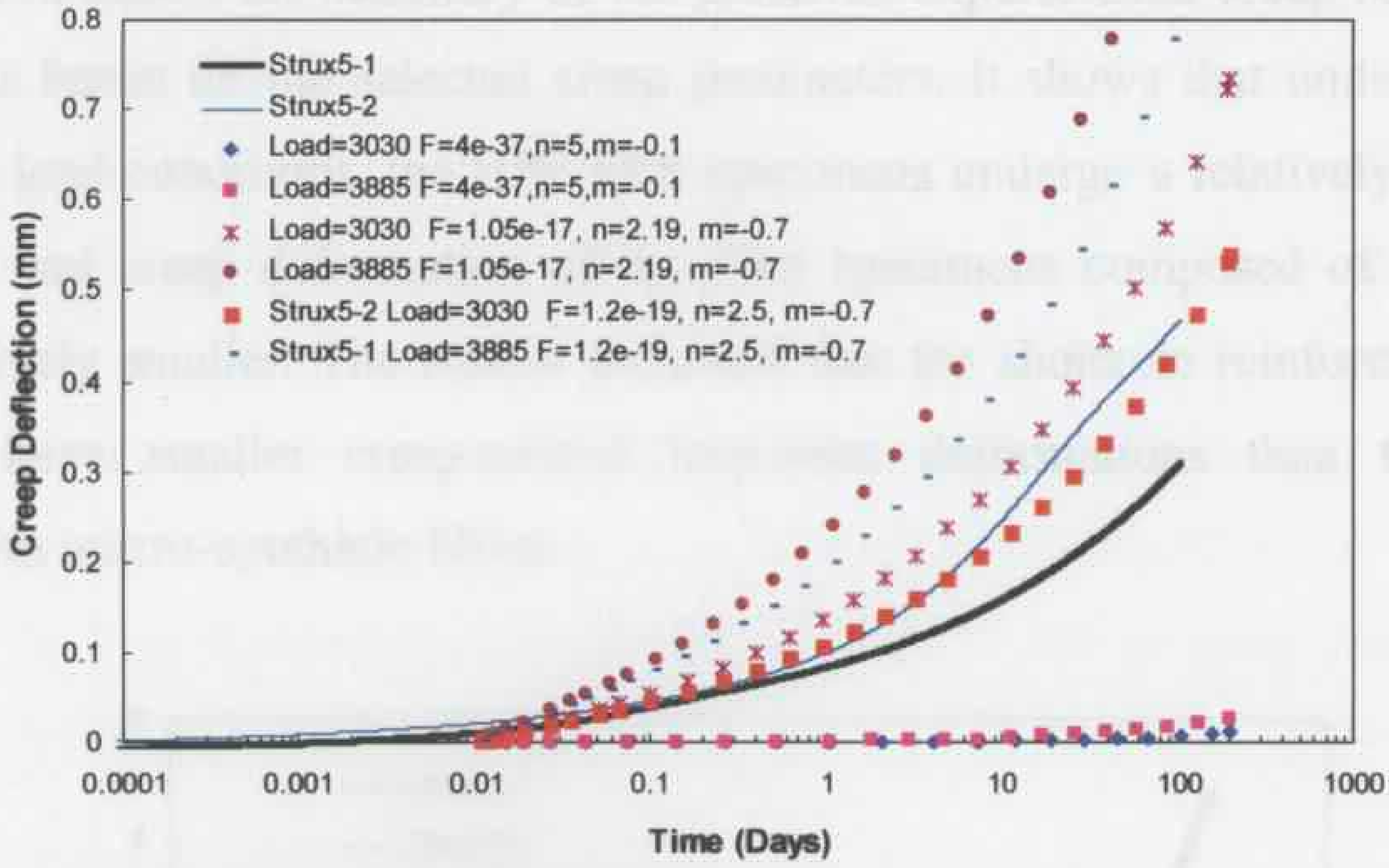

Figure 4.9a: Numerical fits of creep curves of the STRUX specimens.

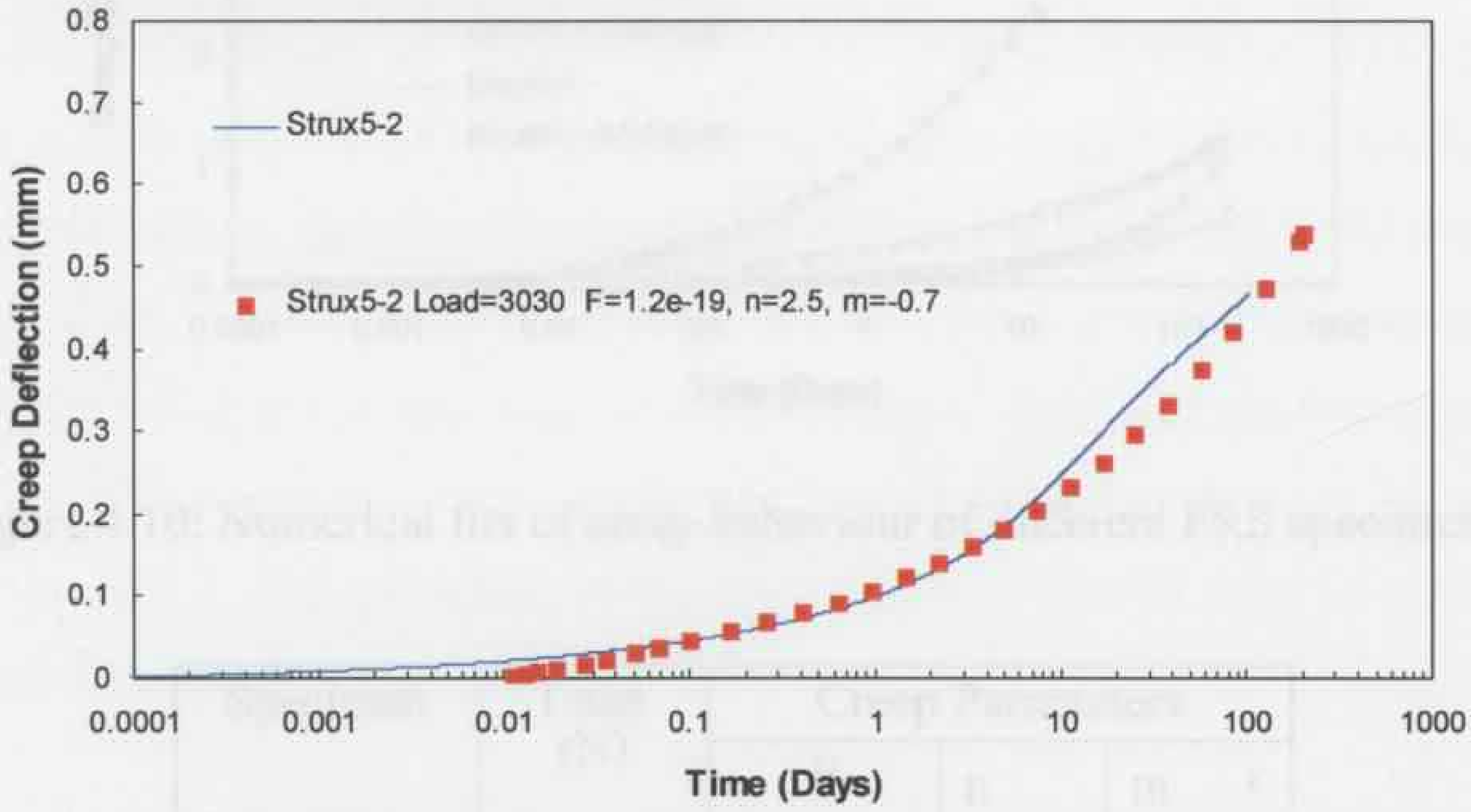

Figure 4.9b: Numerical curves for the selected creep parameters of the STRUX specimens.

4.2.7 SUMMARY

The selected creep parameters for different FRS specimens are summarized in Table 4.6, and Figure 4.10 shows the summary of the preferred experimental creep results and the numerical fits based on the selected creep parameters. It shows that under the present experimental load conditions, the HPP FRS specimens undergo a relatively larger creep deformation, and creep deformation of the FRS specimens composed of NOVO steel fibre is relatively smaller. The results indicated that the shotcrete reinforced with steel fibres may have smaller creep-related long-term deformations than the shotcrete reinforced with macro-synthetic fibres.

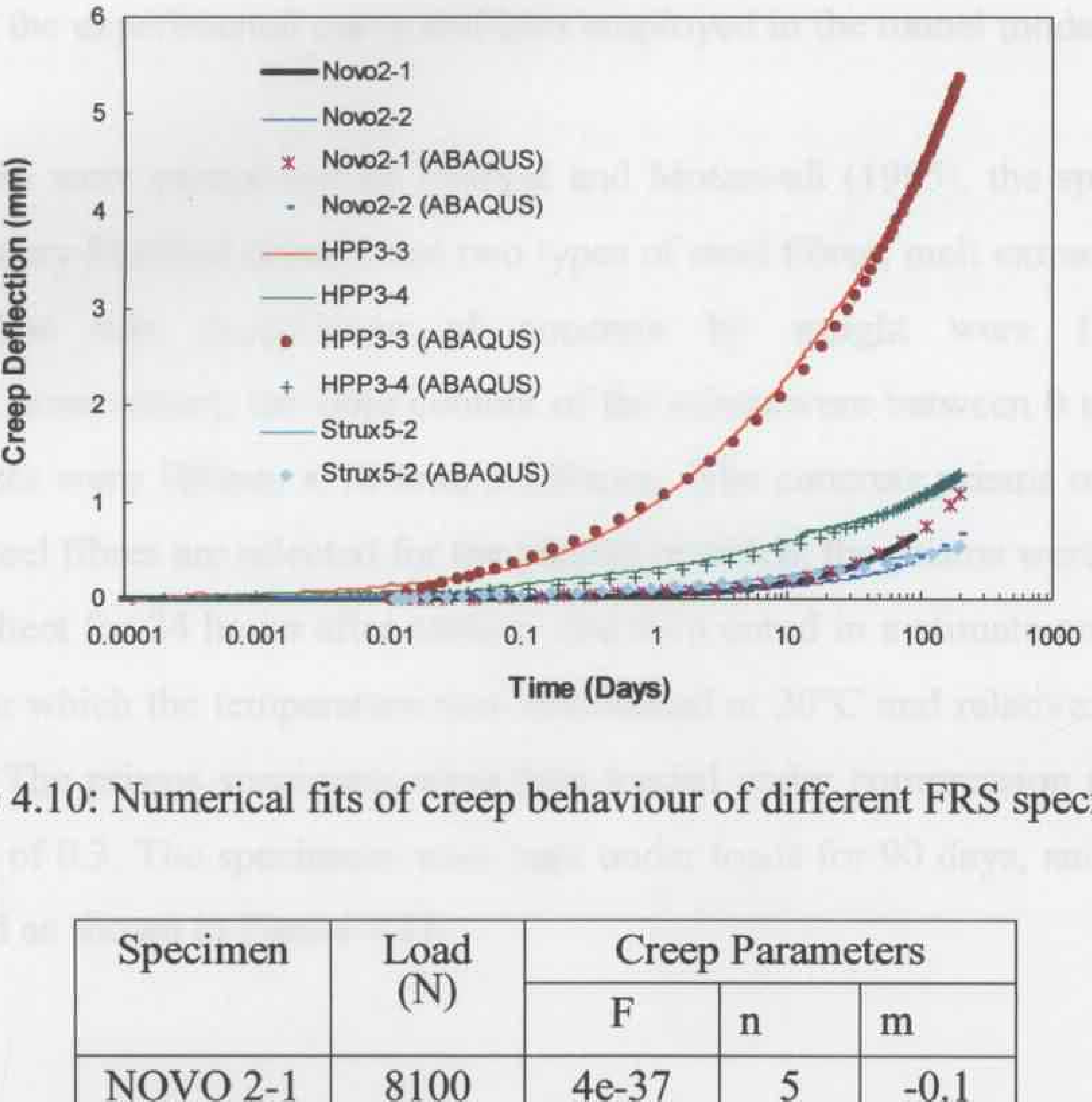

Figure 4.10: Numerical fits of creep behaviour of different FRS specimens.

Specimen	Load (N)	Creep Parameters		
		F	n	m
NOVO 2-1	8100	4e-37	5	-0.1
NOVO 2-2	7120	4e-37	5	-0.1
HPP 3-3	6080	1.05e-17	2.19	-0.7
HPP 3-4	3050	1.05e-17	2.19	-0.7
Strux 5-2	3030	1.2e-19	2.5	-0.7

Table 4.6: Selected creep parameters for different FRS specimens.

4.3 CREEP TESTS FOR SHOTCRETE UNDER COMPRESSION

It has been found that adding steel or macro-synthetic fibre in concrete can improve the mechanical properties and reduce the creep damage. Mangat and Motamedi (1985) carried out several uniaxial creep tests on the steel fibre reinforced cement matrices and provided a simple empirical expression to predict the creep behaviour of the specimens. When fibre reinforced cement matrices are under compression, the creep deformation increases very slowly compared with that of the cracked FRS specimens under bending. Thus in the tunnel support structure, the region under bending will undergo a much larger creep deformation than the region under compression. In the present research, numerical models were built to simulate the uniaxial tests. Different sets of creep parameters were selected to fit the experimental curve and later employed in the tunnel models.

The creep tests were carried out by Mangat and Motamedi (1985), the specimens were made by ordinary Portland cement and two types of steel fibres, melt extract and hooked, separately. The mix proportions of concrete by weight were 1:2.5:1.25:0.58 (cement:sand:stone:water), the fibre content of the mixes were between 0 to 3%, and the specimens sizes were 100mm x 100mm x 500mm. The concrete prisms reinforced with 3% hooked steel fibres are selected for the present research; the prisms were covered with a polythene sheet for 24 hours after casting, and then cured in a climate-controlled room for 28 days in which the temperature was maintained at 20°C and relative humidity was kept at 55%. The prisms specimens were then loaded under compression up to a stress-strength ratio of 0.3. The specimens were kept under loads for 90 days, and creep strains were recorded as shown in Figure 4.11.

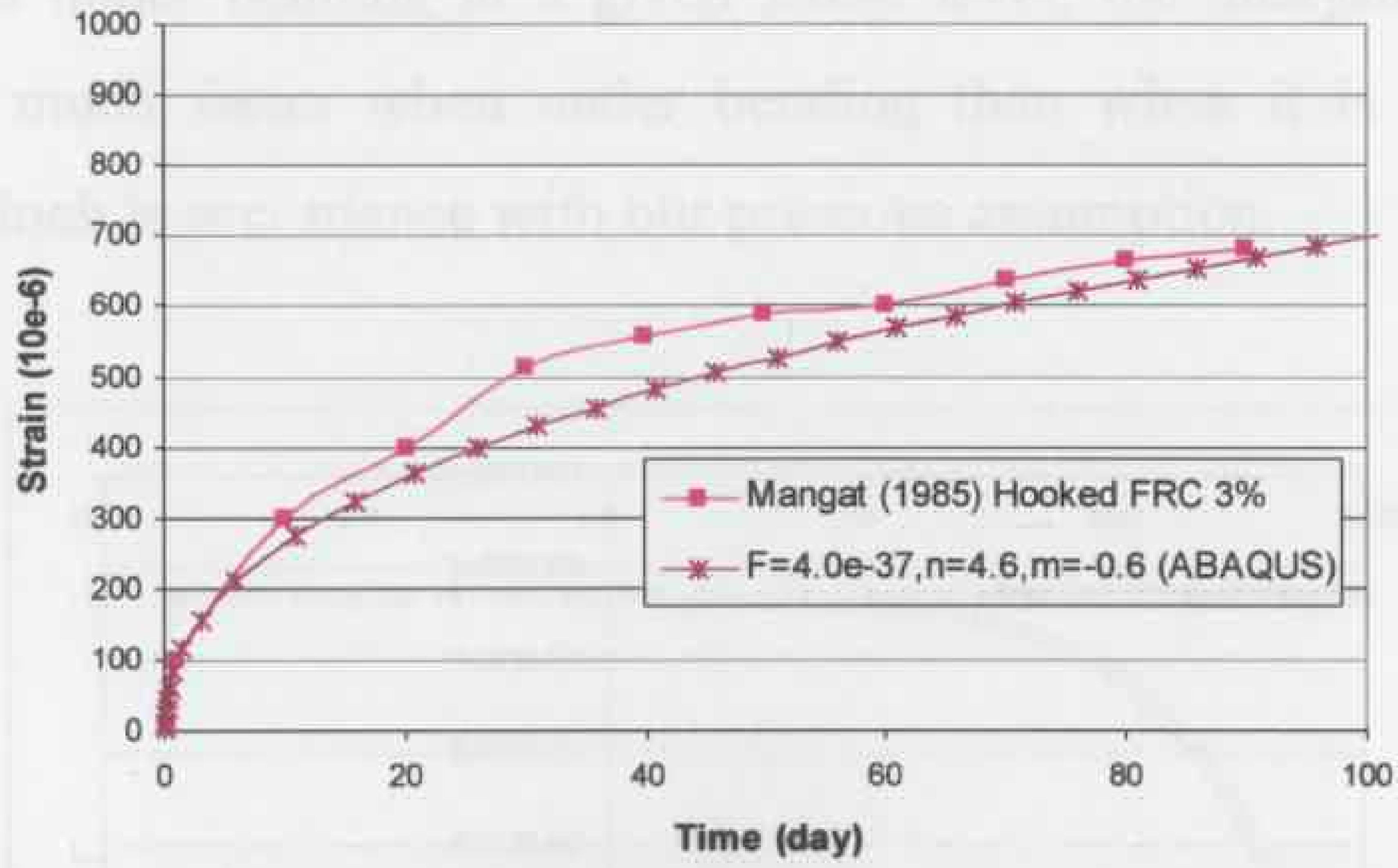

Figure 4.11: Numerical fit of creep behaviour of fibre reinforced cement.

The uniaxial test was simulated using ABAQUS by modelling the concrete prism with a 20-node solid element C3D20R. The mesh division of the model is shown in Figure 4.12. The bottom surface of the prism is fixed against moving in all directions, and a uniform pressure load is applied on the top surface of the prism. The boundary conditions for the model are shown in Figure 4.12.

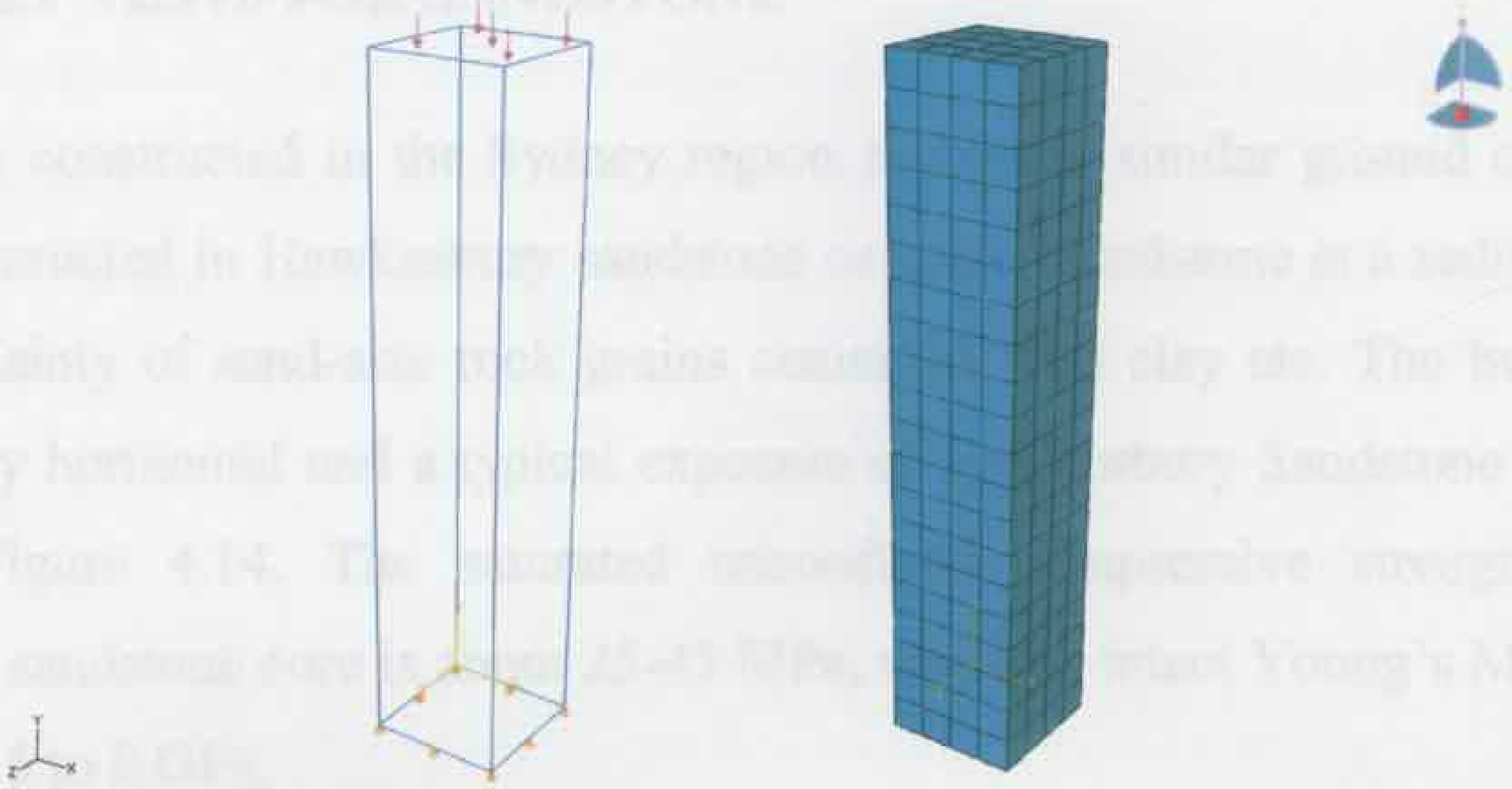

Figure 4.12: Numerical model of uniaxial creep test of fibre reinforced cement.

With a set of selected creep parameters F=4.0e-37, n=4.6, m=-0.6, the numerical creep strain curve can fit well with the experimental data of Mangat and Motamedi (1985) as shown in Figure 4.11. If we compare the creep deformation of NOVO specimens under compression and under bending at a given stress level, the analysis indicated that the material creeps much faster when under bending than when it is under compression (Figure 4.13), which is accordance with our previous assumption.

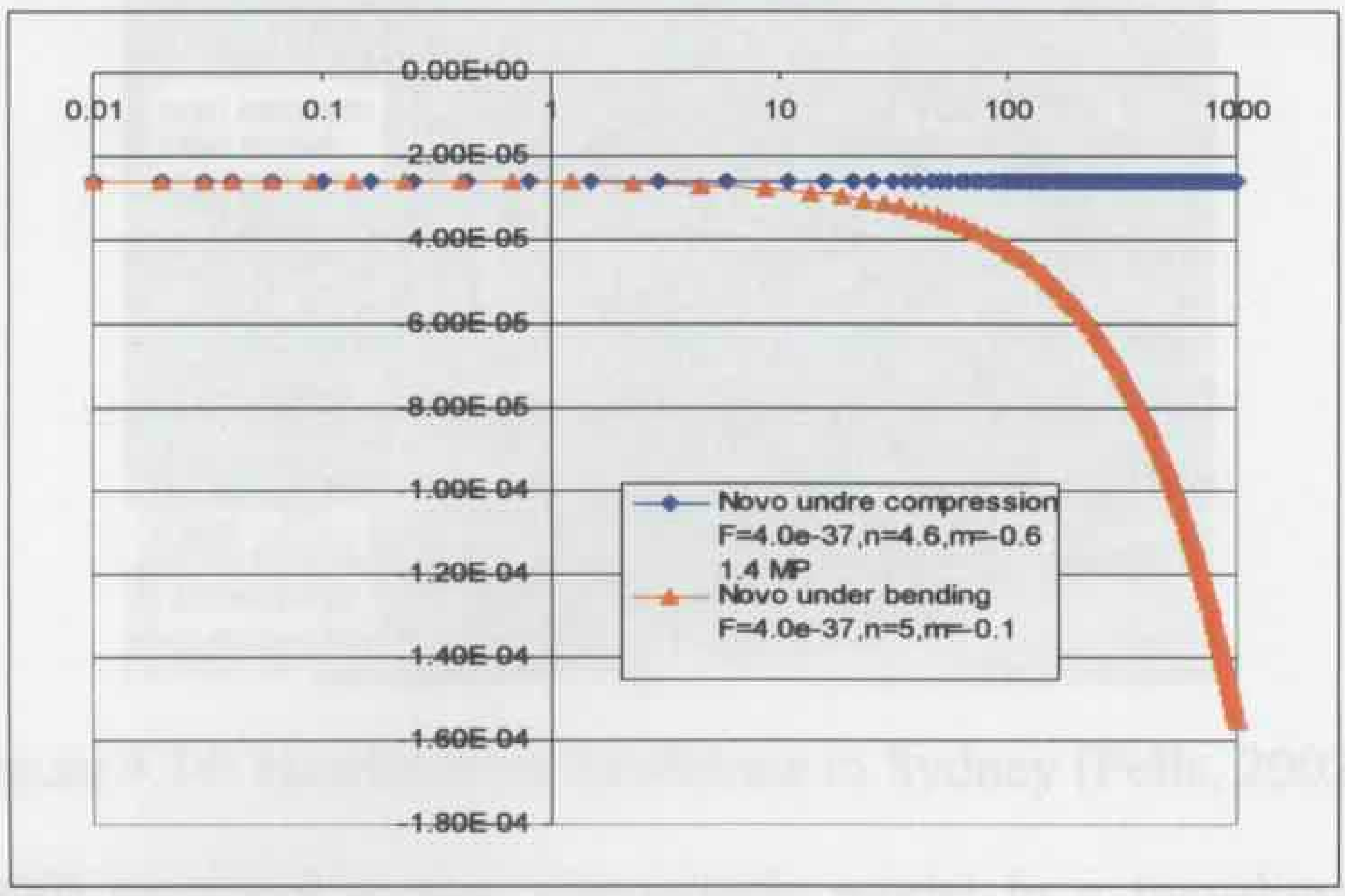

Figure 4.13: Numerical creep deformation of NOVO FRS under compression and bending.

4.4 CREEP TESTS FOR SANDSTONE

Most tunnels constructed in the Sydney region encounter similar ground conditions, as they are constructed in Hawkesbury sandstone or shale. Sandstone is a sedimentary rock composed mainly of sand-size rock grains cemented with clay etc. The bedding of the rock is nearly horizontal and a typical exposure of Hawkesbury Sandstone in Sydney is shown in Figure 4.14. The saturated unconfined compressive strength (UCS) of Hawkesbury sandstone core is about 25-45 MPa, while its intact Young's Modulus value is between 2.5 to 8 GPa.

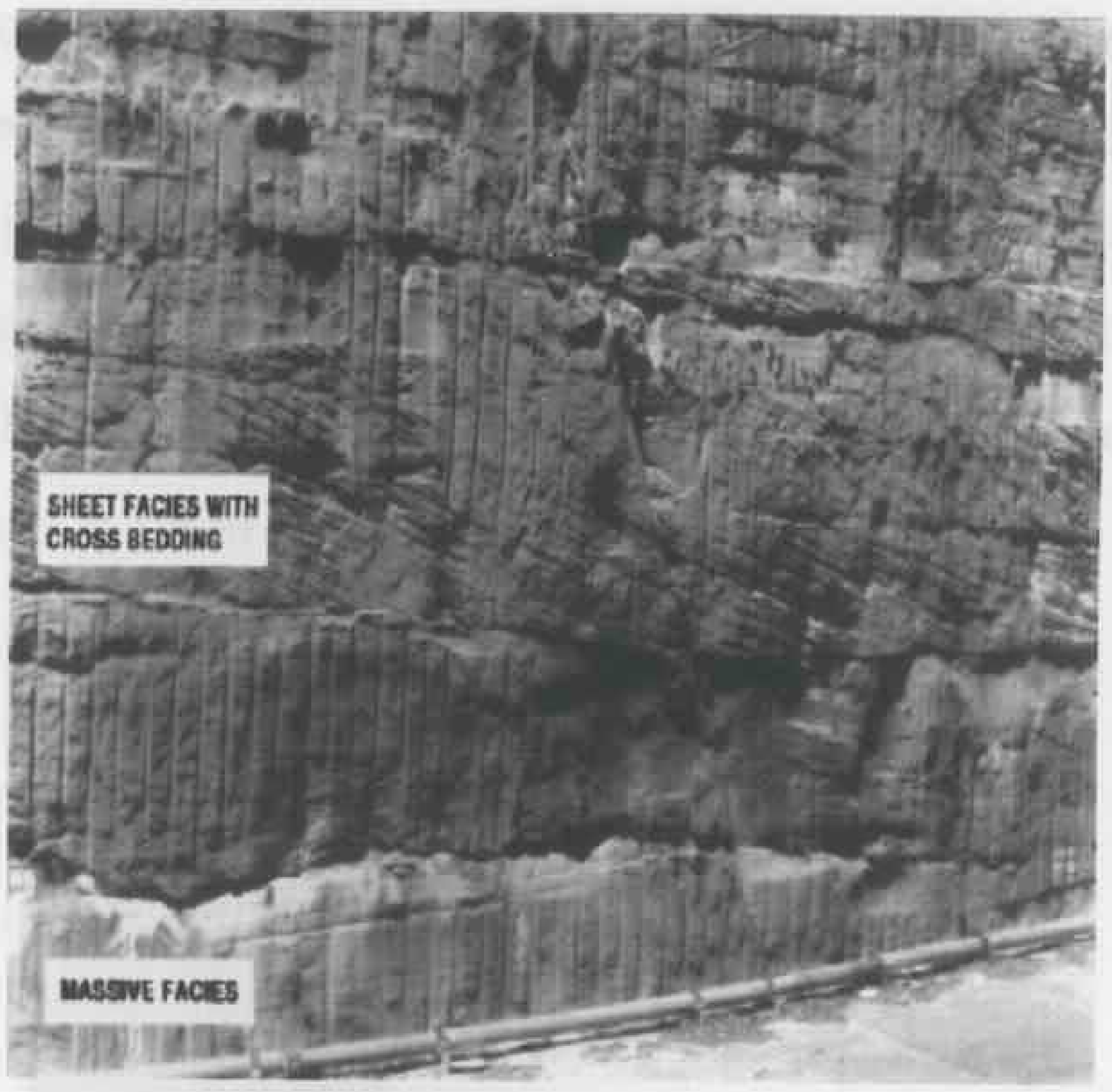

Figure 4.14: Hawkesbury Sandstone in Sydney (Pells, 2002).

Pellet et al. (2000) proposed a new viscoplastic model in a two-dimensional explicit finite-difference program to simulate a uniaxial specimen creep test. In the present research, a three-dimensional model was built up to simulate the creep test using ABAQUS. The uniaxial creep tests were carried out on homogenous dry sandstone specimens of 54mm diameter and 108mm height. The average experimental value of Young's modulus is 5.85GPa with a variation coefficient of 9.6% and a creep axial strain curve of the specimen under an axial constant stress of 5.2MPa as shown in Figure 4.15. The creep strain results show a nearly linear relationship with log-time.

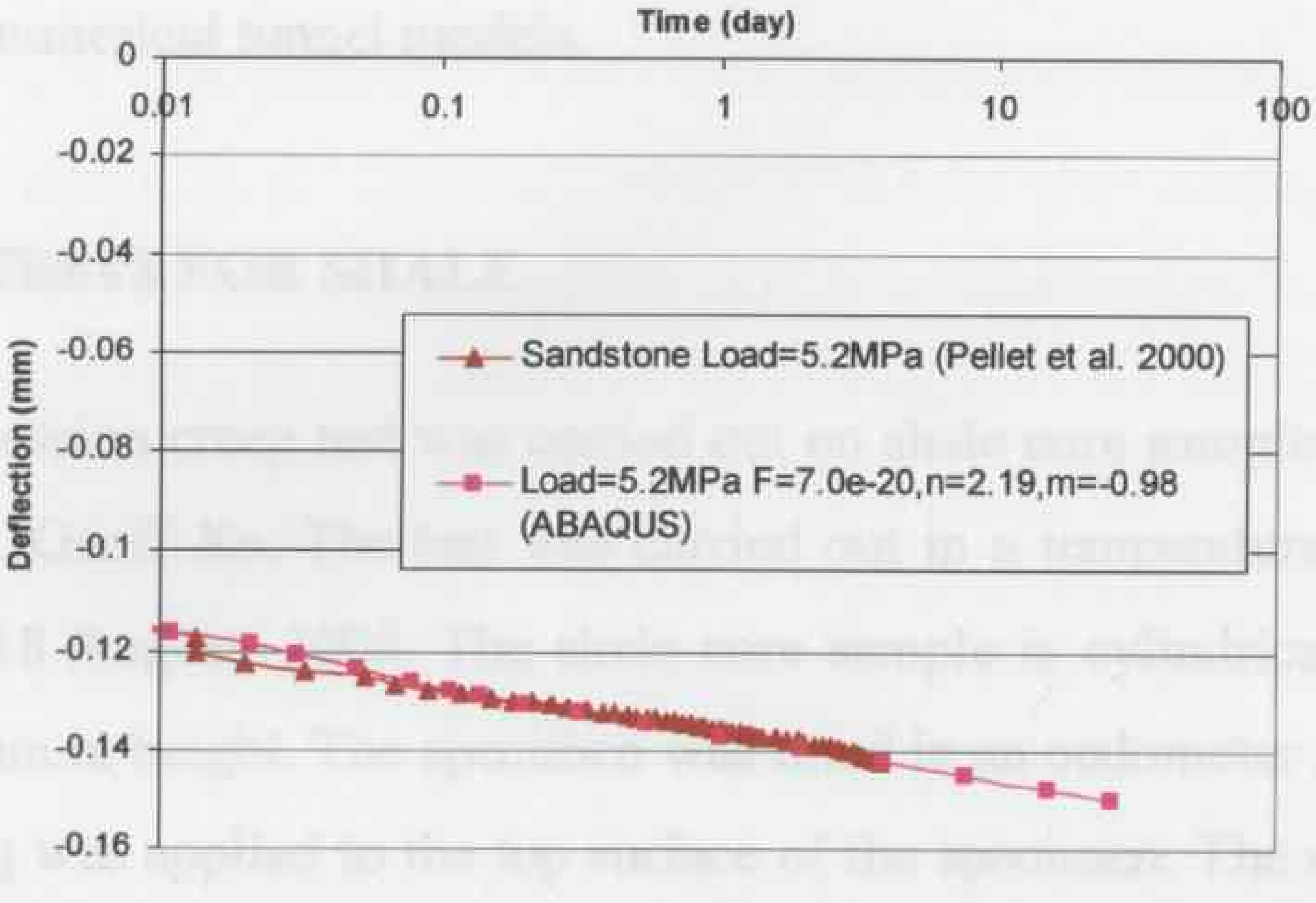

Figure 4.15: Numerical creep fit of uniaxial creep test for sandstone.

Pellet et al. (2000) used a simplified two-dimensional numerical model to simulate the test, while in the present research, the sandstone specimen was built up using a solid element C3D20R in a three-dimensional finite element program ABAQUS. The boundary conditions applied to the specimen are set so as to model the experiment; a uniform pressure load of 5.2MPa is applied on the top surface of the sandstone core while the bottom of the specimen is fixed as shown in Figure 4.16.

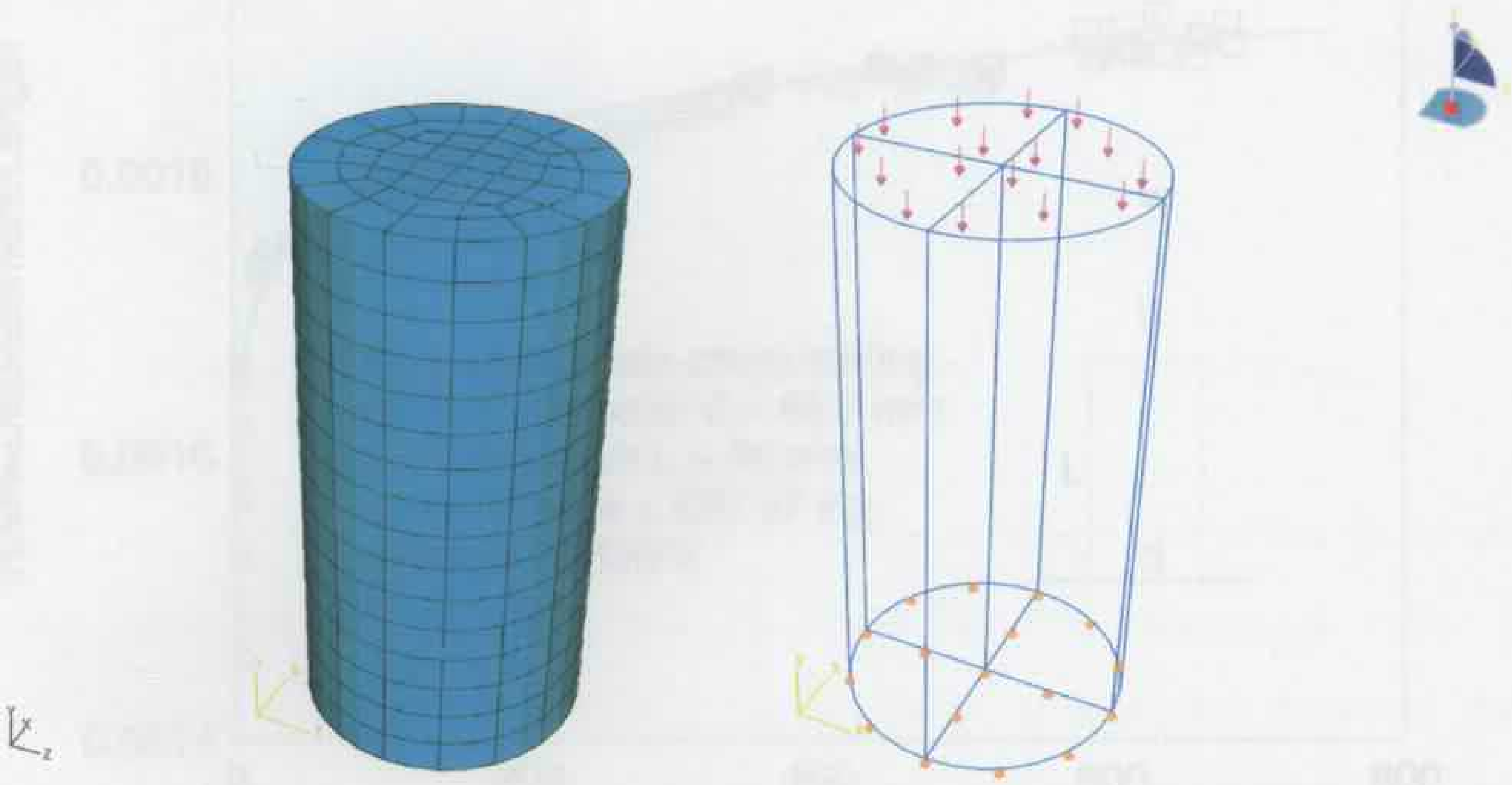

Figure 4.16: Numerical model of uniaxial creep test of sandstone.

The experiment creep curve was fitted by the numerical results using a set of visco-elastic parameters F=7.0e-20, n=2.19, m=-0.98 as shown in Figure 4.15. The parameters are later employed in the finite element analysis to represent the creep behaviour of sandstone in the numerical tunnel models.

4.5 CREEP TESTS FOR SHALE

A uniaxial compression creep test was carried out on shale core sample in the University of Sydney by Dr. Geoff Xu. The test was carried out in a temperature controlled room from 20 July to 18 August, 2006. The shale core sample is cylindrical with a 44.7mm diameter and 56mm in height. The specimen was fixed in an oedometer ring and a gravity load of 520.47 Kg was applied to the top surface of the specimen. The creep strain curve is shown in Figure 4.17 indicating that the creep deformation occurs at a higher rate in the first 2 days and then decreases to a steadier rate.

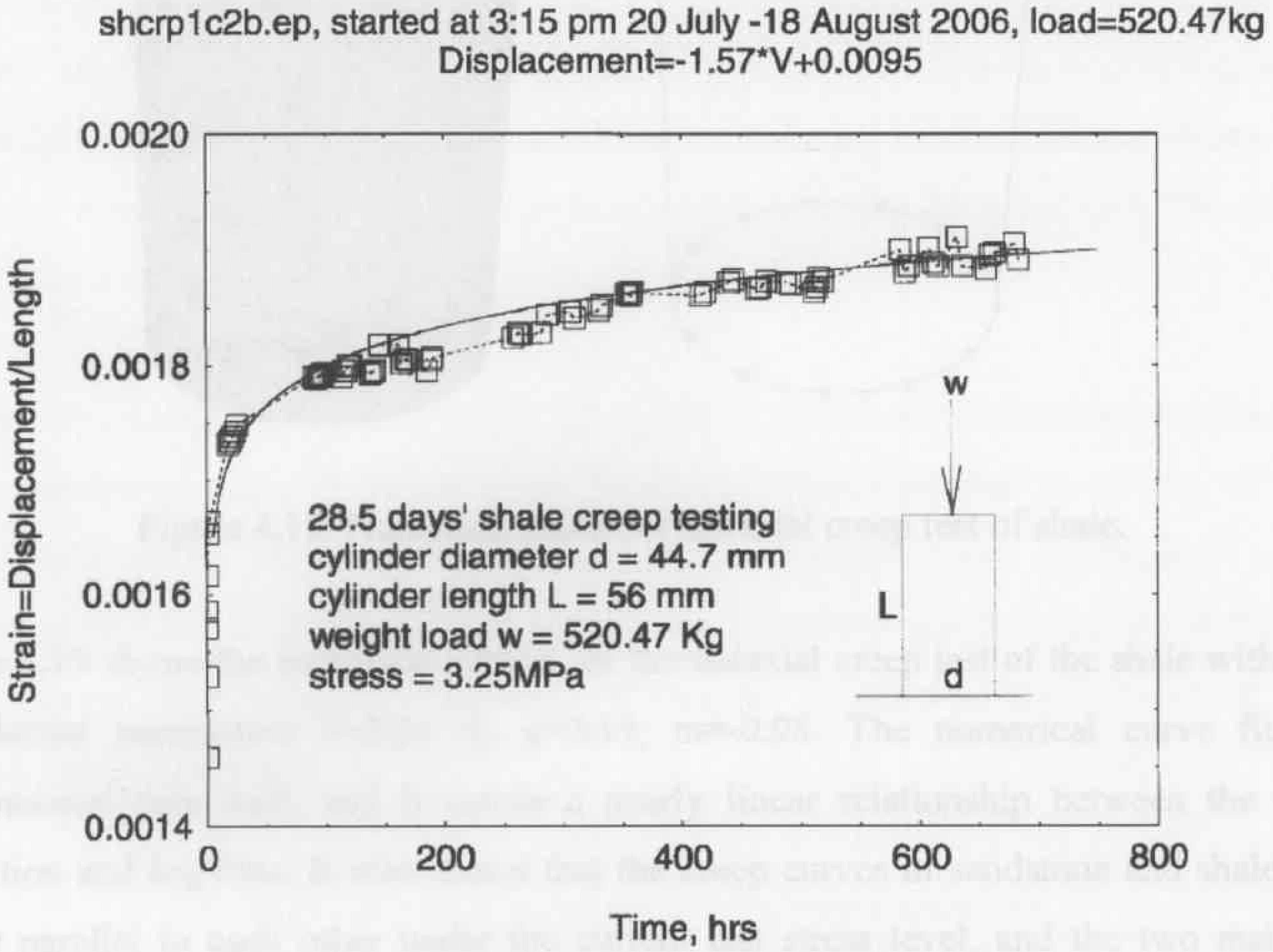

Figure 4.17: Creep test result of shale.

A three-dimensional model was built up to simulate the test using ABAQUS. The model was composed of a solid element C3D20R and the mesh division and boundary conditions of the model is shown in Figure 4.18. The bottom surface of the cylinder is fixed against movement in all directions, and the circular side surface is fixed against expanding in the lateral direction. The gravity load was transferred as a uniform pressure load of 3.25MPa applied to the top surface of the specimen.

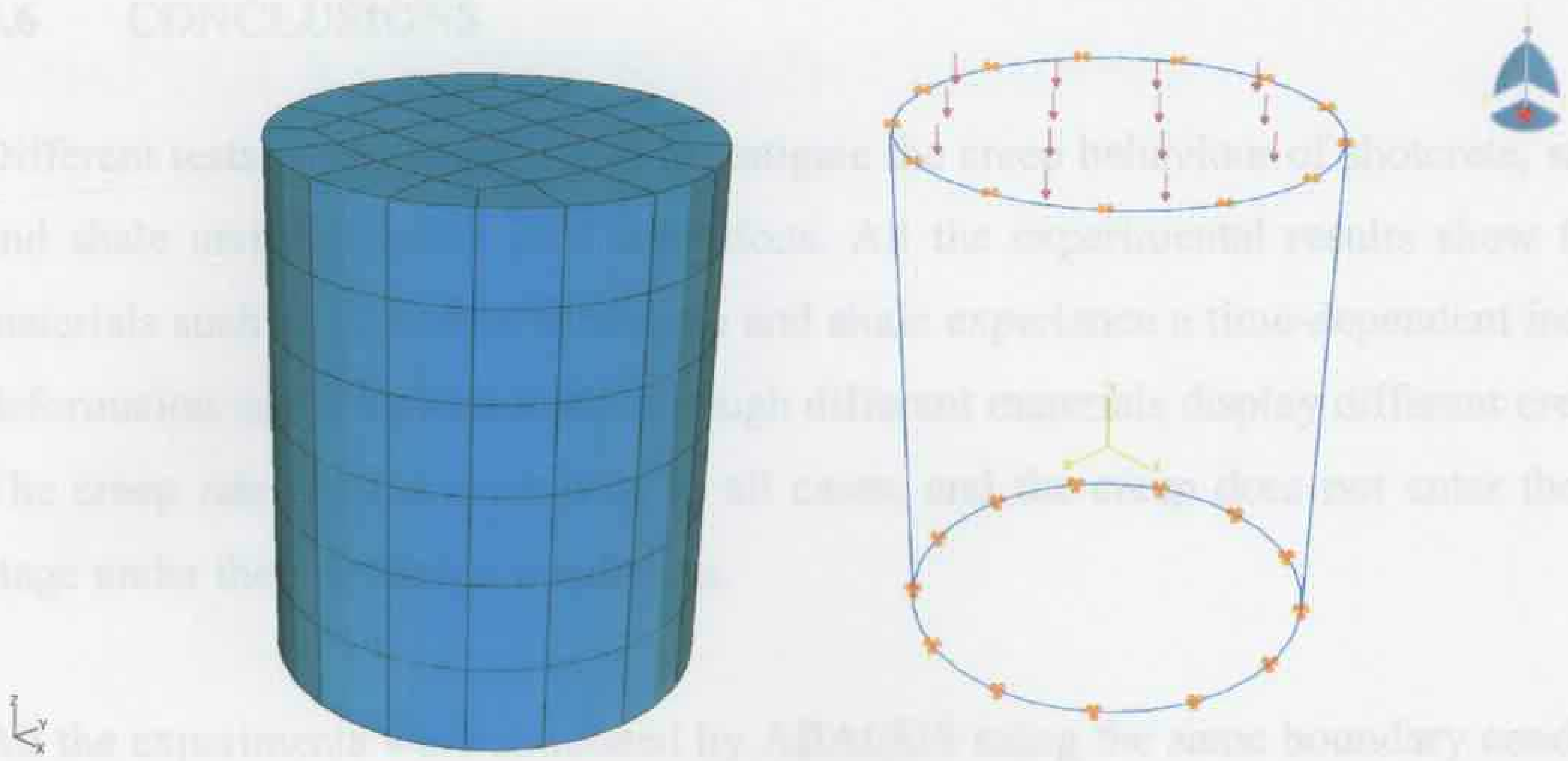

Figure 4.18: Numerical model of uniaxial creep test of shale.

Figure 4.19 shows the numerical results for the uniaxial creep test of the shale with a set of selected parameters F=2.5e-18, n=2.19, m=-0.98. The numerical curve fits the experimental data well, and it shows a nearly linear relationship between the creep deflection and log-time. It also shows that the creep curves of sandstone and shale look nearly parallel to each other under the current test stress level, and the two materials display similar creep behaviours.

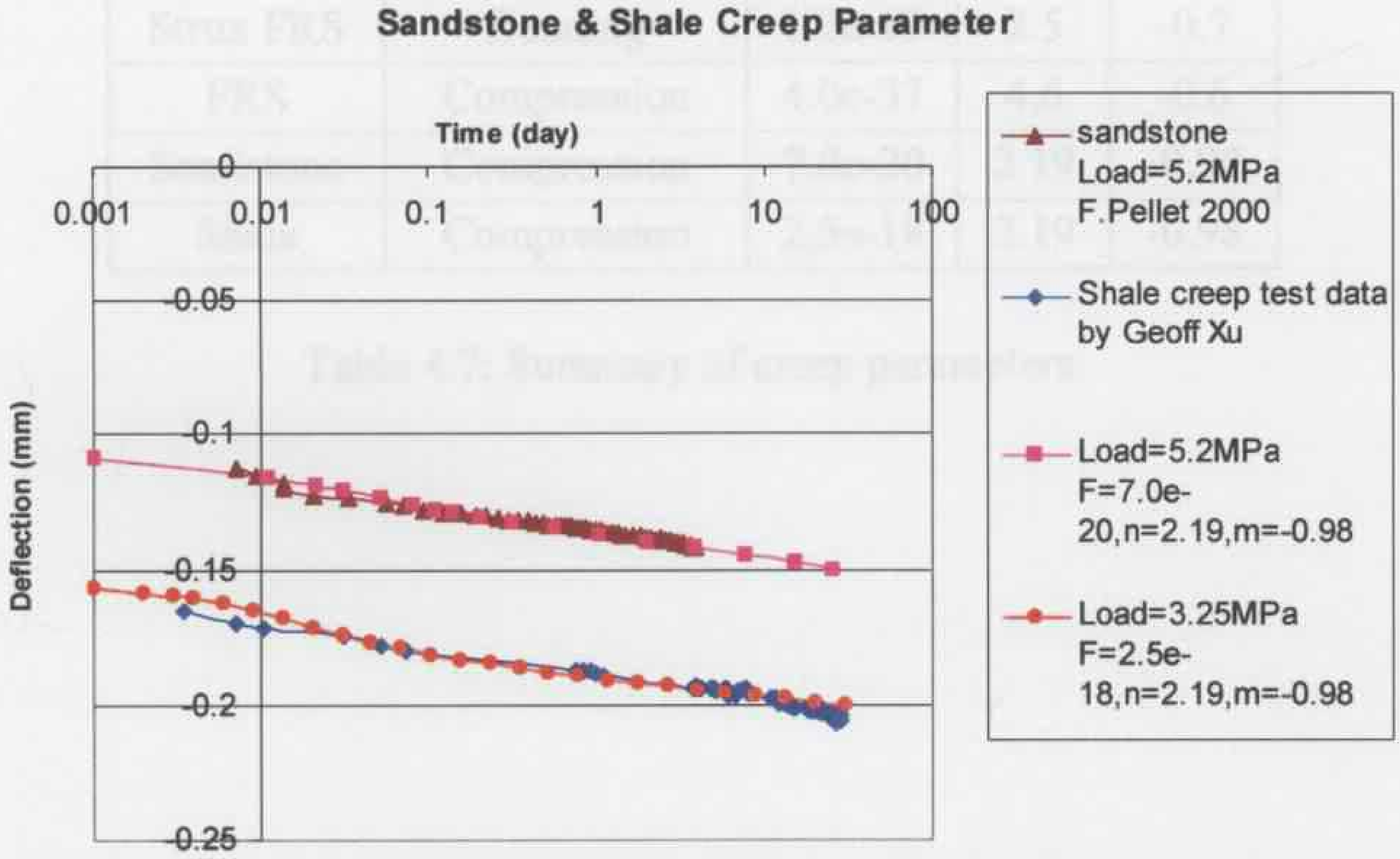

Figure 4.19: Numerical creep fit of uniaxial creep test for shale.

4.6 CONCLUSIONS

Different tests were carried out to investigate the creep behaviour of shotcrete, sandstone and shale under different load conditions. All the experimental results show that geo-materials such as shotcrete, sandstone and shale experience a time-dependent increase in deformation under a given load, although different materials display different creep rates. The creep rate reduces with time in all cases, and the creep does not enter the tertiary stage under the current test conditions.

All the experiments were simulated by ABAQUS using the same boundary conditions as in the laboratory tests. Different creep parameters were selected to fit the different experimental curves under the different loading conditions, and a summary of the selected parameters is given in Table 4.7. In the following numerical creep analysis of tunnel support structures, the shotcrete and rock are assumed to creep based on these selected creep parameters.

Material	Load Condition	Creep Parameters		
		F	n	m
NOVO FRS	Bending	4e-37	5	-0.1
HPP FRS	Bending	1.05e-17	2.19	-0.7
Strux FRS	Bending	1.2e-19	2.5	-0.7
FRS	Compression	4.0e-37	4.6	-0.6
Sandstone	Compression	7.0e-20	2.19	-0.98
Shale	Compression	2.5e-18	2.19	-0.98

Table 4.7: Summary of creep parameters.

CHAPTER 5 - FINITE ELEMENT ANALYSIS

5.1 INTRODUCTION

The Finite element method has been used in the present research as outlined in the previous chapter. In this chapter, the basic steps and concepts used to develop the finite element code SAFEA (Semi Analytic Finite Element Analysis) is presented. The program was written in the FORTRAN language and can be used for solving three-dimensional elastic analysis and time-dependent creep analysis problems, including simulating laboratory creep tests, tunnel excavation and tunnel creep deformation analysis.

A commercial finite element program ABAQUS was also used in the present research. A power hardening law which is embedded in the program was used to represent the creep behaviour of the materials in the analysis. The results obtained from ABAQUS were compared with the results of SAFEA and/or field data.

5.2 SAFEA

The program SAFEA was developed based on Fortran Code TD11, which was developed by Prof. John Small. The original program was a three-dimensional finite element code which could be used to carry out analysis of elastic-plastic problems in three dimensions. An eight-node shell element was added into the code to represent the shotcrete lining, and a logarithmic visco-elastic function was introduced to carry out time-dependent creep analysis in the present research.

5.2.1 ELEMENT TYPES

The initial input data file for the finite element model is written by using a normal text editor. A program GENTOP is then used to read in the initial data and generate a three-dimensional finite element mesh for the analysis processor. Here the tunnel structure model consists of three types of elements; solid elements are used to represent the rock, shell elements are used to model the shotcrete lining, and rock bolts are represented by beam elements. A typical simple tunnel structure mesh generated by GENTOP is shown in Figure 5.1.

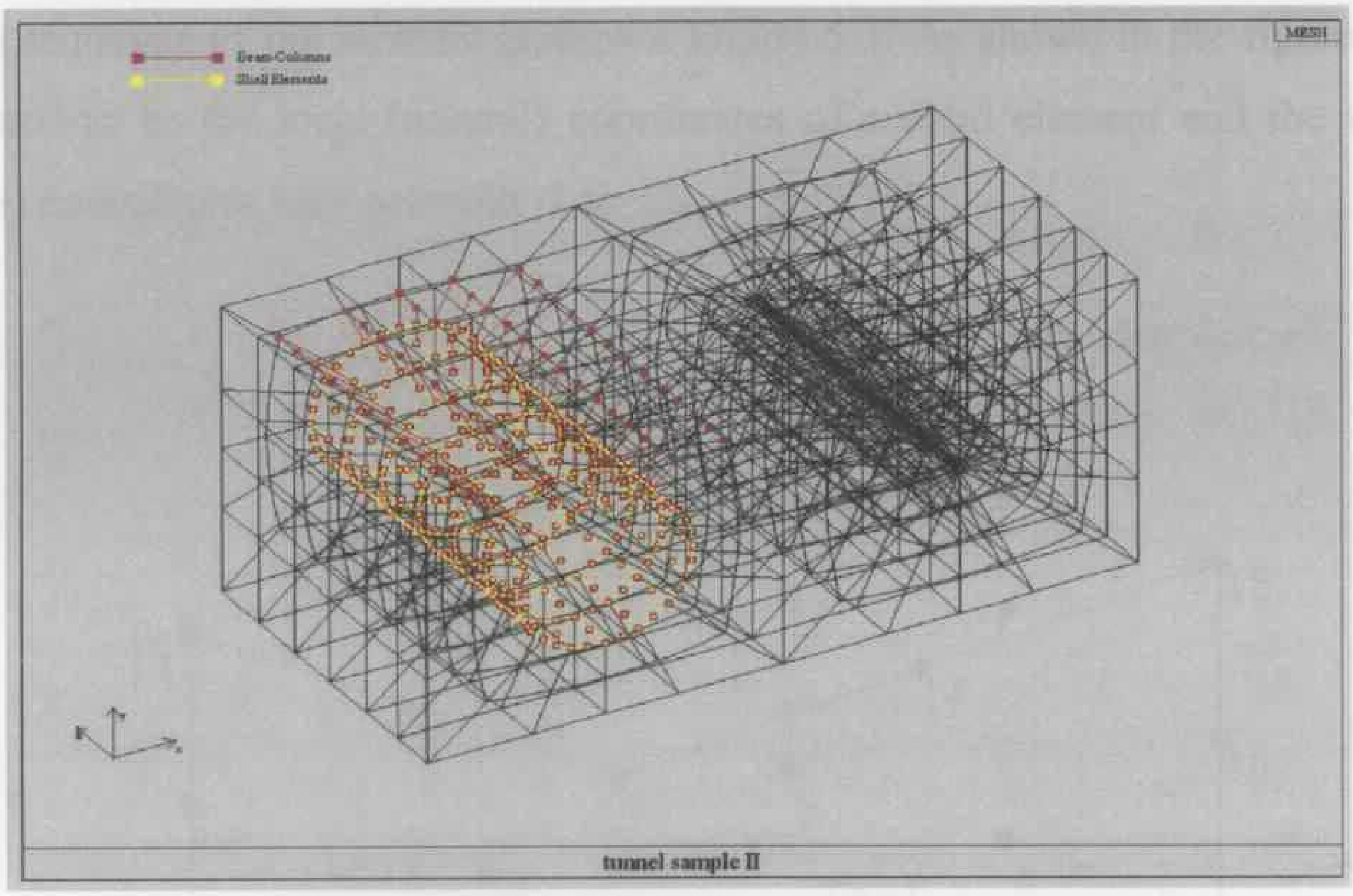

Figure 5.1: Finite element mesh of tunnel structure.

5.2.1.1 20-node solid element

A 20-node solid element is employed in the program to represent the rock surrounding the tunnel structure or the rock specimen in any laboratory tests that are modelled. The code for the element has been developed in the original FORTRAN code of TD11 and a typical solid rock element in the tunnel model is shown in Figure 5.2.

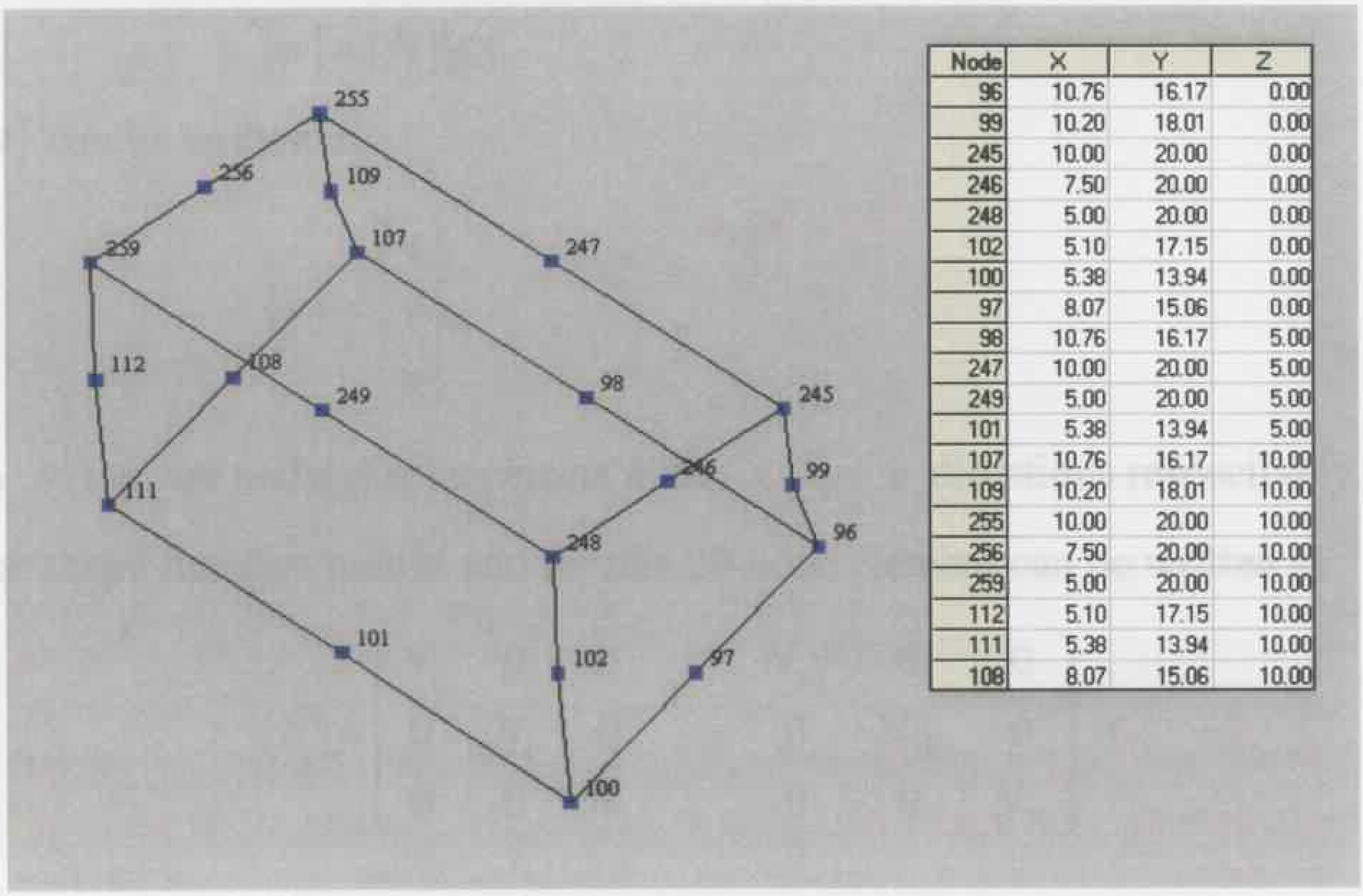

Node	X	Y	Z
96	10.76	16.17	0.00
99	10.20	18.01	0.00
245	10.00	20.00	0.00
246	7.50	20.00	0.00
248	5.00	20.00	0.00
102	5.10	17.15	0.00
100	5.38	13.94	0.00
97	8.07	15.06	0.00
98	10.76	16.17	5.00
247	10.00	20.00	5.00
249	5.00	20.00	5.00
101	5.38	13.94	5.00
107	10.76	16.17	10.00
109	10.20	18.01	10.00
255	10.00	20.00	10.00
256	7.50	20.00	10.00
259	5.00	20.00	10.00
112	5.10	17.15	10.00
111	5.38	13.94	10.00
108	8.07	15.06	10.00

Figure 5.2: A 20-node solid element.

The node sequence of the element is shown Figure 5.3. As shown in the figure, *S, T, U* are assumed to be the local (natural) coordinates of a solid element and the values of these three coordinates vary between -1 to +1.

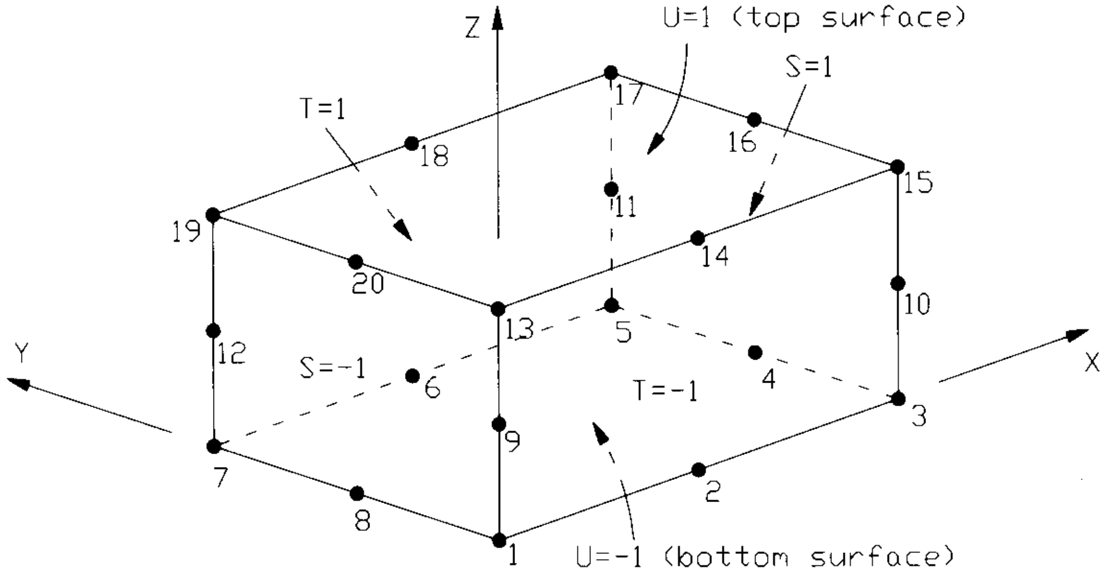

Figure 5.3: A 20-node solid element.

In the global Cartesian coordinate system, the displacement ψ of the element can be expressed as

$$\{\psi\}=[N]\{d\} \tag{5.1}$$

where $\{\psi\}$ can be written as

$$\{\psi\}=\begin{Bmatrix} u \\ v \\ w \end{Bmatrix}$$

where u, v, w are nodal displacements in the x, y, z directions respectively.

$[N]$ is the shape function matrix and for this 20-node element can be written as

$$[N]=\begin{bmatrix} N_1 & 0 & 0 & & N_{20} & 0 & 0 \\ 0 & N_1 & 0 & \cdots & 0 & N_{20} & 0 \\ 0 & 0 & N_1 & & 0 & 0 & N_{20} \end{bmatrix}$$

$\{d\}$ is the nodal displacement matrix and can be expressed as

$$\{d\} = \begin{Bmatrix} u_1 \\ v_1 \\ w_1 \\ \vdots \\ u_{20} \\ v_{20} \\ w_{20} \end{Bmatrix}$$

The local coordinates of the element can also be interpolated using the shape functions as

$$\begin{aligned} x &= \sum_{i=1}^{20} N_i x_i \\ y &= \sum_{i=1}^{20} N_i y_i \\ z &= \sum_{i=1}^{20} N_i z_i \end{aligned} \tag{5.2}$$

where x_i, y_i, z_i are the global Cartesian coordinates of the 20 nodes of the element.

For the corner nodes of the element, N_i has the following values:

$$\begin{aligned} N_1 &= \frac{1}{8}\cdot(1-S)(1-T)(1-U)(-S-T-U-2.0) \\ N_3 &= \frac{1}{8}\cdot(1+S)(1-T)(1-U)(S-T-U-2.0) \\ N_5 &= \frac{1}{8}\cdot(1+S)(1+T)(1-U)(S+T-U-2.0) \\ N_7 &= \frac{1}{8}\cdot(1-S)(1+T)(1-U)(-S+T-U-2.0) \\ N_{13} &= \frac{1}{8}\cdot(1-S)(1-T)(1+U)(-S-T+U-2.0) \\ N_{15} &= \frac{1}{8}\cdot(1+S)(1-T)(1+U)(S-T+U-2.0) \\ N_{17} &= \frac{1}{8}\cdot(1+S)(1+T)(1+U)(S+T+U-2.0) \\ N_{19} &= \frac{1}{8}\cdot(1-S)(1+T)(1+U)(-S+T+U-2.0) \end{aligned} \tag{5.3}$$

For the mid-side nodes, the shape functions are

$$
\begin{aligned}
N_2 &= \frac{1}{4}\cdot(1-T)(1-U)(1-S^2)\\
N_4 &= \frac{1}{4}\cdot(1+S)(1-U)(1-T^2)\\
N_6 &= \frac{1}{4}\cdot(1+T)(1-U)(1-S^2)\\
N_8 &= \frac{1}{4}\cdot(1-S)(1-U)(1-T^2)\\
N_9 &= \frac{1}{4}\cdot(1-S)(1-T)(1-U^2)\\
N_{10} &= \frac{1}{4}\cdot(1+S)(1-T)(1-U^2)\\
N_{11} &= \frac{1}{4}\cdot(1+S)(1+T)(1-U^2)\\
N_{12} &= \frac{1}{4}\cdot(1-S)(1+T)(1-U^2)\\
N_{14} &= \frac{1}{4}\cdot(1-T)(1+U)(1-S^2)\\
N_{16} &= \frac{1}{4}\cdot(1+S)(1+U)(1-T^2)\\
N_{18} &= \frac{1}{4}\cdot(1+T)(1+U)(1-S^2)\\
N_{20} &= \frac{1}{4}\cdot(1-S)(1+U)(1-T^2)
\end{aligned}
\qquad (5.4)
$$

The strain-displacement relationship is

$$\{\varepsilon\} = [B]\cdot\{d\} \qquad (5.5)$$

and the derivatives of the shape functions are then calculated to form the *B* Matrix,

$$
\begin{aligned}
N_{i,x} &= \frac{\partial N_i}{\partial x} = \frac{\partial N_i}{\partial S}\frac{\partial S}{\partial x} + \frac{\partial N_i}{\partial T}\frac{\partial T}{\partial x} + \frac{\partial N_i}{\partial U}\frac{\partial U}{\partial x} \qquad i = 1\ldots 20\\
N_{i,y} &= \frac{\partial N_i}{\partial y} = \frac{\partial N_i}{\partial S}\frac{\partial S}{\partial y} + \frac{\partial N_i}{\partial T}\frac{\partial T}{\partial y} + \frac{\partial N_i}{\partial U}\frac{\partial U}{\partial y} \qquad i = 1\ldots 20\\
N_{i,z} &= \frac{\partial N_i}{\partial z} = \frac{\partial N_i}{\partial S}\frac{\partial S}{\partial z} + \frac{\partial N_i}{\partial T}\frac{\partial T}{\partial z} + \frac{\partial N_i}{\partial U}\frac{\partial U}{\partial z} \qquad i = 1\ldots 20
\end{aligned}
\qquad (5.6)
$$

From equations (5.1-5.6), we can also express the displacements *u, v, w* by natural coordinates *S, T, U,* and the derivates of the shape functions can be written as

$$\begin{bmatrix} \dfrac{\partial N_i}{\partial S} \\ \dfrac{\partial N_i}{\partial T} \\ \dfrac{\partial N_i}{\partial U} \end{bmatrix} = [J] \begin{bmatrix} \dfrac{\partial N_i}{\partial x} \\ \dfrac{\partial N_i}{\partial y} \\ \dfrac{\partial N_i}{\partial z} \end{bmatrix} \qquad i = 1 \ldots 20 \tag{5.7}$$

where $[J]$ is the Jacobian matrix, and can be written in the following form:

$$[J] = \begin{bmatrix} \dfrac{\partial N_1}{\partial S} & \dfrac{\partial N_2}{\partial S} & \cdots & \dfrac{\partial N_{20}}{\partial S} \\ \dfrac{\partial N_1}{\partial T} & \dfrac{\partial N_2}{\partial T} & \cdots & \dfrac{\partial N_{20}}{\partial T} \\ \dfrac{\partial N_1}{\partial U} & \dfrac{\partial N_2}{\partial U} & \cdots & \dfrac{\partial N_{20}}{\partial U} \end{bmatrix} \cdot \begin{bmatrix} x_1 & y_1 & z_1 \\ x_2 & y_2 & z_2 \\ \vdots & \vdots & \vdots \\ x_{20} & y_{20} & z_{20} \end{bmatrix} \tag{5.8}$$

By inverting the *J* matrix, we can get the global derivatives

$$\begin{bmatrix} \dfrac{\partial N_i}{\partial x} \\ \dfrac{\partial N_i}{\partial y} \\ \dfrac{\partial N_i}{\partial z} \end{bmatrix} = [J]^{-1} \begin{bmatrix} \dfrac{\partial N_i}{\partial S} \\ \dfrac{\partial N_i}{\partial T} \\ \dfrac{\partial N_i}{\partial U} \end{bmatrix} \qquad i = 1 \ldots 20 \tag{5.9}$$

The stress-strain relationship is

$$\{\sigma\} = [D] \cdot [B] \cdot \{d\} \tag{5.10}$$

Here, the elastic D matrix is written in terms of the bulk modulus *K* and the shear modulus *G*

$$[D] = \begin{bmatrix} K+4G/3 & K-2G/3 & K-2G/3 & 0 & 0 & 0 \\ K-2G/3 & K+4G/3 & K-2G/3 & 0 & 0 & 0 \\ K-2G/3 & K-2G/3 & K+4G/3 & 0 & 0 & 0 \\ 0 & 0 & 0 & G & 0 & 0 \\ 0 & 0 & 0 & 0 & G & 0 \\ 0 & 0 & 0 & 0 & 0 & G \end{bmatrix} \tag{5.11}$$

If $\underline{\varepsilon}$ is defined as $\left(\varepsilon_x, \varepsilon_y, \varepsilon_z, \varepsilon_{xy}, \varepsilon_{yz}, \varepsilon_{zx}\right)^T$ then

$$[B] = \begin{bmatrix} N_{1,x} & 0 & 0 & N_{2,x} & 0 & 0 & \cdots & N_{20,x} & 0 & 0 \\ 0 & N_{1,y} & 0 & 0 & N_{2,y} & 0 & \cdots & 0 & N_{20,y} & 0 \\ 0 & 0 & N_{1,z} & 0 & 0 & N_{2,z} & \cdots & 0 & 0 & N_{20,z} \\ N_{1,y} & N_{1,x} & 0 & N_{2,y} & N_{2,x} & 0 & \cdots & N_{20,y} & N_{20,x} & 0 \\ 0 & N_{1,z} & N_{1,y} & 0 & N_{2,z} & N_{2,y} & \cdots & 0 & N_{20,z} & N_{20,y} \\ N_{1,z} & 0 & N_{1,x} & N_{2,z} & 0 & N_{2,x} & \cdots & N_{20,z} & 0 & N_{20,x} \end{bmatrix} \tag{5.12}$$

The element stiffness matrix is then calculated as

$$[K] = \int_V [B]^T [D][B] dV \tag{5.13}$$

Numerical integration can be used in the usual fashion to evaluate the integral of Equation 5.13. Gaussian integration is used with 2 Gauss points in each axis direction (i.e. 2 x 2 x 2). The Gauss coordinates of the element are $(-\sqrt{1/3}, \sqrt{1/3})$, and the Gauss weights at the integration points are 1.0. The 2 x 2 x 2 Gauss point positions in the element are displayed in Figure 5.4.

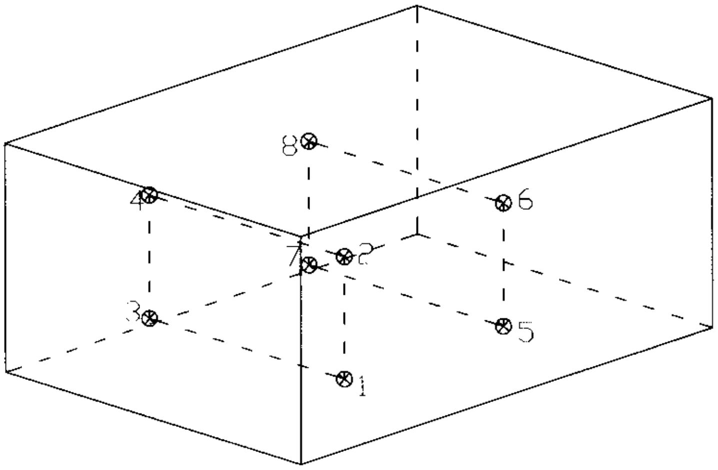

Figure 5.4: Gauss points of a 20-node solid element.

This three-dimensional 20-node solid element has been successfully employed in the program TD11, and its validity and performance has already been tested and so is not detailed in the present work.

5.2.1.2 8-node shell element

An 8-node shear deformable curved shell element was added in the program to represent the shotcrete lining. In the tunnel model, the shell element shares eight nodes of the 20-node solid element on one surface. Thus the shell and solid elements are treated as being tied together at the nodes, and the relative displacement between the rock and shotcrete lining such as slip is ignored in the model. As shotcrete bonds tightly to the rock, this is thought to be a reasonable model. A typical shell element in the tunnel model is shown in Figure 5.5.

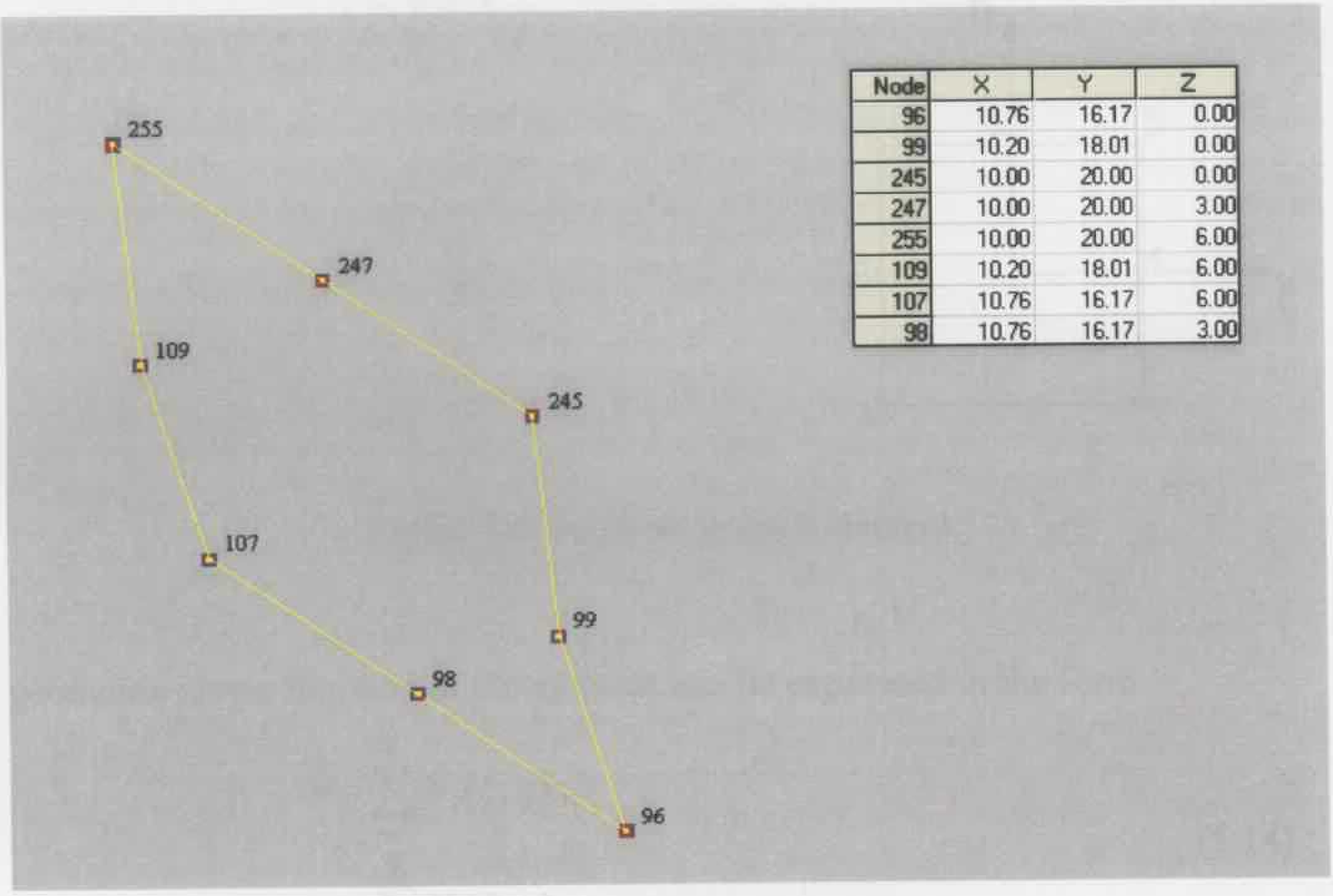

Node	X	Y	Z
96	10.76	16.17	0.00
99	10.20	18.01	0.00
245	10.00	20.00	0.00
247	10.00	20.00	3.00
255	10.00	20.00	6.00
109	10.20	18.01	6.00
107	10.76	16.17	6.00
98	10.76	16.17	3.00

Figure 5.5: An 8-node shell element.

Figure 5.6 shows a typical geometric description of the isoparametric shell element, the eight nodes in the element are in counter-clockwise order and each has six degrees of freedom, the thickness of the shell is a constant and defined as *t*. The origin of the element's natural curvilinear coordinates is set at the centre of the shell element, and coordinate components ξ, η are assumed to vary between -1 to +1.

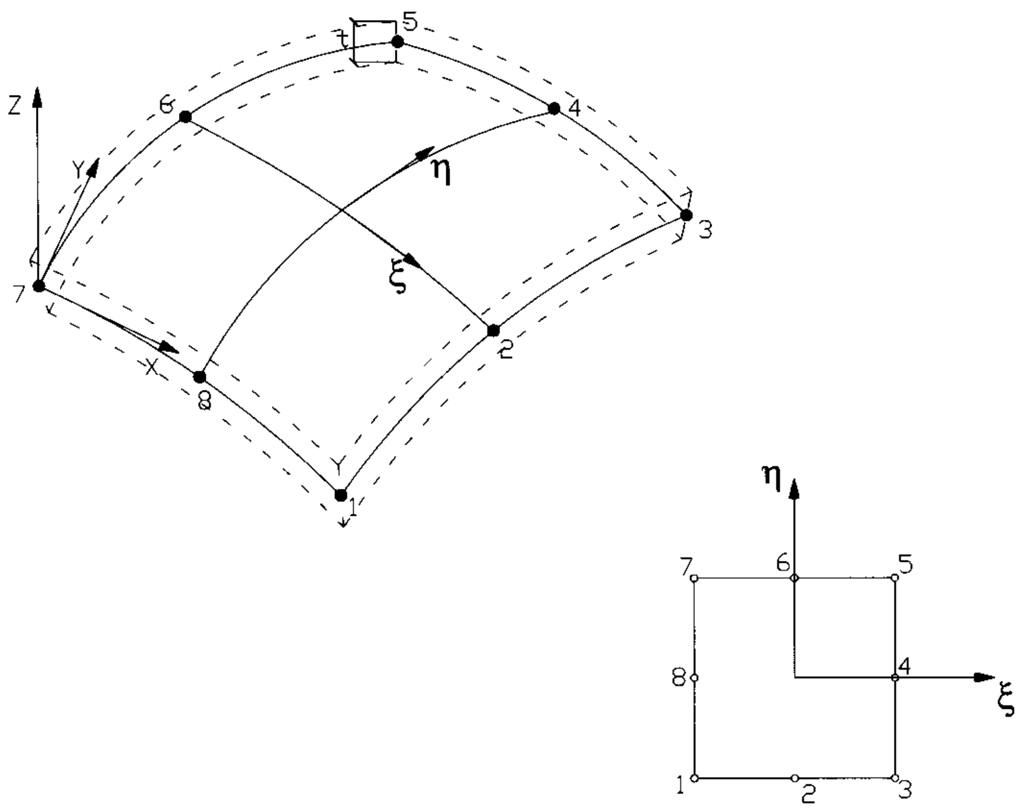

Figure 5.6: An 8-node shell element.

The geometric shape function of the element can be expressed in the form

$$x = \sum_{i=1}^{8} N_i(\xi,\eta)x_i$$
$$y = \sum_{i=1}^{8} N_i(\xi,\eta)y_i \qquad (5.14)$$

The shape functions N_i may be written as follows for the shell element:

$$\begin{aligned}
N_1 &= \frac{1}{4}\cdot(1.0-\xi)(1.0-\eta)(-\xi-\eta-1.0)\\
N_2 &= \frac{1}{2}\cdot(1.0-\xi^2)(1.0-\eta)\\
N_3 &= \frac{1}{4}\cdot(1.0+\xi)(1.0-\eta)(\xi-\eta-1.0)\\
N_4 &= \frac{1}{2}\cdot(1.0-\eta^2)(1.0+\xi)\\
N_5 &= \frac{1}{4}\cdot(1.0+\xi)(1.0+\eta)(\xi+\eta-1.0)\\
N_6 &= \frac{1}{2}\cdot(1.0-\xi^2)(1.0+\eta)\\
N_7 &= \frac{1}{4}\cdot(1.0-\xi)(1.0+\eta)(-\xi+\eta-1.0)\\
N_8 &= \frac{1}{2}\cdot(1.0-\eta^2)(1.0-\xi)
\end{aligned} \tag{5.15}$$

while the derivatives of shape functions with respect to ξ can be written as

$$\begin{aligned}
N_{1,\xi} &= \frac{1}{4}\cdot(\eta+2\xi-2\xi\eta-\eta^2)\\
N_{2,\xi} &= -\xi+\xi\eta\\
N_{3,\xi} &= \frac{1}{4}\cdot(-\eta+2\xi-2\xi\eta+\eta^2)\\
N_{4,\xi} &= \frac{1}{2}(1-\eta^2)\\
N_{5,\xi} &= \frac{1}{4}\cdot(\eta+2\xi+2\xi\eta+\eta^2)\\
N_{6,\xi} &= -\xi-\xi\eta\\
N_{7,\xi} &= \frac{1}{4}\cdot(-\eta+2\xi+2\xi\eta-\eta^2)\\
N_{8,\xi} &= \frac{1}{2}(-1+\eta^2)
\end{aligned} \tag{5.16}$$

and the derivatives of shape functions with respect to η can be written as

$$\begin{aligned}
N_{1,\eta} &= \frac{1}{4}\cdot(\xi + 2\eta - 2\xi\eta - \xi^2) \\
N_{2,\eta} &= \frac{1}{2}(-1+\xi^2) \\
N_{3,\eta} &= \frac{1}{4}\cdot(-\xi + 2\eta + 2\xi\eta - \xi^2) \\
N_{4,\eta} &= -\eta - \xi\eta \\
N_{5,\eta} &= \frac{1}{4}\cdot(\xi + 2\eta + 2\xi\eta + \xi^2) \\
N_{6,\eta} &= \frac{1}{2}(1-\xi^2) \\
N_{7,\eta} &= \frac{1}{4}\cdot(-\xi + 2\eta - 2\xi\eta + \xi^2) \\
N_{8,\eta} &= -\eta + \xi\eta
\end{aligned} \tag{5.17}$$

The resultant forces $N = \{N_\xi, N_\eta, N_{\xi\eta}\}^T$, bending moments $M = \{M_\xi, M_\eta, M_{\xi\eta}\}^T$ and transverse shear forces $Q = \{Q_\xi, Q_\eta\}^T$ can be obtained by multiplying the D matrix by the deformation variables $\{\varepsilon_\xi, \varepsilon_\eta, \gamma_{\xi\eta}, \lambda_\xi, \lambda_\eta, \lambda_{\xi\eta}, \Gamma_\xi, \Gamma_\eta\}^T$. The elastic D matrix of the shell element which contains the material mechanical parameters (modulus E and Poisson's ratio v) and the shell thickness t can be expressed as

$$[D] = \begin{bmatrix}
\frac{Et}{(1-v^2)} & \frac{Et\cdot v}{(1-v^2)} & 0 & 0 & 0 & 0 & 0 & 0 \\
\frac{Et\cdot v}{(1-v^2)} & \frac{Et}{(1-v^2)} & 0 & 0 & 0 & 0 & 0 & 0 \\
0 & 0 & \frac{Et}{2(1+v)} & 0 & 0 & 0 & 0 & 0 \\
0 & 0 & 0 & \frac{Et^3}{12(1-v^2)} & \frac{Et^3\cdot v}{12(1-v^2)} & 0 & 0 & 0 \\
0 & 0 & 0 & \frac{Et^3\cdot v}{12(1-v^2)} & \frac{Et^3}{12(1-v^2)} & 0 & 0 & 0 \\
0 & 0 & 0 & 0 & 0 & \frac{Et^3}{24(1+v)} & 0 & 0 \\
0 & 0 & 0 & 0 & 0 & 0 & \frac{Et}{2.4(1+v)} & 0 \\
0 & 0 & 0 & 0 & 0 & 0 & 0 & \frac{Et}{2.4(1+v)}
\end{bmatrix} \tag{5.18}$$

The B matrix is defined as

$$[B]=\begin{bmatrix} N_{1,x} & 0 & 0 & 0 & 0 & \cdots & \\ 0 & N_{1,y} & 0 & 0 & 0 & \cdots & \\ N_{1,y} & N_{1,x} & 0 & 0 & 0 & \cdots & \\ 0 & 0 & 0 & N_{1,x} & 0 & \cdots & etc. for\ \ all\ \ 8\ \ nodes \\ 0 & 0 & 0 & 0 & N_{1,y} & \cdots & \\ 0 & 0 & 0 & N_{1,y} & N_{1,x} & \cdots & \\ 0 & 0 & -N_{1,x} & N & 0 & \cdots & \\ 0 & 0 & -N_{1,y} & 0 & N & \cdots & \end{bmatrix} \qquad (5.19)$$

The stiffness matrix $[K]$ is then calculated by numerical integration $\int_A B^T DBdA$ using a 2×2 Gauss point scheme. The Gaussian integration constants are set up as (-0.5773503, 0.5773503), and the location of the 2 x 2 Gauss points is shown in Figure 5.7.

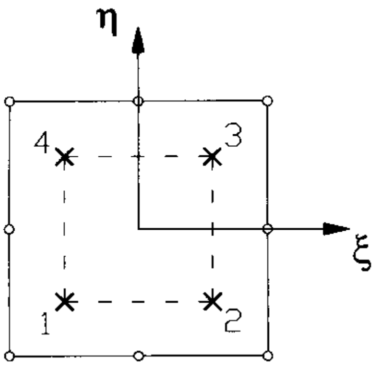

Figure 5.7: Gauss points of shell element.

A simple half circular arch was modelled to test the validity of the shell element. The radius and the width of the arch are taken as arbitrary values of 1000 and 100, respectively. The thickness of the arch is set as 0.3. One end point of the arch is fixed against movements and rotations in all directions, the other point of this side of the arch is fixed against movement in the y-direction, and one end point on the other side of the arch is fixed against movements in all directions. A unit point vertical load was applied at the middle edge of the arch. The boundary conditions of the arch are shown in Figure 5.8.

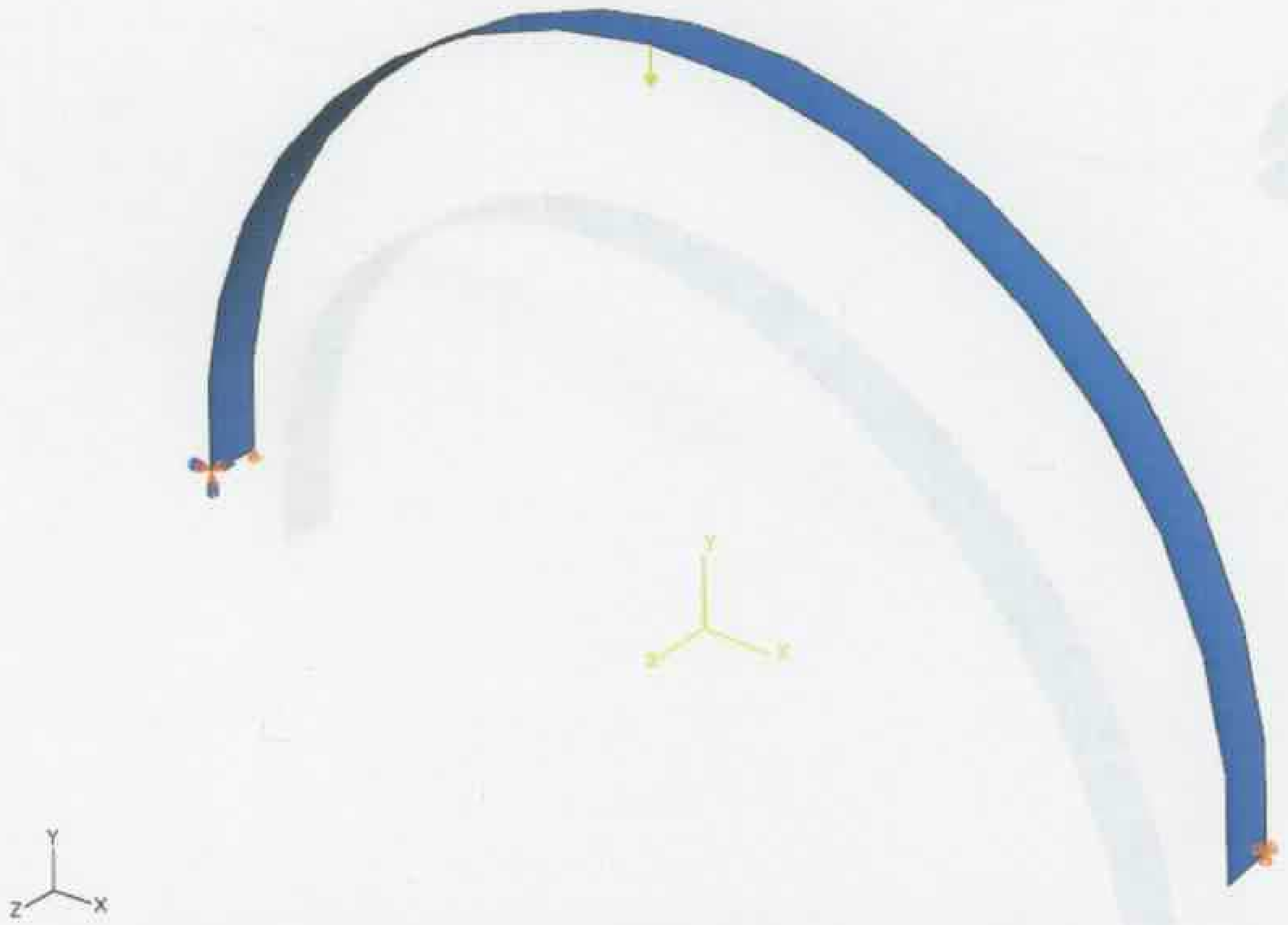

Figure 5.8: Boundary conditions of the shell elements arch.

The arch was divided equally into 48 shell element partitions as shown in Figure 5.9a. A more coarse mesh division with 12 shell elements as shown in Figure 5.9b was also used in the analysis to test the sensitivity of the solution to the number of elements in the problem.

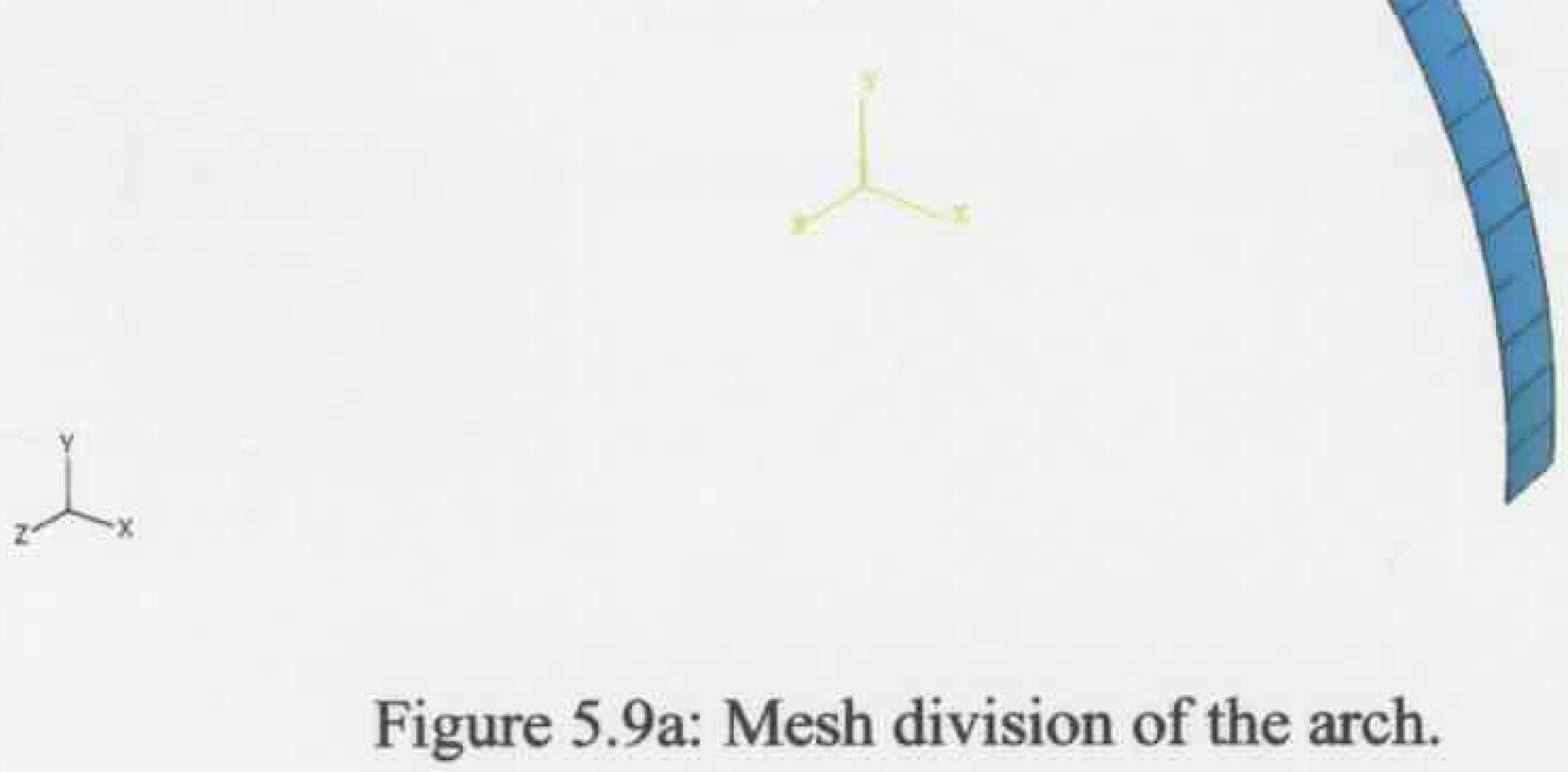

Figure 5.9a: Mesh division of the arch.

Figure 5.9b: Coarse mesh division of the arch.

Under the vertical point load, the deformation of the arch is as shown in Figure 5.10. The arch was modelled by the present FORTRAN shell element code as well as in ABAQUS using shell element S8R. The displacement results calculated by both programs are presented in Figures 5.11a, 5.11b and 5.11c. It can be seen that the results obtained from the code of the shell element in the SAFEA program gave a good fit to the results obtained from the commercial finite element program ABAQUS.

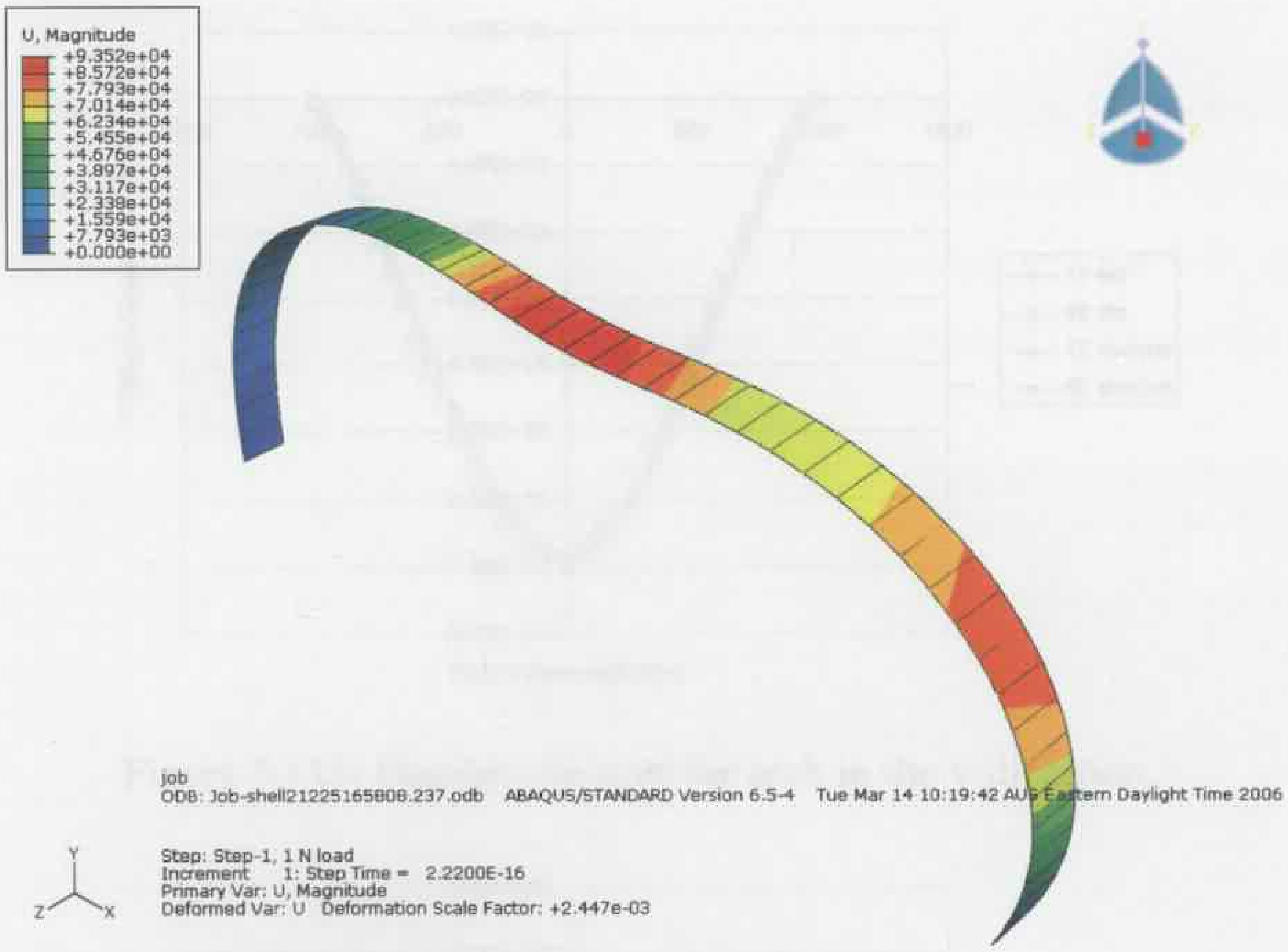

Figure 5.10: Deformation of the arch.

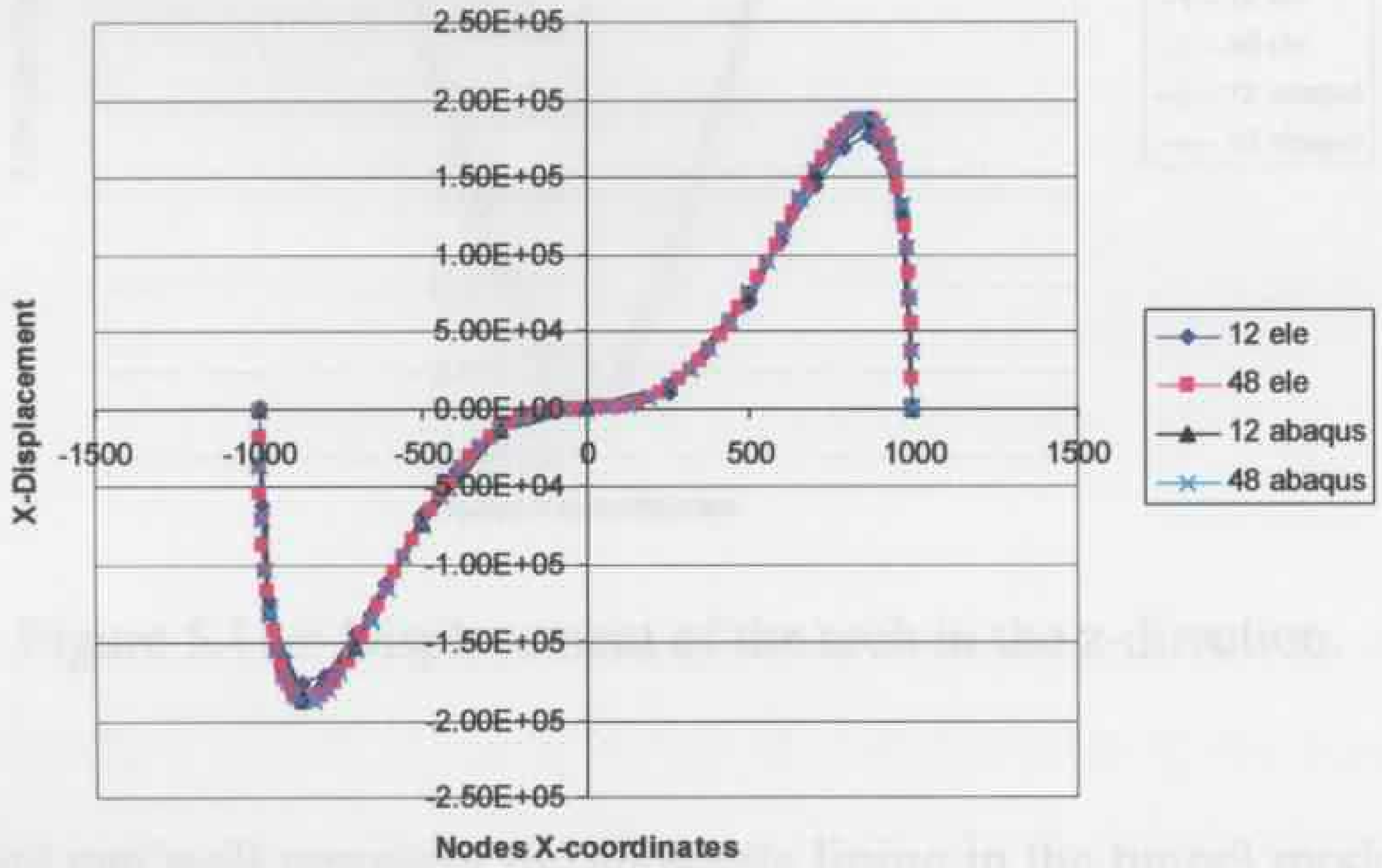

Figure 5.11a: Displacement of the arch in the x-direction.

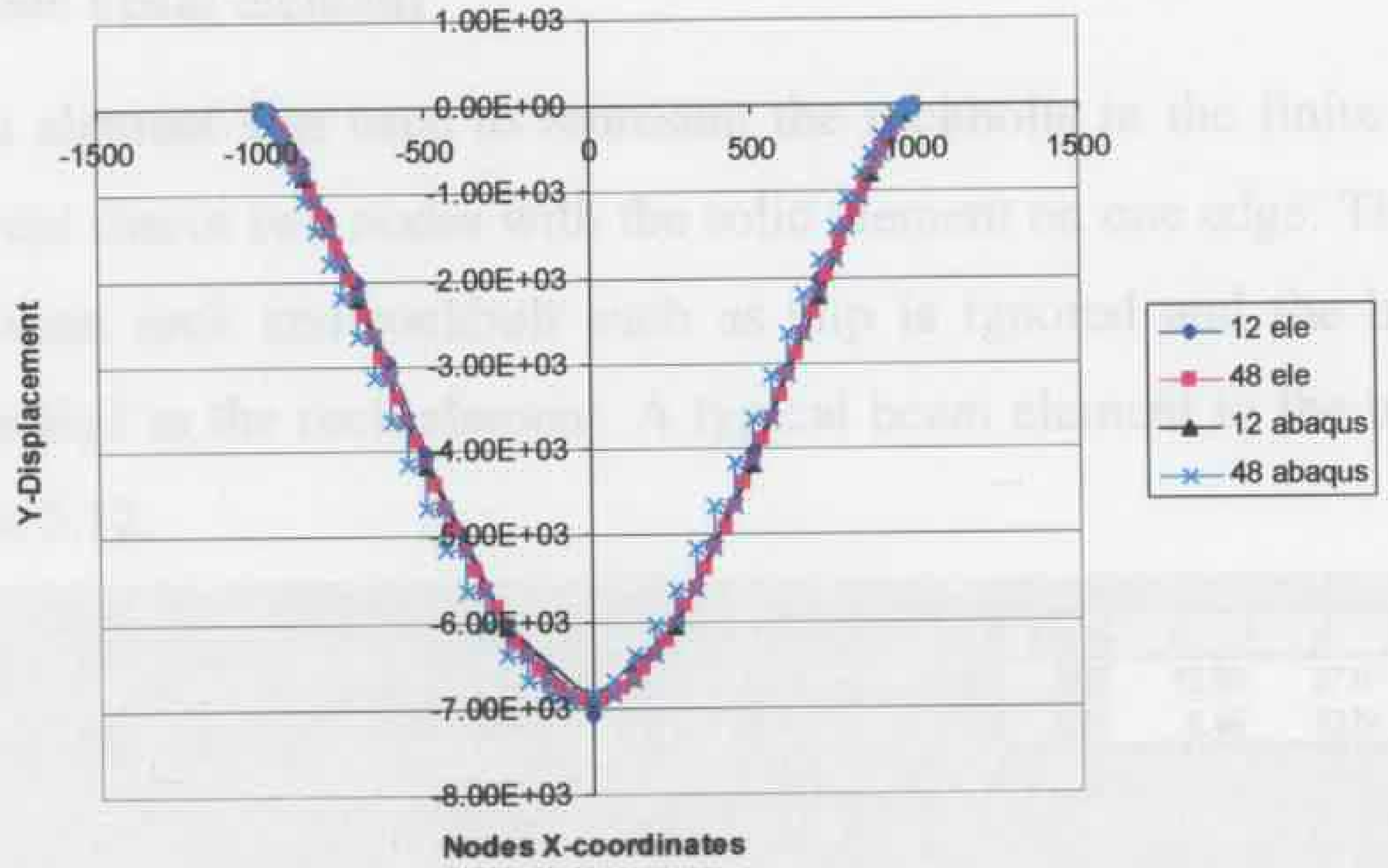

Figure 5.11b: Displacement of the arch in the y-direction.

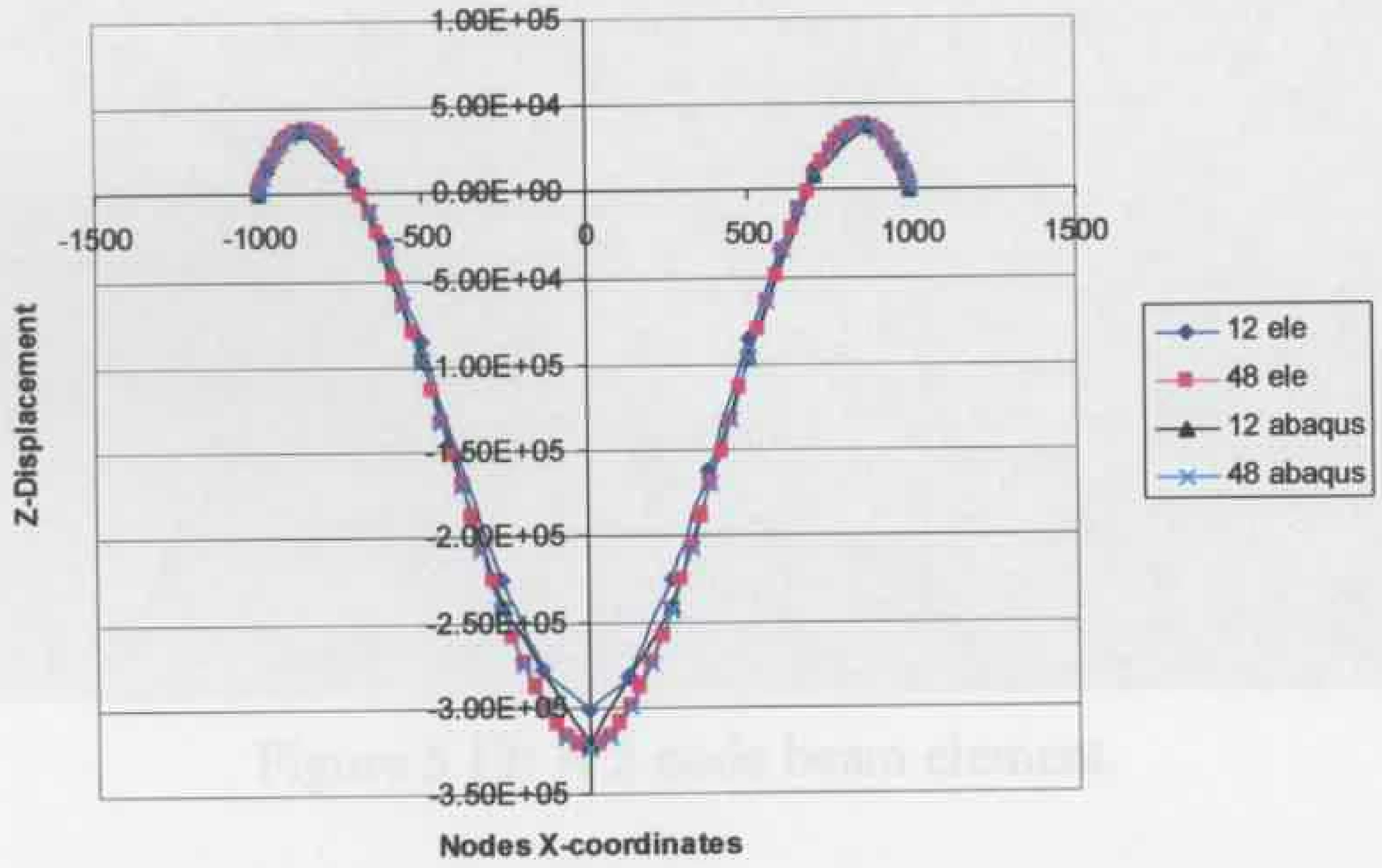

Figure 5.11c: Displacement of the arch in the z-direction.

The shell element can well represent the shotcrete lining in the tunnel model for the static elastic analysis, and a 'time' variable is later introduced in the model for the creep deformation analysis.

5.2.1.3 2-node beam element

A 2-node beam element was used to represent the rockbolts in the finite element code. The beam element shares two nodes with the solid element on one edge. Thus the relative movement between rock and rockbolt such as slip is ignored and the bolt element is treated as embedded in the rock element. A typical beam element in the tunnel model is shown in Figure 5.12.

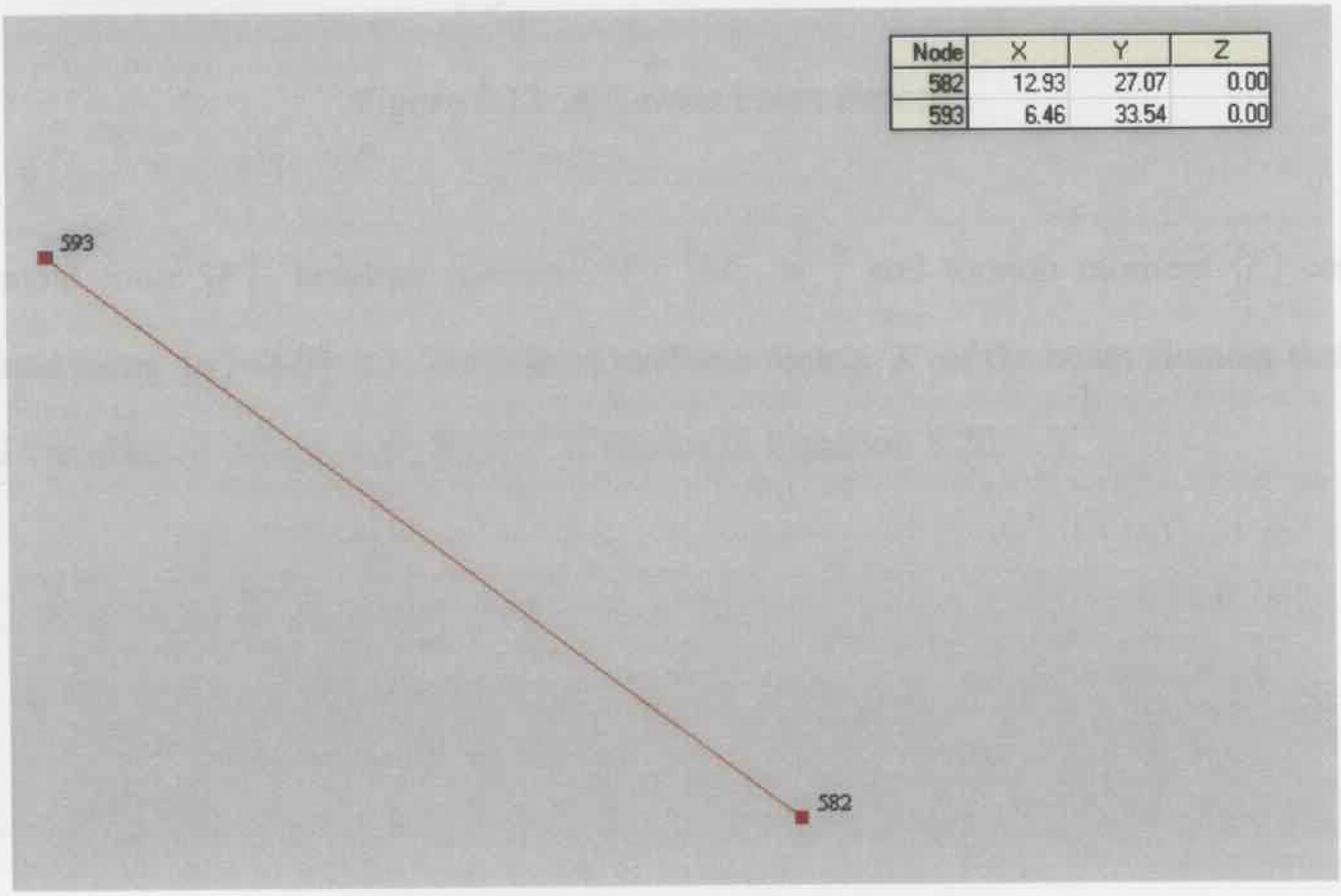

Node	X	Y	Z
582	12.93	27.07	0.00
593	6.46	33.54	0.00

Figure 5.12: A 2-node beam element.

The beam element is defined by the coordinates of the two end nodes, as well as material properties such as the elastic modulus E, the cross sectional area A, the second moment of area I_y, I_z and the torsion constant J. For a normal circular rockbolt element, the second moment of area $I_y = I_z = \frac{\pi D^4}{64}$, and the torsion constant $J = \frac{\pi D^4}{32}$. A typical geometric description of the beam element is shown in Figure 5.13.

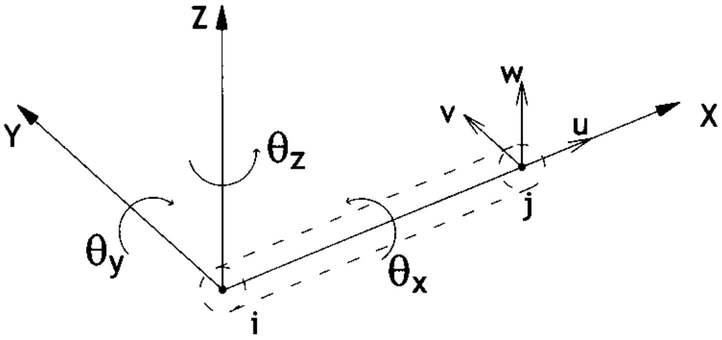

Figure 5.13: A 2-node beam element.

The axial force $\{F\}$, bending moment $M = \{M_y, M_z\}^T$ and torsion moment $\{T\}$ can be obtained using $\{\sigma\} = [D] \cdot \{\varepsilon\}$. The elastic stiffness matrix K of the beam element that has nodal variables $\underline{\delta} = (u, v, w, \theta_x, \theta_y, \theta_z)^T$ is shown in Equation 5.20.

$$[K]=\begin{bmatrix}
\frac{EA}{l} & 0 & 0 & 0 & 0 & 0 & -\frac{EA}{l} & 0 & 0 & 0 & 0 & 0 \\
0 & \frac{12EI_z}{l^3} & 0 & 0 & 0 & \frac{6EI_z}{l^2} & 0 & -\frac{12EI_z}{l^3} & 0 & 0 & 0 & \frac{6EI_z}{l^2} \\
0 & 0 & \frac{12EI_y}{l^3} & 0 & \frac{6EI_y}{l^2} & 0 & 0 & 0 & -\frac{12EI_y}{l^3} & 0 & -\frac{6EI_y}{l^2} & 0 \\
0 & 0 & 0 & \frac{GJ}{l} & 0 & 0 & 0 & 0 & 0 & -\frac{GJ}{l} & 0 & 0 \\
0 & 0 & \frac{6EI_y}{l^2} & 0 & \frac{4EI_y}{l} & 0 & 0 & 0 & -\frac{6EI_y}{l^2} & 0 & \frac{2EI_y}{l} & 0 \\
0 & \frac{6EI_z}{l^2} & 0 & 0 & 0 & \frac{4EI_z}{l} & 0 & -\frac{6EI_z}{l^2} & 0 & 0 & 0 & \frac{2EI_z}{l} \\
-\frac{EA}{l} & 0 & 0 & 0 & 0 & 0 & \frac{EA}{l} & 0 & 0 & 0 & 0 & 0 \\
0 & -\frac{12EI_z}{l^3} & 0 & 0 & 0 & -\frac{6EI_z}{l^2} & 0 & \frac{12EI_z}{l^3} & 0 & 0 & 0 & -\frac{6EI_z}{l^2} \\
0 & 0 & -\frac{12EI_y}{l^3} & 0 & -\frac{6EI_y}{l^2} & 0 & 0 & 0 & \frac{12EI_y}{l^3} & 0 & -\frac{6EI_y}{l^2} & 0 \\
0 & 0 & 0 & -\frac{GJ}{l} & 0 & 0 & 0 & 0 & 0 & \frac{GJ}{l} & 0 & 0 \\
0 & 0 & -\frac{6EI_y}{l^2} & 0 & \frac{2EI_y}{l} & 0 & 0 & 0 & -\frac{6EI_y}{l^2} & 0 & \frac{4EI_y}{l} & 0 \\
0 & \frac{6EI_z}{l^2} & 0 & 0 & 0 & \frac{2EI_z}{l} & 0 & -\frac{6EI_z}{l^2} & 0 & 0 & 0 & \frac{4EI_z}{l}
\end{bmatrix} \qquad (5.20)$$

These three different types of element (20 node solid, 8 node shell, and 2 node bar) are used to represent the rock, lining and rockbolts respectively in the present code. In the tunnel model, the material properties of the rock and the lining are treated as varying with time, and how this is done is addressed in section 5.2.3.

5.2.2 ELASTIC ANALYSIS

The FORTRAN code SAFEA can be used to carry out elastic analysis and time-dependent creep analysis. For the elastic analysis, it can be used to calculate the instantaneous deformation of specimens under a load, and it can also simulate the instant deformation of a tunnel section during excavation and generate the forces applied on the tunnel opening section.

For a static elastic analysis, a load, which can be a point load, line load or surface load, is applied to a body, and the deformation and stress of the body can be obtained. An example of a cube specimen under a surface load is provided below. The dimensions of the specimen are 54 x 54 x 108 mm^3, and the elastic material properties are $E = 4.976e9Pa,\ \ v = 0.3$. The bottom surface of the specimen is fixed against movement in all directions, and a surface load of $2.0MPa$ is applied to the top surface of the specimen. The boundary conditions and the mesh division of the model are shown in Figure 5.14.

The displacement in the vertical direction calculated by SAFEA is presented in Figure 5.15a, the results obtained by ABAQUS are shown in Figure 5.15b. As may be seen, the two programs gave similar results. The displacements on the top surface of the specimen calculated by the two programs are -4.34080e-02mm (SAFEA) and -4.34084e-02mm (ABAQUS), the difference is only 9.21481e-06.

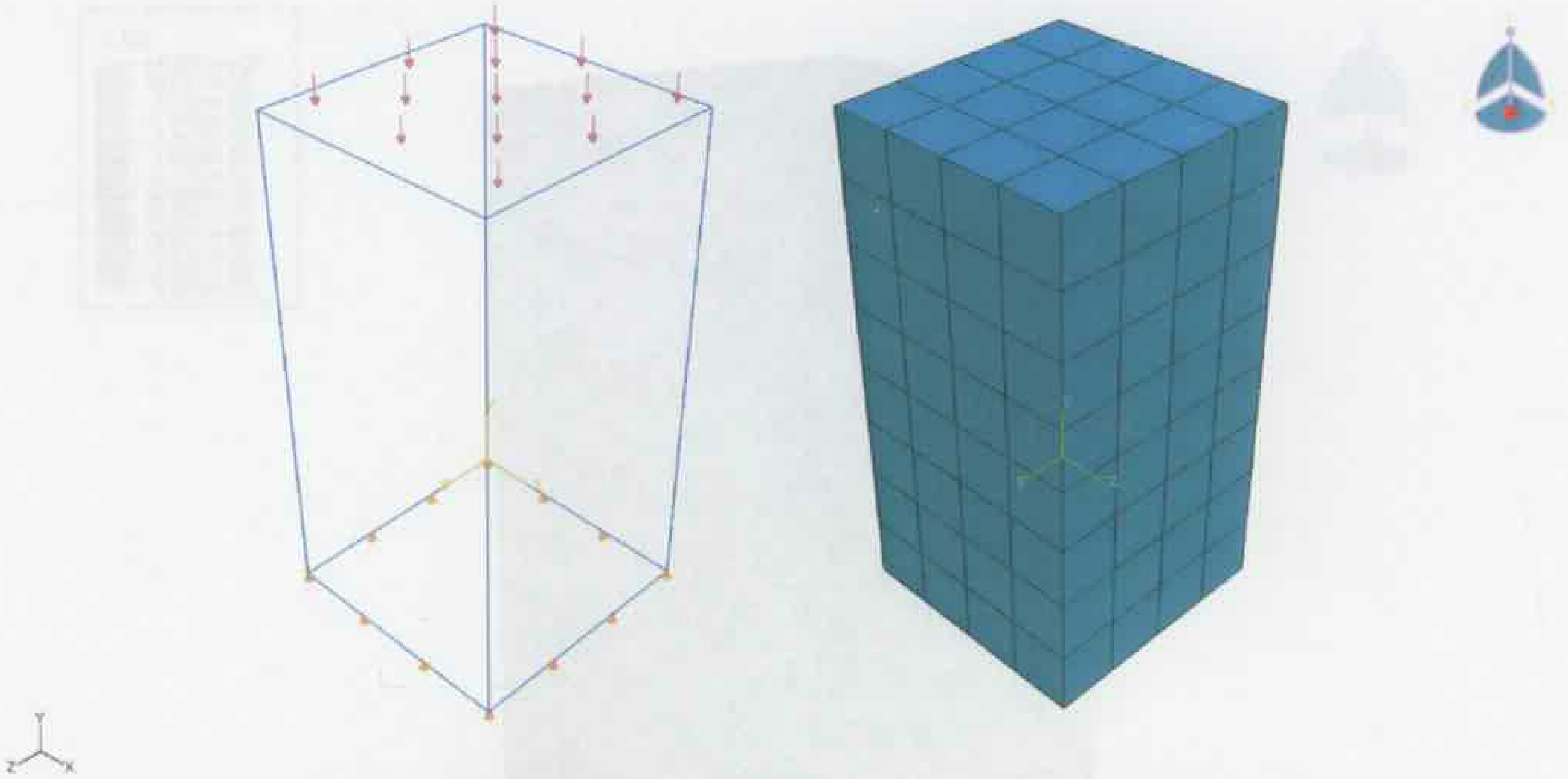

Figure 5.14: Cube specimen under a surface load.

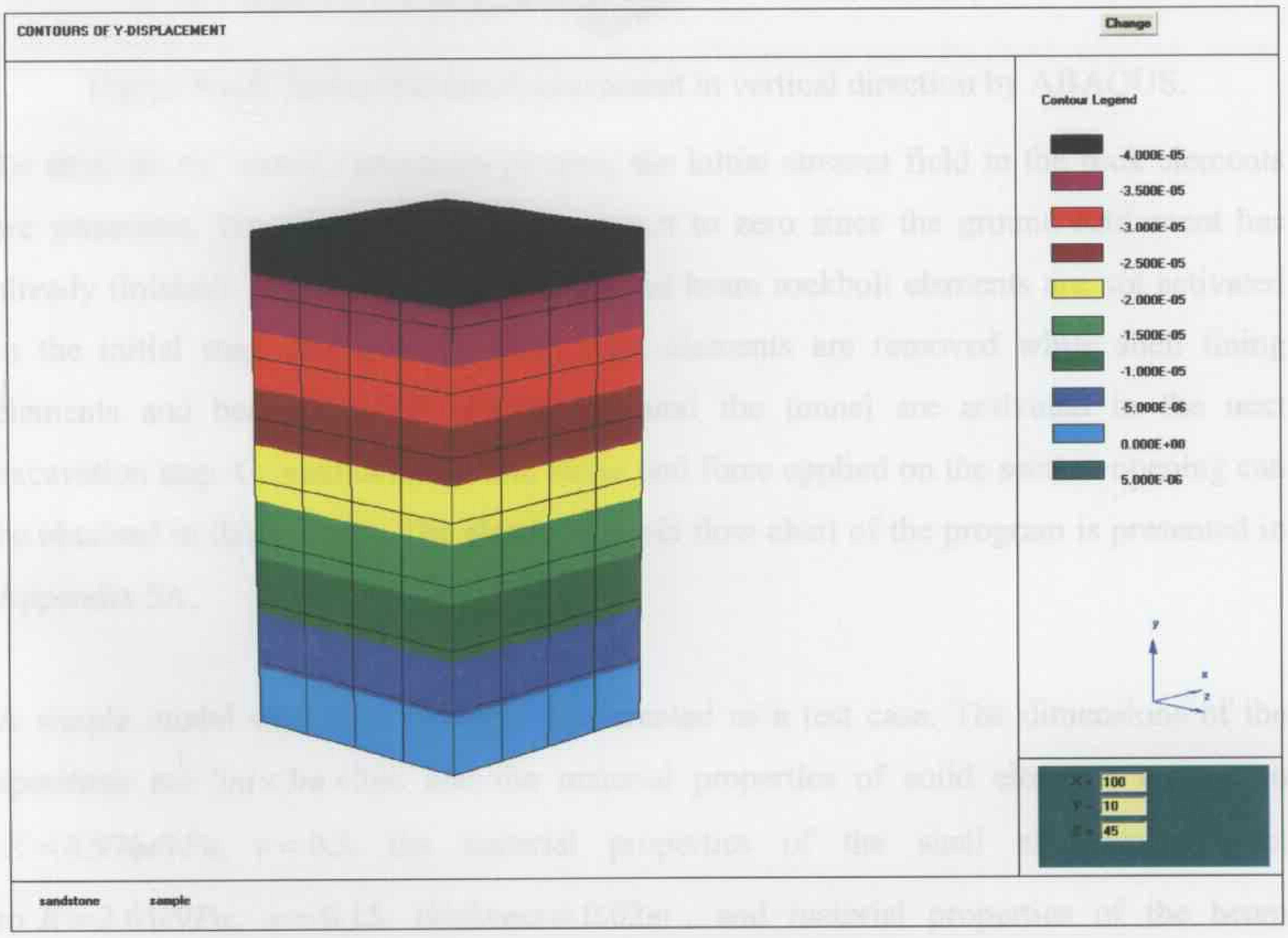

X = 100
Y = 10
Z = 45

Figure 5.15a: Instantaneous displacement in vertical direction by SAFEA.

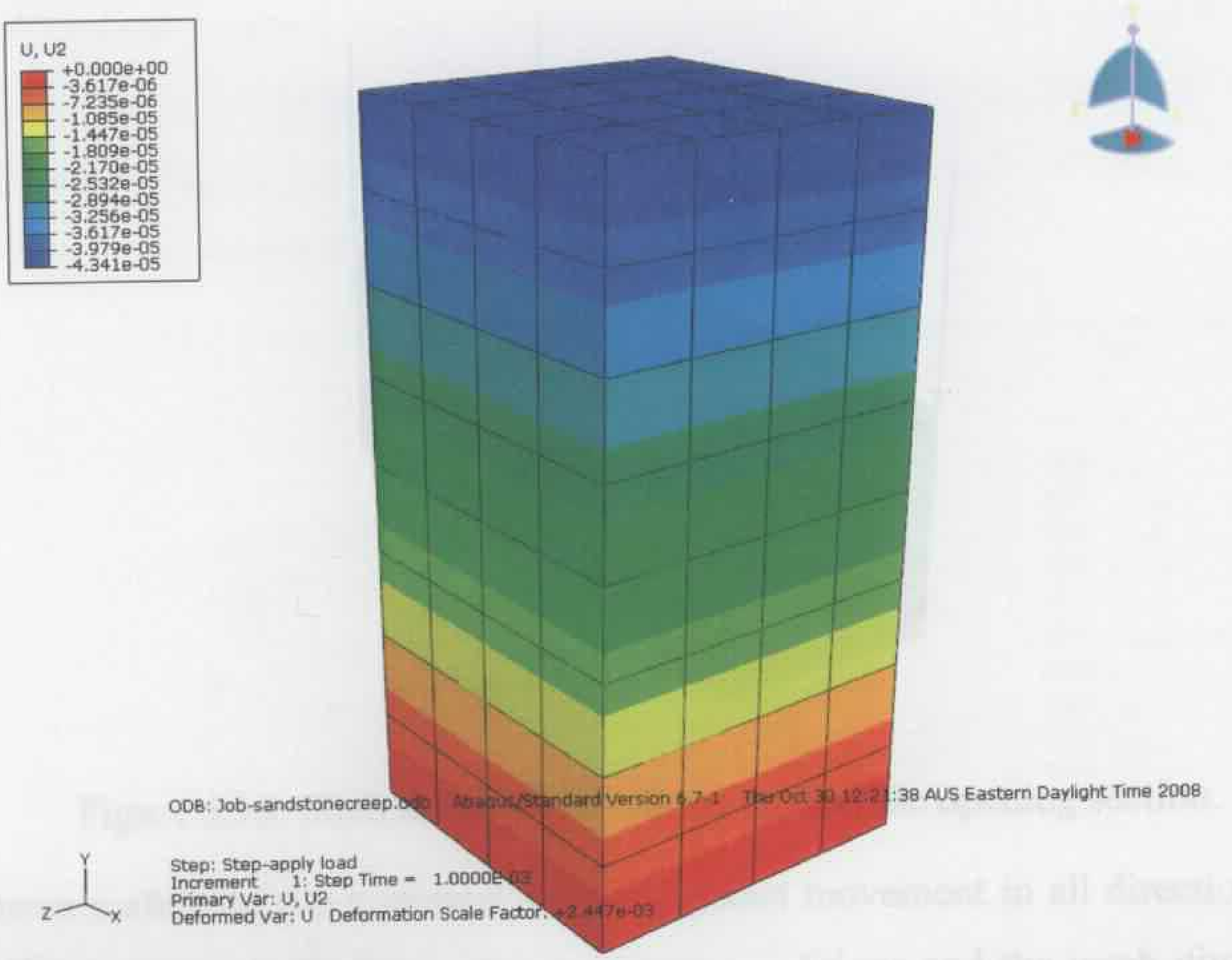

Figure 5.15b: Instantaneous displacement in vertical direction by ABAQUS.

To simulate the tunnel excavation process, the initial stresses field in the rock elements are generated. The initial deformation is reset to zero since the ground settlement has already finished. The shell lining elements and beam rockbolt elements are not activated in the initial step, and then the solid rock elements are removed while shell lining elements and beam rockbolt elements around the tunnel are activated in the next excavation step. Ground deformation, stress and force applied on the section opening can be obtained in this process. The elastic analysis flow chart of the program is presented in Appendix 5A.

A simple model with nine elements was created as a test case. The dimensions of the specimen are $3m \times 3m \times 3m$, and the material properties of solid elements are set to $E = 4.976e9Pa,\ \ v = 0.3$, the material properties of the shell elements are set to $E = 3.61e9Pa,\ \ v = 0.15,\ \ thickness = 0.02m$, and material properties of the beam elements are set to $E = 2.5e9Pa,\ \ area = 0.0314m^2$. The middle solid element was excavated, the shell elements were applied around the opening and the beam elements were positioned above the opening as shown in Figure 5.16.

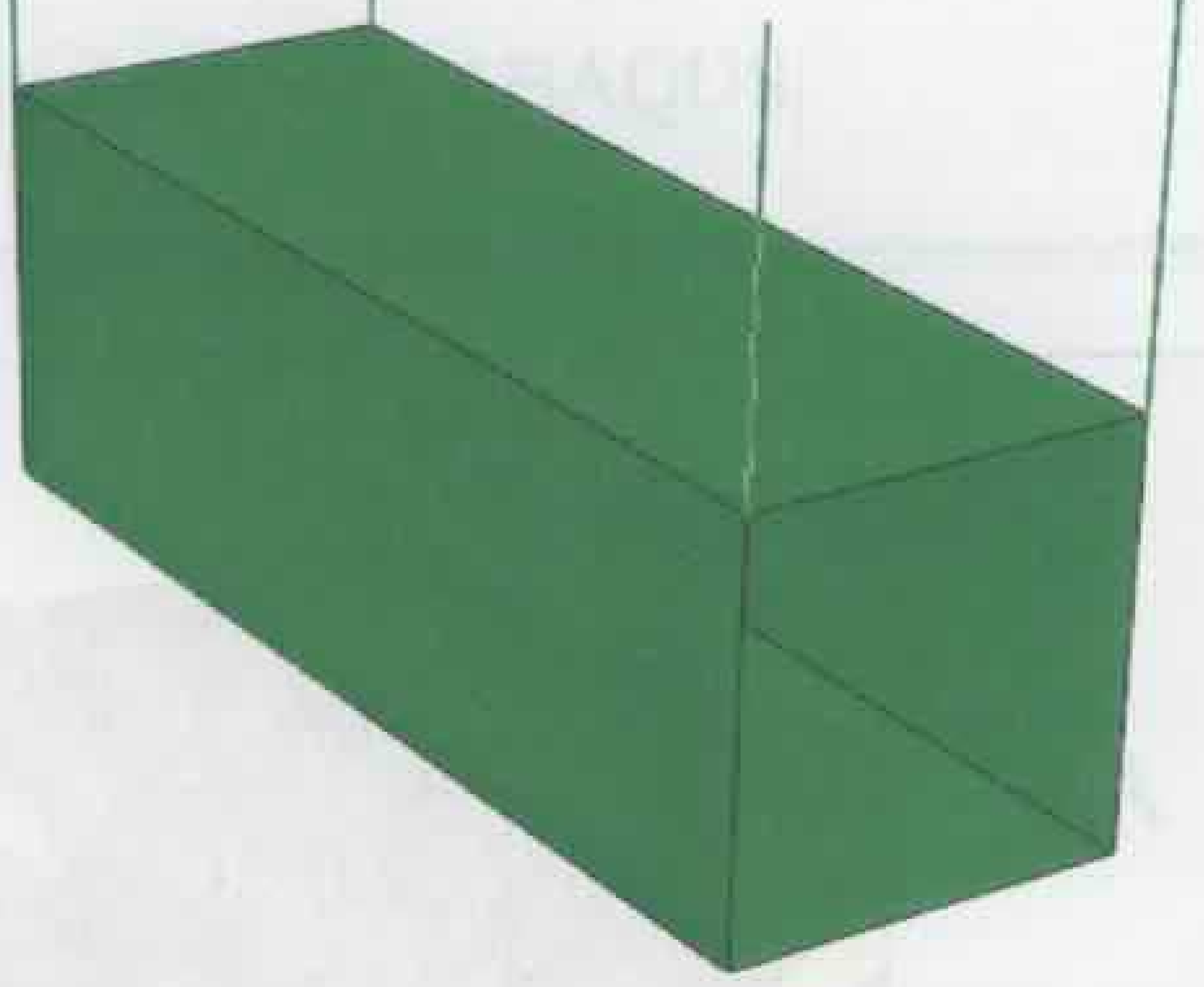

Figure 5.16: Shell and beam elements around the opening section.

The bottom surface of the specimen is fixed against movement in all directions; the self unit weight is set as *24000N/m*^{3}. The boundary conditions and the mesh division of the model are shown in Figure 5.17.

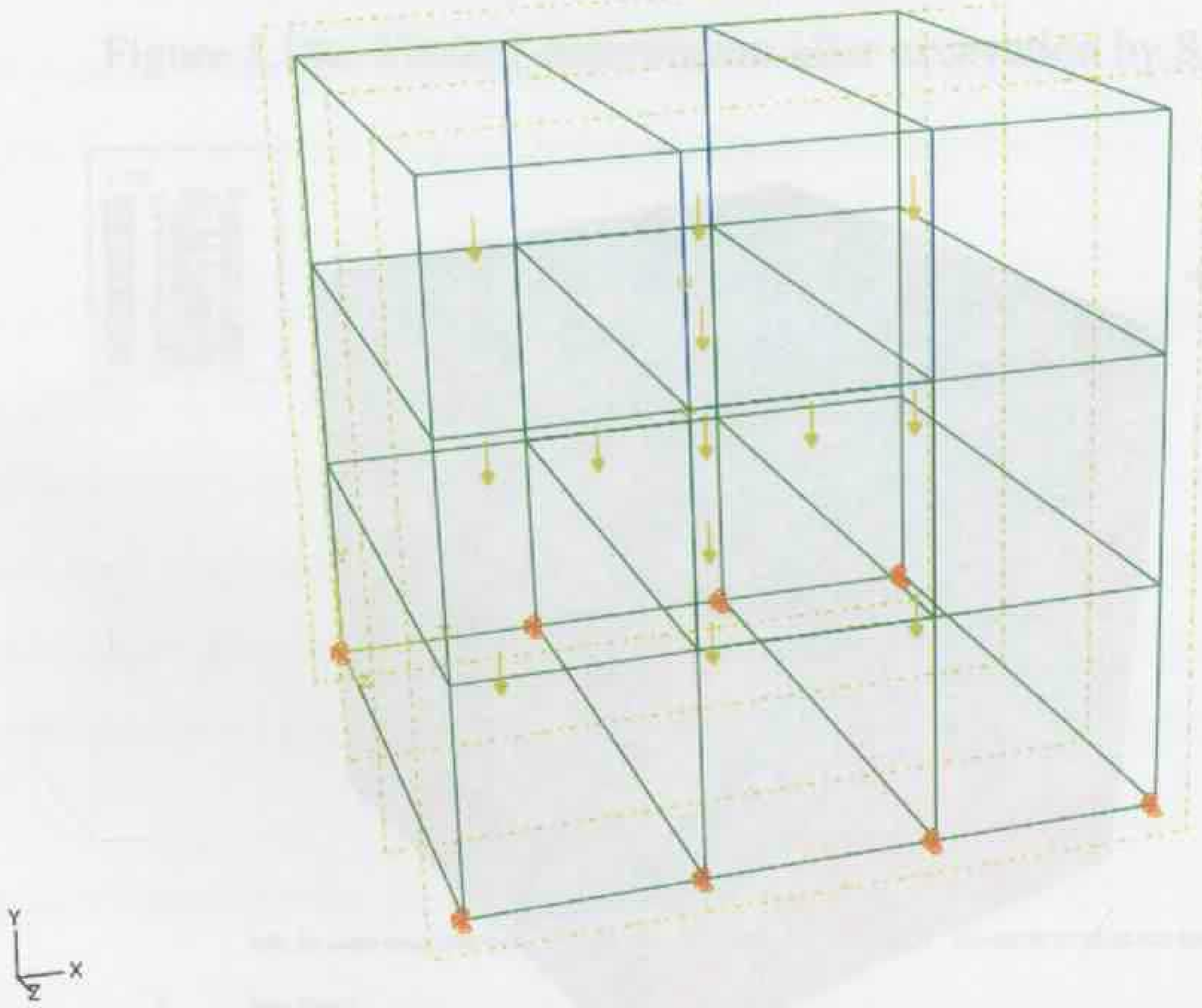

Figure 5.17: Boundary conditions for element excavation example.

The displacement in the vertical direction calculated by SAFEA and ABAQUS are presented in Figures 5.18a and 5.18b, respectively. The vertical displacements at points A and B shown in Figure 5.18a are given in Table 5.1. The results obtained by SAFEA agree well with the results obtained from ABAQUS.

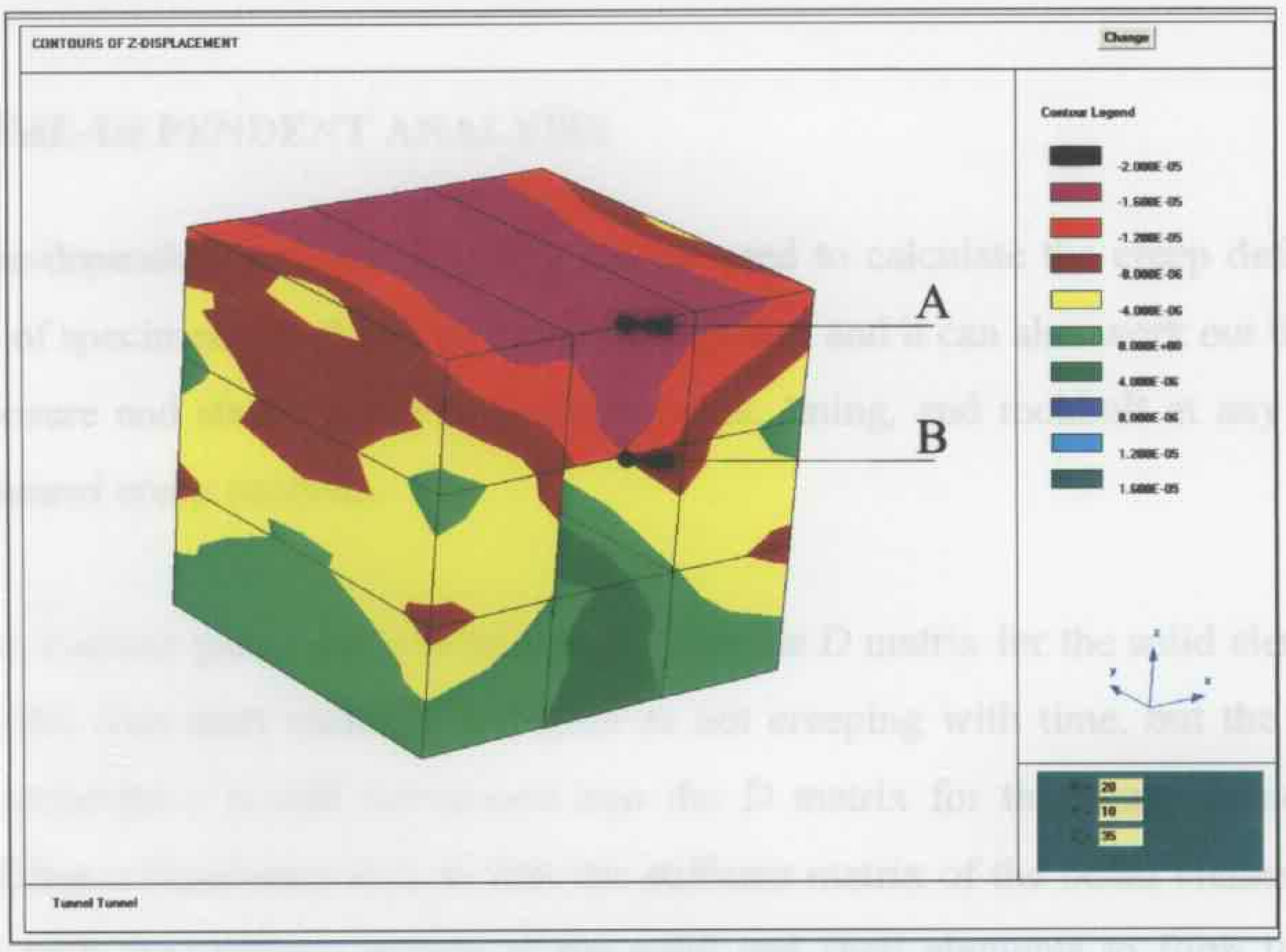

Figure 5.18a: Vertical deformation after excavation by SAFEA.

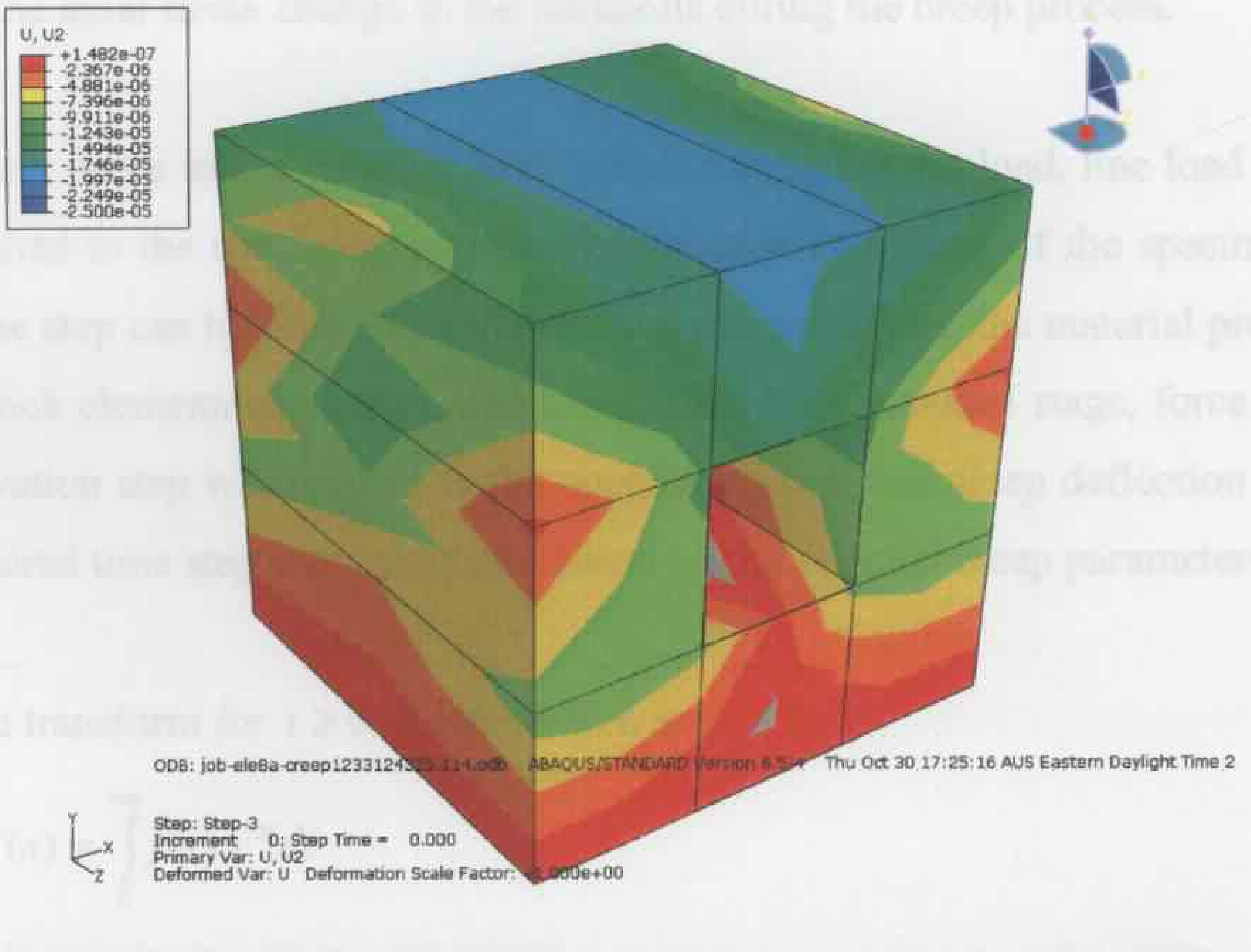

Figure 5.18b: Vertical deformation after excavation by ABAQUS.

Displacement	ABAQUS	SAFEA	Difference
A	-1.81778E-05	-1.8489E-05	-0.016832
B	-1.56314E-05	-1.5908E-05	-0.017387

Table 5.1 Results of vertical displacement by SAFEA and by ABAQUS.

5.2.3 TIME-DEPENDENT ANALYSIS

In the time-dependent analysis, SAFEA can be used to calculate the creep deformation and stress of specimens used in a laboratory creep test, and it can also work out the tunnel section closure and stress in the surrounding rock, lining, and rockbolt at any required time in a tunnel creep analysis.

A complex Laplace parameter s is introduced into the D matrix for the solid element and shell element. The steel rockbolt is treated as not creeping with time, but the complex Laplace parameter s is still introduced into the D matrix for the beam element (as a constant E has a transforms E/s) so that the stiffness matrix of the beam element can be combined with the stiffness matrix of the solid and shell elements to form the global stiffness matrix. In the present code, only axial force of the beam element is calculated to investigate the axial stress change in the rockbolts during the creep process.

In a laboratory creep test, a constant load, which can be a point load, line load or surface load, is applied to the specimen, and the deformation and stress of the specimen at any required time step can be obtained. In the tunnel creep analysis, the material properties of excavated rock elements are set to zero to simulate the excavated stage, force generated in the excavation step was applied to the opening section and creep deflection and stress for any required time step was calculated based on the selected creep parameters.

The Laplace transform for $t \geq 0$ can be written as

$$£\{f(t)\} = F(s) = \int_{0}^{+\infty} f(t)e^{-st}dt$$

where $f(t)$ is the original function with a real argument t, $F(s)$ is the image function with a complex argument s.

The mechanical properties of the materials are assumed to vary with time (or 'relax') according to a logarithmic function of time. The bulk modulus K and shear modulus G are given by

$$\begin{aligned} K(t) &= K_0(A + B\ln(1+\alpha\cdot t)) \\ G(t) &= G_0(A + B\ln(1+\alpha\cdot t)) \end{aligned} \tag{5.21}$$

The Laplace transforms of equations 5.21 are

$$\begin{aligned} \overline{K} &= \frac{K_0 A}{s} + \frac{K_0 B}{s} e^{s/\alpha} K_1(s/\alpha) \\ \overline{G} &= \frac{G_0 A}{s} + \frac{G_0 B}{s} e^{s/\alpha} G_1(s/\alpha) \end{aligned} \tag{5.22}$$

where K_1 and G_1 are exponential integrals defined as

$$\begin{aligned} K_1(\varsigma) &= \int_{\varsigma}^{\infty} \frac{e^u}{u} du \\ G_1(\varsigma) &= \int_{\varsigma}^{\infty} \frac{e^u}{u} du \end{aligned} \tag{5.23}$$

and the D matrix is written as

$$[D(t)] = \begin{bmatrix} K(t)+4G(t)/3 & K(t)-2G(t)/3 & K(t)-2G(t)/3 & 0 & 0 & 0 \\ & K(t)+4G(t)/3 & K(t)-2G(t)/3 & 0 & 0 & 0 \\ & & K(t)+4G(t)/3 & 0 & 0 & 0 \\ & & & G(t) & 0 & 0 \\ & \text{Symmetry} & & & G(t) & 0 \\ & & & & & G(t) \end{bmatrix} \tag{5.24}$$

Applying a Laplace transform, this can be written as

$$\overline{D} = \begin{bmatrix} \overline{K}+4\overline{G}/3 & \overline{K}-2\overline{G}/3 & \overline{K}-2\overline{G}/3 & 0 & 0 & 0 \\ & \overline{K}+4\overline{G}/3 & \overline{K}-2\overline{G}/3 & 0 & 0 & 0 \\ & & \overline{K}+4\overline{G}/3 & 0 & 0 & 0 \\ & & & \overline{G} & 0 & 0 \\ & \text{Symmetry} & & & \overline{G} & 0 \\ & & & & & \overline{G} \end{bmatrix} \tag{5.25}$$

where the bar denotes a Laplace transform.

In the FORTRAN code SAFEA, a Laplace Transform is used to simplify the convolution integral equation to an easily solvable algebraic equation, and a Laplace variable s is introduced into the D matrix. Since the different materials have different creep properties, different creep parameters are selected in the program. For the rock element, a subroutine called DMAT is used to form the D matrix, and the bulk modulus K and shear modulus G are transformed by applying a Laplace transform to the function of time in Equation 5.25. For the shotcrete shell element, a subroutine called DMATS is used to form the D matrix, and the D matrix is again transformed by a Laplace transform. For the steel beam element, steel is considered as not creeping with time, and the elastic modulus E is treated as constant, and so the transformed modulus $\overline{E} = \frac{E}{s}$ is used in the D matrix.

From equation 3.48, we get $\overline{\sigma} = s\overline{R} \cdot \overline{\varepsilon}$, and applying the equation in our case, we can get

$$\overline{f} = s\overline{K} \cdot \overline{\delta} \tag{5.26}$$

So in the program, the stiffness matrix $\overline{K}$ is a function of the Laplace variable s, and a three-dimensional finite element solver is then used to solve the equation based on the transformed field variables. Finally, the complex results are inverted into the solution in real time by a direct numerical inversion - Talbot's method (Talbot, 1979). This involves using complex arithmetic in the equation solver. The creep analysis flow chart for the code is presented in Appendix 5B.

5.3 ABAQUS

The commercial finite element program ABAQUS was also used in the present research to simulate the laboratory creep tests, tunnel excavation and creep analysis. ABAQUS is a general finite element analysis program and has been successfully employed in solving geotechnical engineering problems (Christian, 1999; Zhu and Wang, 2004 and Zhu et al., 2006). The instantaneous deformation analysis was based on the elastic material properties, while the time-dependent creep deformation analysis was assumed to obey a hardening power law.

In the present research, a twenty-node quadratic brick element with reduced integration (2x2x2 integration points) C3D20R was selected to discretise the shotcrete panels and rock cubes in the laboratory tests, and the rock in the tunnel models. The element shape and node numbering sequence are shown in Figure 5.19. The element has a similar shape and integration scheme as the 20-node solid element used in SAFEA, and behaves very well in general conditions and rarely exhibits hour glassing problems even with the use of reduced integration (Jeff, 1997).

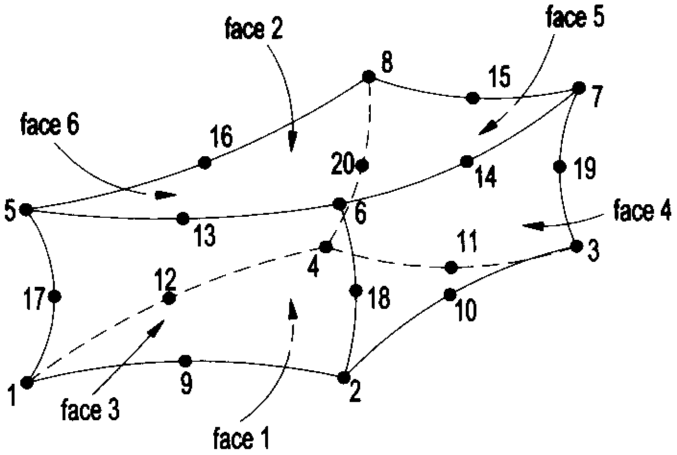

Figure 5.19: 20-node solid element (ABAQUS, 2003).

An 8-node doubly curved thick shell element with reduced integration (2x2 integration points) S8R was used to model the shotcrete lining in the tunnel models. The node numbering sequence and integration scheme are shown in Figure 5.20. The transverse shear in the lining is not ignored, but the change in thickness with deformation is ignored for these elements (ABAQUS, 2003). These shell elements were activated after the excavation of the tunnel section and the interface specified as tied to the exposed tunnel surface in the analysis.

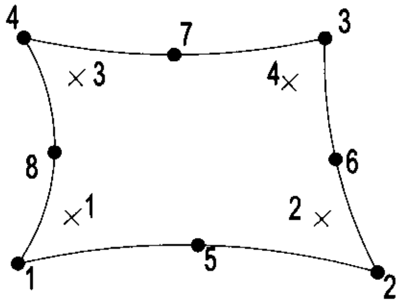

Figure 5.20: 8-node shell element (ABAQUS, 2003).

A 2-node linear displacement 3-D stress/displacement truss element T3D2 was used to represent the rockbolts in the analysis. The node order and integration scheme are shown in Figure 5.21. This simple element can only support an axial force but not bending moment, the cross-section and material properties are constant along its length. The elements were activated at the same time as the shell elements after the excavation of the tunnel section, and treated as embedded in the solid rock element (i.e. attached to the nodes of the 20 node element).

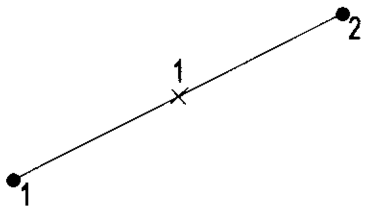

Figure 5.21: 2-node truss element (ABAQUS, 2003).

ABAQUS can easily handle elastic analysis for specimens under a constant load in the laboratory. To simulate the tunnel excavation, some particular characteristics of the problem need to be taken into consideration. When the ground gravity force is applied to the solid elements, the ground will deform due to the gravity force. However, in the natural condition, the ground settlement due to the self-weight has already finished, and the ground deformation due to the gravity force should be set to zero. In ABAQUS, an initial stress field was generated using equations presented by Pells (2002), and the initial ground settlement was zero since the ground deformation has already finished. An example of the subroutine to generate the initial 3D ground stress in ABAQUS is given in Appendix 5C.

In ABAQUS, the process of tunnel excavation is controlled by removing and activating the corresponding rock, lining and rockbolt elements. All elements in the tunnel model are created in the initial mesh, while the lining and rockbolt elements are set to inactive in the initial analysis step. During the excavation, the tunnel face progresses by removing the rock elements in each step, and activating the corresponding lining and rockbolt elements at this section in the following step. The deviator stress around the excavated section is calculated during the process. An example of the steps taken during tunnel excavation is shown in Figures 5.22a & 5.22b.

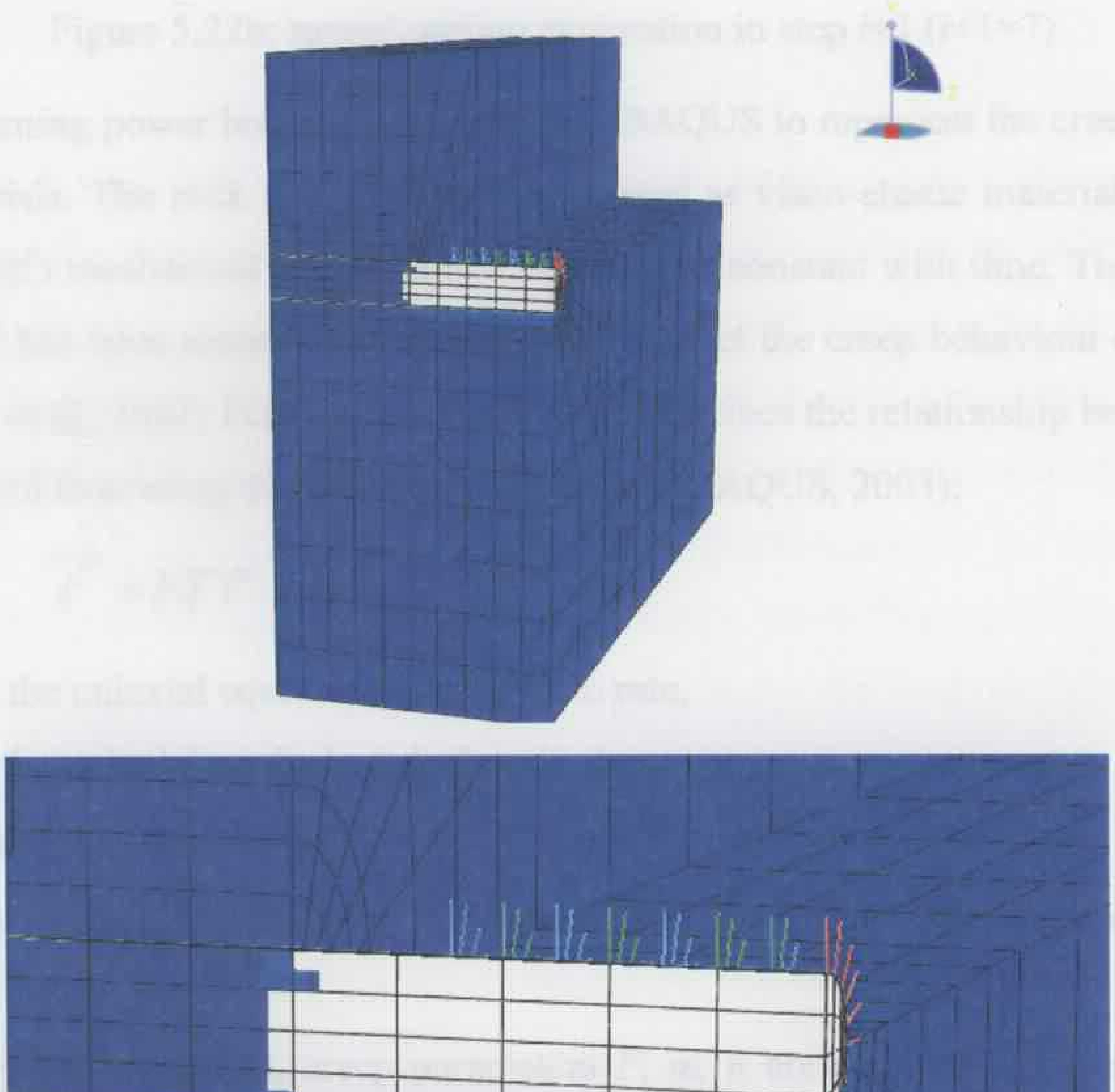

Figure 5.22a: tunnel section excavation in step *i* (*i*=6).

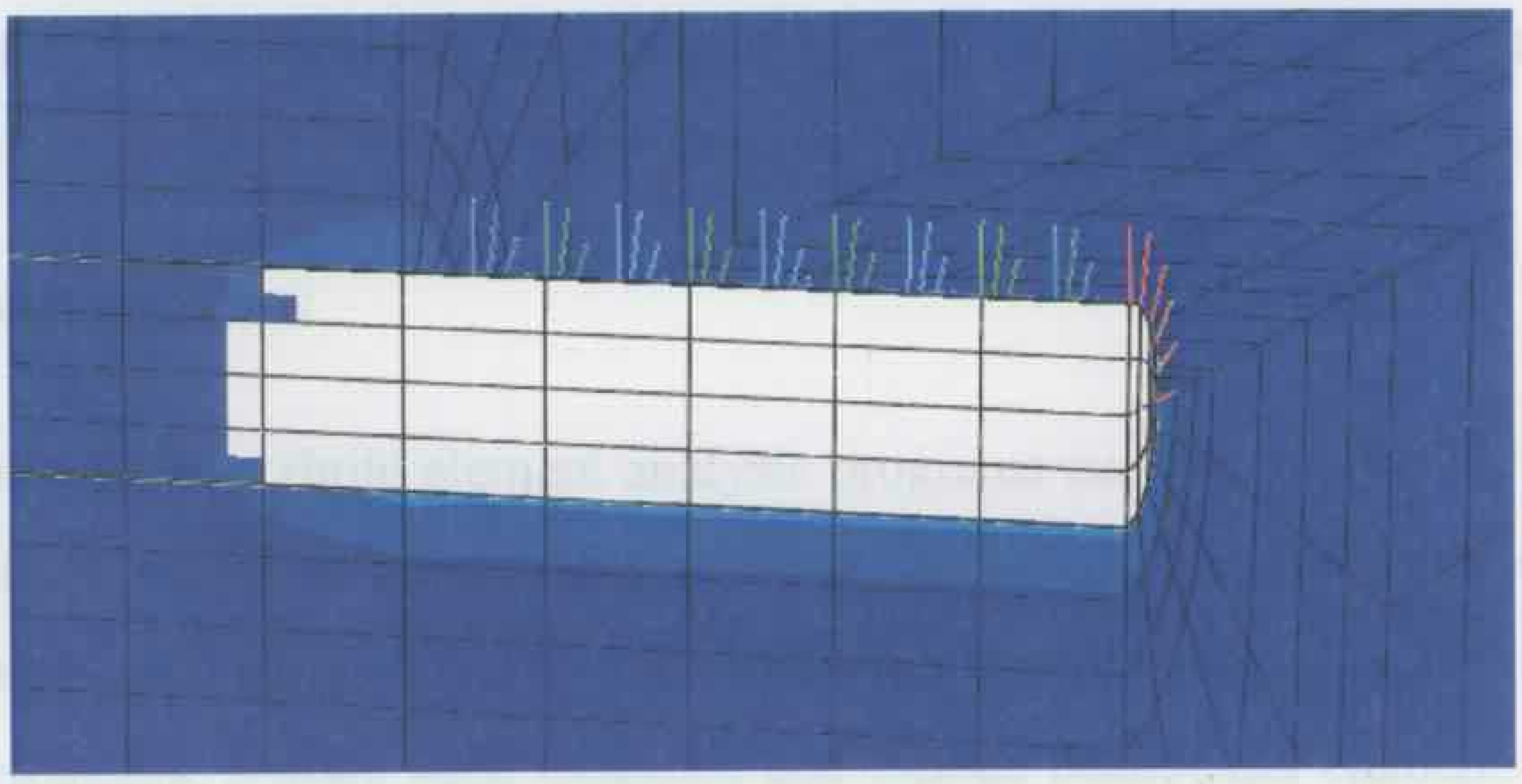

Figure 5.22b: tunnel section excavation in step *i*+1 (*i*+1=7).

A time hardening power law model is used in ABAQUS to represent the creep behaviour of the materials. The rock and shotcrete are treated as visco-elastic materials, while the steel rockbolt's mechanical properties are regarded as constant with time. The power law creep model has been successfully employed to predict the creep behaviour of rock salts (Ghaboussi, et al., 1981; Fernandez, 1994) and it describes the relationship between strain rate, stress and time using the following equation (ABAQUS, 2003):

$$\bar{\varepsilon}^{cr} = F\tilde{q}^{n}t^{m} \tag{5.27}$$

where $\bar{\varepsilon}^{cr}$ is the uniaxial equivalent creep strain rate,

$\tilde{q}$ is the uniaxial equivalent deviatoric stress,

t is the total time.

F, m, n are creep parameters and can be determined from experimental results.

In the laboratory creep test, creep parameters *F, m, n* are selected to fit the numerical results with the experimental curve, and later applied in the numerical tunnel models. It has been found that the deviator stress generated in the tunnel excavation process is a maximum in the region surrounding the tunnel opening. It is assumed that the creep deformation only occurs when the material is under a changed stress region, and the rock does not creep under its self weight. So only the region surrounding the tunnel opening is treated as the 'creep zone', the rock elements in the remaining part of the mesh are treated as not undergoing creep in the tunnel models. It is necessary to set this 'creep zone' to avoid the whole model undergoing a creep deformation due to the applied gravity loads on the ground, which is unrealistic since the initial deformation of the ground under gravity load has already finished before the excavation of the tunnel.

5.4 CONCLUSIONS

In this chapter, the two finite element analysis programs used in the present research are introduced. Both programs can be used to model time-dependent laboratory creep tests, simulate tunnel excavation and carry out creep analysis for a tunnel and its support. 20-node solid elements, 8-node shell elements and 2-node beam/truss elements are used to model the rock, lining and rockbolts respectively in both programs.

The FORTRAN code SAFEA needs initial data to be prepared with a normal text editor and does not have an interactive input interface. The output data from SAFEA is also in text format, and so it needs another program call GENPLT to plot the required output such as deformation and stress. For the deformation and stress at a required node or in an element, the numerical values can be printed to an output file for examination. It is not convenient to use, but the whole calculation process is transparent to the user and can be controlled by the programmer. ABAQUS has friendly interactive input interface, and a powerful output function. It can be easily operated by the user and does not need programming ability.

In SAFEA, the bulk and shear modulus of the material is assumed to obey some time-dependent function (e.g. a logarithmic function), and the program uses a Laplace transform and Talbot inversion that uses complex arithmetic to obtain the solution. In ABAQUS, a power creep law model is embedded in the program and can be used directly to perform the creep analysis, and the program performs the integral calculation by assuming that the increment in the field variables varies linearly over a finite increment of time. With selected parameters, SAFEA and ABAQUS can both give reasonable and close results. However, SAFEA can calculate the final result at a given time point directly and does not need to calculate the interim values to get the final result as the algorithm in ABAQUS does.

The power law model in ABAQUS is able to simulate the creep behaviour of materials under different stress levels. The logarithmic function used in SAFEA can not reflect the change of creep rate under different stress level automatically. However if the parameters are selected for an appropriate stress level as is done for the classic Mesri's (1973) creep law (which also does not consider the stress level in the creep behaviour for the materials) it can still provide a reasonable engineering solution.

APPENDIX 5A ELASTIC ANALYSIS FLOW CHART

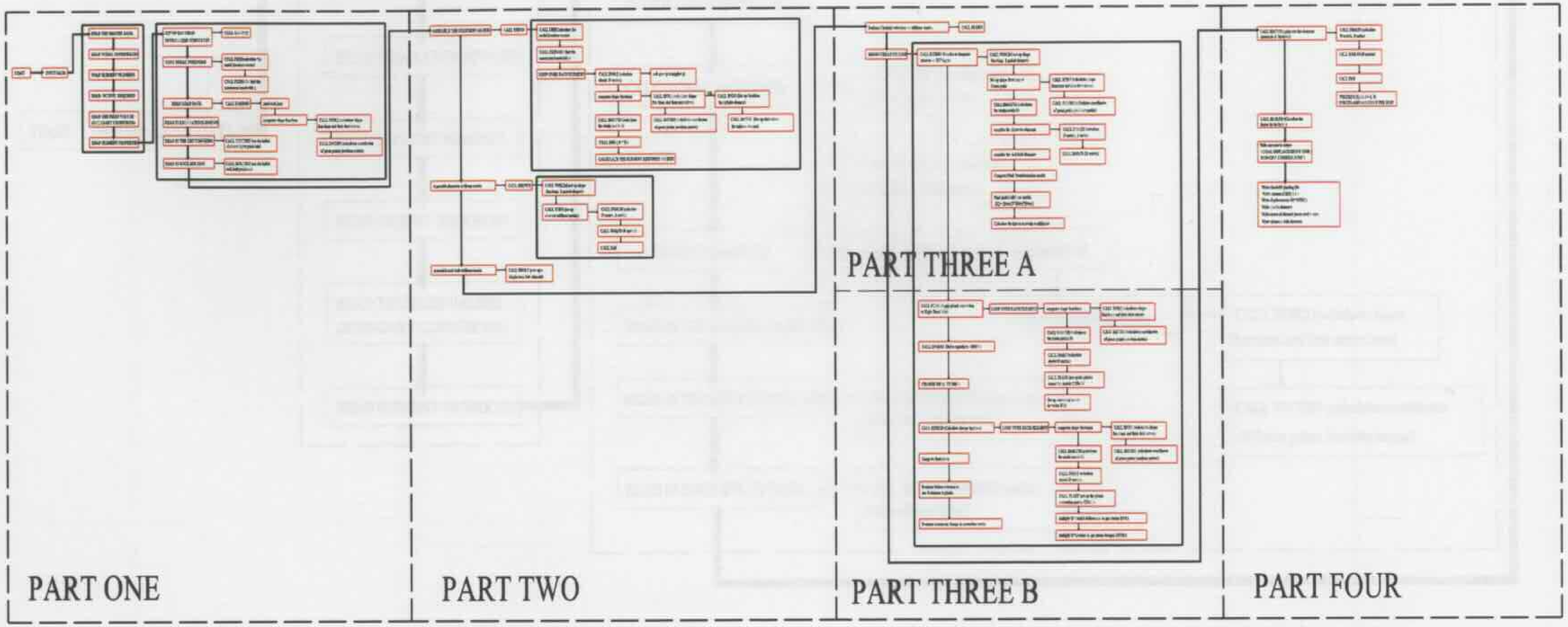

Figure 5A.1: Overall layout of elastic analysis flow chart (see enlarged sections in Figures 5A.2 to 5A.5).

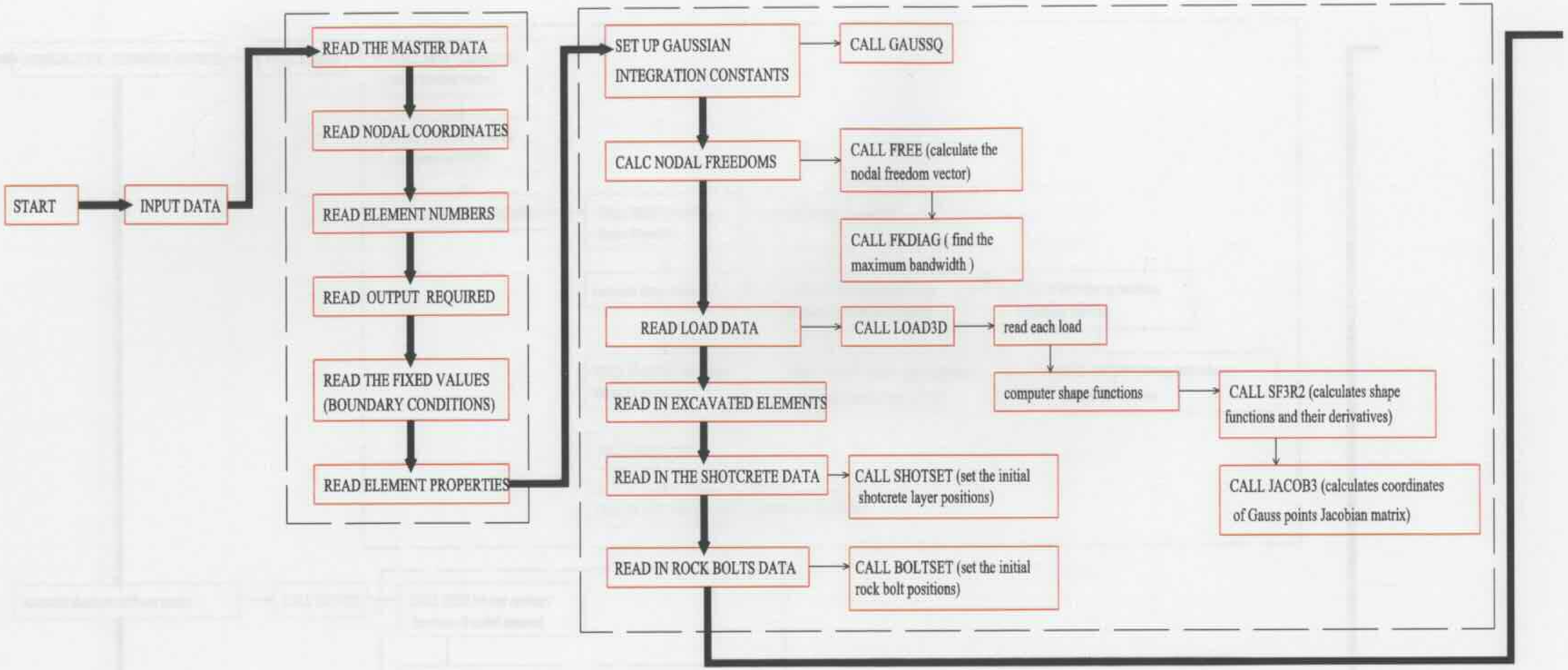

Figure 5A.2: Elastic analysis flow chart - part one.

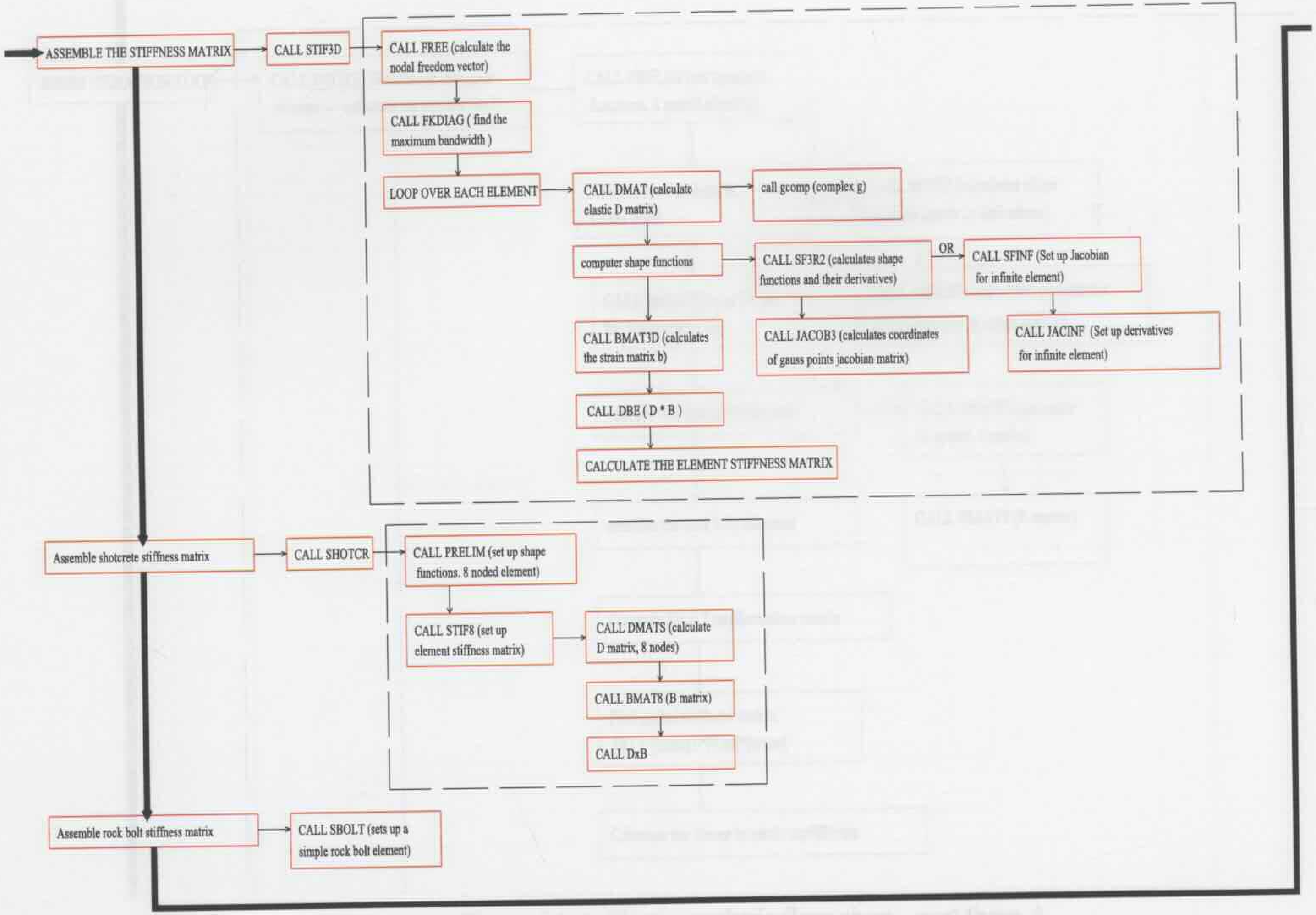

Figure 5A.3: Elastic analysis flow chart - part two.

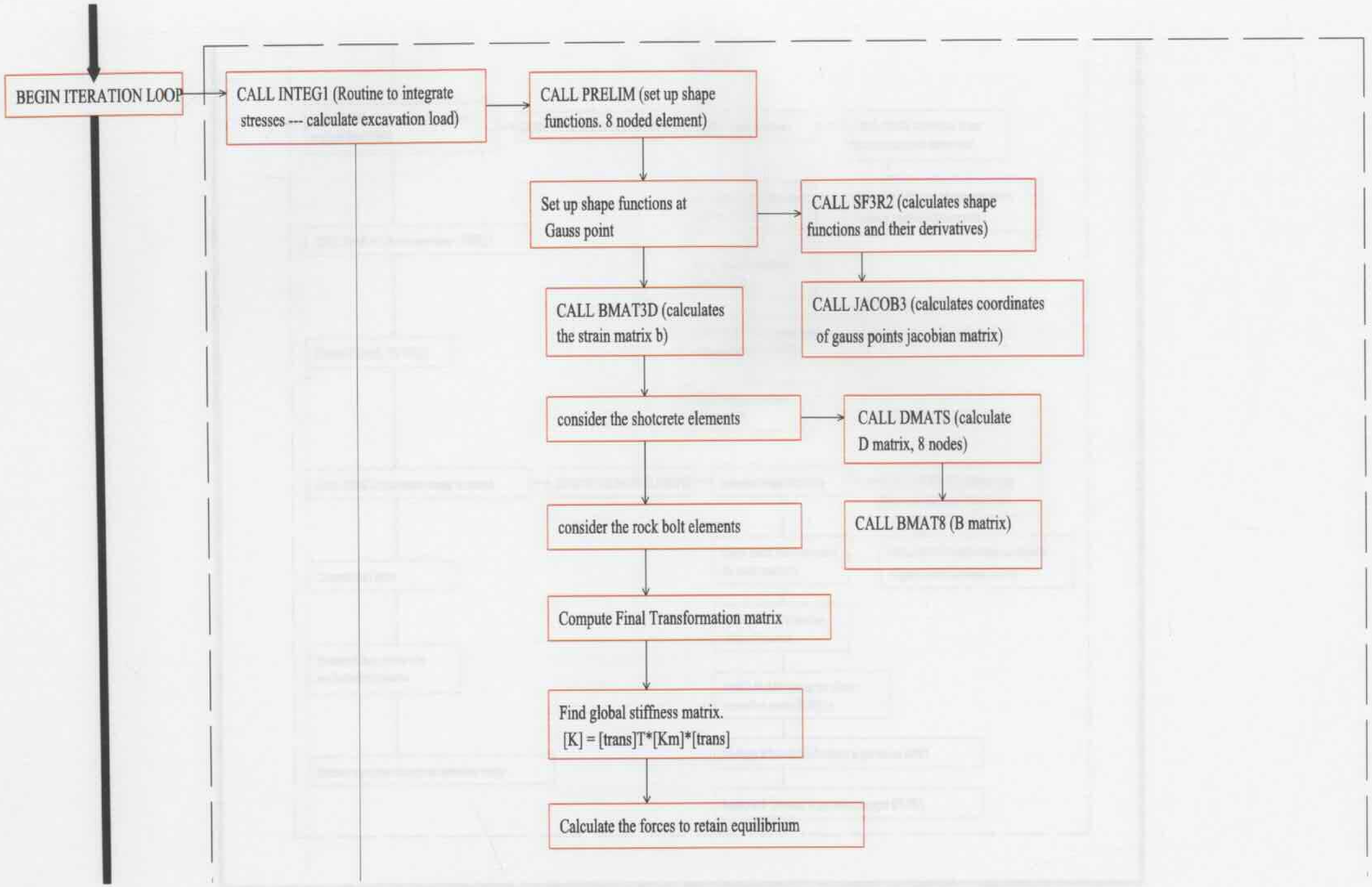

Figure 5A.4: Elastic analysis flow chart - part three A.

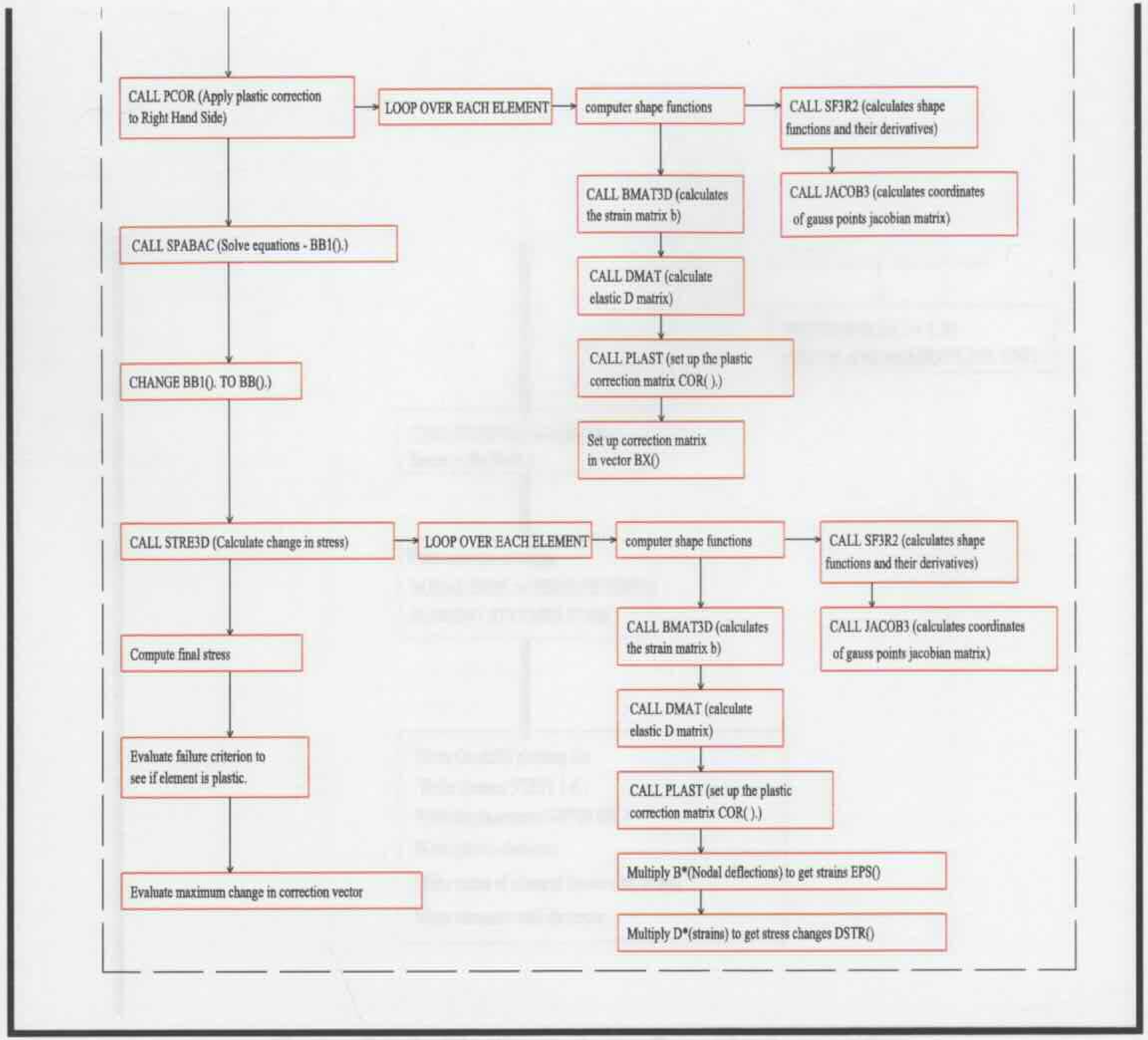

Figure 5A.4: Elastic analysis flow chart - part three B.

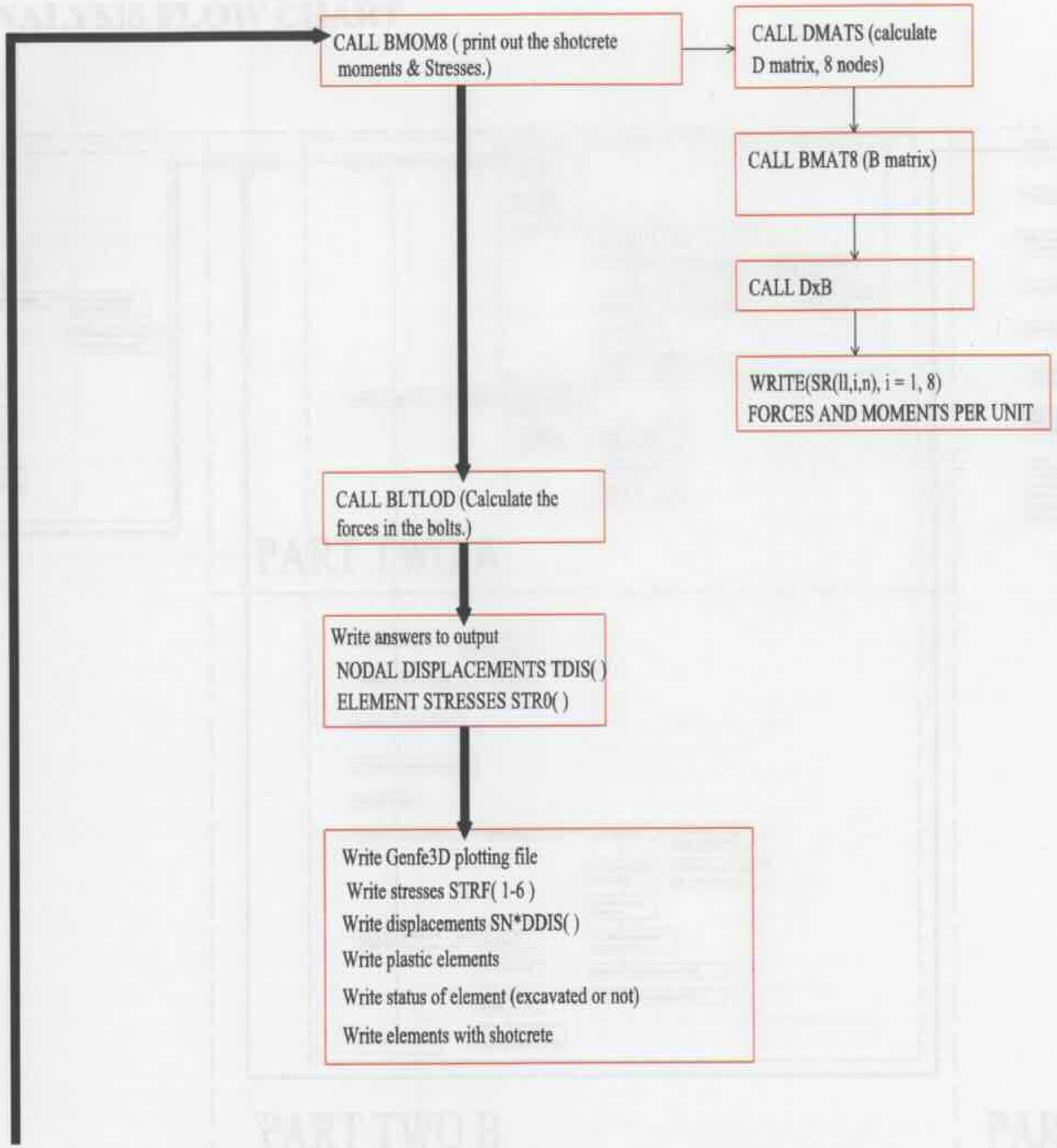

Figure 5A.5: Elastic analysis flow chart - part four.

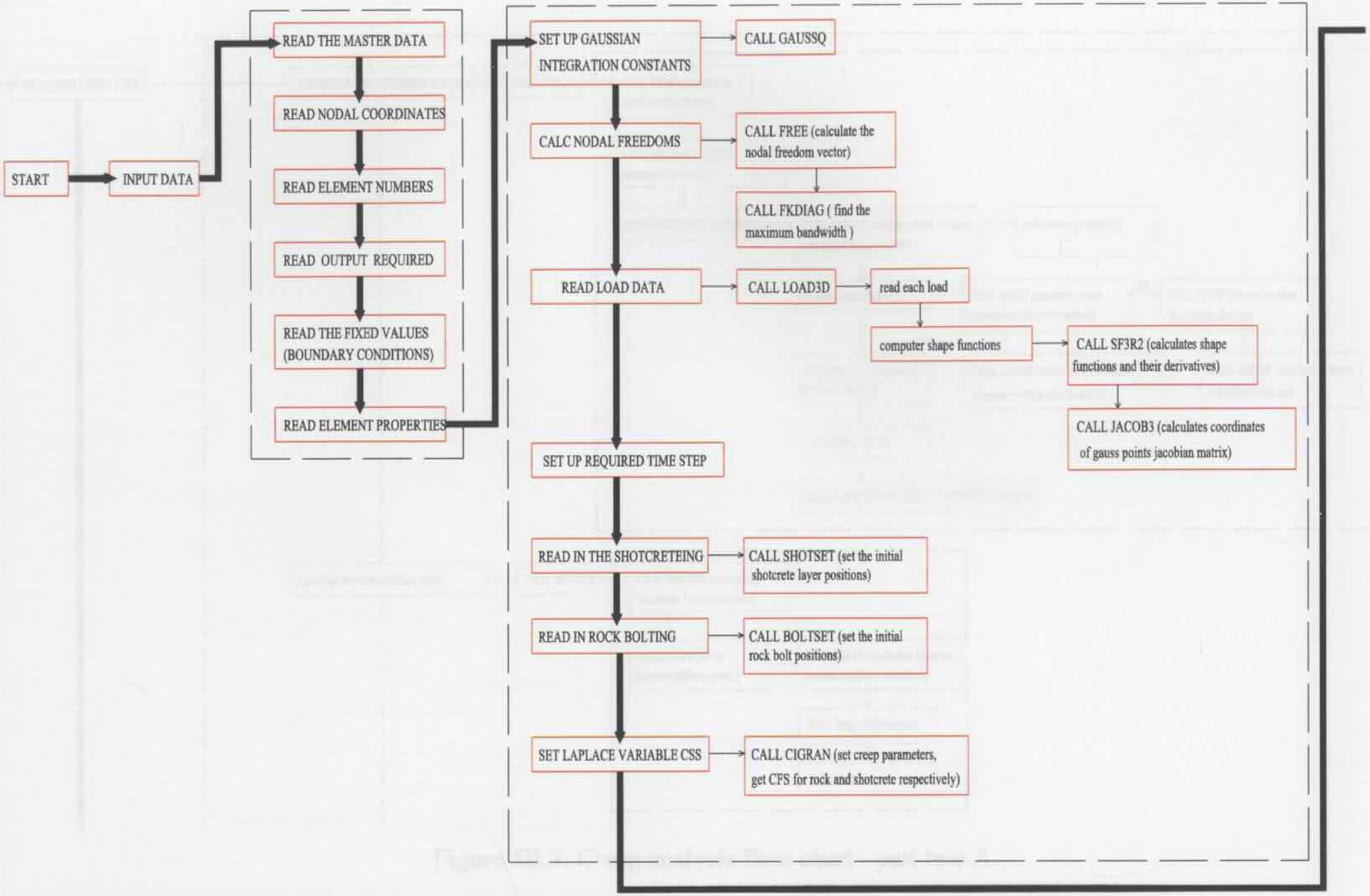

Figure 5B.2: Creep analysis flow chart - part one.

APPENDIX 5B CREEP ANALYSIS FLOW CHART

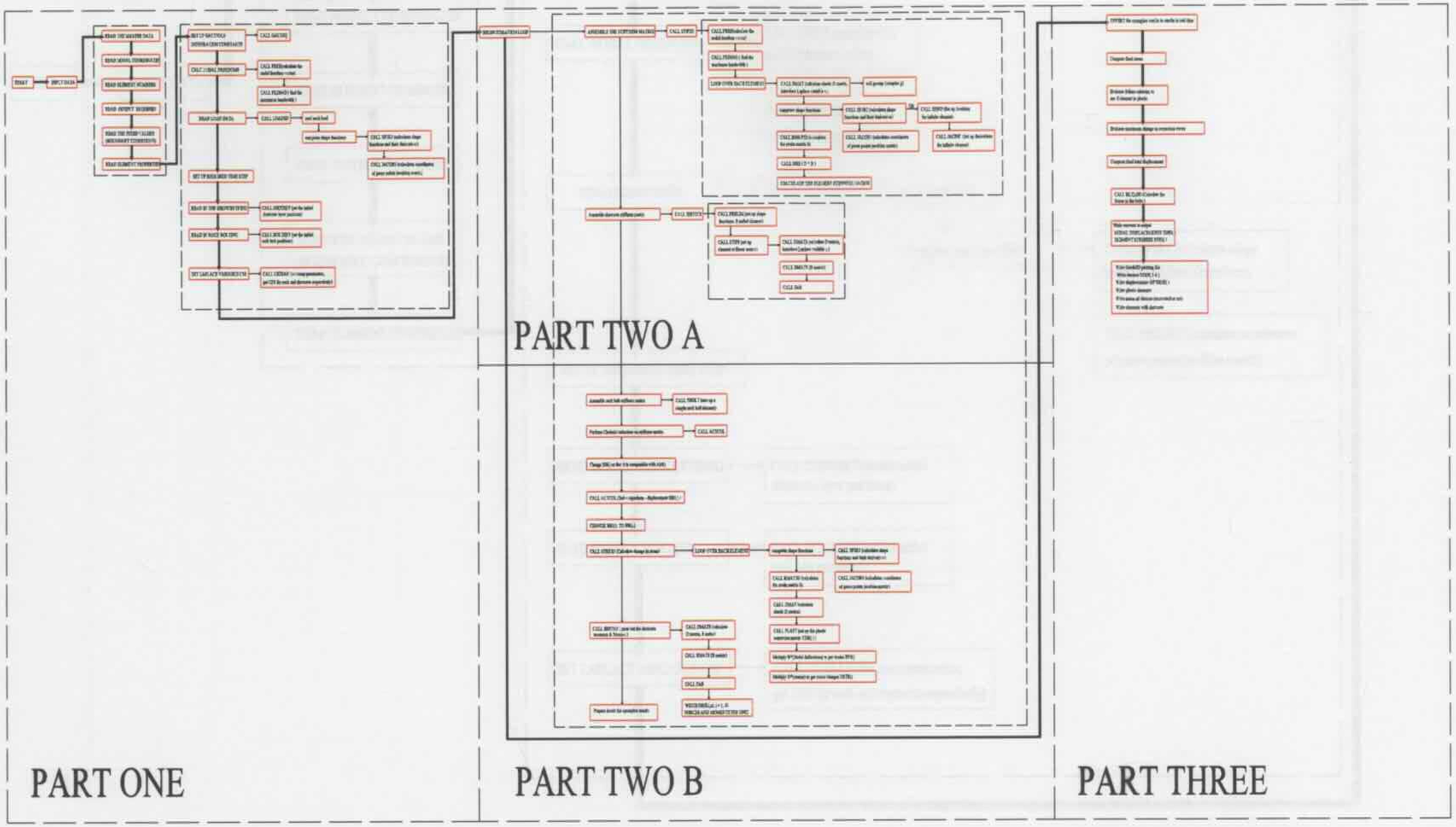

Figure 5B.1: Overall layout of creep analysis flow chart (see enlarged sections in Figures 5B.2 to 5B.5).

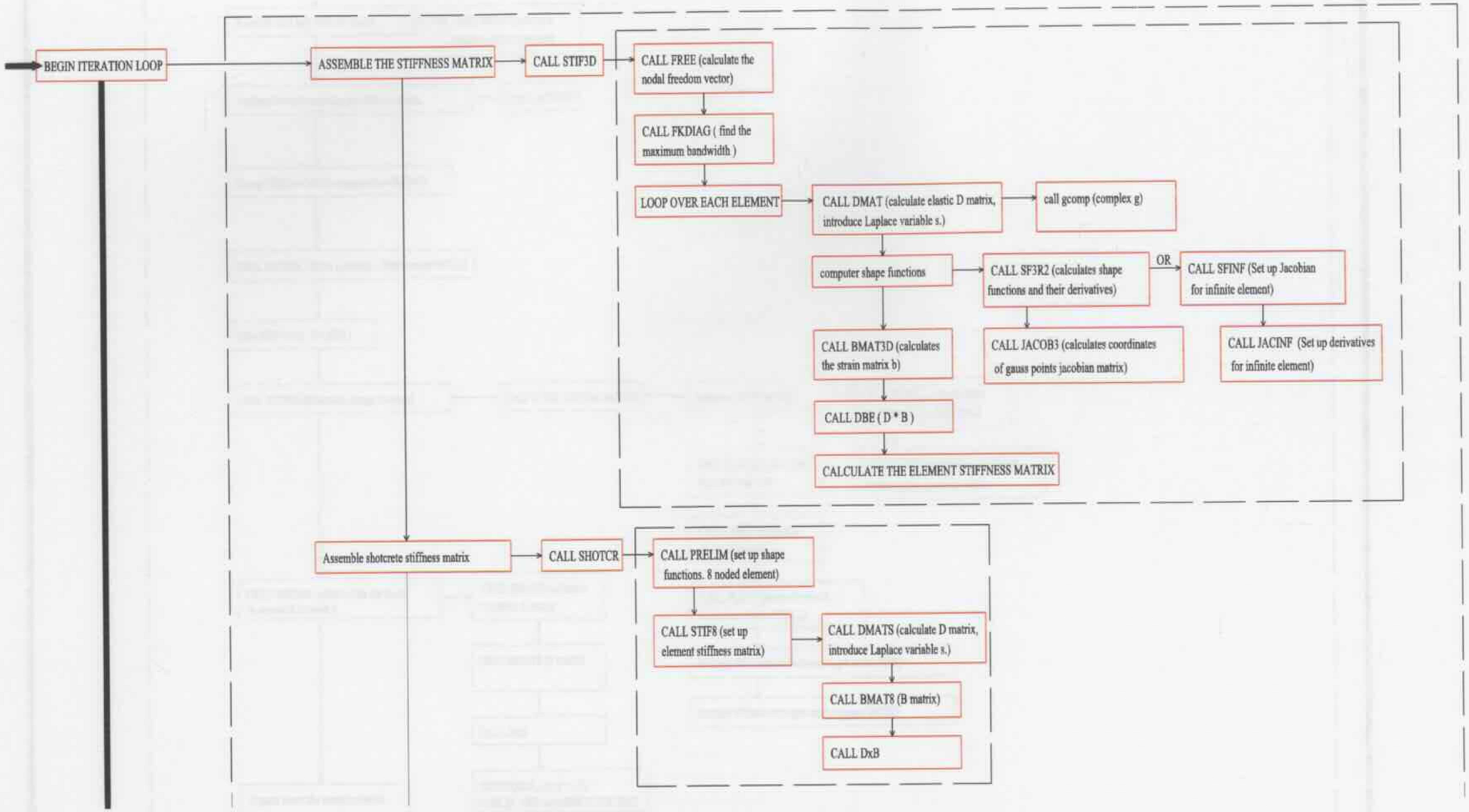

Figure 5B.3: Creep analysis flow chart - part two A.

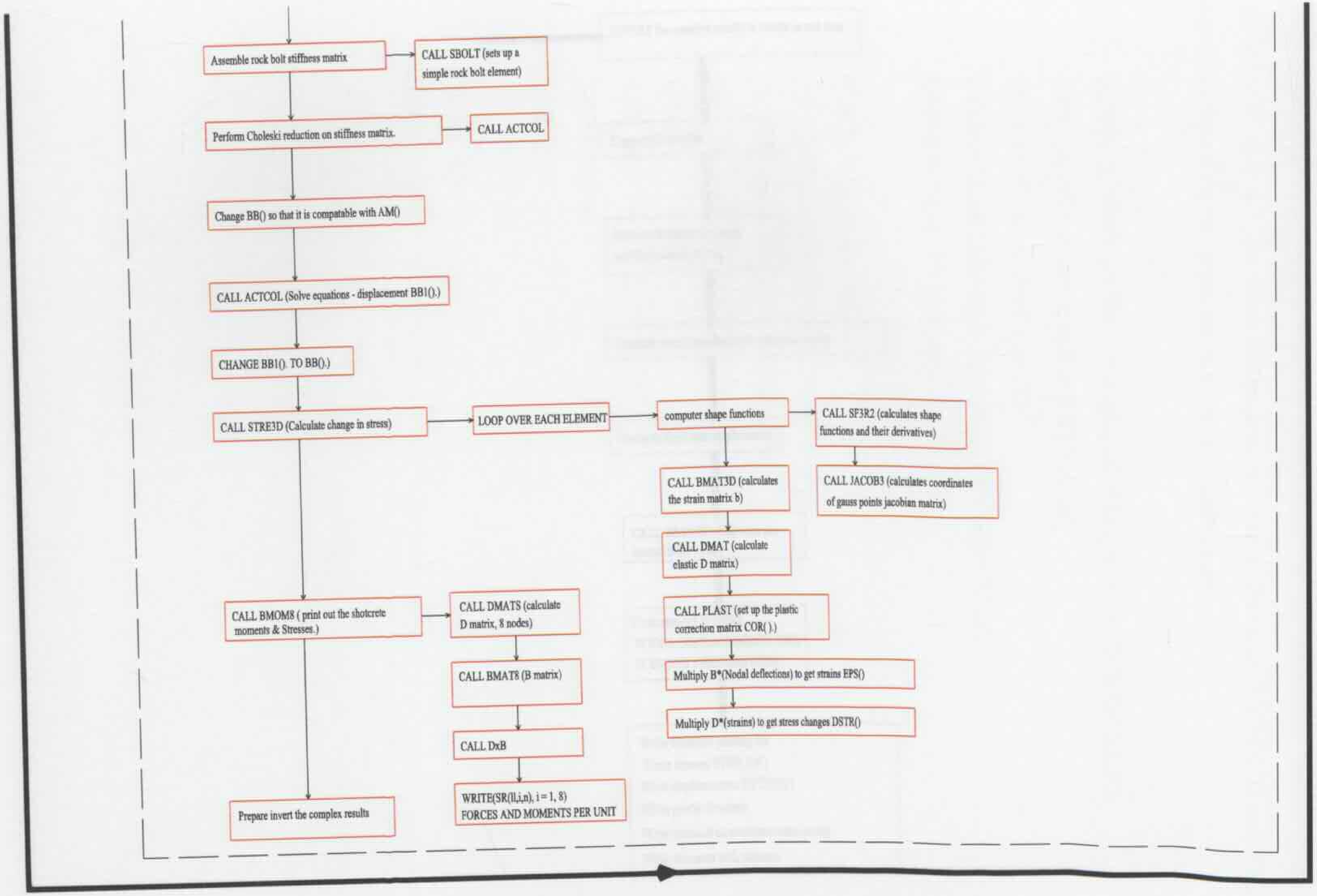

Figure 5B.4: Creep analysis flow chart - part two B.

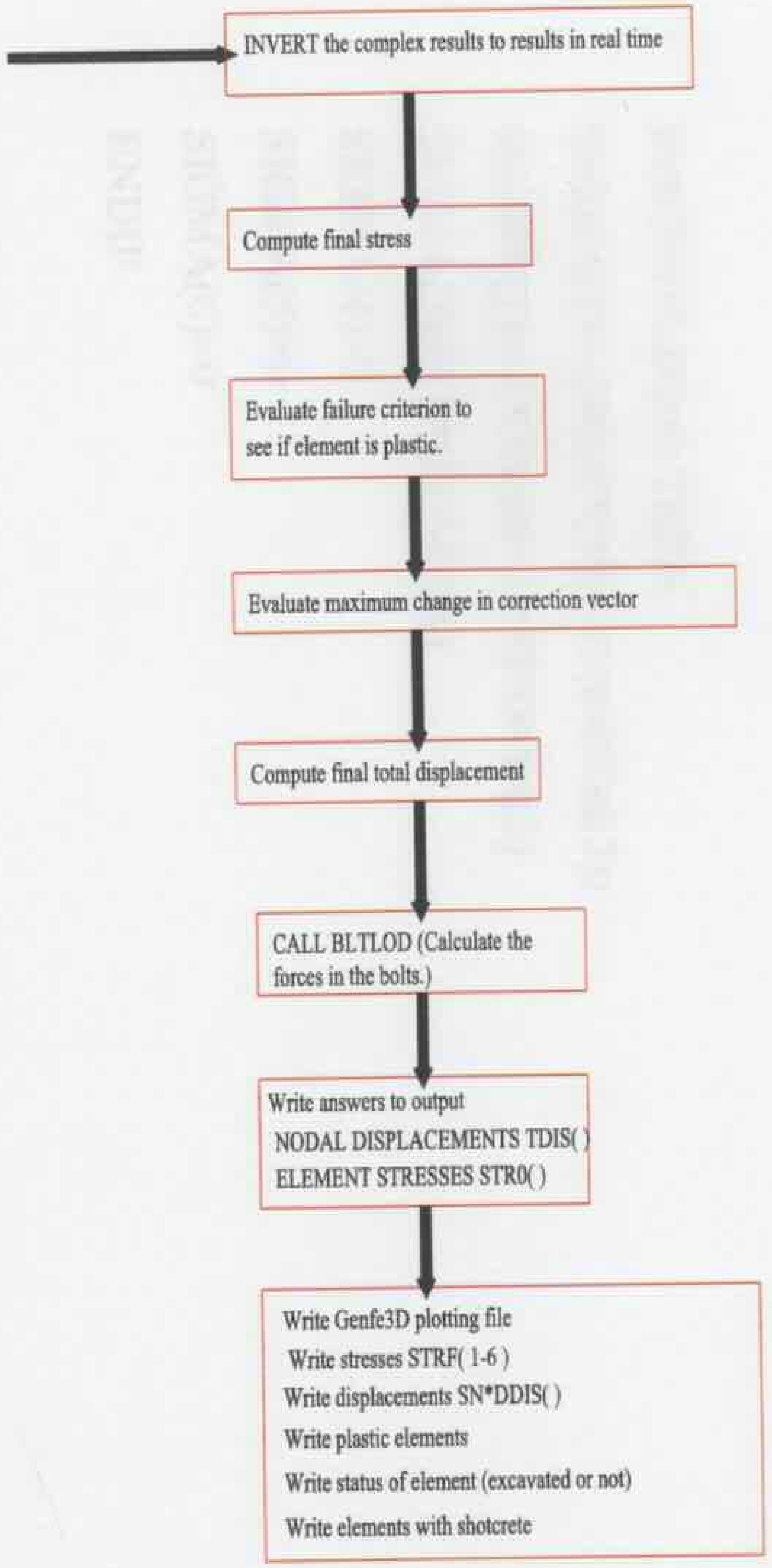

Figure 5B.5: Creep analysis flow chart - part three.

APPENDIX 5C SUBROUTINE TO GENERATE INITIAL STRESS IN ABAQUS

The subroutine is to generate initial stress field for the ABAQUS tunnel model. The SIGMA(2) represent the stress component in vertical direction, SIGMA(1) and SIGMA(3) represent the stress components in horizontal directions.

```
SUBROUTINE SIGINI(SIGMA,COORDS,NTENS,NCRDS,NOEL,
NPT,LAYER, KSPT,LREBAR,REBARN)
INCLUDE 'ABA_PARAM.INC'
DIMENSION SIGMA(NTENS),COORDS(NCRDS)
CHARACTER*80 REBARN

IF(NTENS.EQ.6) THEN
SIGMA(2)=-24000*(90.0-COORDS(2))
SIGMA(1)=-1500000+1.2*SIGMA(2)
SIGMA(3)=0.5*SIGMA(1)
SIGMA(4)=0
SIGMA(5)=0
SIGMA(6)=0
ENDIF

RETURN
END
```

CHAPTER 6 - CASE STUDY - CIRCULAR TUNNEL

6.1 INTRODUCTION

Tunnels have different cross sectional shapes which typically relate to the function of the tunnels, the methods of construction and the ground situations in which they were constructed. A circular tunnel section is a typical traditional shaped tunnel section and has been widely used in practice. Due to the characteristics of the cross-section, the circular tunnel has many advantages. The distributed stress in the circular tunnel is more even and it usually has smaller internal forces compared with other tunnel shapes. The circular section can be excavated with simpler equipment compared with the equipment used for other specific shaped tunnels and it is also easier to control the progressing axis during construction.

6.2 NUMERICAL TUNNEL MODELS

Some parametric solutions for circular tunnels supported by shotcrete linings were obtained to investigate the time-dependent behaviour of these tunnels. The tunnels were excavated at different depths and under different ground conditions, and a macro-synthetic fibre reinforced shotcrete was used for the lining.

6.2.1 TUNNEL MODEL MESH

A tunnel section is symmetrical and so only half of the section was modelled to reduce the mesh size. Circular tunnels of 6 meters diameter were assumed to be constructed at 10 meters depth (ZTT10), 30 meters depth (ZTT30) and 80 meters depth (ZTT80) respectively in a sandstone rock which creeps according to Pellet's (2000) data. ZTT30a modelled the circular tunnel at 30m depth in the 'soft' rock, while ZTT30b represented a tunnel excavated in shale at 30m depth. The cross-sections of the tunnel models constructed at 10m and 30m depth are shown in Figures 6.1a&b. The 80m deep tunnel uses the same mesh as the tunnel excavated at 30m depth, and the 50m of rock above the mesh was transferred as a pressure load applied to the top ground surface of the model (Figure 6.1c).

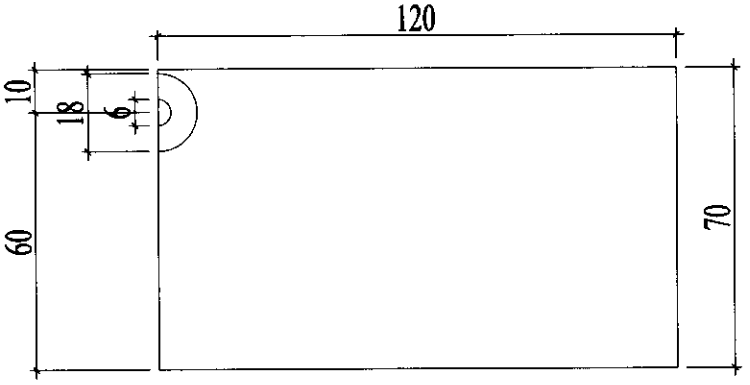

Figure 6.1a: Cross-section of tunnel model at 10m depth (unit: m).

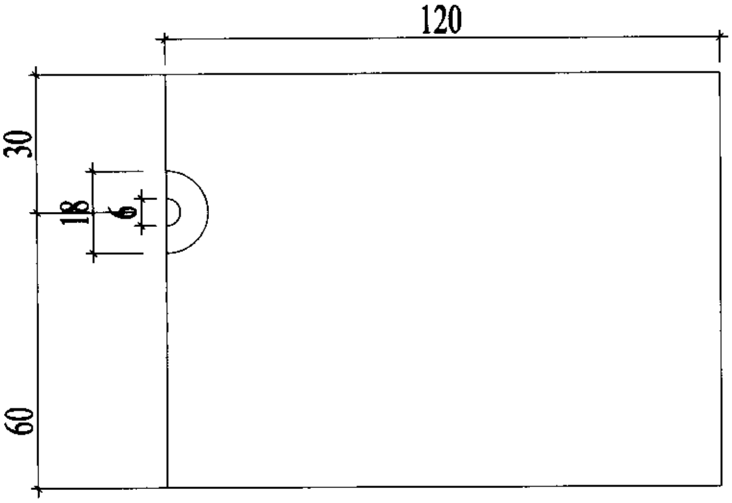

Figure 6.1b: Cross-section of tunnel model at 30m depth (unit: m).

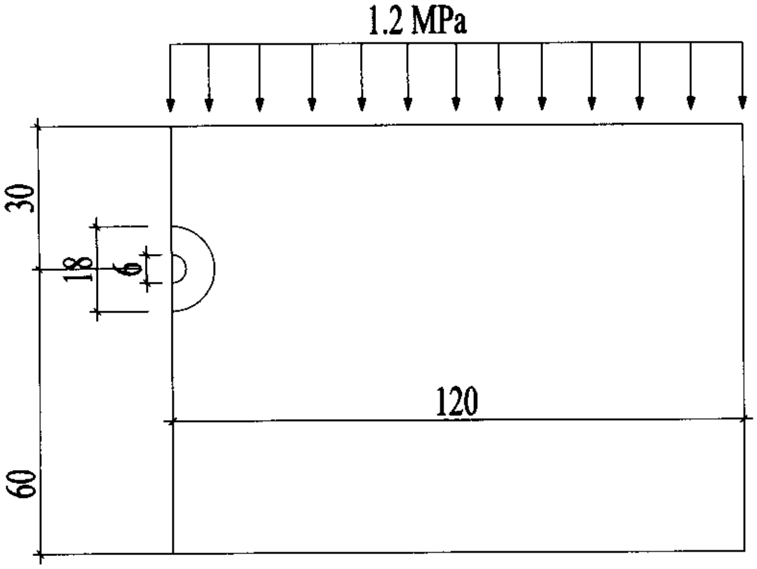

Figure 6.1c: Cross-section of tunnel model at 80m depth (unit: m).

The horizontal length of the tunnel was set as 60m (10 times the tunnel's diameter) and the tunnel mesh was divided in 10 even partitions in the tunnel horizontal axial direction so that the tunnel deformation in the middle section would not be affected significantly by the face boundary restraints. The results show that the displacements and stresses in the middle sections are smooth and do not vary much along the longitudinal direction, which indicates that the longitudinal length of the model is sufficient to avoid the boundary effects. The finite element meshes generated for SAFEA are shown in Figures 6.2a &b.

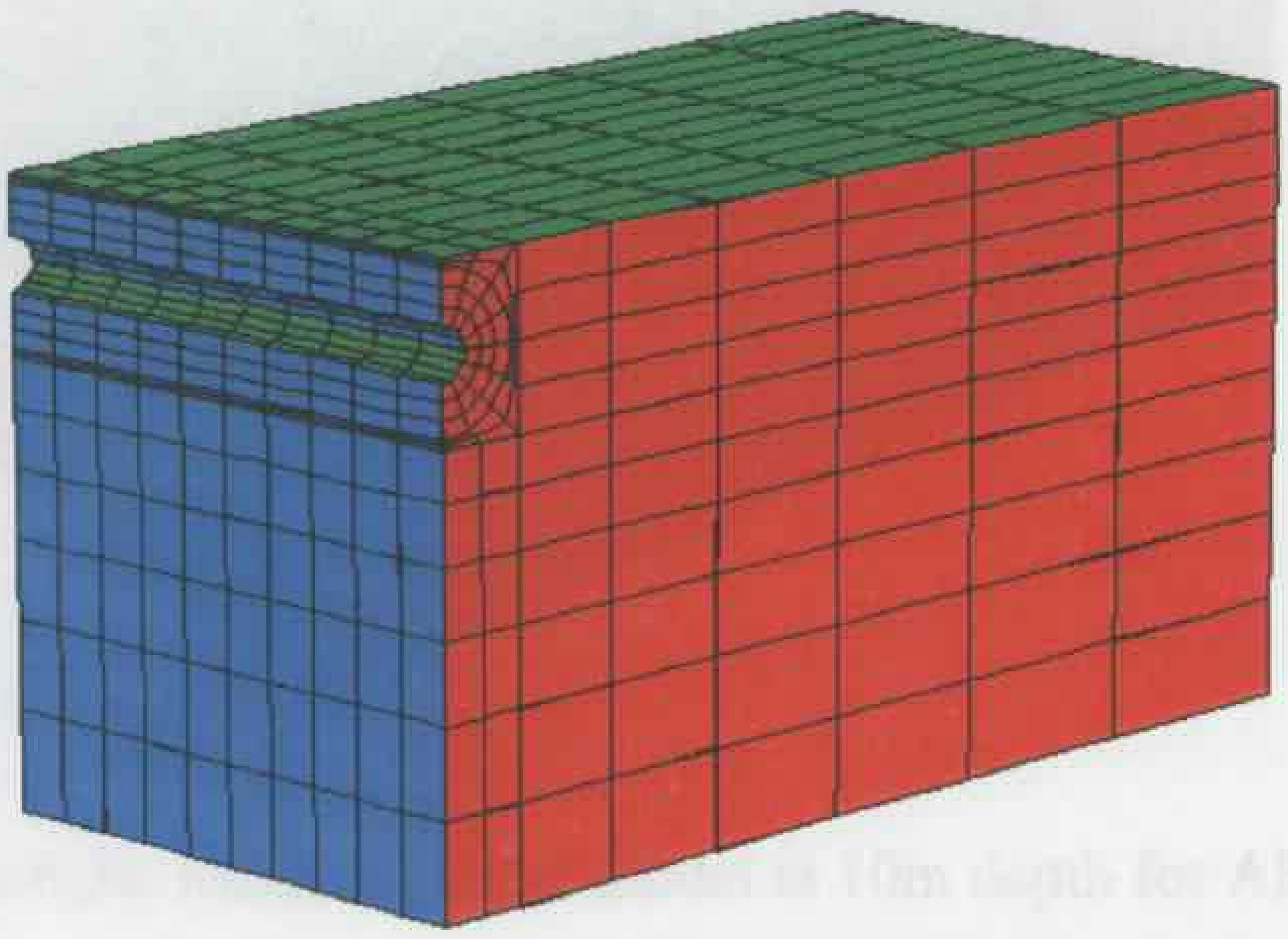

Figure 6.2a: Mesh of tunnel model at 10m depth for SAFEA.

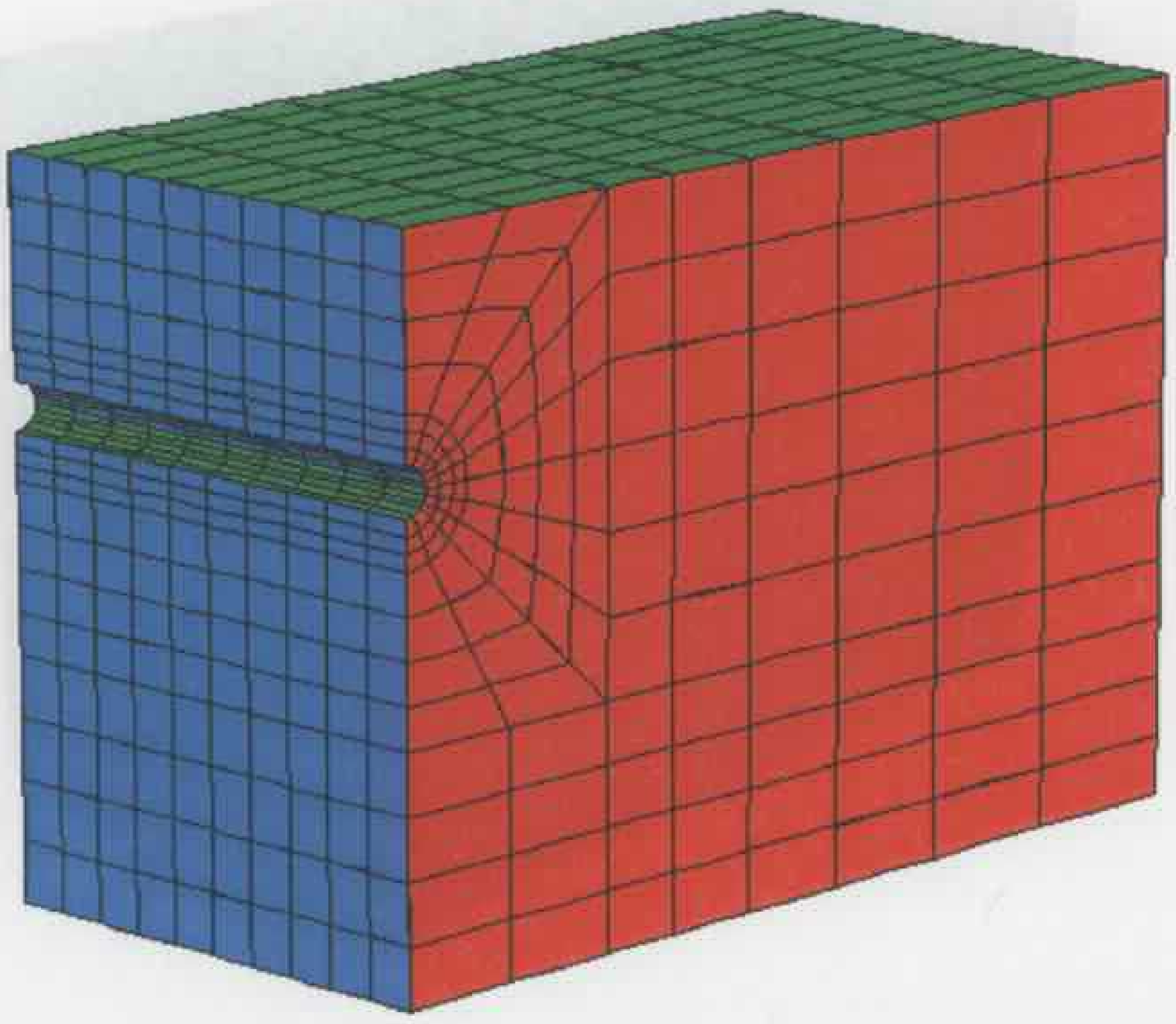

Figure 6.2b: Mesh of tunnel model at 30m & 80m depths for SAFEA.

Similar circular tunnel models were also built up in ABAQUS as shown in Figures 6.3a &b. The shotcrete lining was applied to the whole circumference of the tunnel section, and the shell mesh is shown in Figure 6.4.

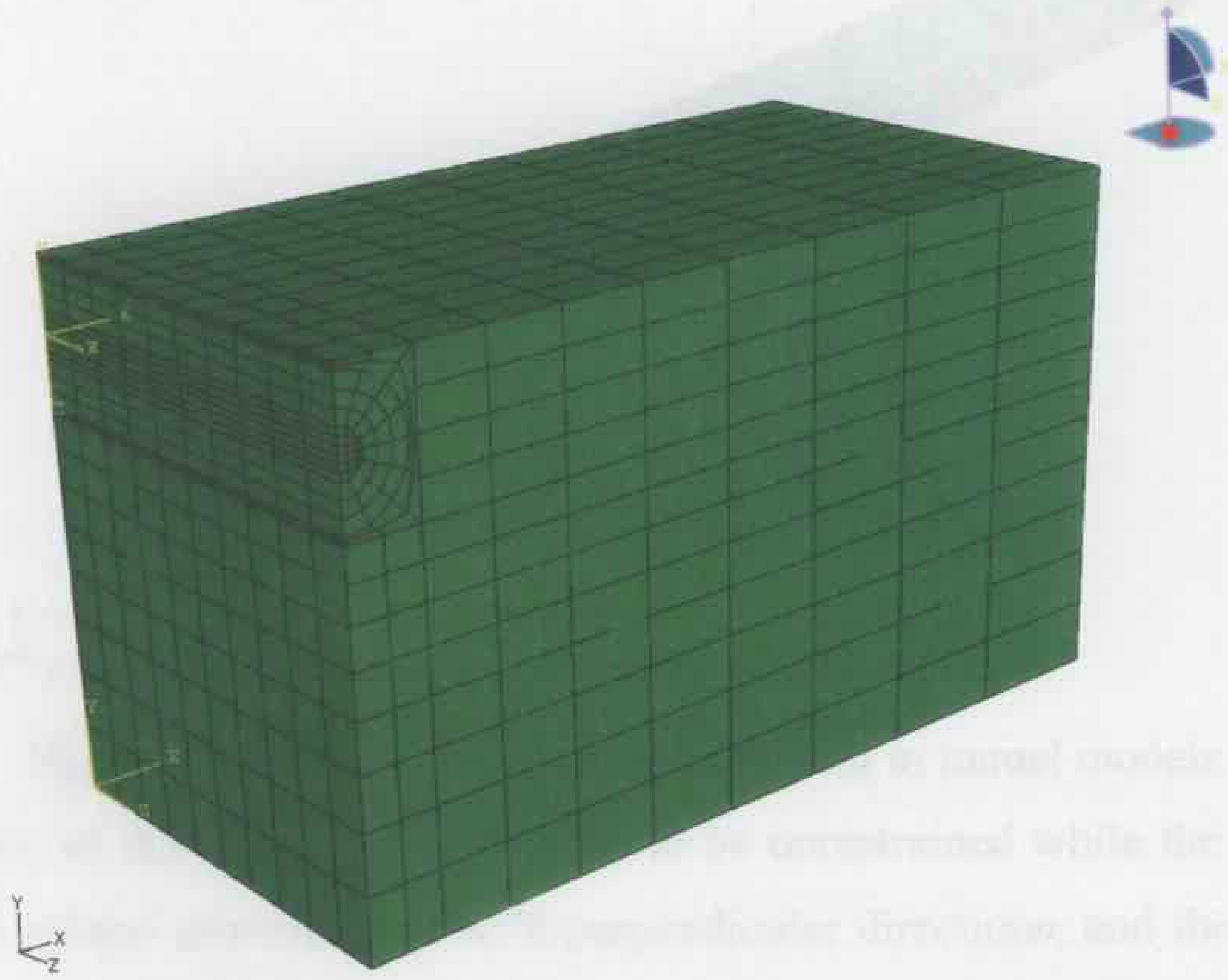

Figure 6.3a: Mesh of tunnel model at 10m depth for ABAQUS.

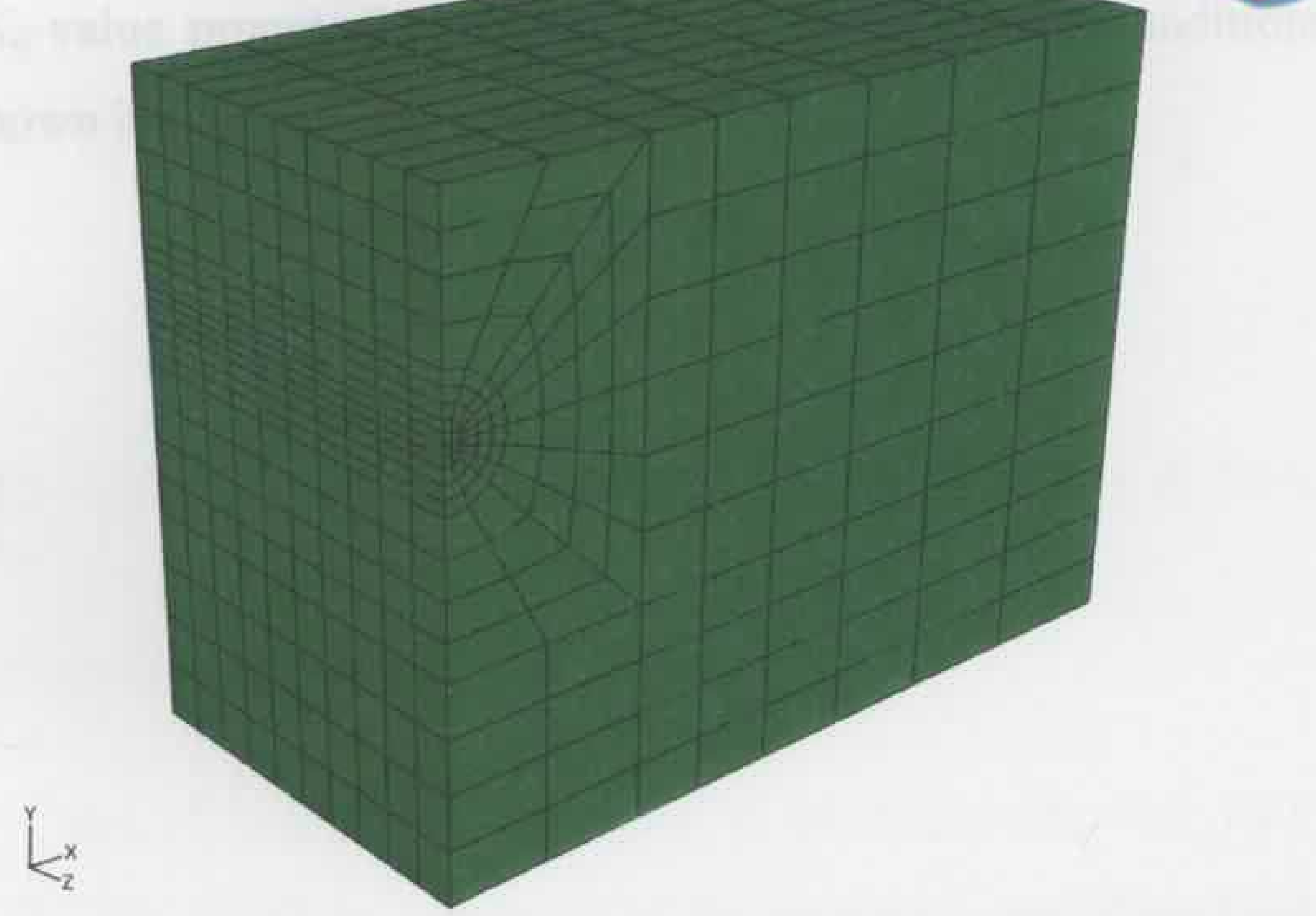

Figure 6.3b: Mesh of tunnel model at 30m & 80m depths for ABAQUS.

Figure 6.4: Shell mesh for shotcrete lining in tunnel models.

The top surface of the tunnel model was set to be unrestrained while the base and sides are restrained against movement in both perpendicular directions, and the self weight of the rock mass was 24000N/m^3. The initial stress field was generated using Equation 6.1 by a subroutine similar to the one in Appendix 5C. The stress filed calculated using Equation 6.1 is based on previous experience (Pells, 2002) and is typical for the Sydney area. The stress values calculated by the equations are imposed on the model directly and the normal K_0-value process is not used here. The boundary conditions of the tunnel models are shown in Figures 6.5a &b.

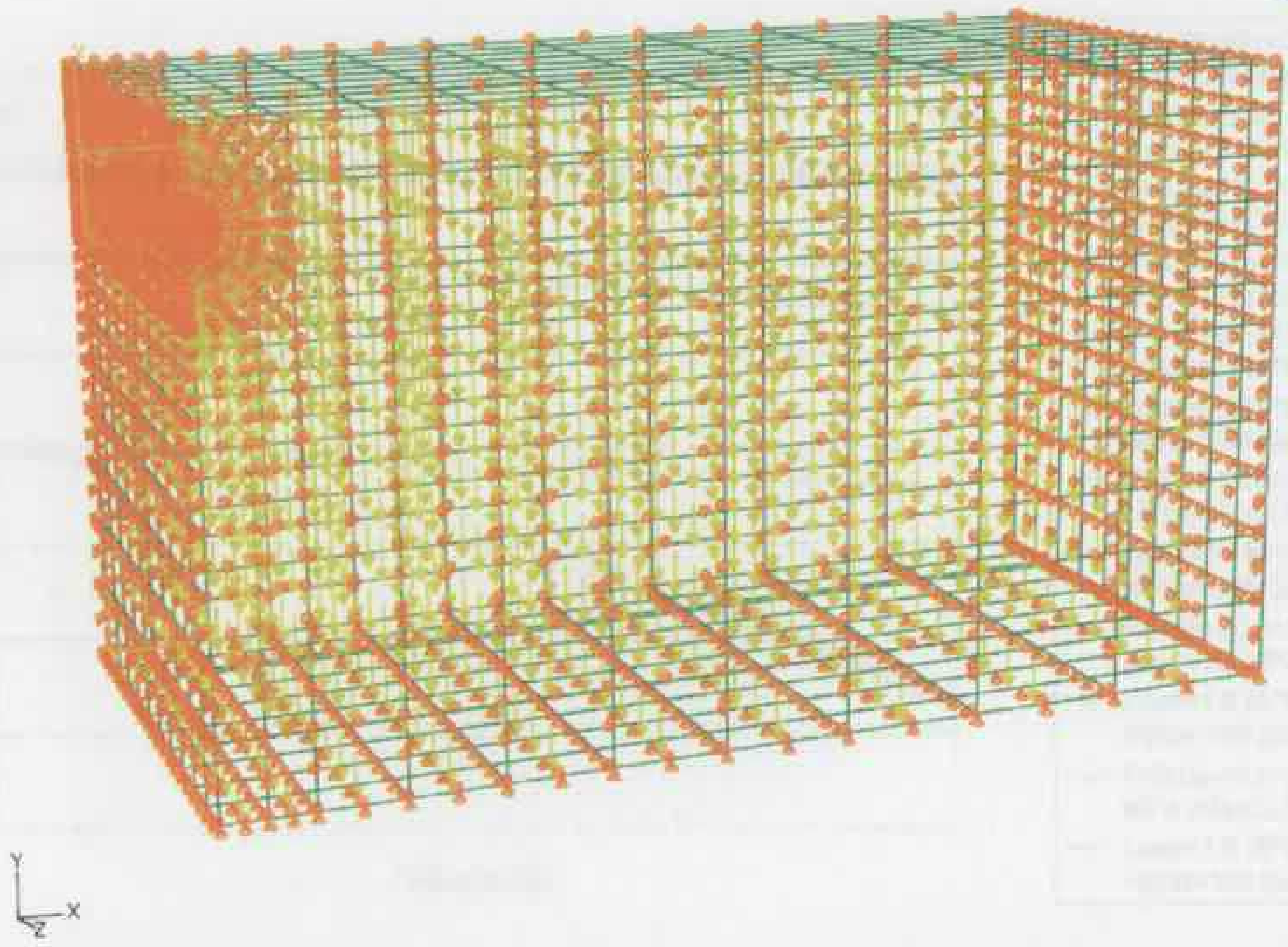

Figure 6.5a: Boundary conditions of tunnel model at 10m depth.

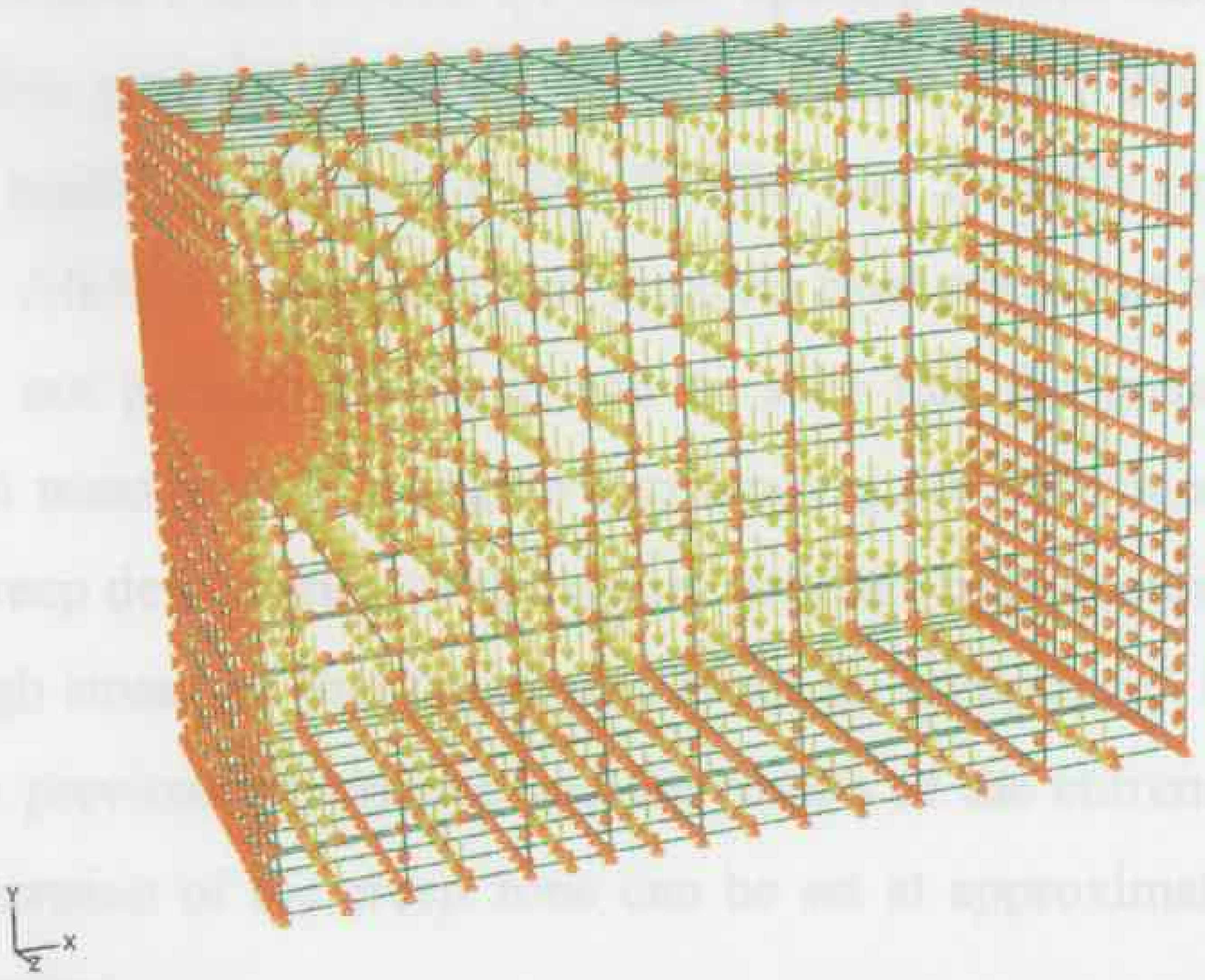

Figure 6.5b: Boundary conditions of tunnel model at 30m & 80m depths.

6.2.2 MATERIAL PROPERTIES

The circular tunnel excavation was modelled in sandstone (ZTT10, ZTT30 and ZTT80) and shale (ZTT30b), the creep behaviour of the sandstone and shale have been presented in Chapters 4.4 & 4.5. To examine the creep behaviour of tunnels in 'soft' rock (ZTT30a), a set of parameters (F=3.0e-19, n=2.2, m=-0.9) was selected for a fictional rock which creeps faster than the sandstone as shown in Figure 6.6. The experimental pressure loads applied to the specimens are also listed in the Figure.

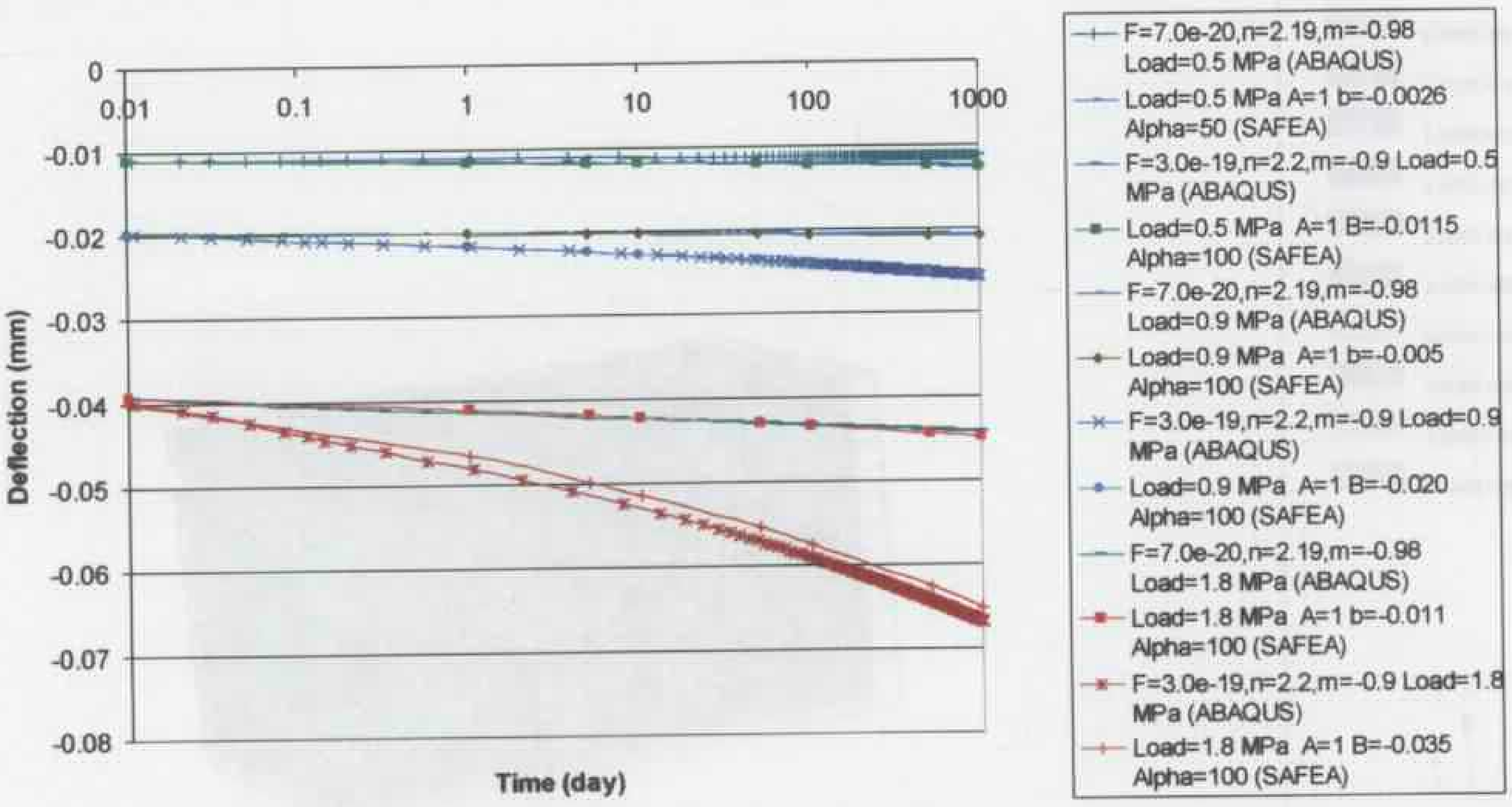

Figure 6.6: Numerical fit of creep behaviour of 'soft' rock.

The changing of deviator stress around the tunnel opening section can be obtained during the tunnel excavation process. Figures 6.7a, 6.7b & 6.7c show the change in deviator stress around the tunnel sections (ZTT10, ZTT30 and ZTT80) obtained by SAFEA respectively, while ABAQUS can only plot the total final stress but not the increment of the stress, so it is not presented here. It can be seen that the generated increment of deviator stress is a maximum in a region surrounding the excavated section, and it is assumed that the creep deformation of the tunnel structure only occurs when the tunnel is under a high enough stress, so that this region is set as 'creep zone' in the tunnel model (Figure 6.8). From previous experience and the results of the current study, it has been found that the dimension of the creep zone can be set at approximately three times the diameter of the opening.

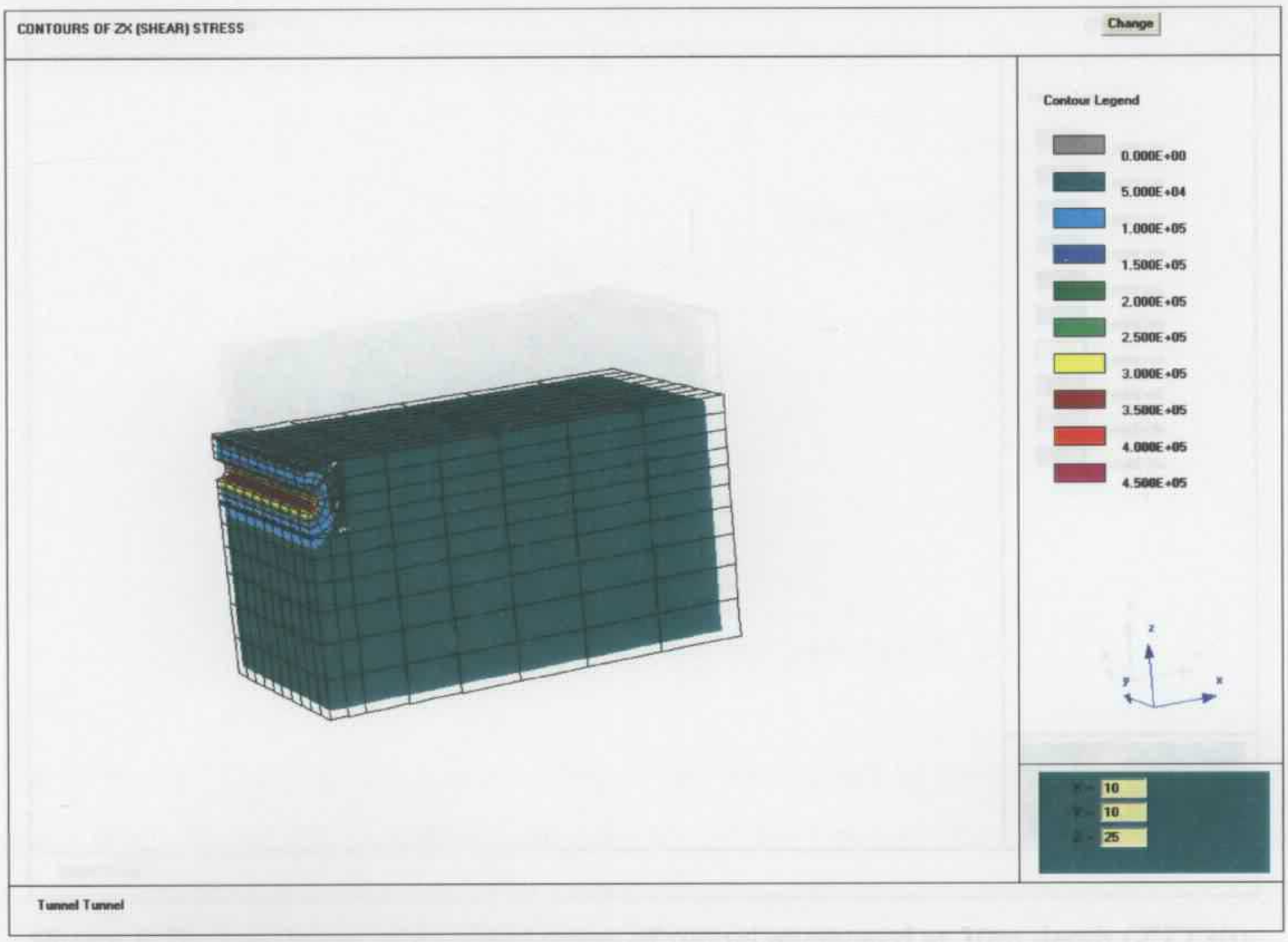

Figure 6.7a: Increment of deviator stress of tunnel excavated at 10m depth (ZTT10).

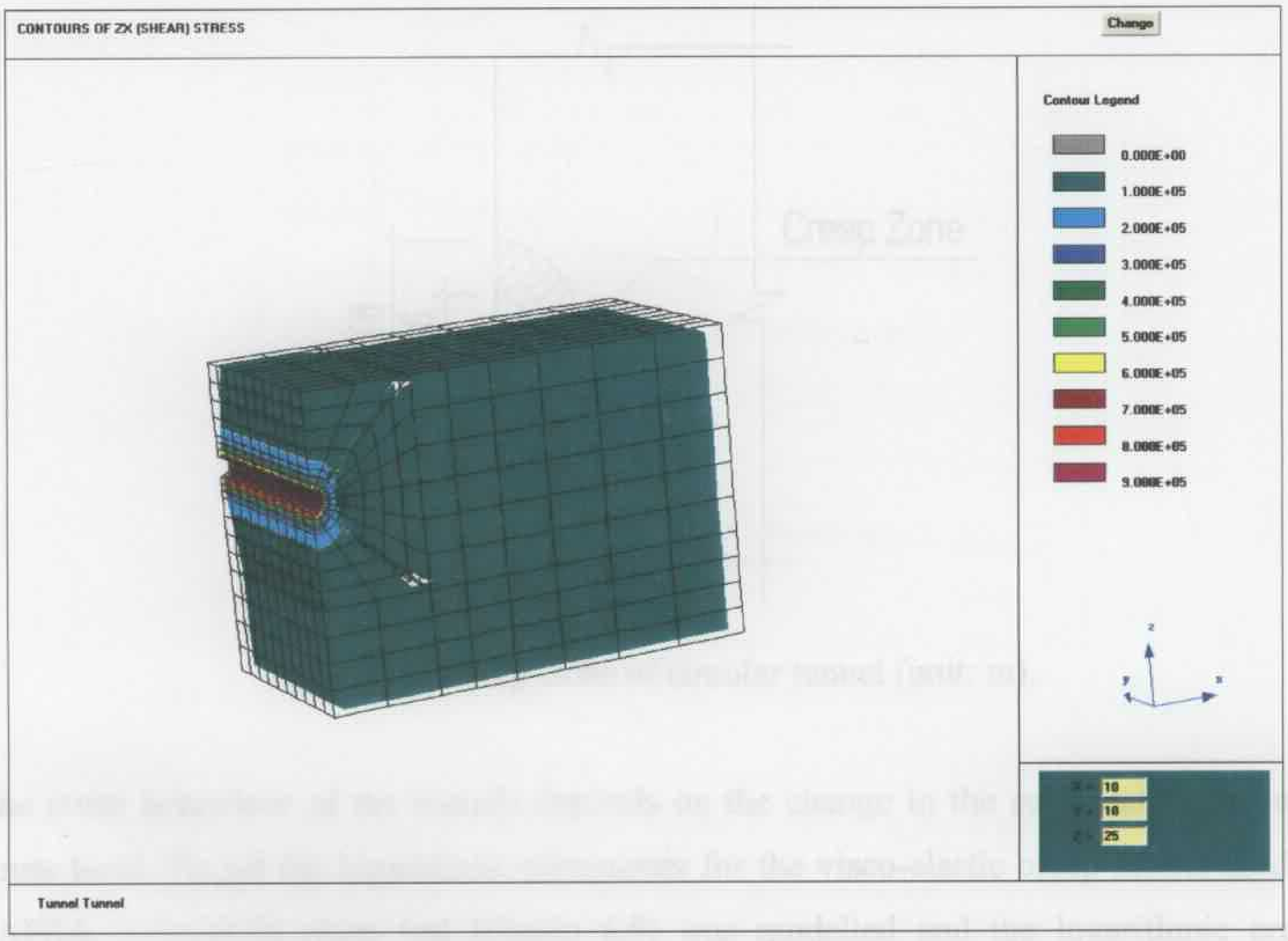

X = 10
Y = 10
Z = 25

Figure 6.7b: Increment of deviator stress of tunnel excavated at 30m depth (ZTT30).

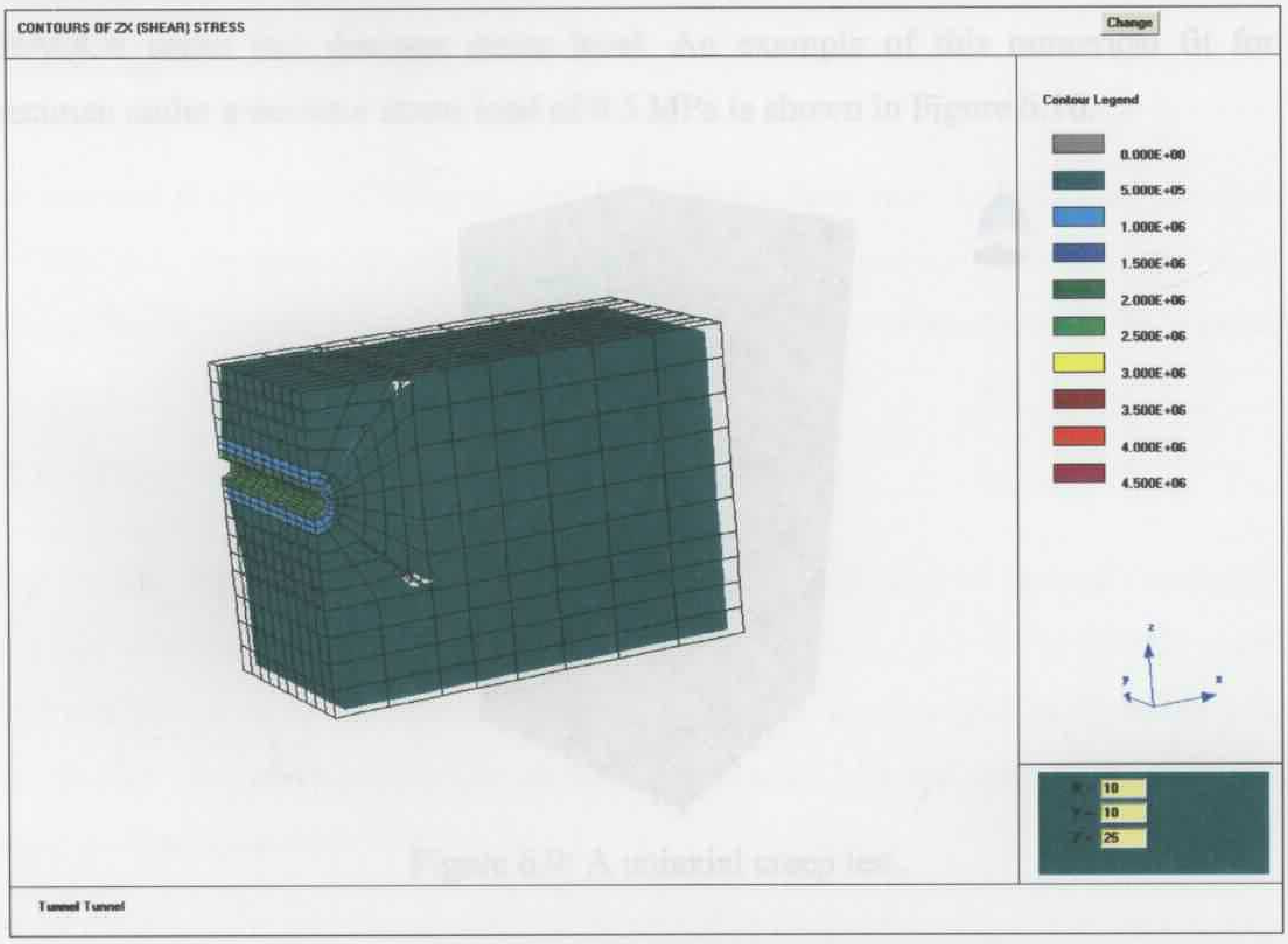

X = 10
Y = 10
Z = 25

Figure 6.7c: Increment of deviator stress of tunnel excavated at 80m depth (ZTT80).

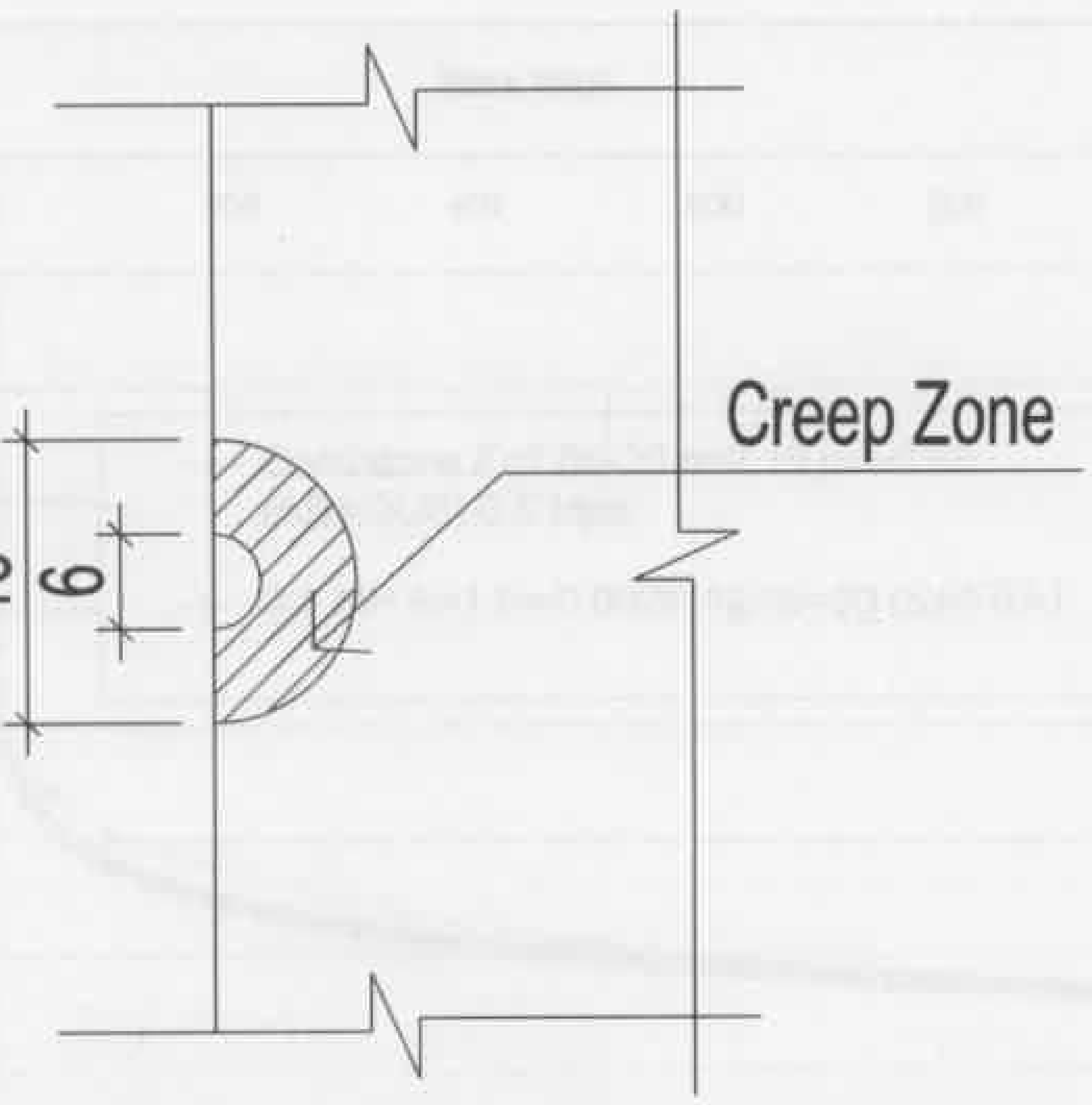

Figure 6.8: Creep Zone of circular tunnel (unit: m).

The creep behaviour of the tunnels depends on the change in the surrounding deviator stress level. To get the logarithmic parameters for the visco-elastic creep model used in SAFEA, a uniaxial creep test (Figure 6.9) was modelled and the logarithmic creep parameters for SAFEA were selected to fit the specimens' deflection curve obtained by ABAQUS under this deviator stress level. An example of this numerical fit for the specimen under a deviator stress load of 0.5 MPa is shown in Figure 6.10.

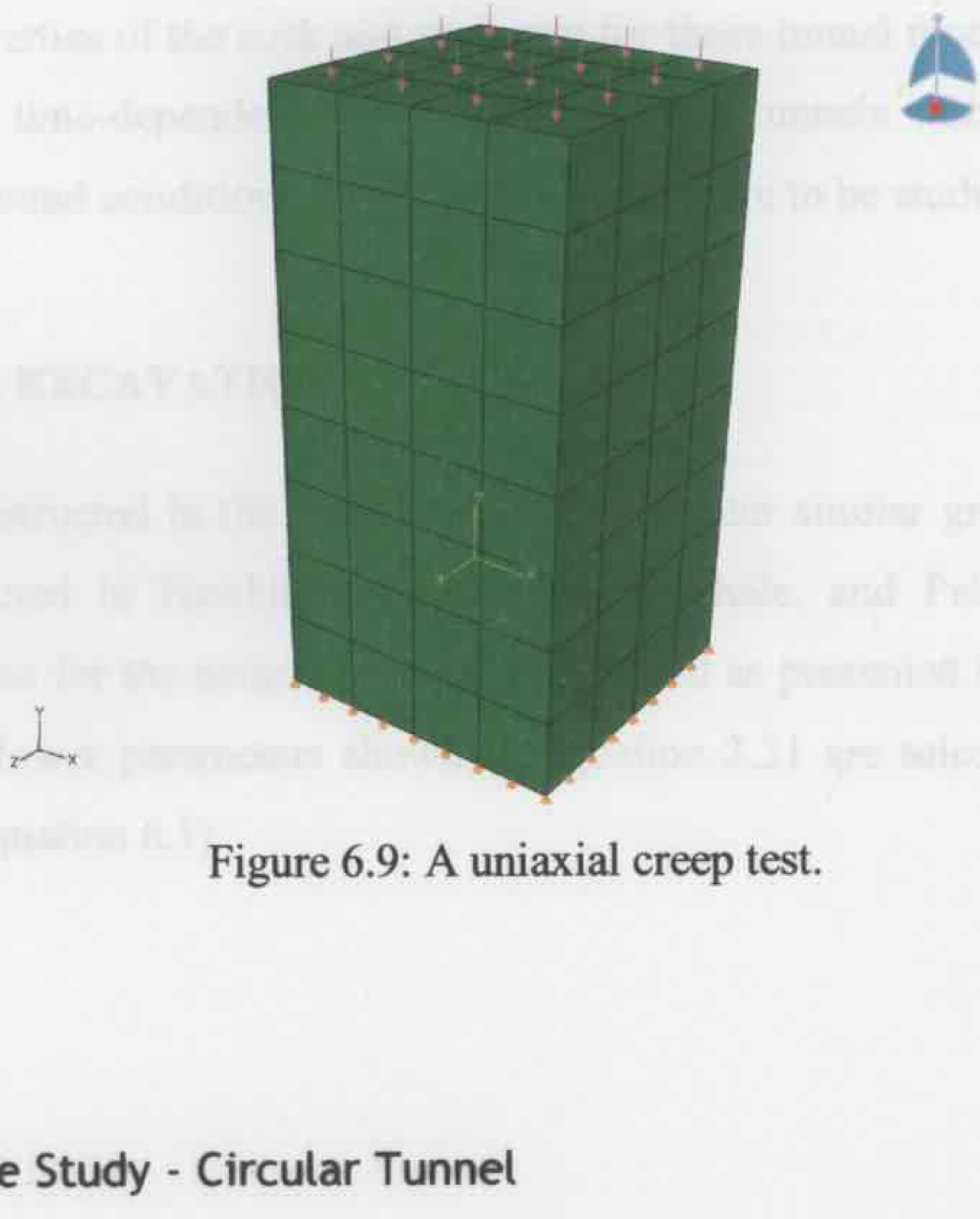

Figure 6.9: A uniaxial creep test.

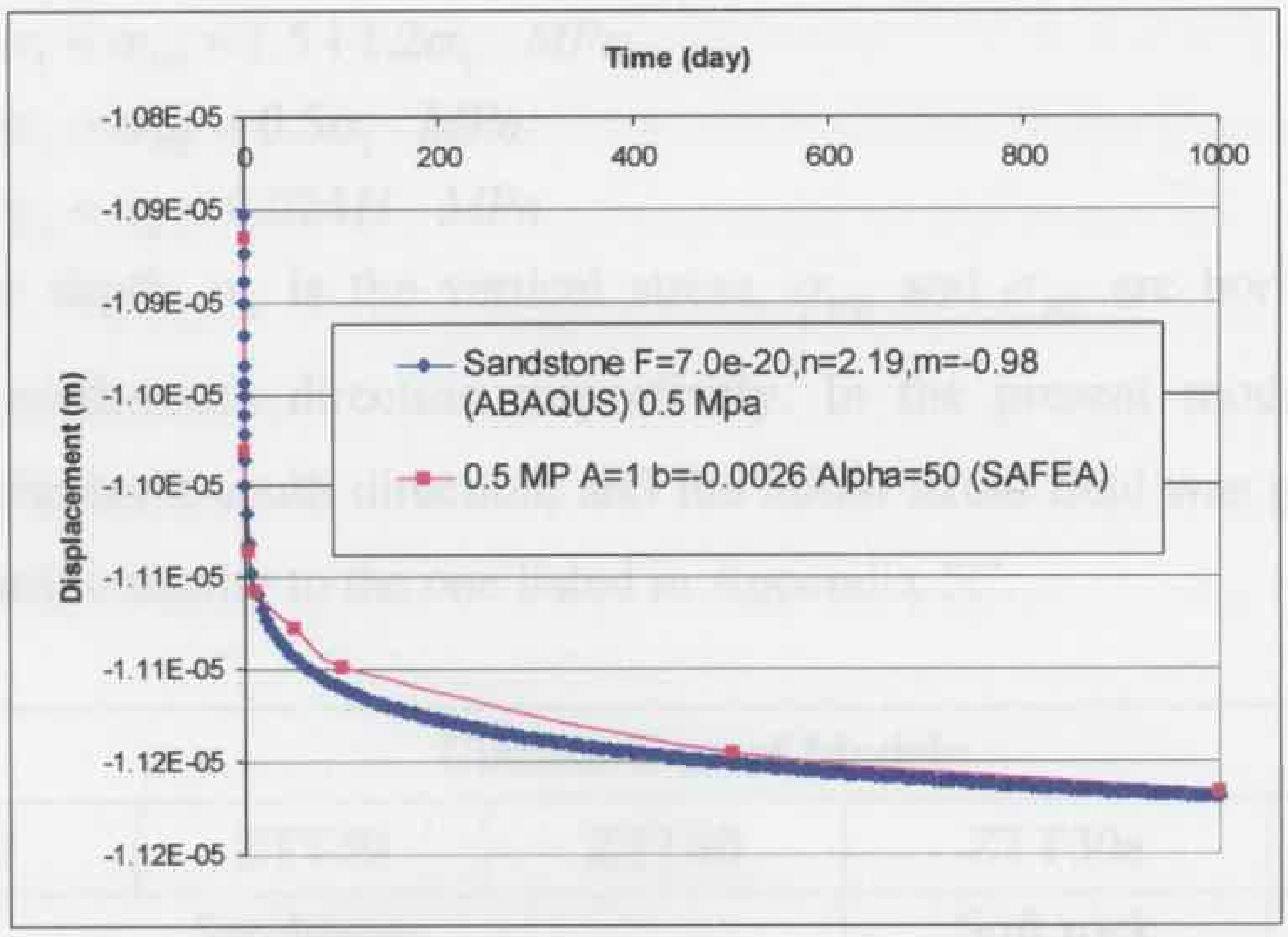

Figure 6.10: Numerical fit for creep test under a stress load of 0.5 MPa.

A macro-synthetic HPP fibre reinforced shotcrete (FRS) has been assumed as the lining in these circular tunnel models. The creep behaviour of this FRS under compression has been presented in Chapter 4.3. The creep parameters of HPP FRS for the logarithmic creep model used in SAFEA are selected to fit the uniaxial creep test deflection curve under the appropriate stress level.

The material properties of the rock and shotcrete for these tunnel models are summarized in Table 6.1, the time-dependent behaviour of circular tunnels with the same size but under different ground conditions (depth and materials) are to be studied in the research.

6.2.3 TUNNEL EXCAVATION

Most tunnels constructed in the Sydney region encounter similar ground conditions, as they are constructed in Hawkesbury sandstone or shale, and Pells (2002) provided empirical equations for the natural regional stress field as presented in Equation 2.21. In this chapter, the lower parameters shown in Equation 2.21 are selected for the circular tunnel models (Equation 6.1).

$$\begin{aligned}\sigma_1 &= \sigma_{NS} = 1.5 + 1.2\sigma_v \quad MPa \\ \sigma_2 &= \sigma_{WE} = 0.5\sigma_1 \quad MPa \\ \sigma_3 &= \sigma_v = 0.024H \quad MPa\end{aligned} \tag{6.1}$$

where H is the depth, σ_v is the vertical stress, σ_{WE} and σ_{NS} are horizontal stress in west-east and north-south direction respectively. In the present models, tunnels are constructed in the north-south direction, and the initial stress field was generated with a modified subroutine similar to the one listed in Appendix 5C.

	Circular Tunnel Models				
	ZTT10	ZTT30	ZTT80	ZTT30a	ZTT30b
Rock	Sandstone E = 4.976e9 Pa ν = 0.3			Soft rock E = 4.976e9 Pa ν = 0.3	Shale E = 1.655e9 Pa ν = 0.3
Creep parameters	F=7.0e-20 n=2.19 m=-0.98 (ABAQUS)			F=3.0e-19 n=2.2 m=-0.9 (ABAQUS)	F=2.5e-18 n=2.19 m=-0.98 (ABAQUS)
	σ = 0.25 MPa A=1 B=-0.0014 α=50 (SAFEA)	σ = 0.5 MPa A=1 B=-0.0026 α=50 (SAFEA)	σ = 1.0 MPa A=1 B=-0.0057 α=50 (SAFEA)	σ = 0.5 MPa A=1 B=-0.0115 α=100 (SAFEA)	σ = 0.65 MPa A=1 B=-0.028 α=100 (SAFEA)
Shotcrete	HPP Fibre E = 3.610e9 Pa ν = 0.15 Thickness=0.2m				
Creep parameters	F=4.0e-37, n=4.6, m=-0.6 (ABAQUS)				
	σ = 0.35 MPa A=1 B=-0.00001 α=1 (SAFEA)	σ = 0.9 MPa A=1 B=-0.00003 α=0.1 (SAFEA)	σ = 2.5 MPa A=1 B=-0.0013 α=0.1 (SAFEA)	σ = 0.9 MPa A=1 B=-0.00003 α=0.1 (SAFEA)	σ = 1.5 MPa A=1 B=-0.0002 α=0.1 (SAFEA)

Table 6.1: Material properties of tunnel models.

Before simulating the excavation step, the initial stress field was generated according to Equation 6.1 and the initial deformation was reset to zero. In the numerical excavation analysis, the shotcrete lining was set as inactivated at the initial step, and the tunnel excavation was simulated by removing the rock elements and activating the lining elements at the corresponding positions in the following step. In these models, a simplified excavation process was used by removing the whole tunnel section rock in one step, since the emphasis of this research is to study the long-term creep behaviour of the tunnel.

Due to the excavation, the instantaneous deformation of the ground is a maximum around the opening section in the vertical direction. An example of the deformation of the circular tunnel at 10m depth (ZTT10) is shown in Figure 6.11, and the deformation scale factor is set as 5000 to make the deformation identifiable. It can be seen that the top section is moving down, while the bottom section is moving up after excavation.

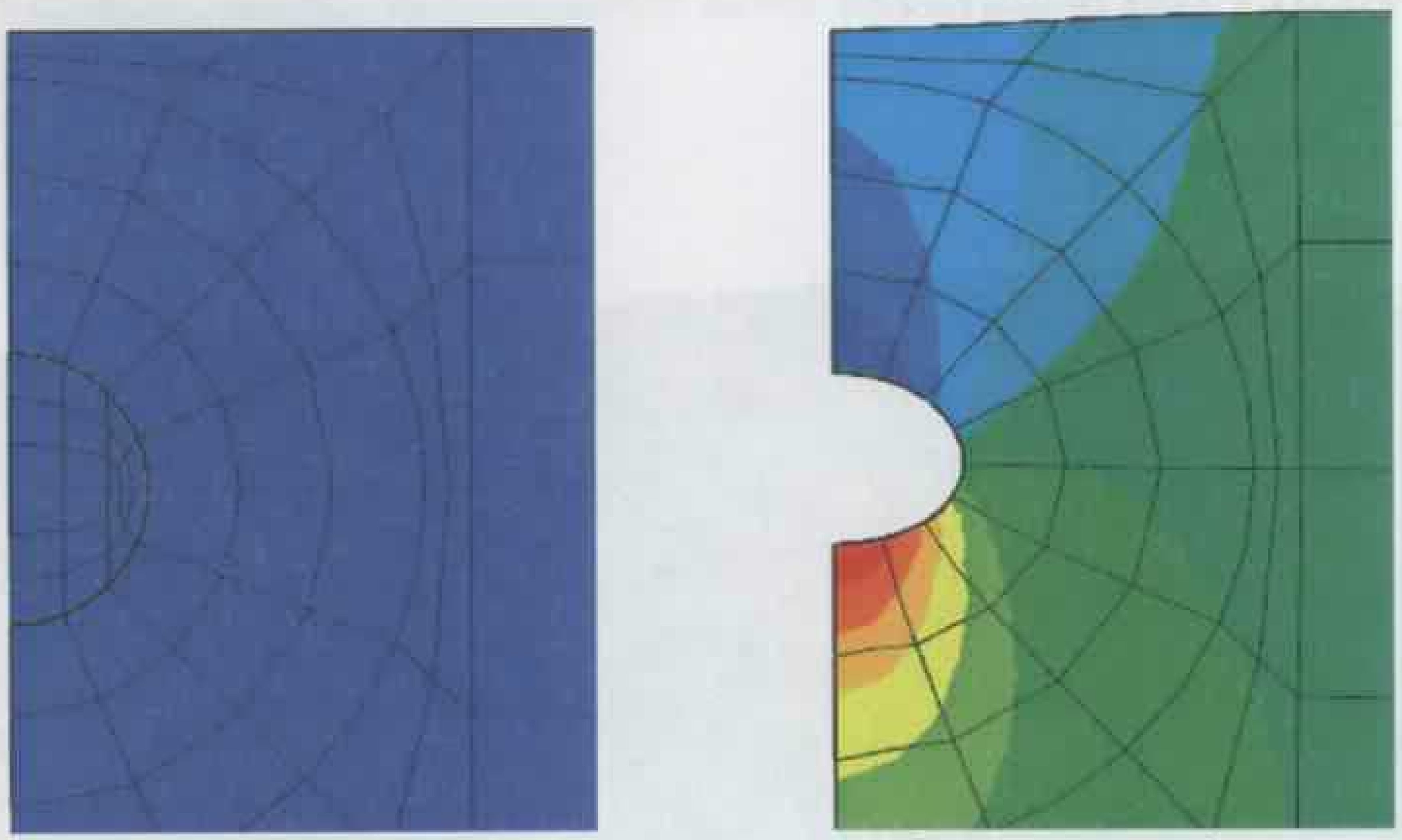

Before Excavation After Excavation

Figure 6.11: Tunnel deformation after excavation.

An example of the vertical deformation of the tunnel models (ZTT10) at 10m depth are shown in Figures 6.12a & 6.12b.

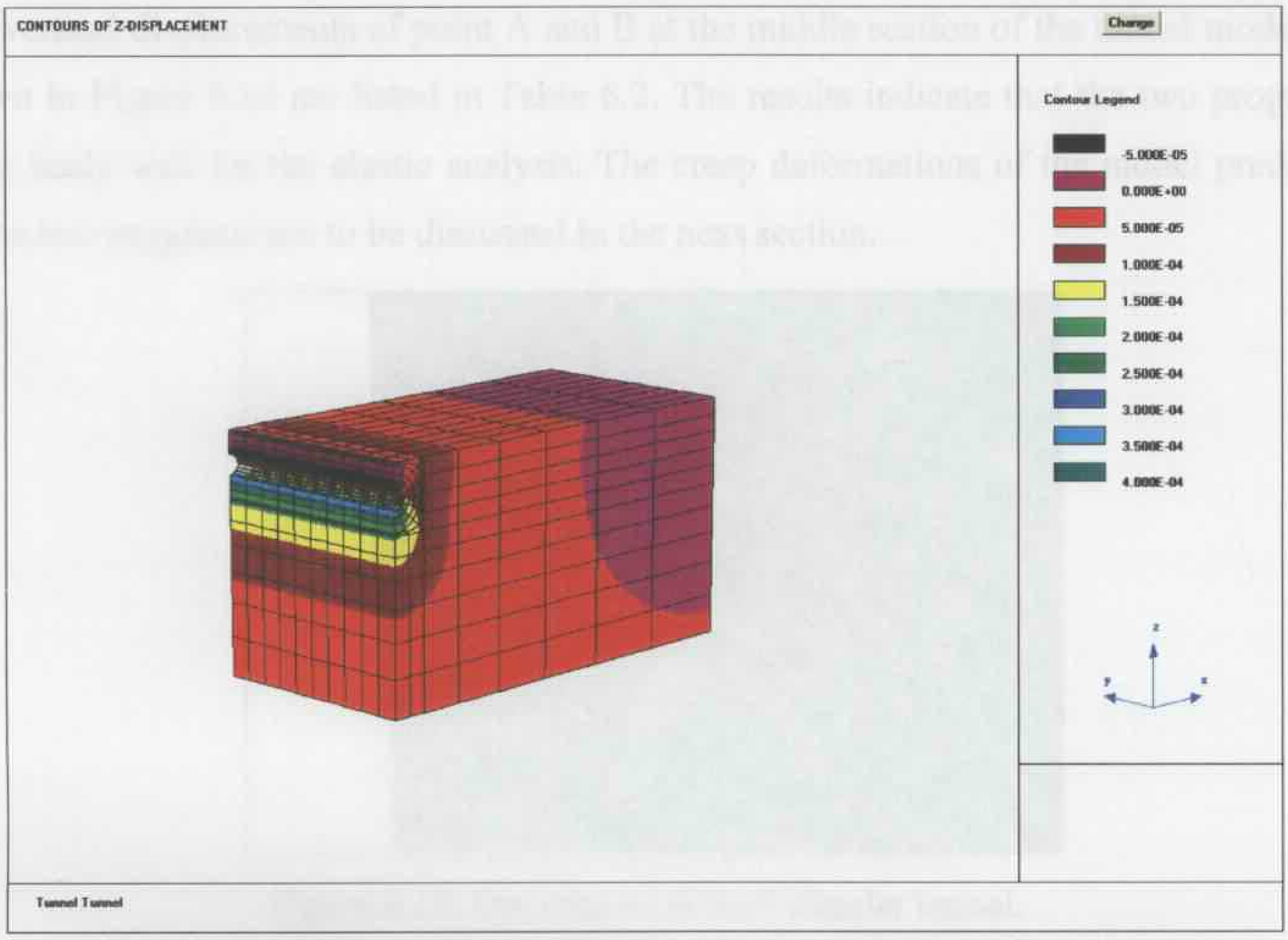

Figure 6.12a: Vertical tunnel deformation after excavation (ZTT10 by SAFEA).

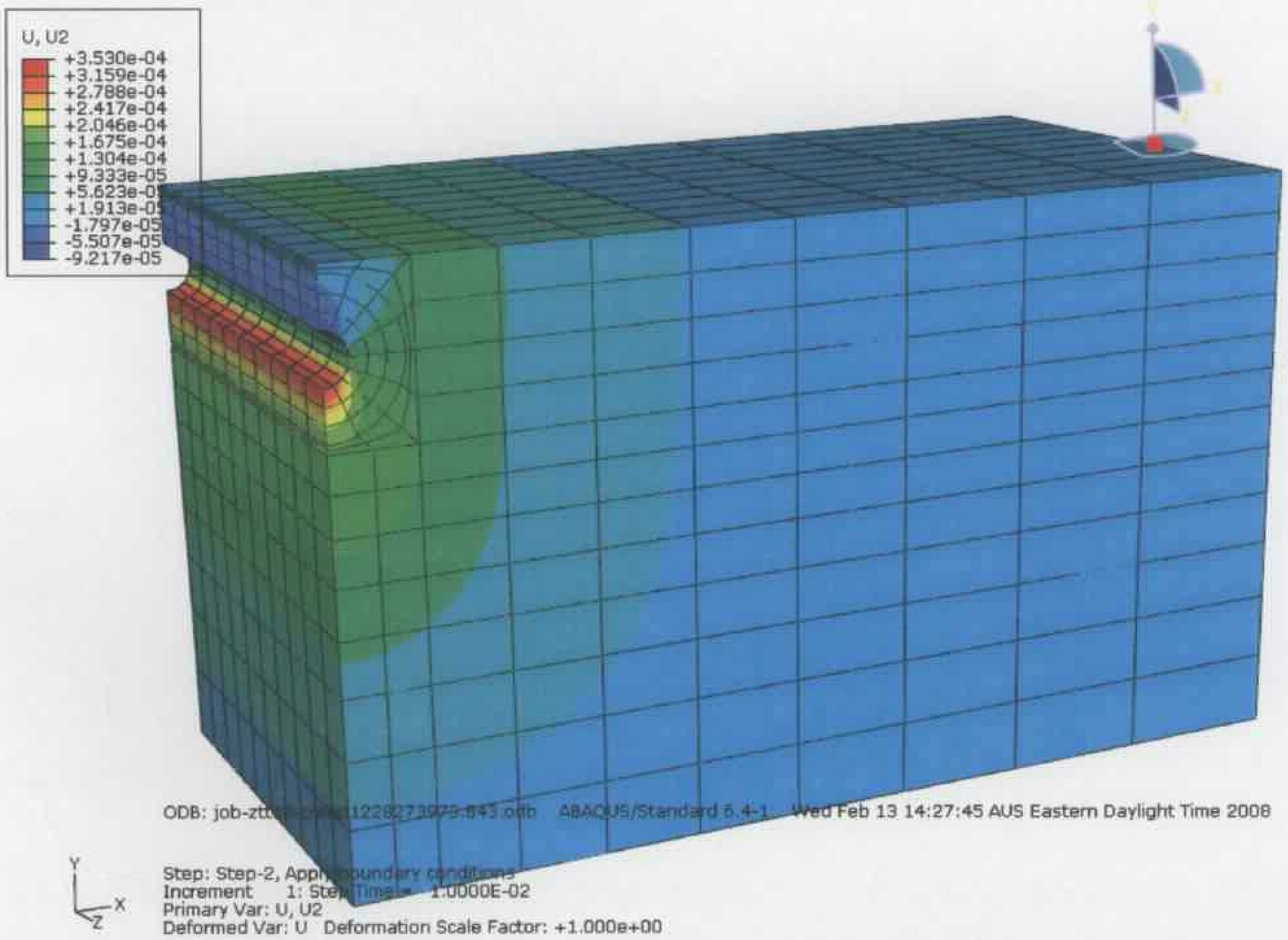

Figure 6.12b: Vertical tunnel deformation after excavation (ZTT10 by ABAQUS).

The vertical displacements of point A and B at the middle section of the tunnel models as shown in Figure 6.13 are listed in Table 6.2. The results indicate that the two programs agree fairly well for the elastic analysis. The creep deformations of the model predicted by the two programs are to be discussed in the next section.

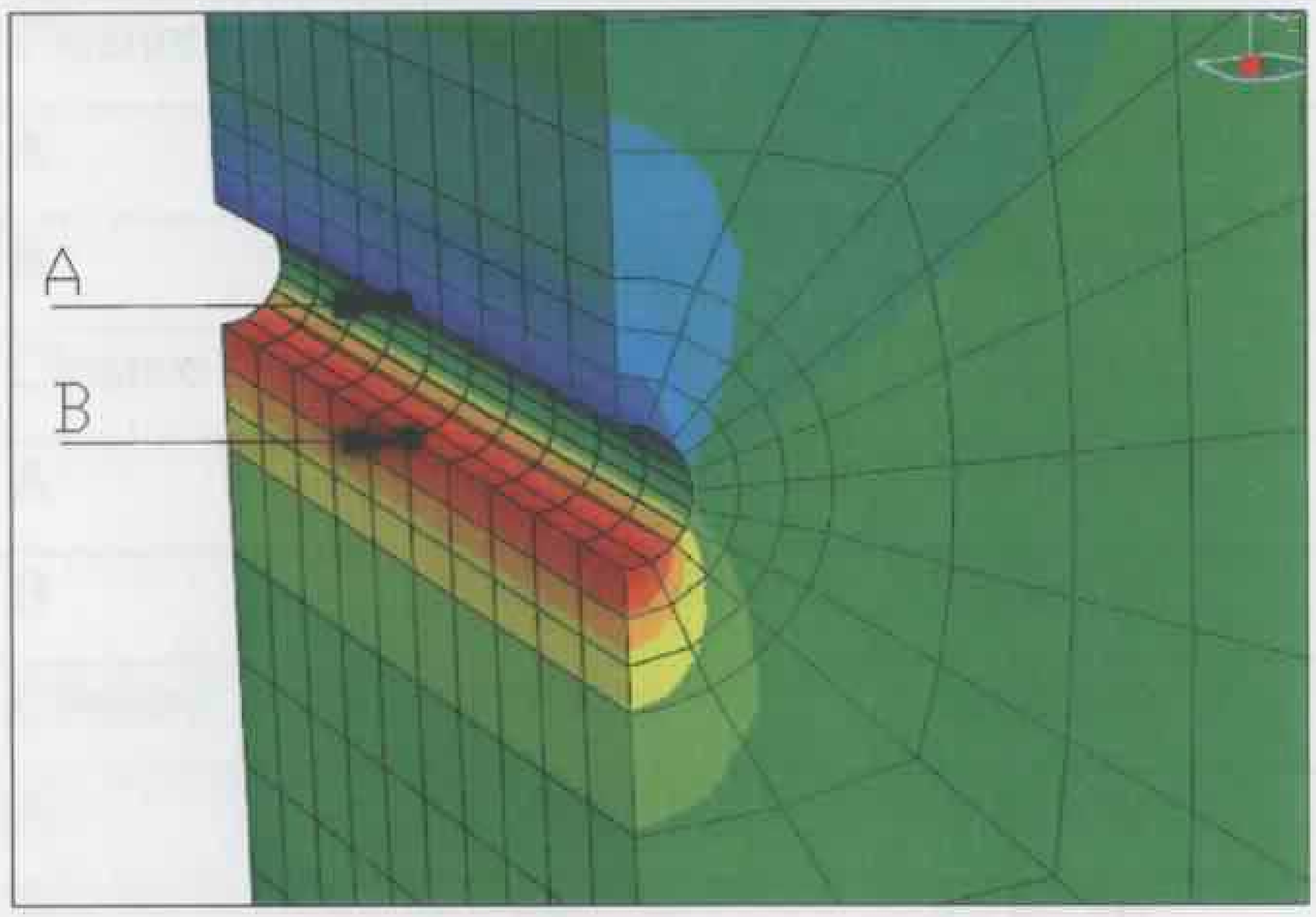

Figure 6.13: Opening section of circular tunnel.

Models	Displacement	ABAQUS (mm)	SAFEA (mm)	Difference (%)
ZTT10	A	-9.21E-02	-9.39E-02	
	B	3.53E-01	3.44E-01	
	Closure	4.45E-01	4.38E-01	1.51
ZTT30	A	-5.49E-01	-5.35E-01	
	B	7.43E-01	7.15E-01	
	Closure	1.29E+00	1.25E+00	3.22
ZTT80	A	-1.75E+00	-1.71E+00	
	B	1.72E+00	1.66E+00	
	Closure	3.47E+00	3.36E+00	3.13
ZTT30a	A	-5.49E-01	-5.35E-01	
	B	7.43E-01	7.15E-01	
	Closure	1.29E+00	1.25E+00	3.22
ZTT30b	A	-1.33E+00	-1.29E+00	
	B	1.61E+00	1.56E+00	
	Closure	2.94E+00	2.85E+00	3.04

Table 6.2: Computed closure of tunnel models during excavation.

The results indicate that the deeper tunnel will have a bigger instantaneous closure deformation than the shallow tunnel, and the tunnel excavated in shale would experience a larger instantaneous closure deformation than the tunnel excavated in sandstone at the same depth.

6.2.4 TUNNEL CREEP ANALYSIS

Force generated in the excavation step was applied to the tunnel section in the SAFEA analysis program and the creep deflection for any time step was calculated based on the selected creep parameters. The creep parameters of the logarithmic model were selected based on the deviator stress level generated from the excavation step and have been listed in Table 6.1. In ABAQUS, a visco-elastic analysis step was added to carry out the time-dependent creep analysis following the excavation step. The time period was set as 1000 days in both programs. In the creep analysis, the deformation and stress in the tunnel models were calculated and recorded by both SAFEA and ABAQUS, the results of the two programs match well and are shown in Figures 6.14a & b.

Figure 6.14a shows the closure displacements of the circular tunnels at 10m/30m/80m depth (ZTT10, ZTT30 and ZTT80 respectively). It can be seen that the closure deformation of the tunnel section has a nearly linear relationship with the logarithm of time, and tunnels do not experience large creep deformation in all of these cases. The results also indicate that the deeper tunnel will have a bigger initial closure deformation and the creep deformation will increase at a faster rate than the shallow tunnel. It is obvious that a deeper tunnel will suffer higher stress which leads to a larger deformation and faster creep deformation rate. The closures are small in this case because of the rock stiffnesses used that are typical of the stiffer rocks in Sydney.

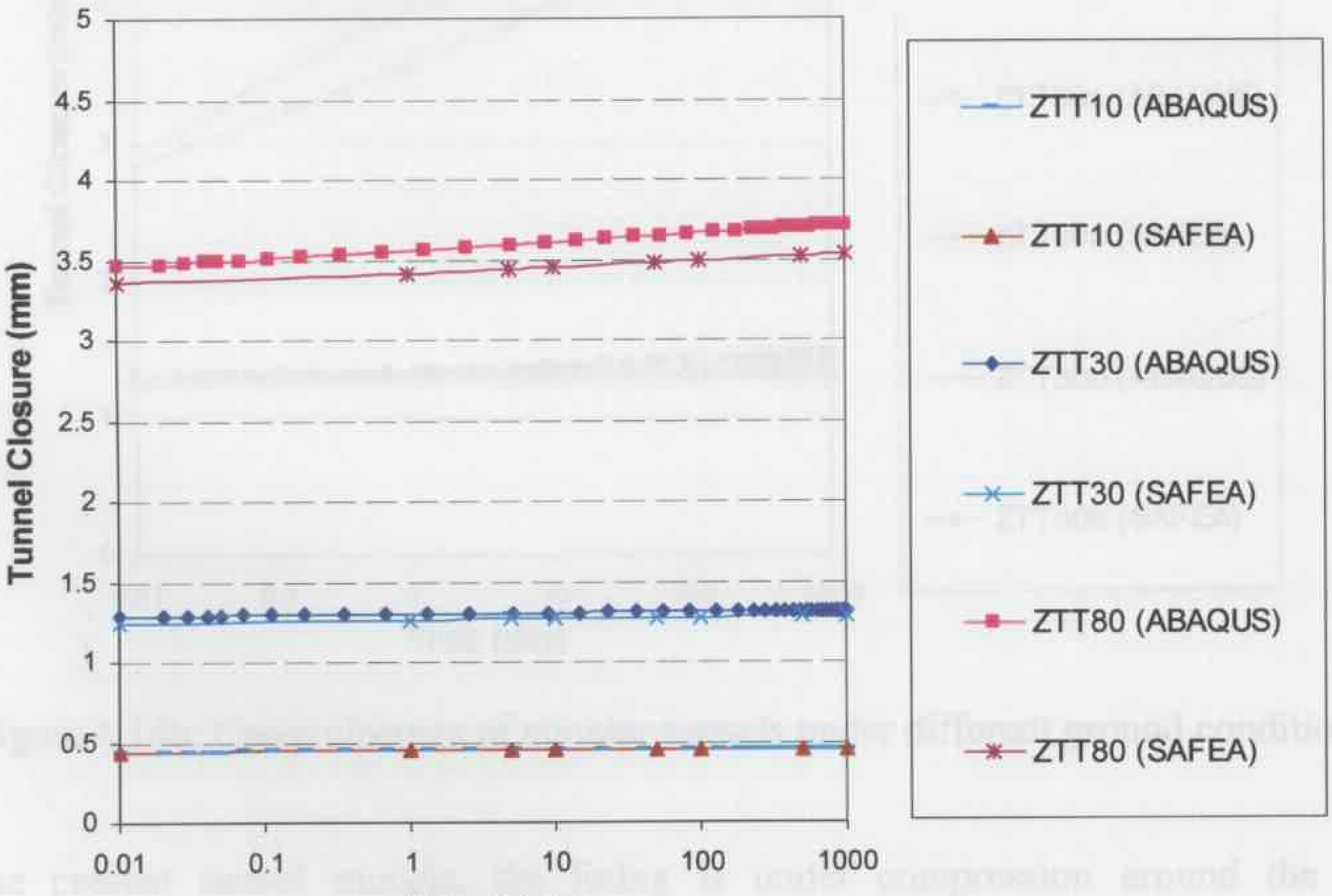

Figure 6.14a: Creep closures of circular tunnels at different depths.

Figure 6.14b shows the closure displacements of the circular tunnels at 30m depth under different ground conditions. The results show that tunnels excavated under different ground conditions will have different instantaneous and time-dependent performances. By comparing the results of ZTT30 and ZTT30a, we can see that they have same initial closure deformation, but the tunnel excavated in the rock which creeps faster will also experience a faster closure deformation rate. While comparing the results of ZTT30 and ZTT30b, we can clearly notice that the tunnel excavated in shale has a higher instantaneous closure deformation and the closure deformation increases much faster than the tunnel constructed in sandstone. The results indicate that the properties and creep behaviours of different rocks affect the tunnels' instantaneous and time-dependent deformation significantly.

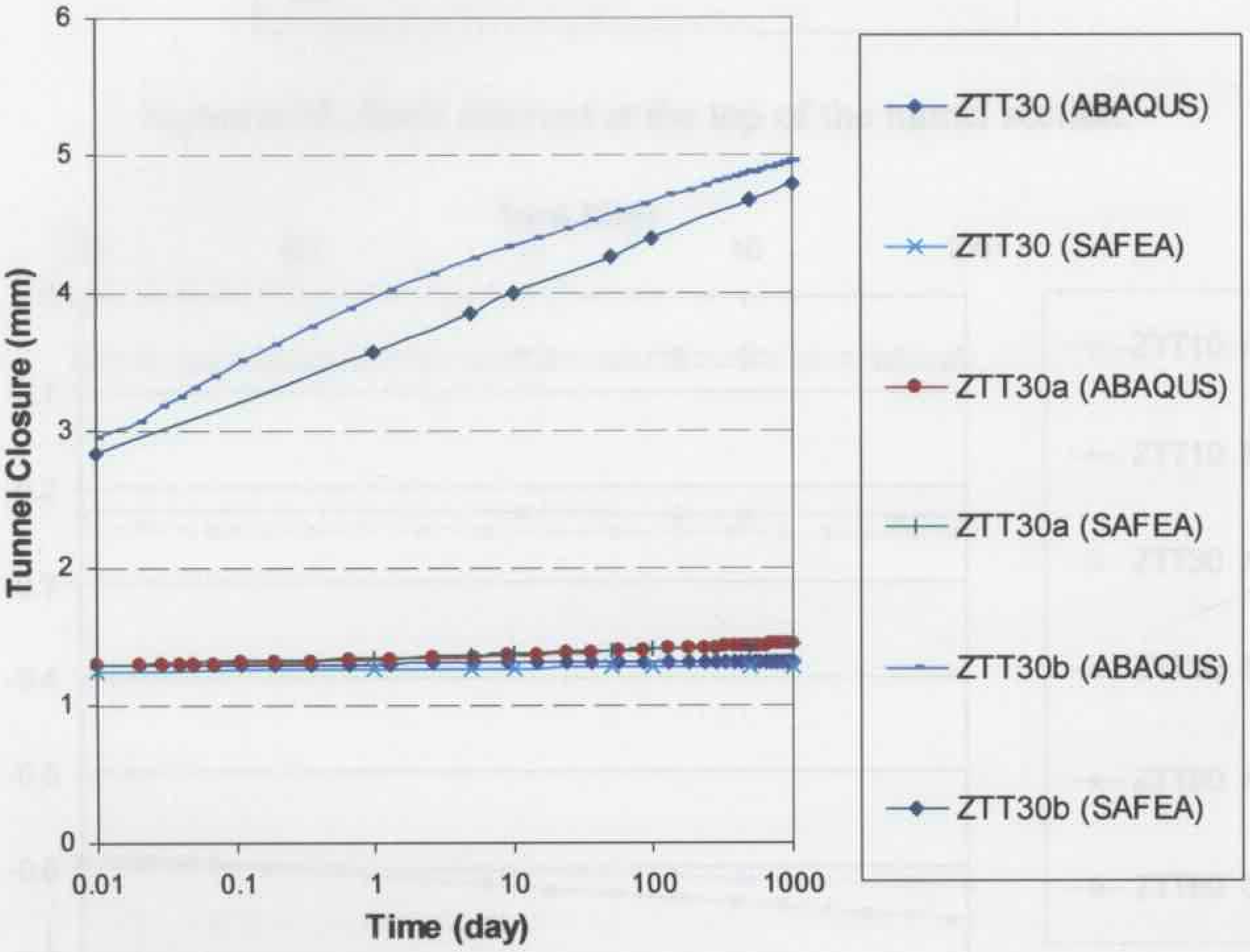

Figure 6.14b: Creep closures of circular tunnels under different ground conditions.

In the present tunnel models, the lining is under compression around the whole circumference of the section and the FRS materials tend to creep slowly under compression. The stress increment in the lining shell element at the top of the tunnel section as shown in Figure 6.15 may also be computed. Figure 6.16a shows the stress in the lining of circular tunnels at 10m/30m/80m depth (ZTT10, ZTT30 and ZTT80 respectively). It can be seen that the stress in the lining increases nearly linearly but very slowly with the logarithm of time. The results also indicate that the deeper tunnel will have a bigger initial stress in the lining and the stress increases at a faster rate than in the shallow tunnel. Stress increase is not great due to the small deformation in the lining.

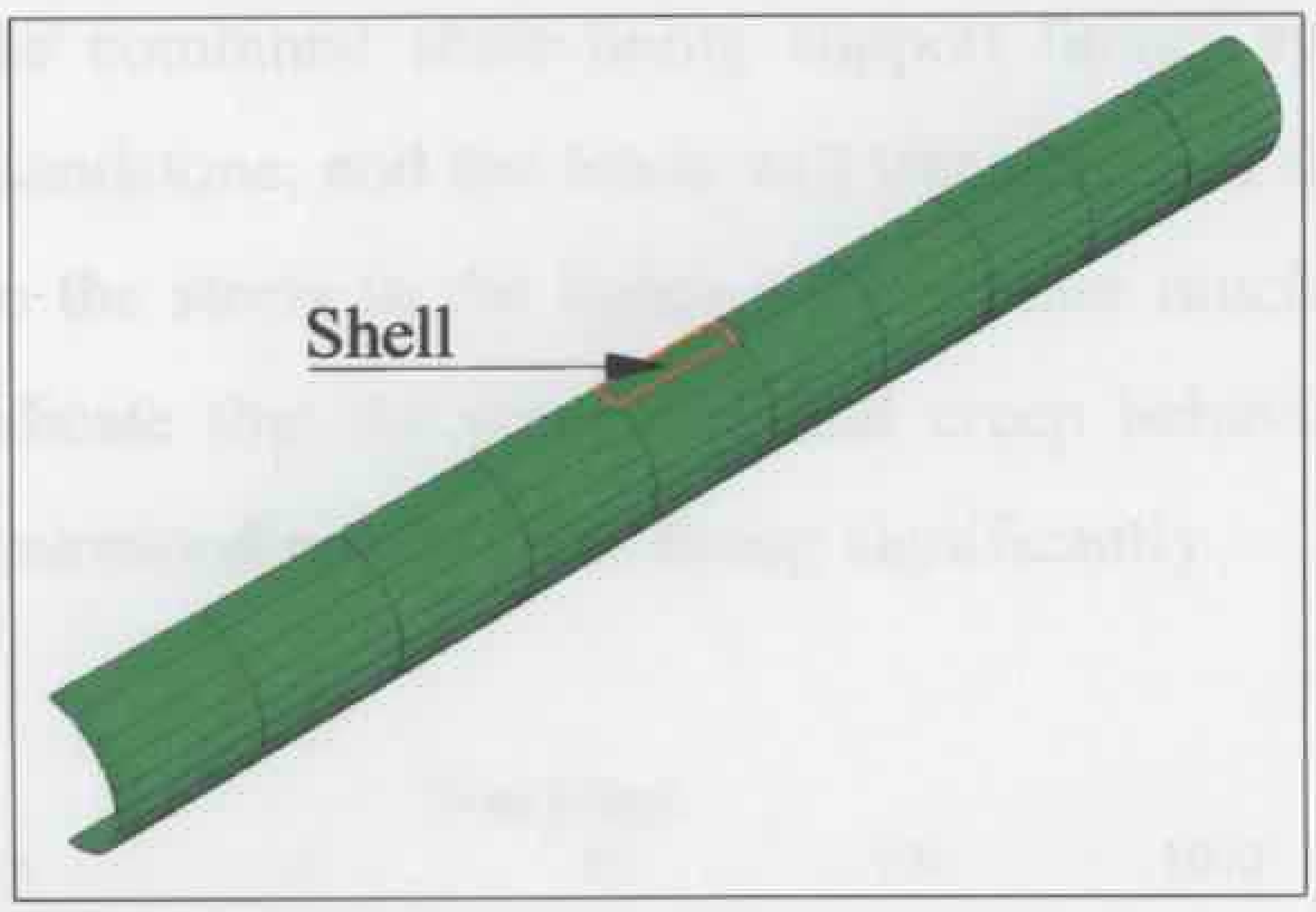

Figure 6.15: Shell element at the top of the tunnel section.

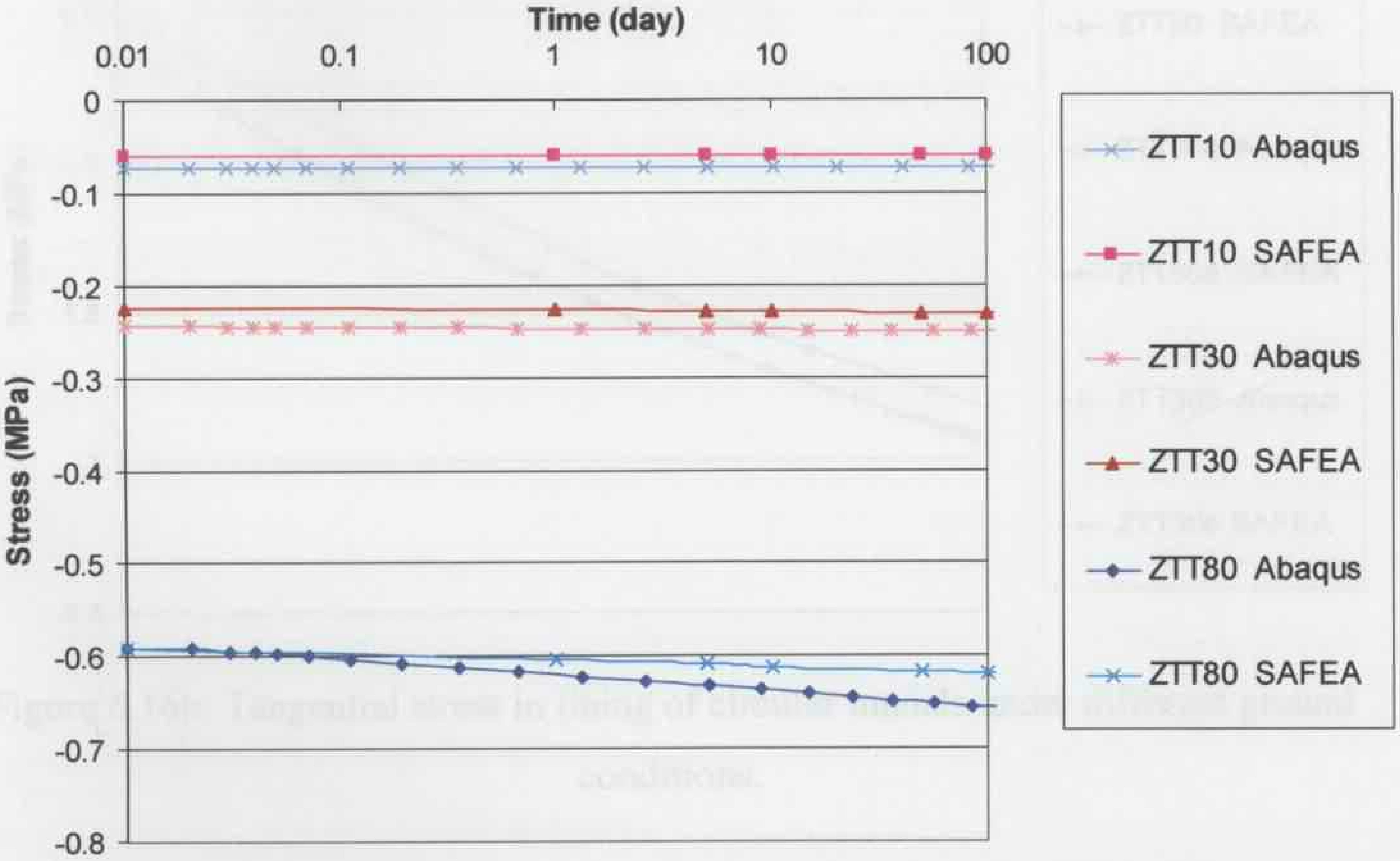

Figure 6.16a: Tangential stress in lining of circular tunnels at different depths.

Figure 6.16b shows the tangential stress in the lining of the circular tunnels at 30m depth under different ground conditions. The initial stress in the lining of the ZTT30 and

ZTT30a models is the same, but the stress in the lining tends to increase at a faster rate when the tunnel is excavated in a rock which creeps faster (ZTT30a). It can also be seen that the tunnel excavated in shale (ZTT30b) has a higher initial stress in the lining and the stress increases much faster than the tunnel constructed in sandstone (ZTT30). It is because the shale has a smaller elastic modulus, thus the shotcrete lining will need to carry more load in the combined shale-lining support tunnel system. Also, the shale creeps faster than the sandstone, and the loads will transfer from the surrounding rock to the shotcrete lining, so the stress in the lining will increase much faster in the ZTT30b model. The results indicate that the properties and creep behaviour of different rocks affect the stress in the surrounding shotcrete lining significantly.

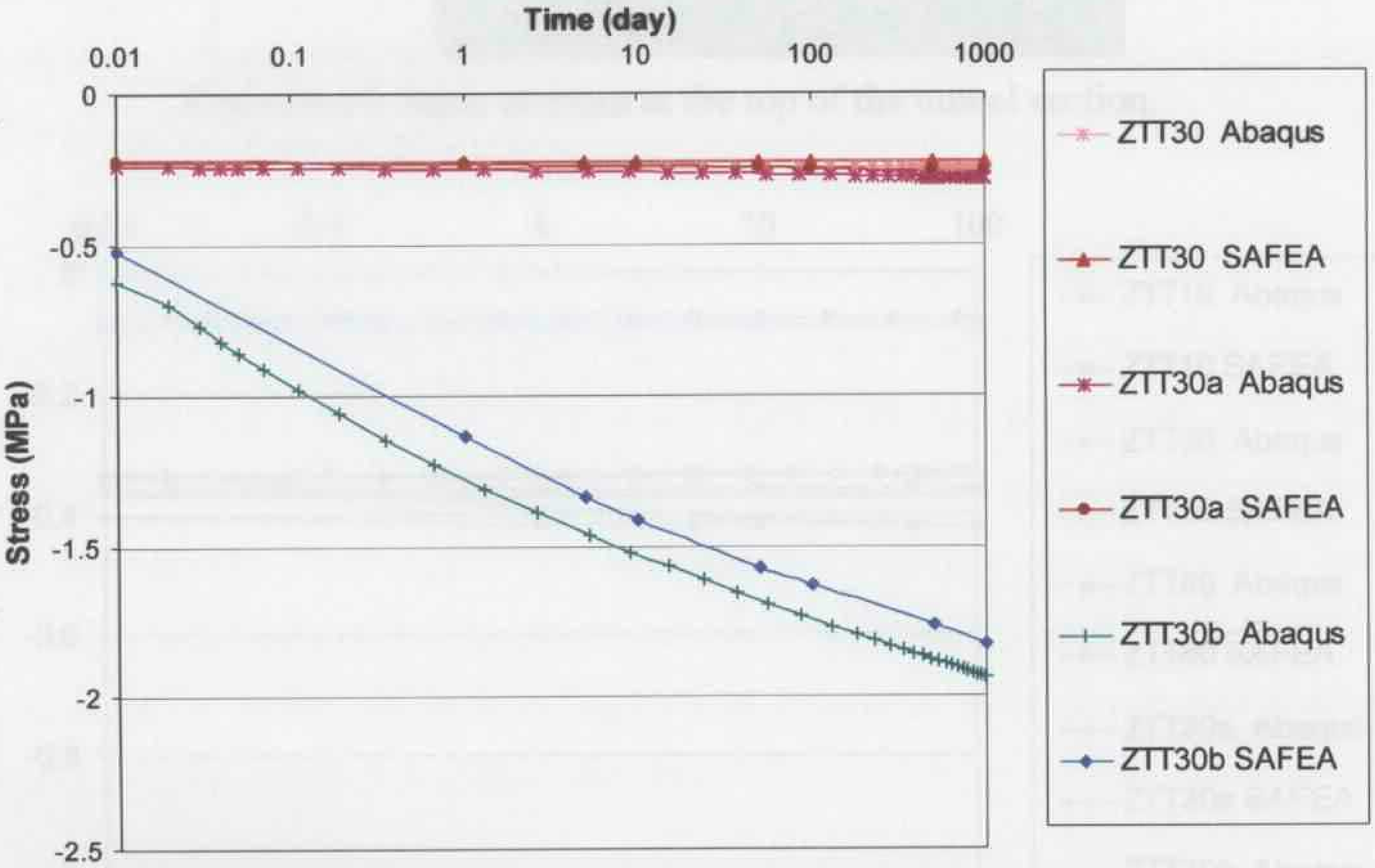

Figure 6.16b: Tangential stress in lining of circular tunnels under different ground conditions.

In the present circular tunnel models, the surrounding rock of the tunnel section is under compression, and so the stress in the rock element at the top of the tunnel sections as shown in Figure 6.17 is of interest. It can be clearly seen in Figure 6.18 that the initial stresses in the rock around the deeper tunnels are higher than in the shallow tunnels, and the different ground properties (shale vs. sandstone) do not affect the initial stresses around the tunnel significantly in theses cases. The results also indicate that the stresses in the sandstone around the tunnels change very slowly or exhibit little change with time, while the stress in the shale around the tunnels increases at a faster rate. In all cases, the stress in the rock around the tunnels is not predicted to change significantly.

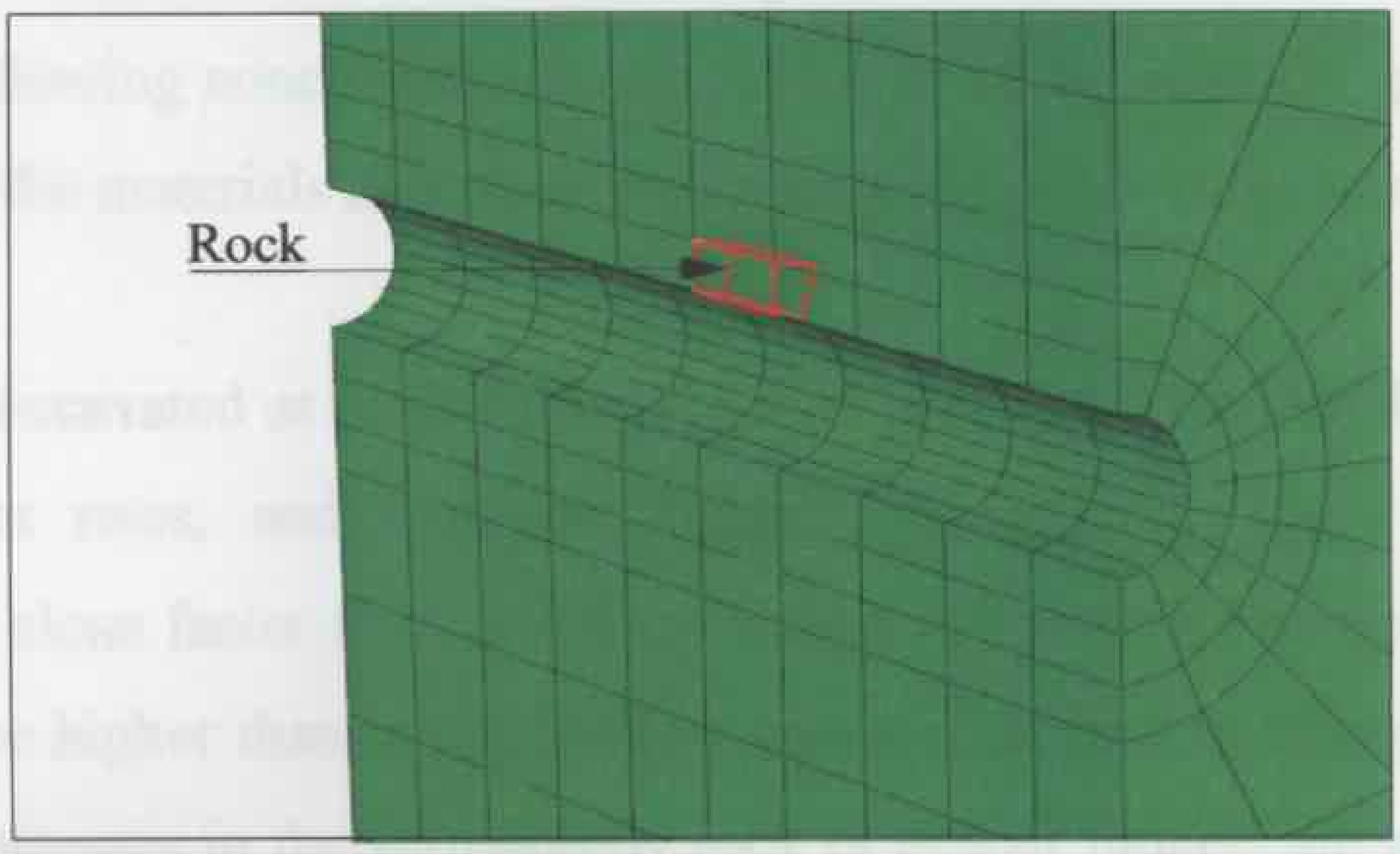

Figure 6.17: Rock element at the top of the tunnel section.

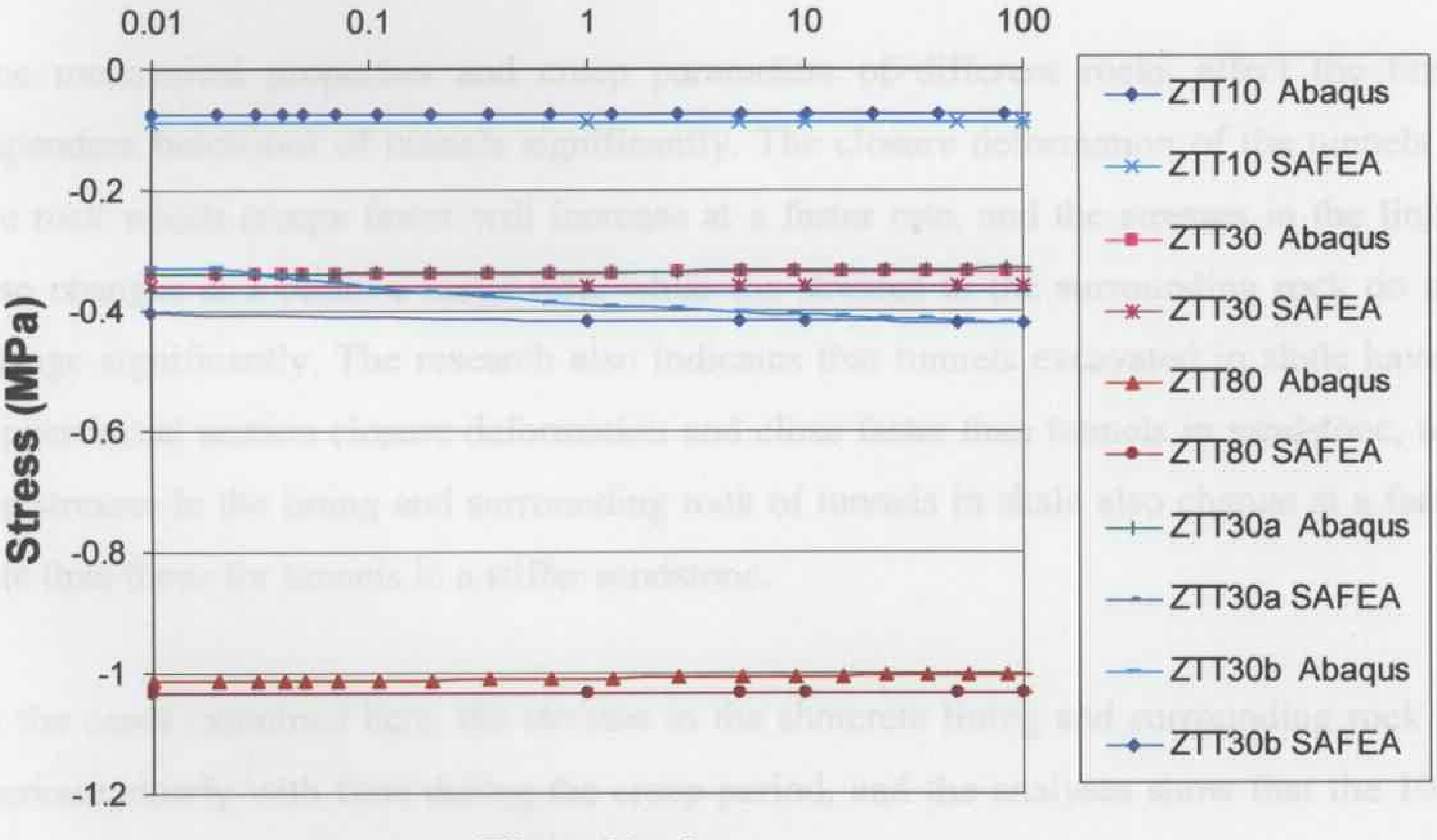

Figure 6.18: Stress in rock surrounding circular tunnels

6.3 CONCLUSIONS

In this chapter, some simple circular tunnels supported by fibre reinforced shotcrete linings were modelled. The tunnels were constructed at different depths and under different ground conditions, and the time-dependent behaviour of these tunnels was analysed. The following conclusions are drawn based on the specific ground conditions, elastic moduli of the materials and creep parameters defined in these numerical models.

Circular tunnels excavated at different depths will have different initial deformation and close at different rates, and a deeper tunnel will generally have a bigger initial deformation and close faster than a shallow tunnel. The initial stresses in the lining of deeper tunnels are higher than in the shallow tunnels and tend to change at a faster rate, while the initial stresses in the surrounding rock of deeper tunnels are also higher but do not change significantly in these cases.

The mechanical properties and creep parameters of different rocks affect the time-dependent behaviour of tunnels significantly. The closure deformation of the tunnels in the rock which creeps faster will increase at a faster rate, and the stresses in the lining also changes at a relative faster rate, while the stresses in the surrounding rock do not change significantly. The research also indicates that tunnels excavated in shale have a bigger initial section closure deformation and close faster than tunnels in sandstone, and the stresses in the lining and surrounding rock of tunnels in shale also change at a faster rate than those for tunnels in a stiffer sandstone.

In the cases examined here, the stresses in the shotcrete lining and surrounding rock all increase slowly with time during the creep period, and the analyses show that the 1000 day creep closure and performance are in an acceptable range for all of the tunnels studied here.

CHAPTER 7 - CASE STUDY - FLAT ROOF TUNNEL

7.1 INTRODUCTION

With the development of infrastructure technology and further functional requirements of the tunnel structure, the use of special-shaped cross section tunnels has become more and more popular for transport infrastructure projects. The horseshoe-shaped cross section with near flat roof is a more efficient shape for transport tunnels; it provides a more effective cross-section and space utilization rate, reduces the excavation size and the amount of spoil from the excavated soil or rock. The advanced tunnel construction technology, which makes use of computer controlled road headers, makes this special-shaped cross-section possible, reduces the cost and enhances the efficiency and space utilization of the tunnel structure.

Fibre reinforced shotcrete (FRS) is widely used as the lining for such tunnel structures, and there are two types of FRS used in Australia, namely steel FRS and macro-synthetic FRS. How the different FRS influences the time-dependent behaviour of the tunnel structure is investigated in this chapter.

7.2 NUMERICAL TUNNEL MODELS

Some flat roof tunnels supported by a combined shotcrete lining and rockbolt system were modelled to study the time-dependent behaviour of these tunnels. The tunnels were selected to be excavated at different depths and under different ground conditions, and three different types of FRS were used for the lining.

7.2.1 TUNNEL MODEL MESH

The flat roof tunnel section is symmetrical and only half of the section was modelled to reduce the mesh size. Finite element meshes for eight tunnel models were created for 50m depth and 100m depth. The tunnels excavated at 100m depth use the same mesh as the tunnel excavated at 50m depth, and the rock above 50m was treated as a pressure load applied to the top surface of the model (Figure 7.1). ZM5/ZM52/ZM53 (50m depth) and ZM5S1/ ZM5S2/ZM5S3 (100m depth) are chosen to be in the rock which creeps according to Pellet's (2000) data for sandstone while ZM59 (50m depth) and ZM5S9 (100m depth) are in the 'soft' rock which creeps faster. Three types of fibre reinforced shotcrete are employed in the models, ZM5/ZM5S1 use Novotex FRS lining, ZM52/ZM5S2/ZM59/ZM5S9 use HPP FRS lining, while ZM53/ZM5S3 use Strux FRS lining.

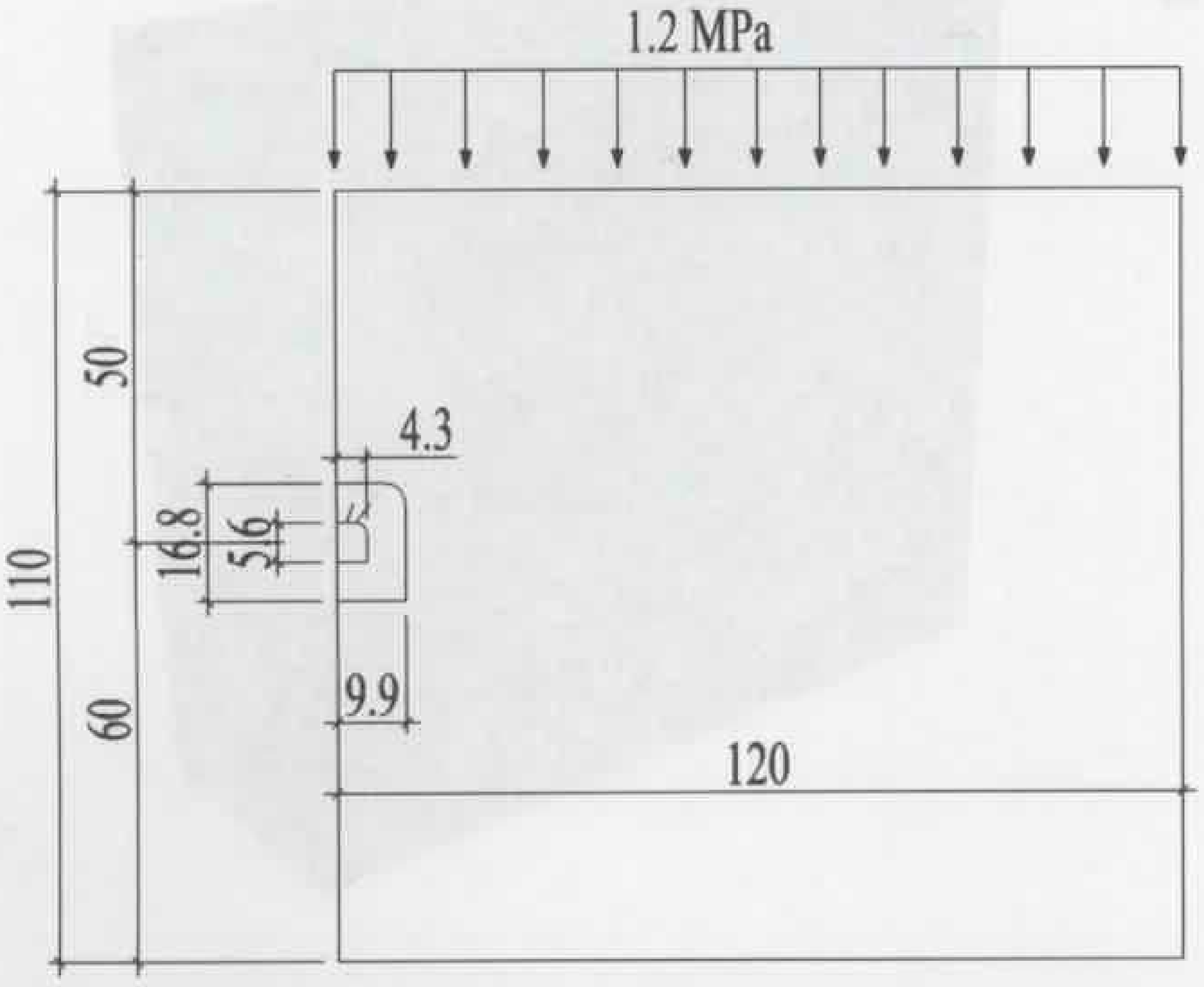

Figure 7.1: Cross-section of tunnel model at 100m depth (unit: m).

The horizontal length of the tunnel was set as 40m and the tunnel mesh was divided in 10 even partitions in the tunnel horizontal axial direction so that the deformation in the middle section would not be affected significantly by the face boundary restraints. The finite element mesh generated for SAFEA is shown in Figure 7.2.

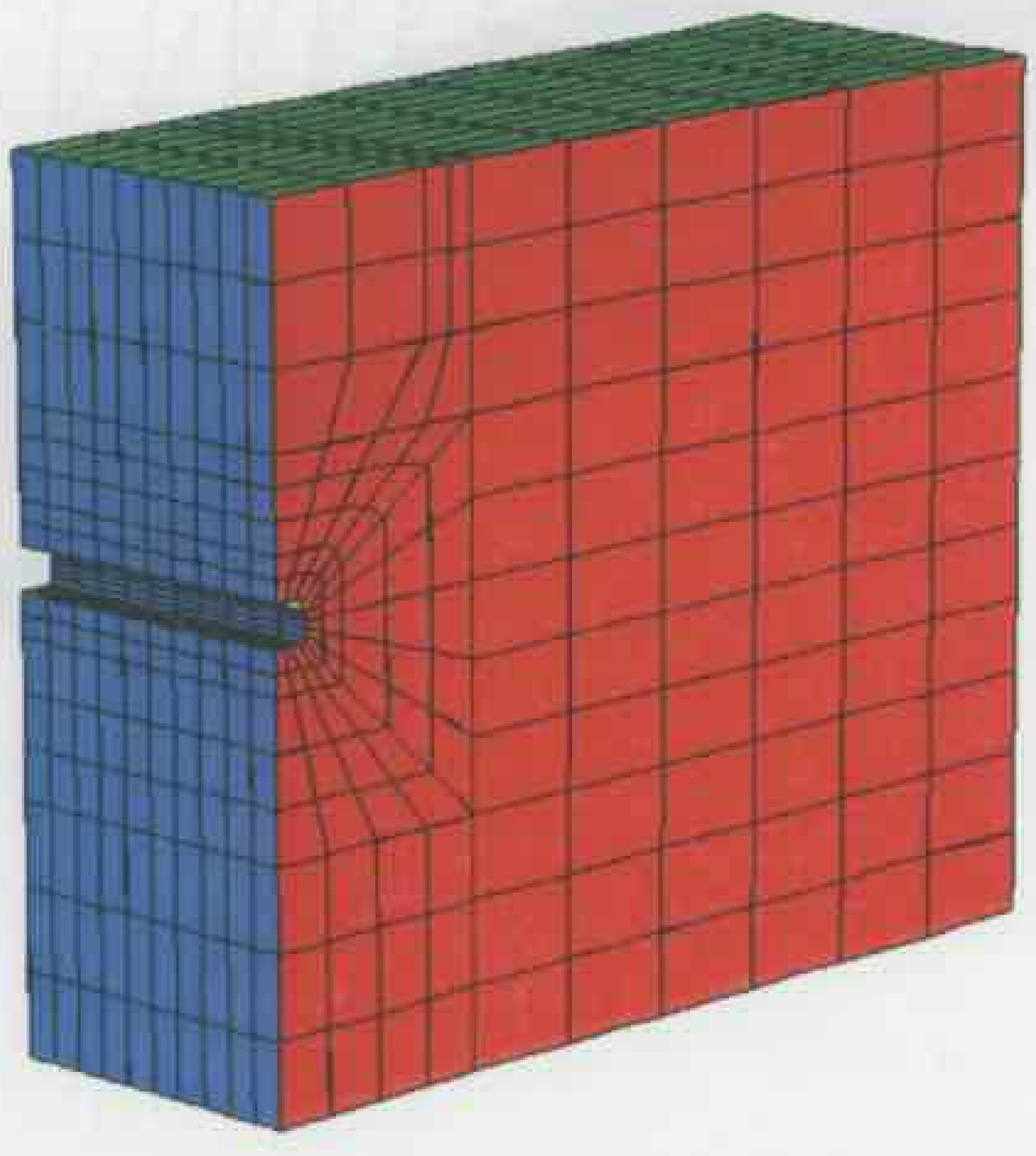

Figure 7.2: Mesh of tunnel model at 50m & 100m depth for SAFEA.

Similar flat roof tunnel models were also built up in ABAQUS as shown in Figure 7.3. The shotcrete lining and rockbolts were applied on the crest of the tunnel section, and the mesh of the lining and rockbolts elements is shown in Figure 7.4.

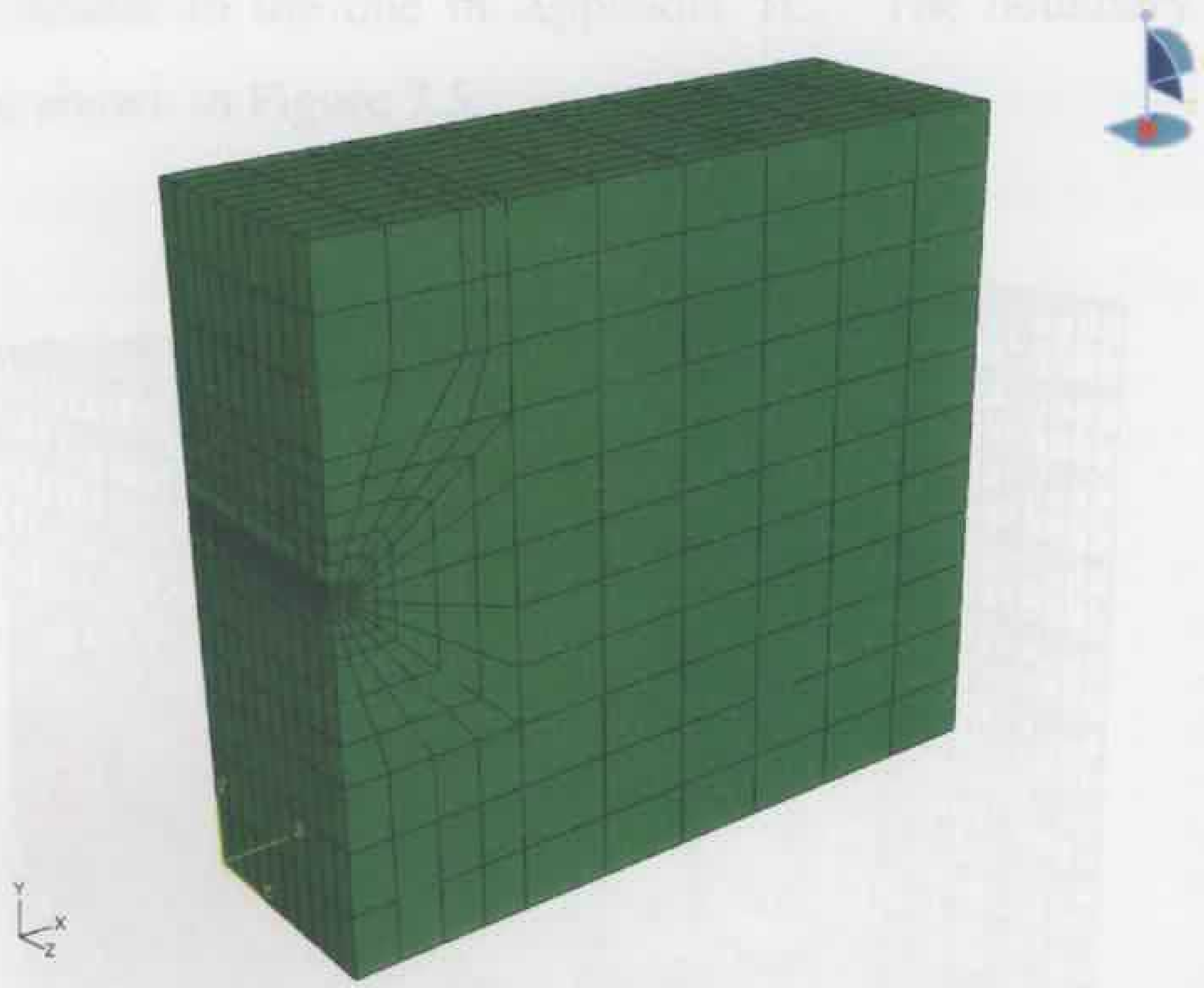

Figure 7.3: Mesh of tunnel model at 50m & 100m depths for ABAQUS.

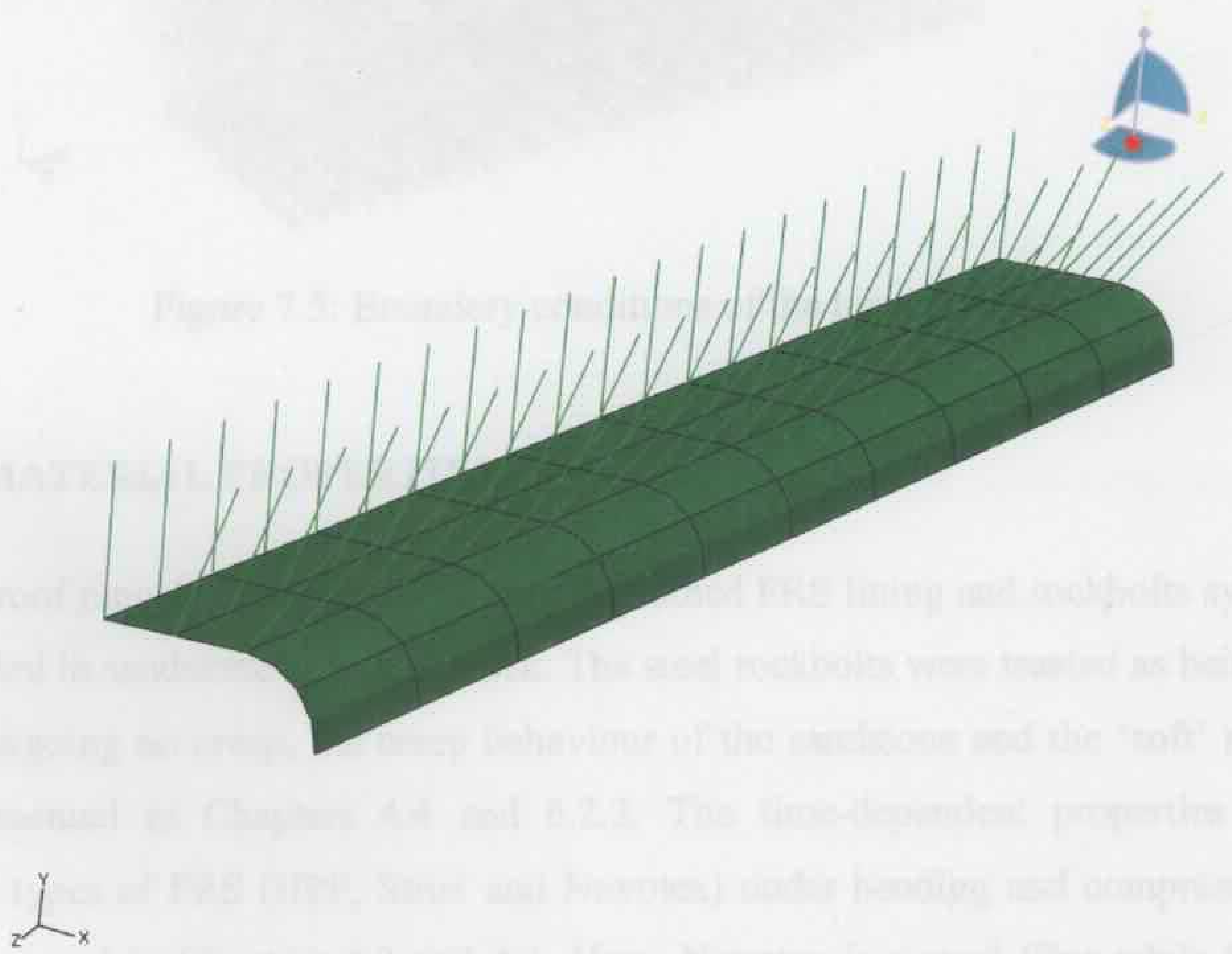

Figure 7.4: Mesh for lining and rockbolt elements in tunnel model.

The top surface of the tunnel model was set to be unrestrained while the base and sides were restrained against movement in both perpendicular directions, and the self weight of the rock mass was $24000 N/m^3$. The initial stress field was generated using Equation 6.1 by a subroutine similar to the one in Appendix 5C. The boundary conditions of the tunnel models are shown in Figure 7.5.

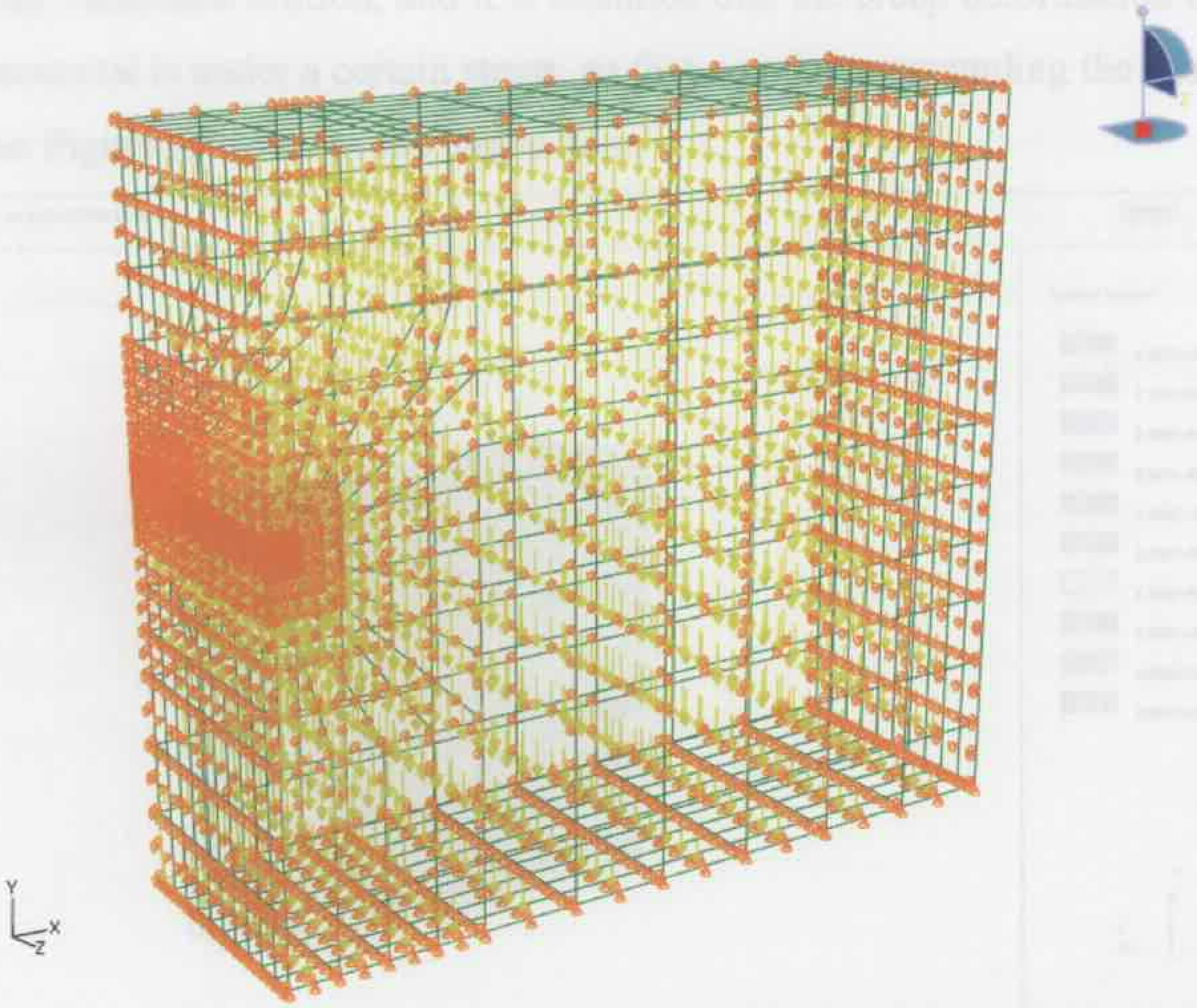

Figure 7.5: Boundary conditions of the tunnel models.

7.2.2 MATERIAL PROPERTIES

The flat roof tunnels were supported by a combined FRS lining and rockbolts system and constructed in sandstone or a 'soft' rock. The steel rockbolts were treated as being elastic and undergoing no creep, the creep behaviour of the sandstone and the 'soft' rock have been presented in Chapters 4.4 and 6.2.2. The time-dependent properties of three different types of FRS (HPP, Strux and Novotex) under bending and compression have been discussed in Chapters 4.2 and 4.3. Here, Novotex is a steel fibre while Strux and HPP are two new kinds of macro-synthetic fibre.

In SAFEA, the change of deviator stress around the tunnel opening section can be obtained during the tunnel excavation process, while ABAQUS can only plot the total final stress but not the increment of the stress. An example of the change of deviator stress around the flat roof tunnel excavated at 100m depth is shown in Figure 7.6 (ZM5S1). The generated increment of deviator stress is a maximum in a surrounding region of the excavated section, and it is assumed that the creep deformation only occurs when the material is under a certain stress, so that a region surrounding the tunnel section as shown in Figure 7.7 is set as the 'creep zone'.

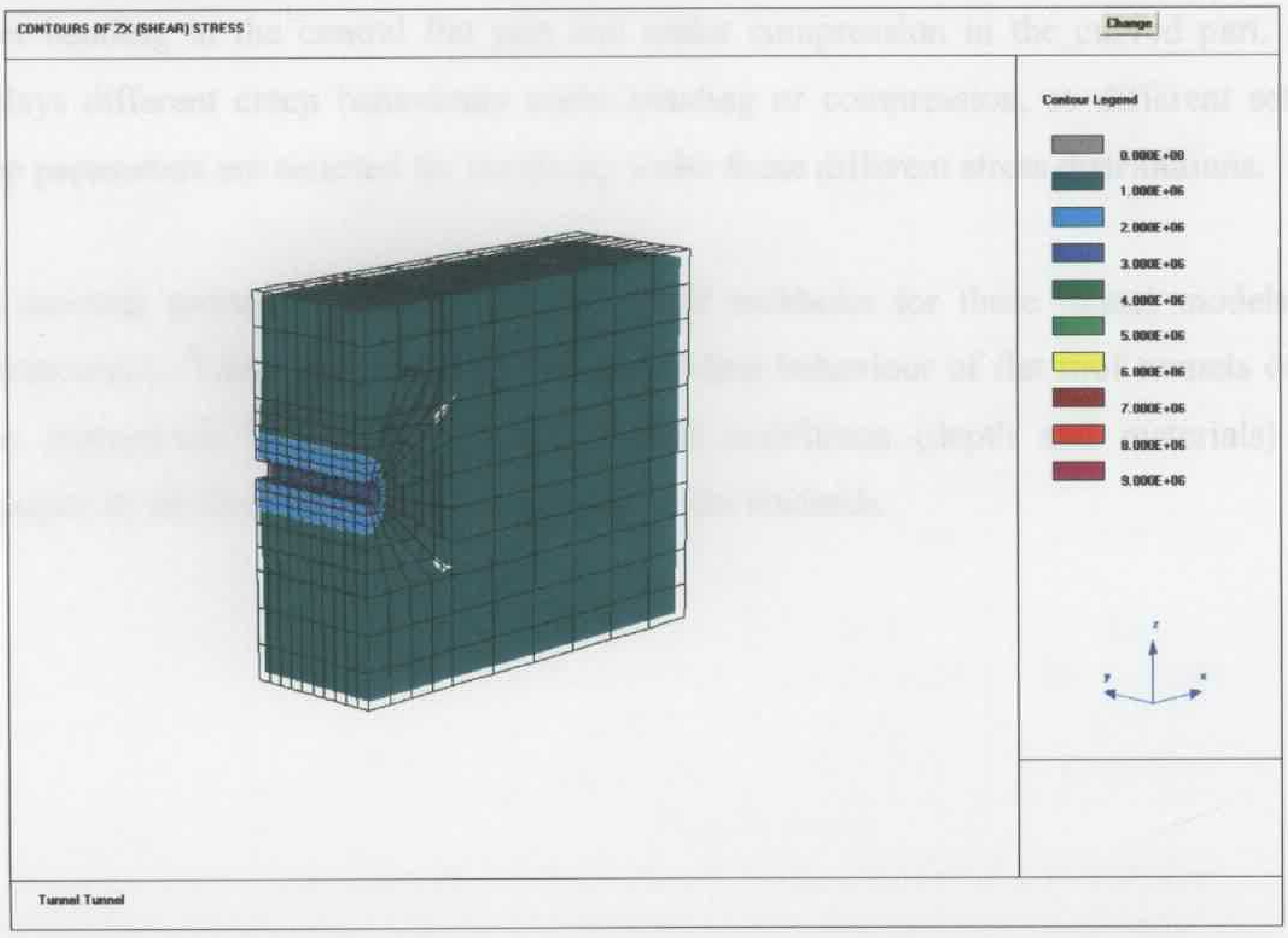

Figure 7.6: Increment of deviator stress of tunnel excavated at 100m depth (ZM5S1).

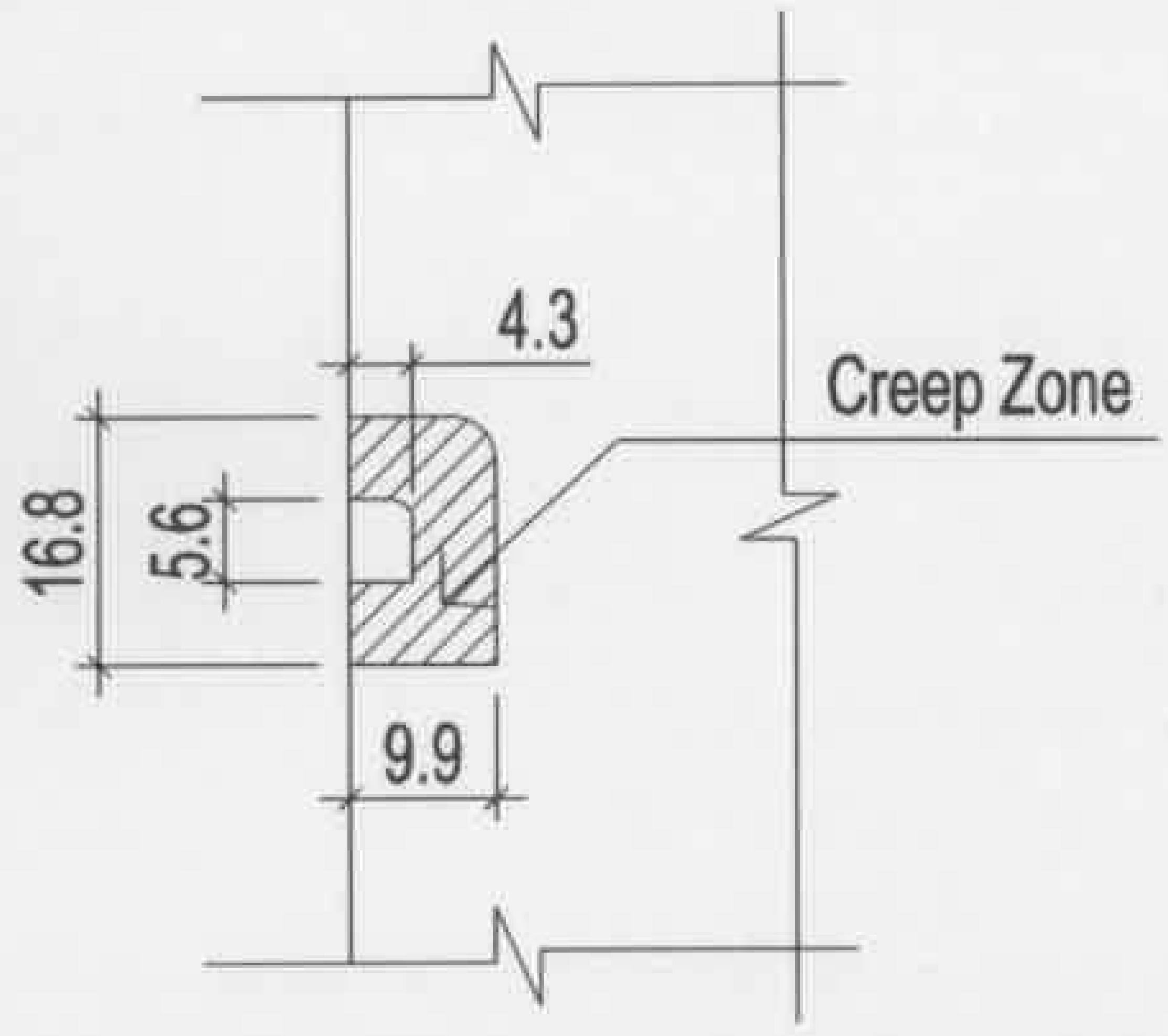

Figure 7.7: Creep Zone of flat roof tunnel (unit: m).

The creep parameters of the logarithmic model were selected based on the deviator stress level generated from the excavation step. A numerical uniaxial creep test as shown in Figure 6.9 was modelled by ABAQUS with the power creep model. The power creep parameters of sandstone, 'soft' rock, and three FRS were extrapolated between values from the lab tests as prescribed in previous Chapter; the numerical deflection curve under a certain load is fitted by SAFEA with selected logarithmic creep parameters.

In the excavation analysis, it can be seen that in the crest of a flat roof tunnel, the lining is under bending in the central flat part and under compression in the curved part. FRS displays different creep behaviours under bending or compression, so different sets of creep parameters are selected for the lining under these different stress distributions.

The material properties of the rock, FRS and rockbolts for these tunnel models are summarized in Tables 7.1a&b. The time-dependent behaviour of flat roof tunnels of the same dimensions but under different ground conditions (depth and materials) and supported by different FRS are to be studied in the research.

	Tunnel Models			
	ZM5	ZM52	ZM53	ZM59
Sandstone	E = 4.976e9 Pa ν = 0.3			
Creep parameters of sandstone	F=7.0e-20 n=2.19 m=-0.98 (ABAQUS)			F=3.0e-19 n=2.2 m=-0.9 (ABAQUS)
	σ = 1.2 MPa A=1 B=-0.0066 α=100 (SAFEA)			σ = 1.2 MPa A=1 B=-0.027 α=100 (SAFEA)
Shotcrete lining	Novotex	HPP	Strux	HPP
	E (Pa)			
	5.848e9	3.610e9	4.149e9	3.610e9
	ν = 0.15 Thickness = 0.2m			
Creep parameters of shotcrete	Compression region F=4.0e-37, n=4.6, m=-0.6 (ABAQUS)			
	σ = 1.4 MPa A=1 B=-0.003 α=0.1 (SAFEA)	σ = 0.9 MPa A=1 B=-0.00005 α=0.1 (SAFEA)	σ = 1.0 MPa A=1 B=-0.00006 α=0.1 (SAFEA)	σ = 0.9 MPa A=1 B=-0.00005 α=0.1 (SAFEA)
	Flexure region			
	F=4.0e-37 n=5.0 m=-0.1 (ABAQUS)	F=1.05e-17 n=2.19 m=-0.7 (ABAQUS)	F=1.2e-19 n=2.5 m=-0.7 (ABAQUS)	F=1.05e-17 n=2.19 m=-0.7 (ABAQUS)
	σ = 0.4 MPa A=1 B=-0.007 α=0.1 (SAFEA)	σ = 0.3 MPa A=1 B=-0.068 α=100 (SAFEA)	σ = 0.4 MPa A=1 B=-0.068 α=100 (SAFEA)	σ = 0.3 MPa A=1 B=-0.068 α=100 (SAFEA)
Rockbolts	M22X3000mm E = 2.0e11 Pa ν = 0.3			

Table 7.1a: Material properties of tunnel models at 50m depth.

	Tunnel Models			
	ZM5S1	ZM5S2	ZM5S3	ZM5S9
Sandstone	E = 4.976e9 Pa ν = 0.3			
Creep parameters of sandstone	F=7.0e-20 n=2.19 m=-0.98 (ABAQUS)			F=3.0e-19 n=2.2 m=-0.9 (ABAQUS)
	σ = 2.3 MPa A=1 B=-0.013 α=100 (SAFEA)			σ = 2.3 MPa A=1 B=-0.043 α=100 (SAFEA)
Shotcrete lining	Novotex	HPP	Strux	HPP
	E (Pa)			
	5.848e9	3.610e9	4.149e9	3.610e9
	ν = 0.15 Thickness = 0.2m			
Creep parameters of shotcrete	Compression region F=4.0e-37, n=4.6, m=-0.6 (ABAQUS)			
	σ = 2.4 MPa A=1 B=-0.018 α=0.1 (SAFEA)	σ = 1.7 MPa A=1 B=-0.00035 α=0.1 (SAFEA)	σ = 2.0 MPa A=1 B=-0.0007 α=0.1 (SAFEA)	σ = 1.7 MPa A=1 B=-0.00035 α=0.1 (SAFEA)
	Flexure region			
	F=4.0e-37 n=5.0 m=-0.1 (ABAQUS)	F=1.05e-17 n=2.19 m=-0.7 (ABAQUS)	F=1.2e-19 n=2.5 m=-0.7 (ABAQUS)	F=1.05e-17 n=2.19 m=-0.7 (ABAQUS)
	σ = 0.9 MPa A=1 B=-0.11 α=0.1 (SAFEA)	σ = 0.6 MPa A=1 B=-0.08 α=100 (SAFEA)	σ = 0.7 MPa A=1 B=-0.081 α=100 (SAFEA)	σ = 0.6 MPa A=1 B=-0.08 α=100 (SAFEA)
Rockbolts	M22X3000mm E = 2.0e11 Pa ν = 0.3			

Table 7.1b: Material properties of tunnel models at 100m depth.

7.2.3 TUNNEL EXCAVATION

The initial ground conditions of these flat roof tunnels were generated using Equation 6.1 as in the circular tunnel models in Chapter 6. In the excavation analysis, the initial stress field was generated according to Equation 6.1 and the initial deformation was reset to zero since the deformation of the ground has already finished before the excavation of the tunnel. In this step, the rock elements to be excavated remained in the mesh and the shotcrete lining and rockbolt elements were set as inactivated. The tunnel model was partitioned into ten sections in the axial direction of the tunnel and elements were then excavated step by step longitudinally. In each step, the rock elements were removed and the shotcrete lining and rock bolt elements at corresponding position were activated at the following step.

Due to the excavation, the instantaneous deformation of the ground is a maximum around the opening section in the vertical direction. An example of the deformation of the flat roof tunnel at 100m depth (ZM5S1) is shown in Figure 7.8, and the deformation scale factor is set as 100 to make the deformation identifiable. It can be seen that the top section is moving down, while the bottom section is moving up after excavation.

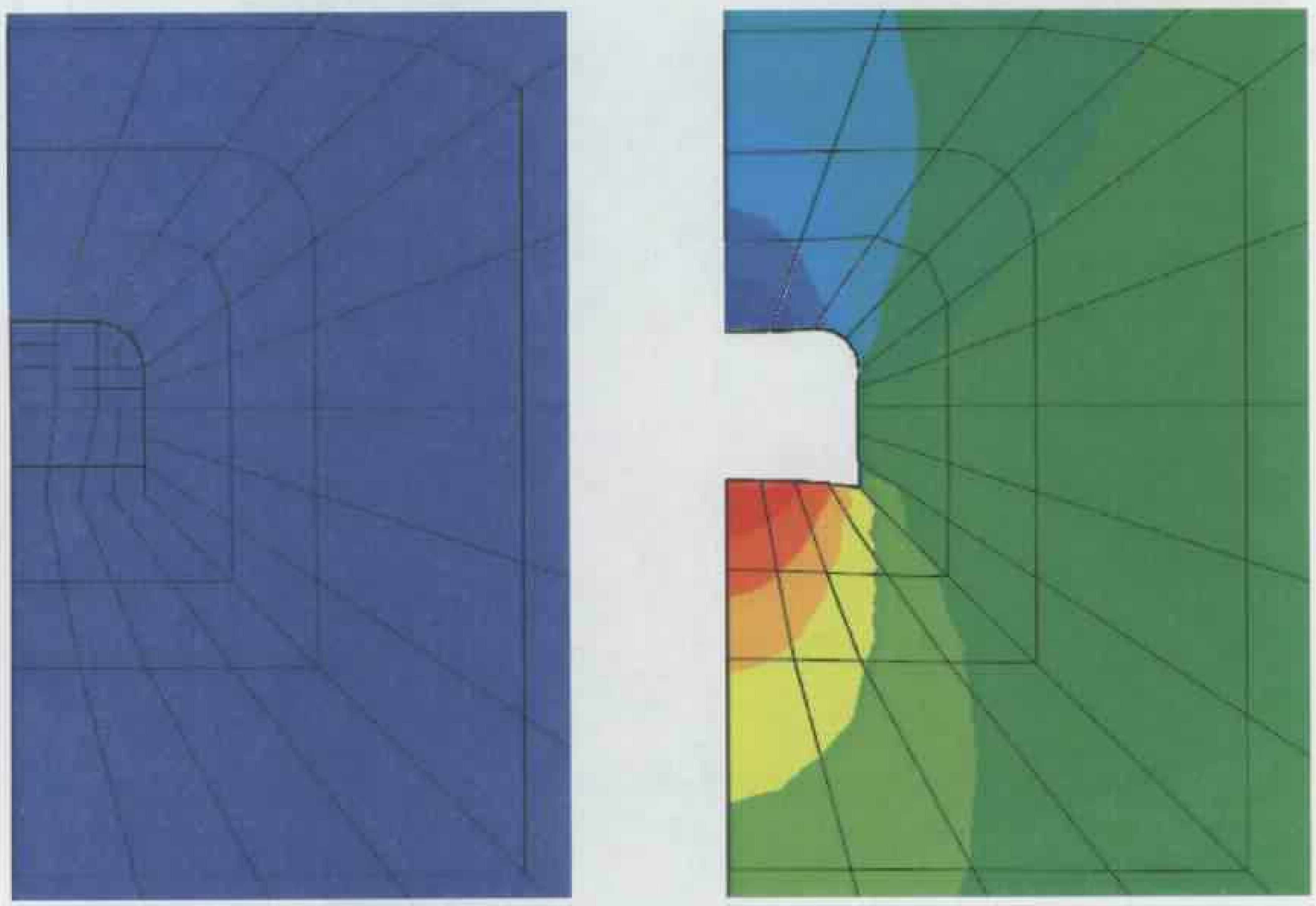

Before Excavation After Excavation

Figure 7.8: Tunnel deformation after excavation.

An example of the vertical deformation of the tunnel models (ZM5S1) at 100m depth are shown in Figures 7.9a&b.

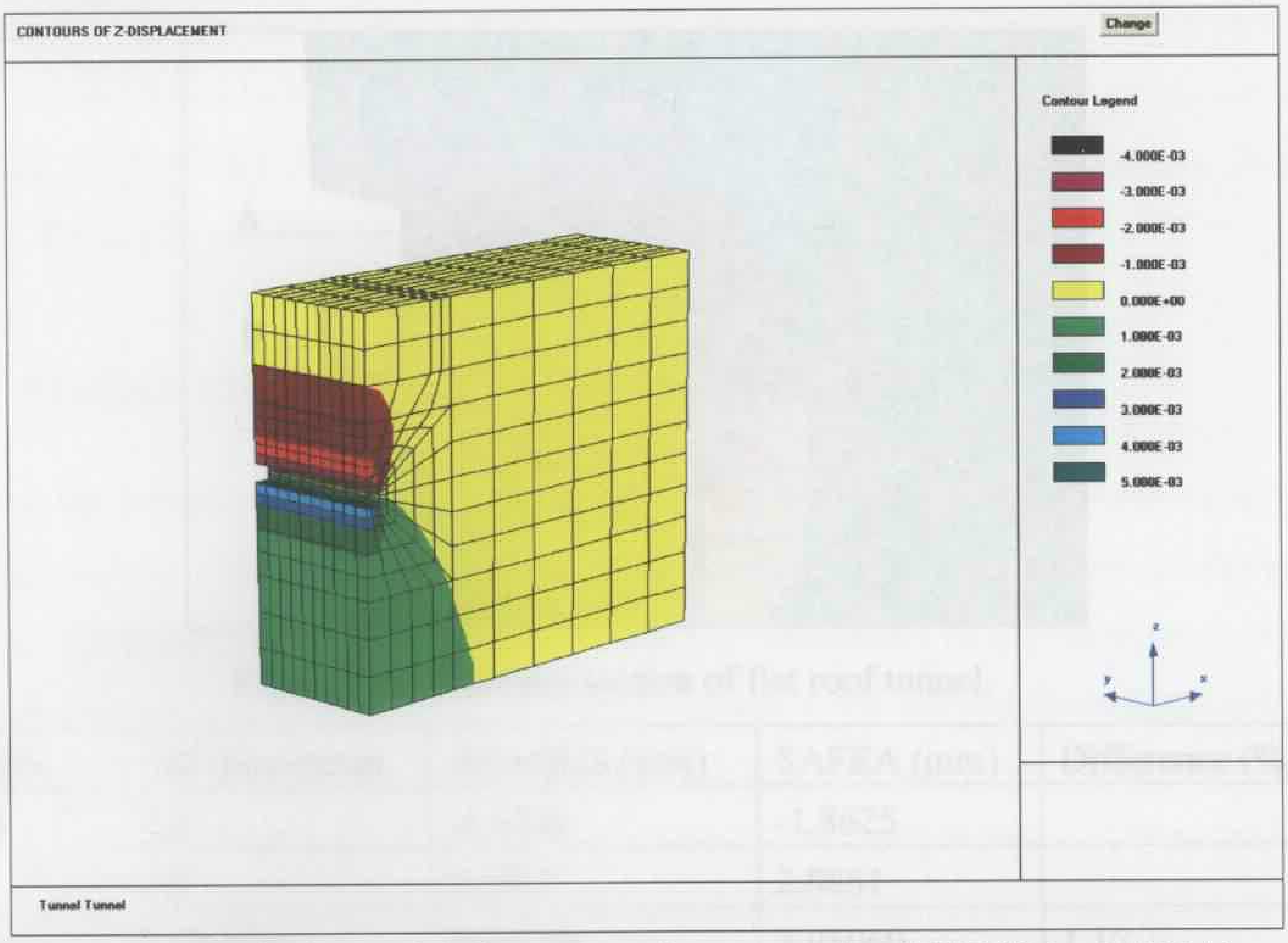

Figure 7.9a: Vertical tunnel deformation after excavation (ZM5S1 by SAFEA).

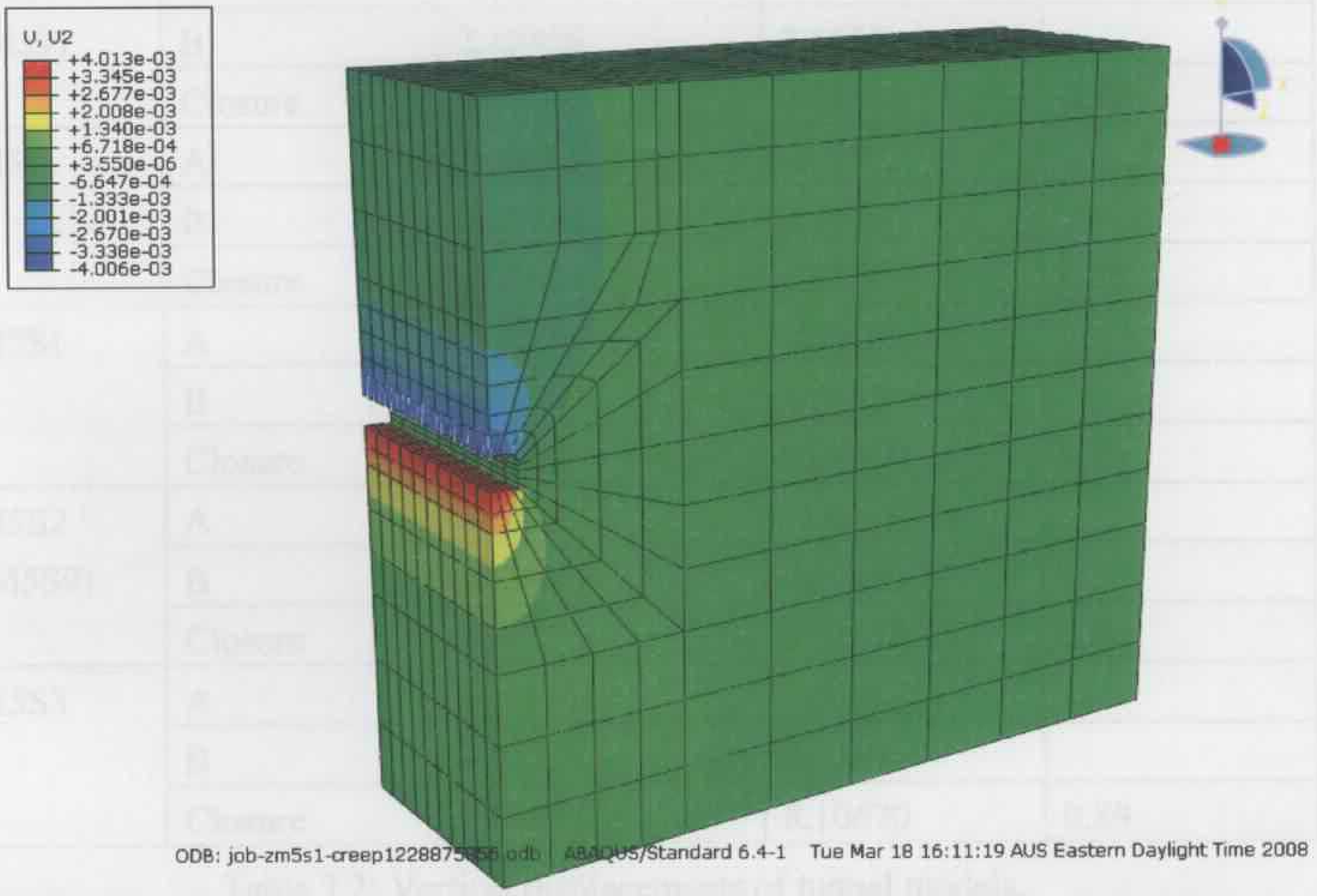

Figure 7.9b: Vertical tunnel deformation after excavation (ZM5S1 by ABAQUS).

The vertical displacements of point A and B located at the middle section of the tunnel models as shown in Figure 7.10 are listed in Table 7.2.

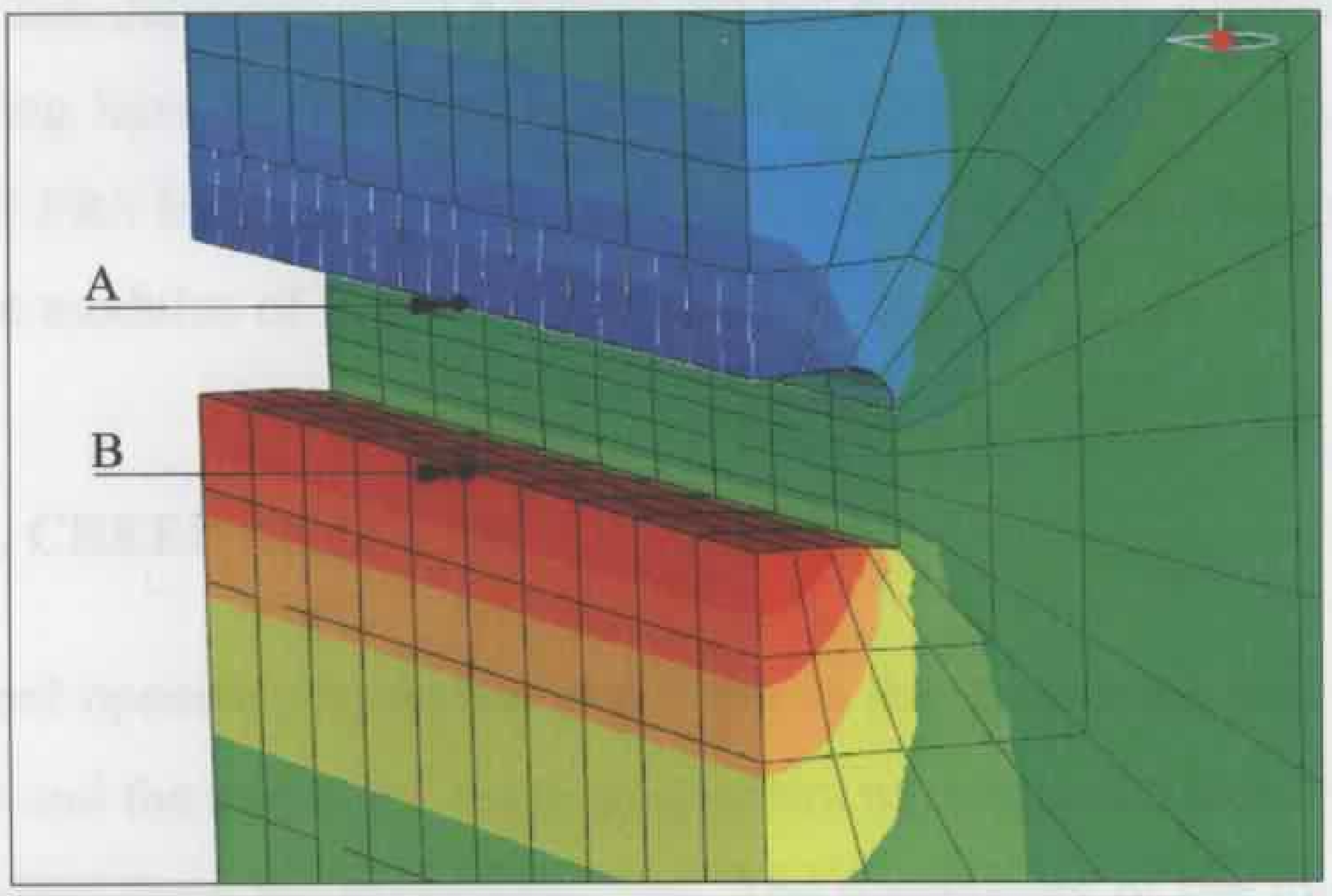

Figure 7.10: Opening section of flat roof tunnel.

Models	Displacement	ABAQUS (mm)	SAFEA (mm)	Difference (%)
ZM5	A	-1.8748	-1.8625	
	B	2.1219	2.0881	
	Closure	3.99670	3.95060	1.17
ZM52	A	-1.88888	-1.8783	
(ZM59)	B	2.12358	2.1651	
	Closure	4.01246	4.04340	0.77
ZM53	A	-1.8852	-1.8742	
	B	2.12314	2.1647	
	Closure	4.00834	4.03890	0.76
ZM5S1	A	-3.99763	-4.0123	
	B	4.01303	4.0683	
	Closure	8.01066	8.08060	0.87
ZM5S2	A	-4.0263	-4.0445	
(ZM5S9)	B	4.01645	4.0716	
	Closure	8.04275	8.11610	0.90
ZM5S3	A	-4.01881	-4.036	
	B	4.01554	4.0707	
	Closure	8.03435	8.10670	0.89

Table 7.2: Vertical displacements of tunnel models.

The results indicate that the deeper tunnel will have a bigger instantaneous closure deformation than the shallow tunnel, and that the different FRS do affect the instantaneous closure deformation of a tunnel but not significantly. Tunnels supported by Novotex FRS lining have the smallest instantaneous closure deformation, while tunnels supported by HPP FRS lining have the largest instantaneous closure deformation. This is because the elastic modulus of Novotex FRS is the highest.

7.2.4 TUNNEL CREEP ANALYSIS

Force on the tunnel opening which was generated in the excavation step was input into the creep analysis and the materials' creep parameters were selected based on the deviator stress level generated from the excavation step. The parameters of the logarithmic creep model for the SAFEA analysis were selected by fitting to the creep deformation curve of a numerical uniaxial creep test generated by ABAQUS with the power creep law under certain loads. Therefore with the selected parameters, the creep behaviour of specimens following the logarithmic creep model should match the creep curve obeying the power creep law under a certain stress level. Since FRS displays different creep rates under bending than under compression, two sets of creep parameters were selected for the curved part and the flat roof part of the lining (Tables 7.1a&b). In the following creep analysis, the shotcrete lining and surrounding rock will creep at different rates and the rockbolts are assumed not to creep with time. For ABAQUS, a visco-elastic analysis step is run to calculate the time-dependent deformation and stress in the rock and lining of the tunnel. The time period was set as 1000 days in both programs; the results of the two programs match well and are shown in the Figures 7.11 and 7.13.

Figure 7.11 shows the vertical closure displacements of the flat roof tunnels, we can see that deeper tunnels (ZM5S1, ZM5S2 and ZM5S3 at 100m depth) will have larger initial deformation and close faster than the shallow tunnels (ZM5, ZM52 and ZM53 at 50m depth). It is clear that tunnels excavated at a greater depth will experience larger deformation and suffer higher stress and thus creep faster than shallow tunnels. Tunnels excavated in the rock which creeps faster (ZM59, ZM5S9) will also close at a significantly faster rate than tunnels excavated in sandstone (ZM52, ZM5S2). But it can be seen that the different fibre reinforced shotcrete linings will not affect the creep deformation of the whole tunnel structure significantly in these cases.

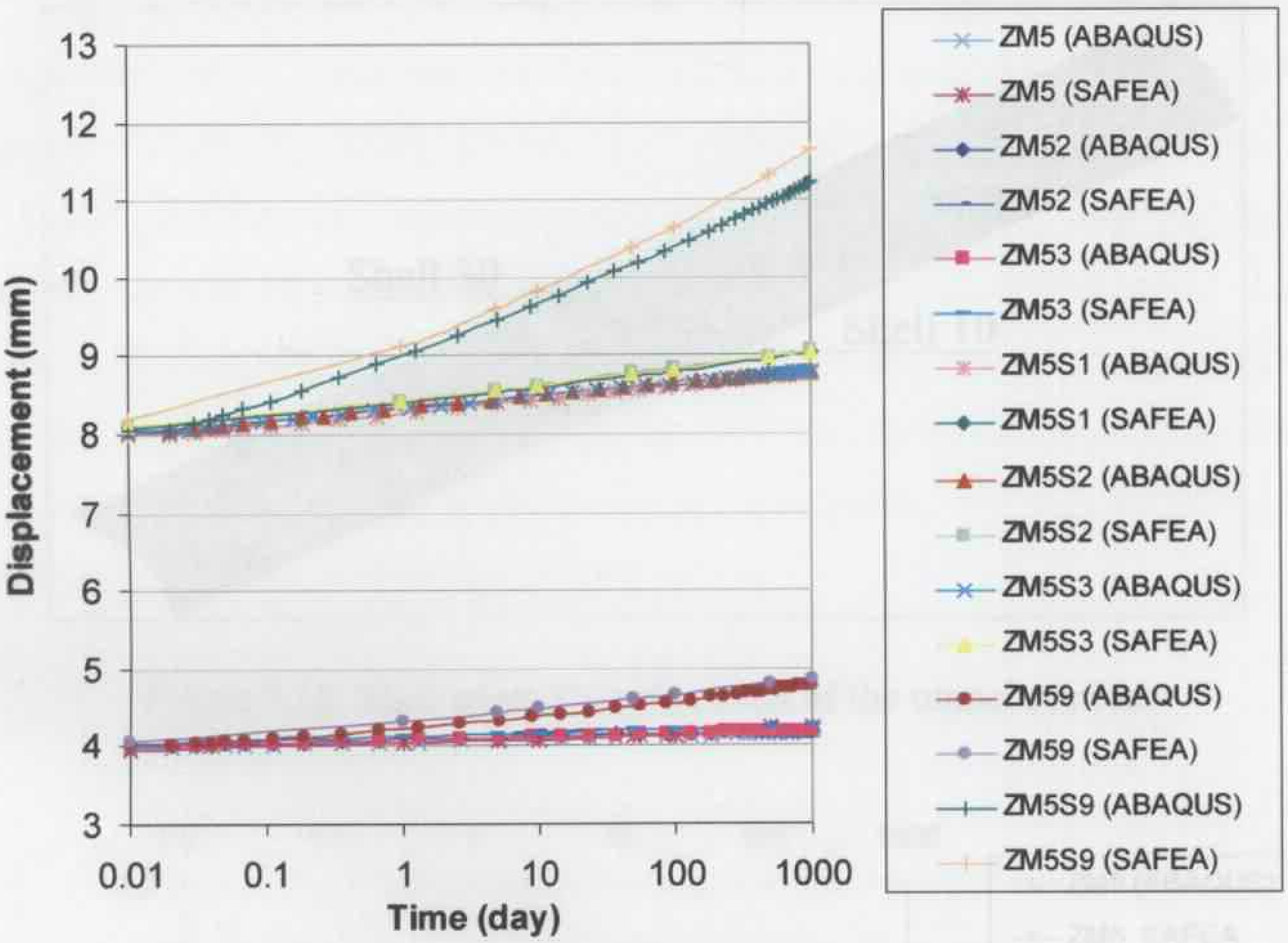

Figure 7.11: Creep closures of flat roof tunnels.

In the crest of a flat roof tunnel, the lining is under bending in the central flat part (shell element No.30) and under compression in the curved part (shell element No.10) as shown in Figure 7.12. Two sets of creep parameters are selected for the lining under different stress distributions, and the stress increments in the lining shell elements at the crest of the tunnel sections are discussed in the following paragraphs.

Figure 7.13a shows that in flat roof tunnels, the tangential stress in the shell element in the centre part of the crown of the tunnels (Shell 30) decreases significantly. The initial lining stresses in the deeper tunnels (ZM5S1, ZM5S2 and ZM5S3 at 100m depth) are bigger and drop at a faster rate than in the shallow tunnels (ZM5, ZM52 and ZM53 at 50m depth). As well, the lining stresses in tunnels excavated in the rock which creeps faster (ZM59, ZM5S9) also decrease at a faster rate. It can also be seen that the stresses in the Novotex, HPP and Strux fibre reinforced shotcrete lining change at a similar rate, so the fibre types do not affect the stress changes in the lining significantly. It is also seen that after a long time period, the final stresses in the lining all drop to a close range for deep and shallow tunnels in a certain rock.

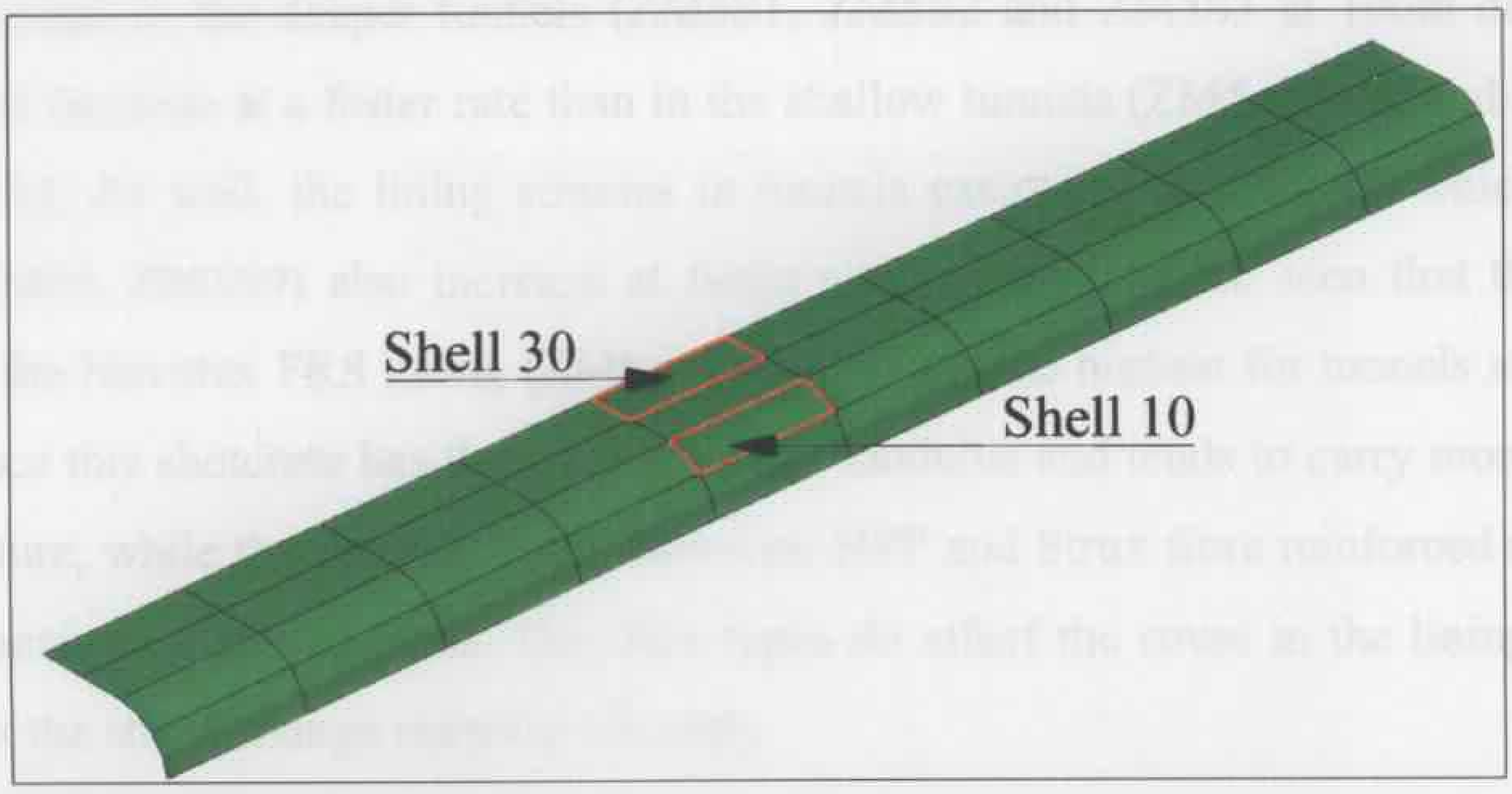

Figure 7.12: Shell elements at the crest of the tunnel section.

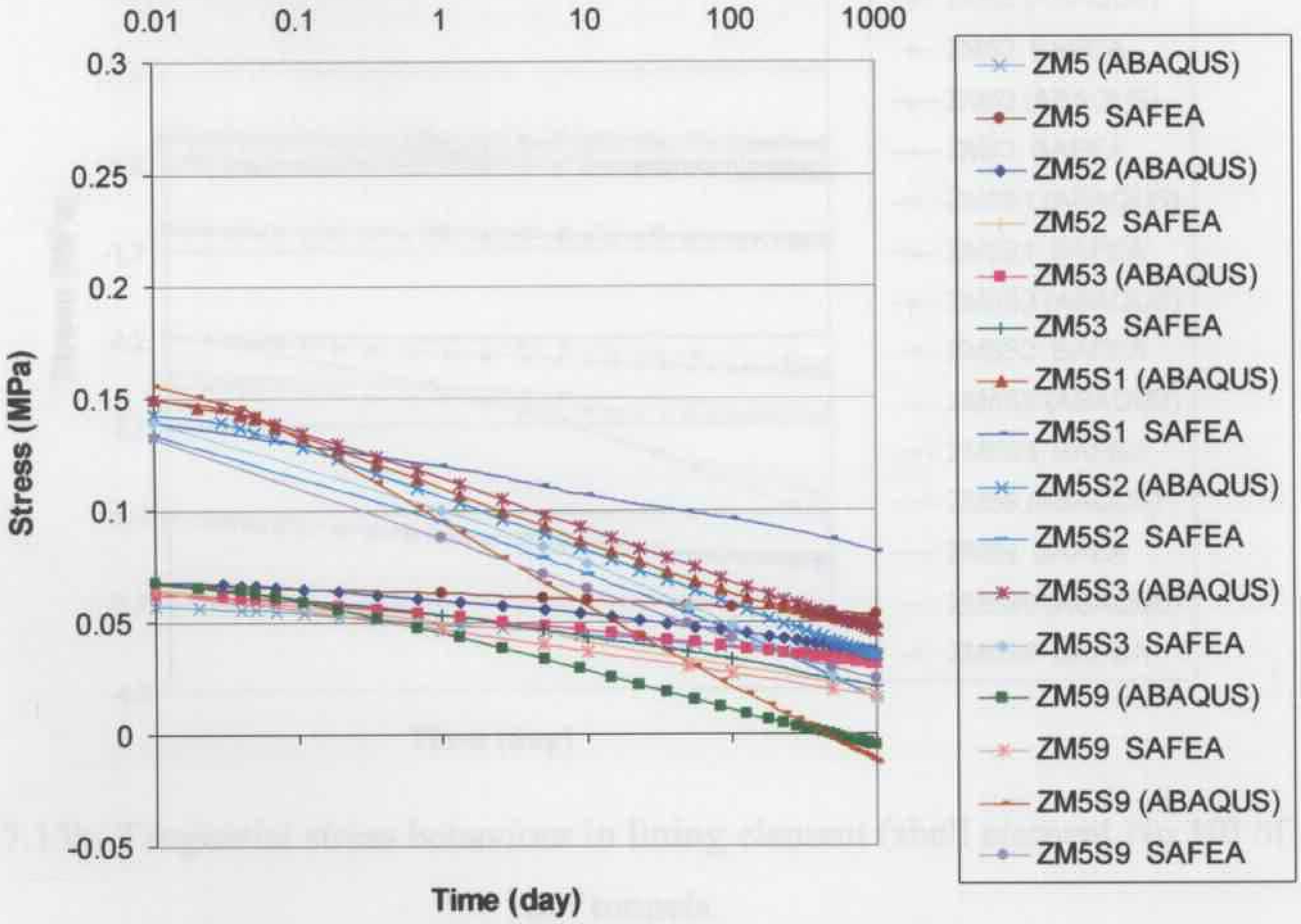

Figure 7.13a: Tangential stress behaviour in lining element (shell element No.30) of flat roof tunnels.

Figure 7.13b shows the tangential stresses in the shell element in the curved part on the crown of the tunnels (Shell element No.10). It can be seen that the linings are under compression and the stresses increase at a nearly linear rate with log-time. The initial lining stresses in the deeper tunnels (ZM5S1, ZM5S2 and ZM5S3 at 100m depth) are bigger and increase at a faster rate than in the shallow tunnels (ZM5, ZM52 and ZM53 at 50m depth). As well, the lining stresses in tunnels excavated in the rock which creeps faster (ZM59, ZM5S9) also increase at faster rates. It can also be seen that the initial stress in the Novotex FRS lining (ZM5 and ZM5S1) is the highest for tunnels at a given depth since this shotcrete has the highest elastic modulus and tends to carry more load in the structure, while the stresses in the Novotex, HPP and Strux fibre reinforced shotcrete linings increase at similar rates. The fibre types do affect the stress in the lining, but do not affect the stress change rates significantly.

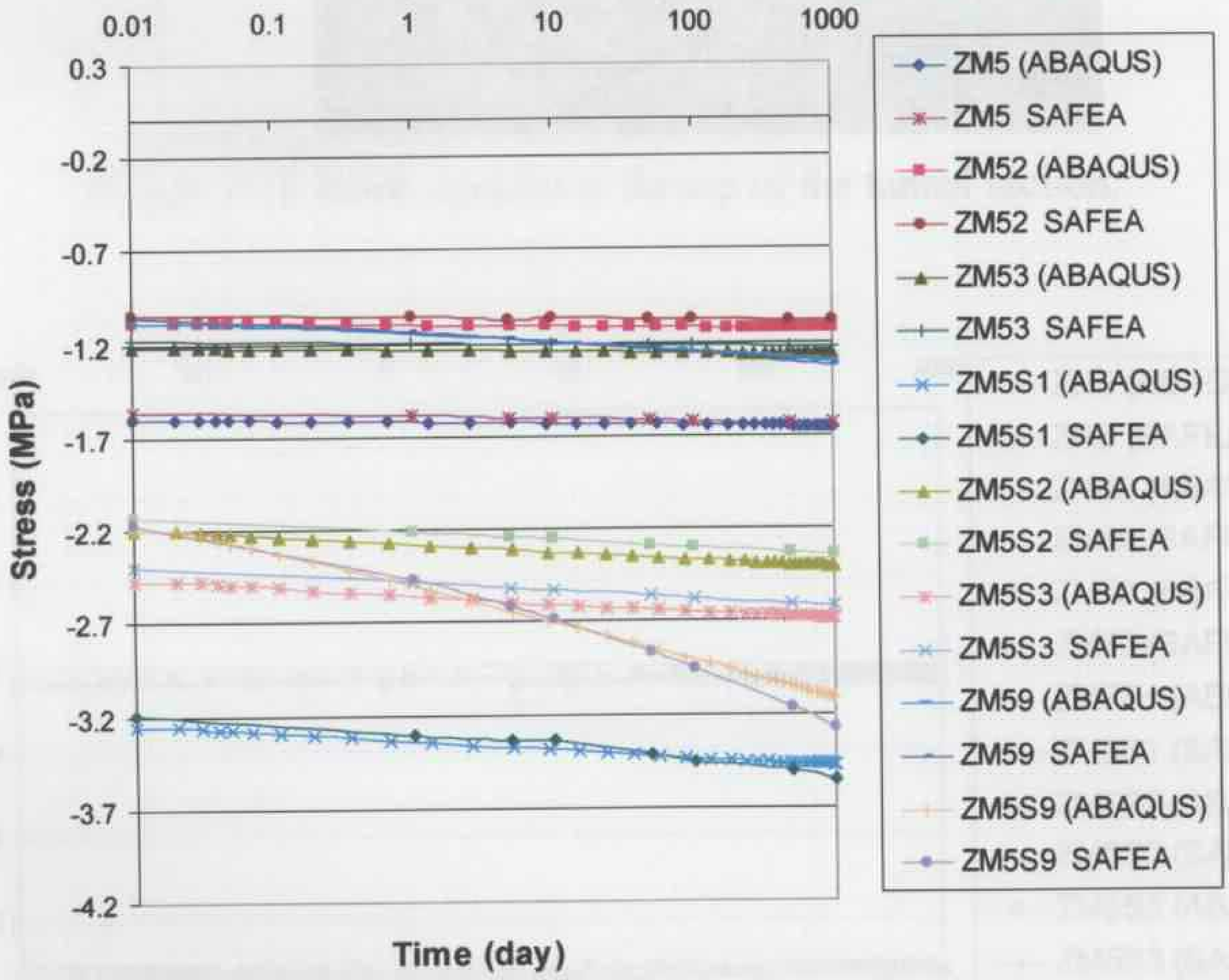

Figure 7.13b: Tangential stress behaviour in lining element (shell element No.10) of flat roof tunnels.

In these flat roof tunnel models, the rock surrounding the tunnel section is under compression, and the stress in the rock element at the top of the tunnel sections as shown in Figure 7.14 is discussed in the following. It can be clearly seen in Figure 7.15 that the initial stresses in the rock around the deeper tunnels are higher than in the shallow tunnels, while in all these cases, the stresses in the rock around the tunnels change very slowly or exhibit little change with time due to the slow creep behaviour.

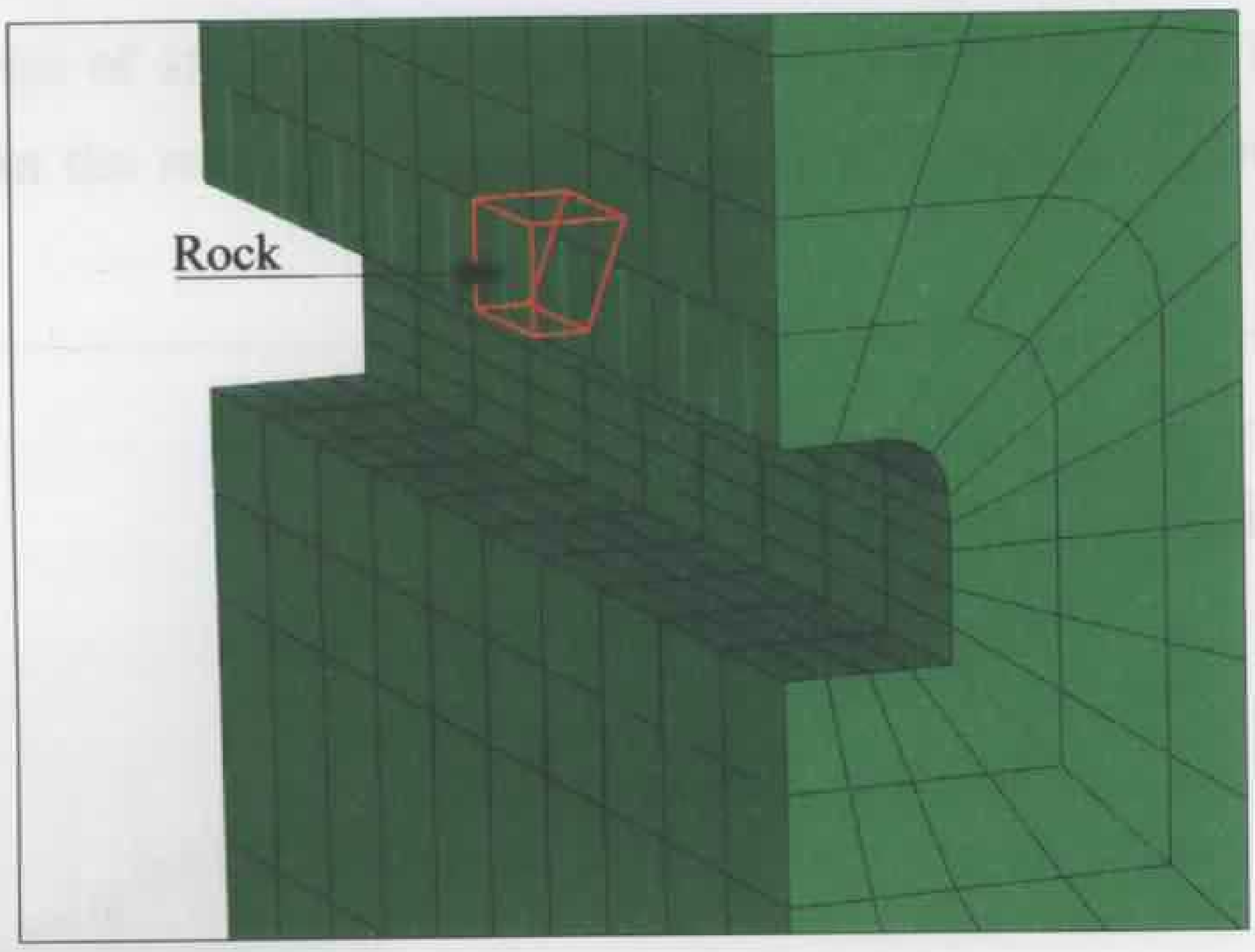

Figure 7.14: Rock element at the top of the tunnel section.

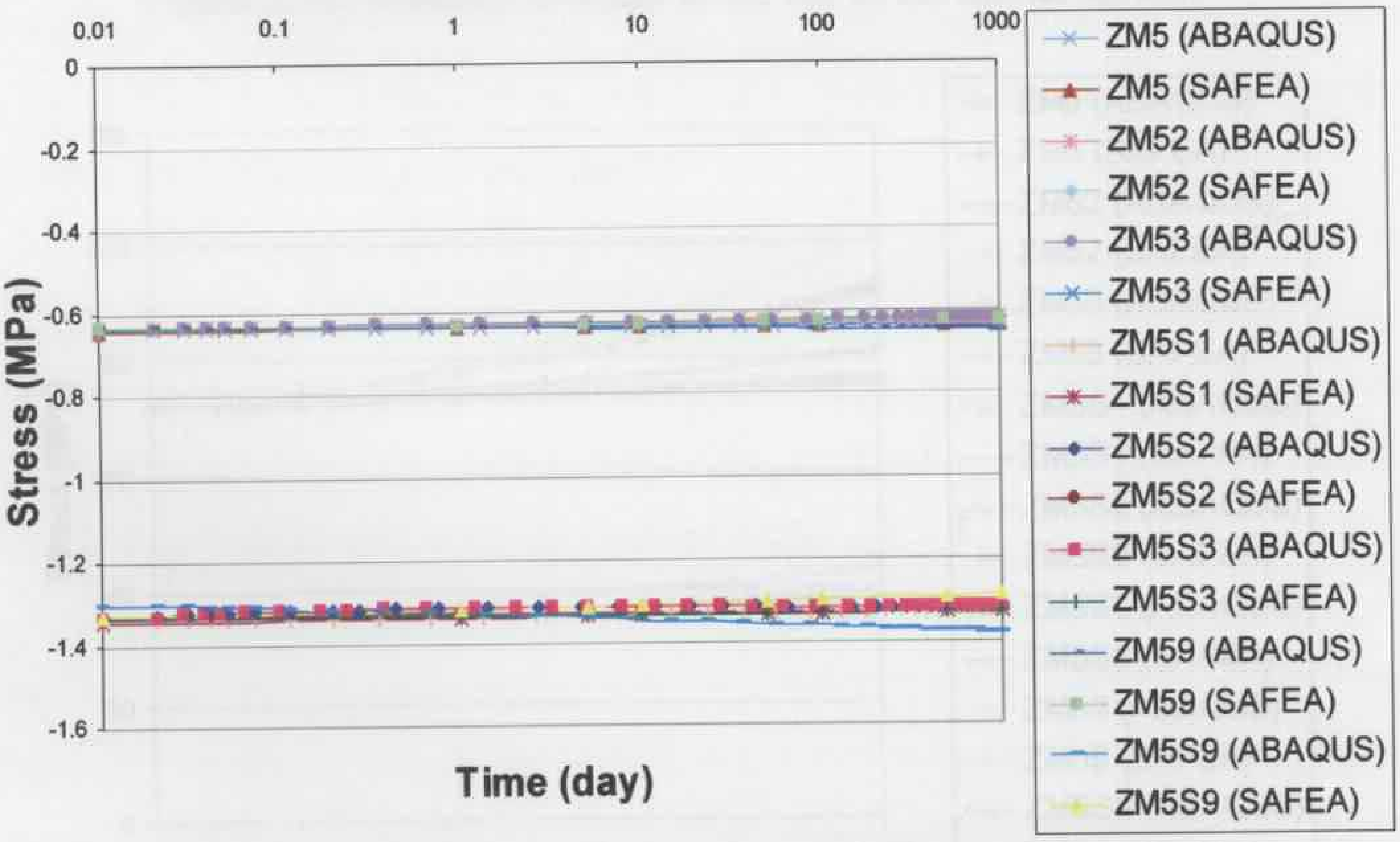

Figure 7.15: Stress in rock surrounding flat roof tunnels

The stress change in the rockbolt element at the middle section of the tunnel model as shown in Figure 7.16 will now be examined. In the flat roof tunnels, the initial tension stresses in the rockbolts of the deeper tunnels (ZM5S1, ZM5S2 and ZM5S3 at 100m depth) are higher and increase at a faster rate than in the shallow tunnels (ZM5, ZM52 and ZM53 at 50m depth), while the different creep behaviour of the FRS materials does not affect the change of stress in the rockbolts a lot. The stresses in the rockbolts of tunnels excavated in the rock which creeps faster (ZM59, ZM5S9) also increased at a faster rate.

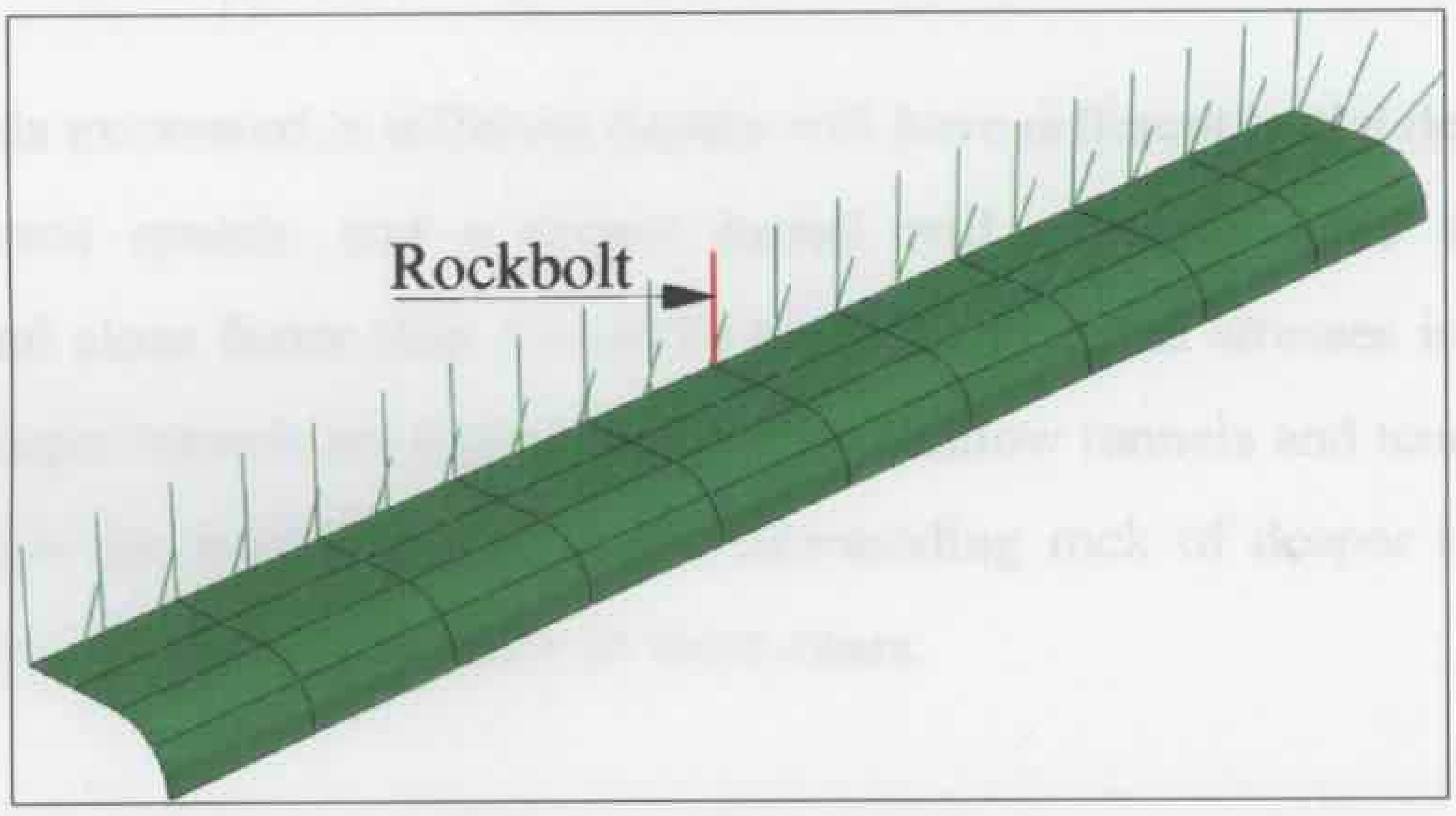

Figure 7.16: Rockbolt element at the top of the tunnel section.

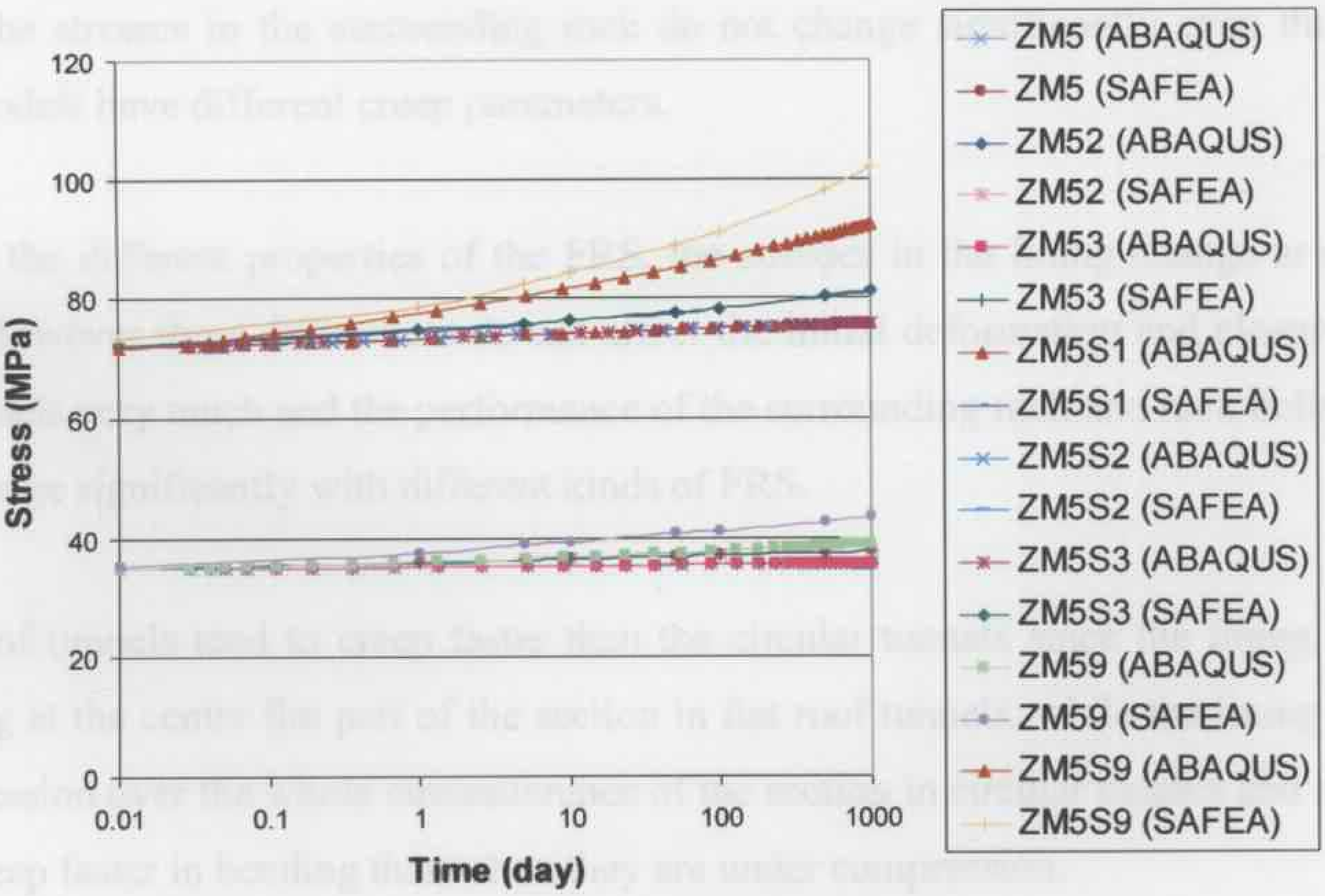

Figure 7.17: Stress in rock bolts in crown of flat roof tunnels.

7.3 CONCLUSIONS

In this chapter, some flat roof tunnels supported by three types of fibre reinforced shotcrete lining and steel rockbolts were modelled. The tunnels were constructed at different depths and under different ground conditions, and the time-dependent behaviour of these tunnels was analysed. The conclusions are drawn based on the specific ground conditions, material elastic moduli and creep parameters selected in the numerical models.

Flat roof tunnels excavated at different depths will have different initial deformations and close at different speeds, and a deeper tunnel will generally have a bigger initial deformation and close faster than a shallow tunnel. The initial stresses in the lining and rockbolts of deeper tunnels are higher than for the shallow tunnels and tend to change at a faster rate, while the initial stresses in the surrounding rock of deeper tunnels are also higher but do not change significantly in these cases.

The closure deformation of the tunnels in the rock which creeps faster will increase at a faster rate, and the stresses in the lining and rockbolts also change at relatively faster rates, while the stresses in the surrounding rock do not change significantly even though the rock models have different creep parameters.

Due to the different properties of the FRS, the stresses in the lining change at different rates. However these differences do not affect the initial deformation and closure rate of the tunnels very much and the performance of the surrounding rock and rock bolts also do not change significantly with different kinds of FRS.

Flat roof tunnels tend to creep faster than the circular tunnels since the lining is under bending at the centre flat part of the section in flat roof tunnels, while the lining is under compression over the whole circumference of the section in circular tunnels and materials will creep faster in bending than when they are under compression.

During the creep period, the stresses in the shotcrete lining, surrounding rock and rock bolts tend to change due to the different time-dependent properties of the materials. In these combined FRS lining and rock bolt tunnel support systems, the stress in the surrounding rock changes slowly, the stress in the lining tends to decrease or increase at different locations, and the stress in the rockbolts tend to increase over time. This implies that if we take into consideration the creep behaviour of the structure in the design stage, we may need to increase the design safety factor of the FRS lining and rockbolts to satisfy the long-term strength requirements of the structure.

For these cases, the analyses show that the 1000 day creep closure and performance are in an acceptable range for the tunnels examined here.

CHAPTER 8 - CASE STUDY - TUNNEL PROJECTS BACK ANALYSIS

8.1 INTRODUCTION

In this chapter, the finite element method was used to investigate the time-dependent performance of some practical tunnel projects. The creep properties of geo-materials can be obtained through laboratory creep tests on the material specimens, or be extrapolated through the back analysis of the time-recorded field observation data of tunnel projects. With the obtained creep parameters of the ground materials, the finite element method can be used to predict the time-dependent deformation and stress in the support systems of tunnels with different shapes and/or constructed at different depths.

Three tunnel projects were selected to be modelled by the finite element programs, the first one is the Frejus Tunnel which connected France and Italy, the second one is the Lane Cove Tunnel which was constructed in Sydney, Australia, and the last one is the Middle Marsyangdi Hydropower (MMH) tunnel in Nepal. The creep parameters for the Hawkesbury sandstone used in the Lane Cove tunnel model was obtained through a laboratory creep test, while the creep parameters for the schistose rock in the Frejus tunnel models and the phyllitic quartzite in the MMH tunnel models were extrapolated through the back analysis of the time-recorded field observation data of tunnel openings. The time-dependent field observation data of the tunnels' deformation was compared with the predicted results obtained through the numerical tunnel models.

8.2 FREJUS TUNNEL

The Frejus road tunnel was constructed to link Modane, France and Bardoneccia, Italy at an average altitude of 1260m (Sulem et al. 1987). The tunnel is 12.8 km long and 14 m wide, the overburden depth of the tunnel varies from about 600 to 1200 m along the length. The tunnel was excavated through schistose rock and supported by rockbolts and shotcrete lining.

8.2.1 NUMERICAL TUNNEL MODEL

A typical cross section of the tunnel is shown in Figure 8.1, the convergence measurements of different tunnel sections at different depths were recorded. The analysis has been carried out based on the time-dependent deformation of the tunnel section in the 1-4 direction as shown in Figure 8.1.

Only half of the tunnel section was modelled since it is symmetrical, and two numerical models were built up. Model Fre1 refers to the tunnel section 5 with an overburden depth of 600 m, while model Fre2 refers to the tunnel section 125 with an overburden depth of 1200 m. The cross section of the numerical tunnel model is shown in Figure 8.2, and the self weight of the ground was assumed to be 24000N/m^3. The 550 m depth rock was transferred as a pressure load of 13.2 MPa applied on the top surface of model Fre1, and again for the 1150 m depth tunnel the overburden pressure was transferred as a pressure load of 27.6 MPa applied on the top surface of model Fre2.

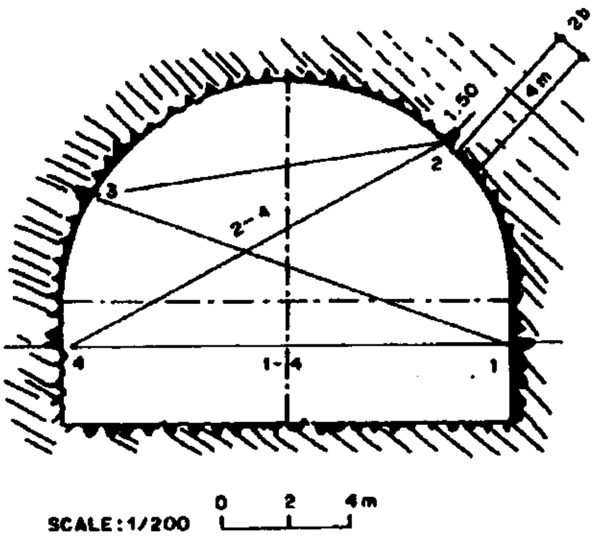

Figure 8.1: Cross section of Frejus tunnel (Sulem et al. 1987).

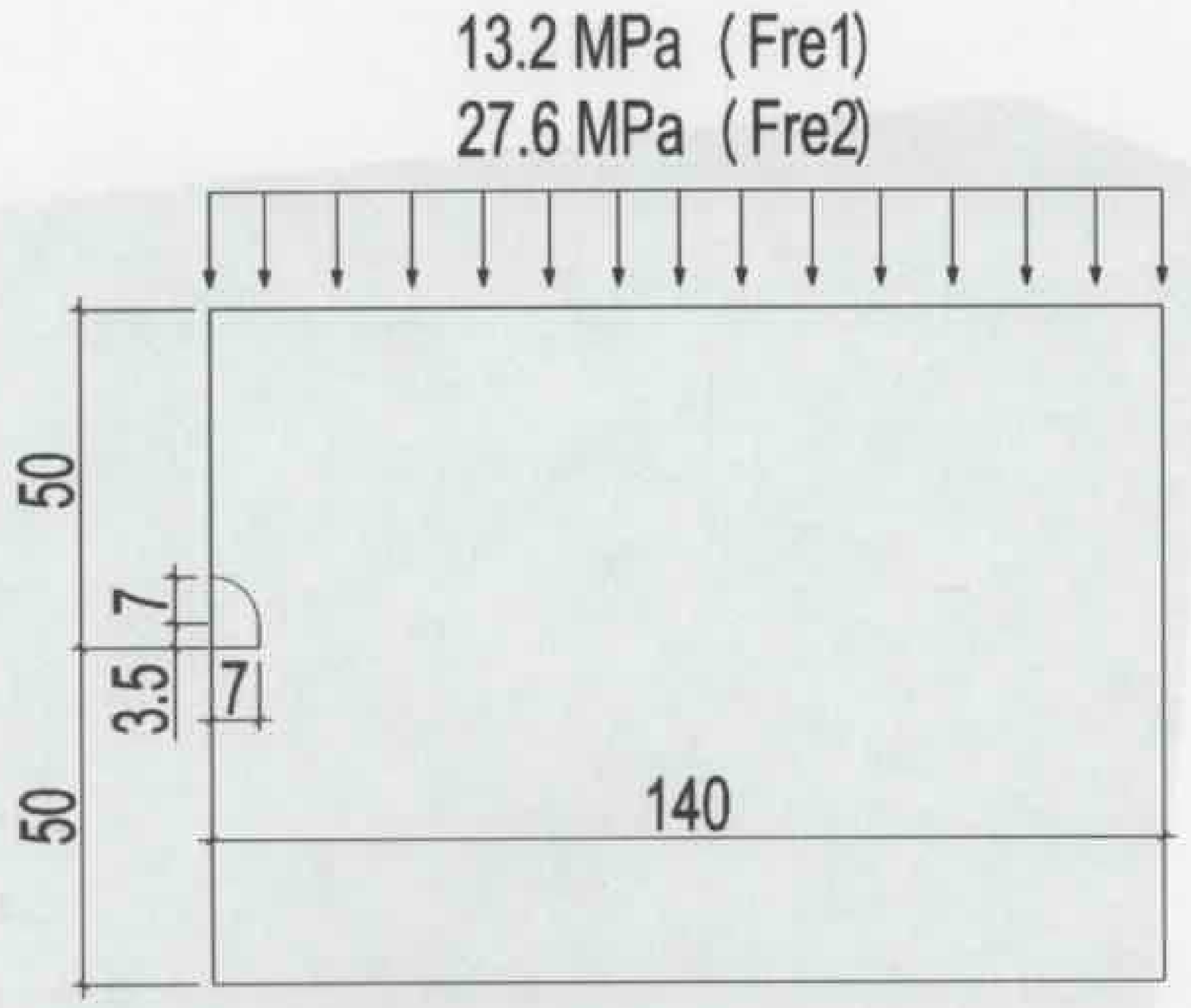

Figure 8.2: Numerical cross section of Frejus tunnel model (unit: m).

The horizontal length of the tunnel was set as 40m and the tunnel mesh was divided into 10 even partitions in the tunnel horizontal axial direction so that the deformation in the middle section would not be affected significantly by the face boundary restraints. The finite element meshes generated for SAFEA and ABAQUS are shown in Figures 8.3a & 8.3b respectively.

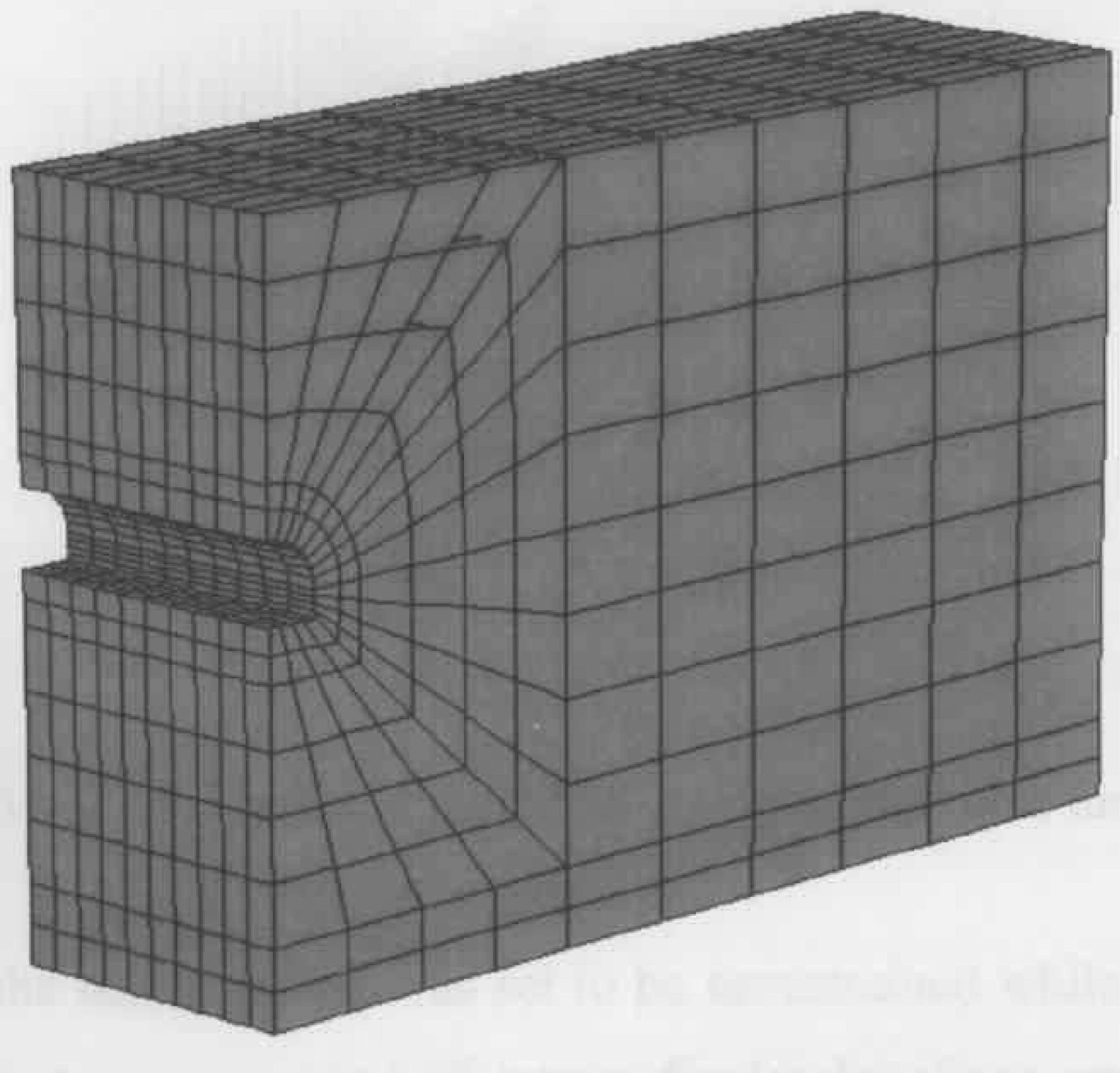

Figure 8.3a: Mesh of Frejus tunnel model for SAFEA.

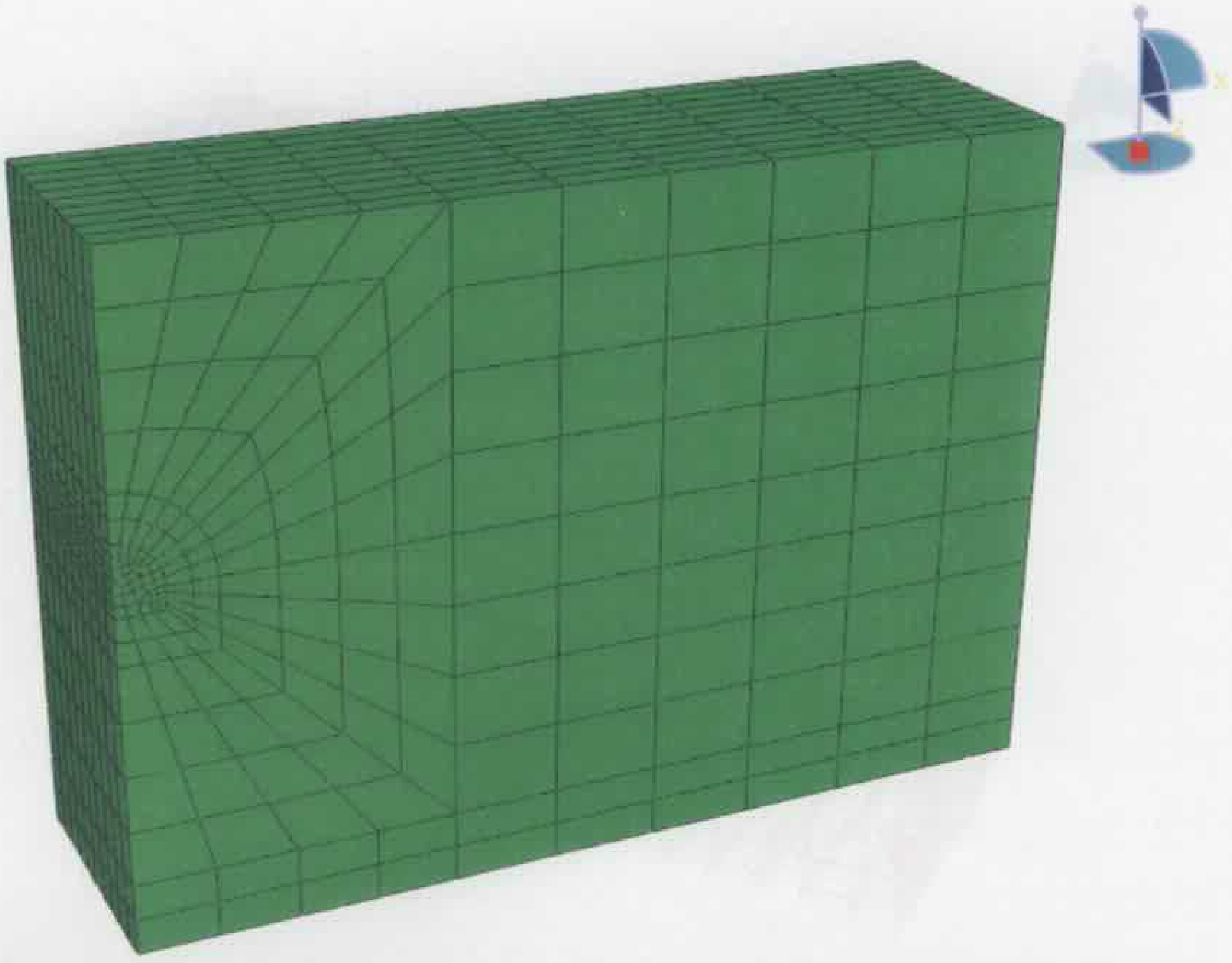

Figure 8.3b: Mesh of Frejus tunnel model for ABAQUS.

A 200mm thick shotcrete lining and 4 m long Φ35 mm steel rockbolts were applied on the crest of the section, and the mesh for the lining and rockbolts is shown in Figure 8.4.

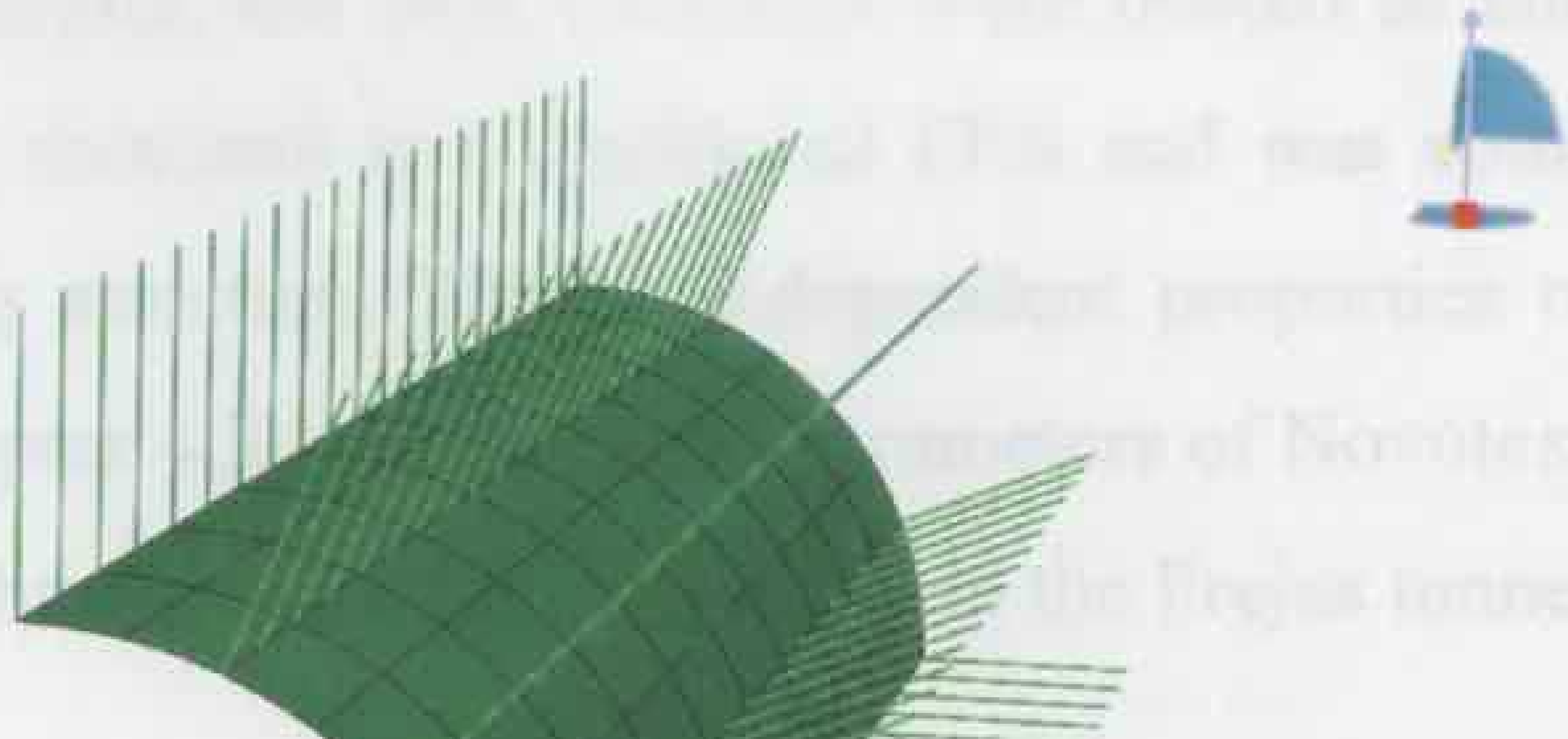

Figure 8.4: Mesh of lining and rockbolts elements in Frejus tunnel model.

The top surface of the tunnel model was set to be unrestrained while the base and sides were restrained against movement in both perpendicular directions, and the self weight of the ground was assumed to be 24000N/m^3. The surface loads of 13.2 MPa for Fre1 (or 27.6 MPa for Fre2) were applied on the geometric model. The boundary conditions for the tunnel model are shown in Figure 8.5.

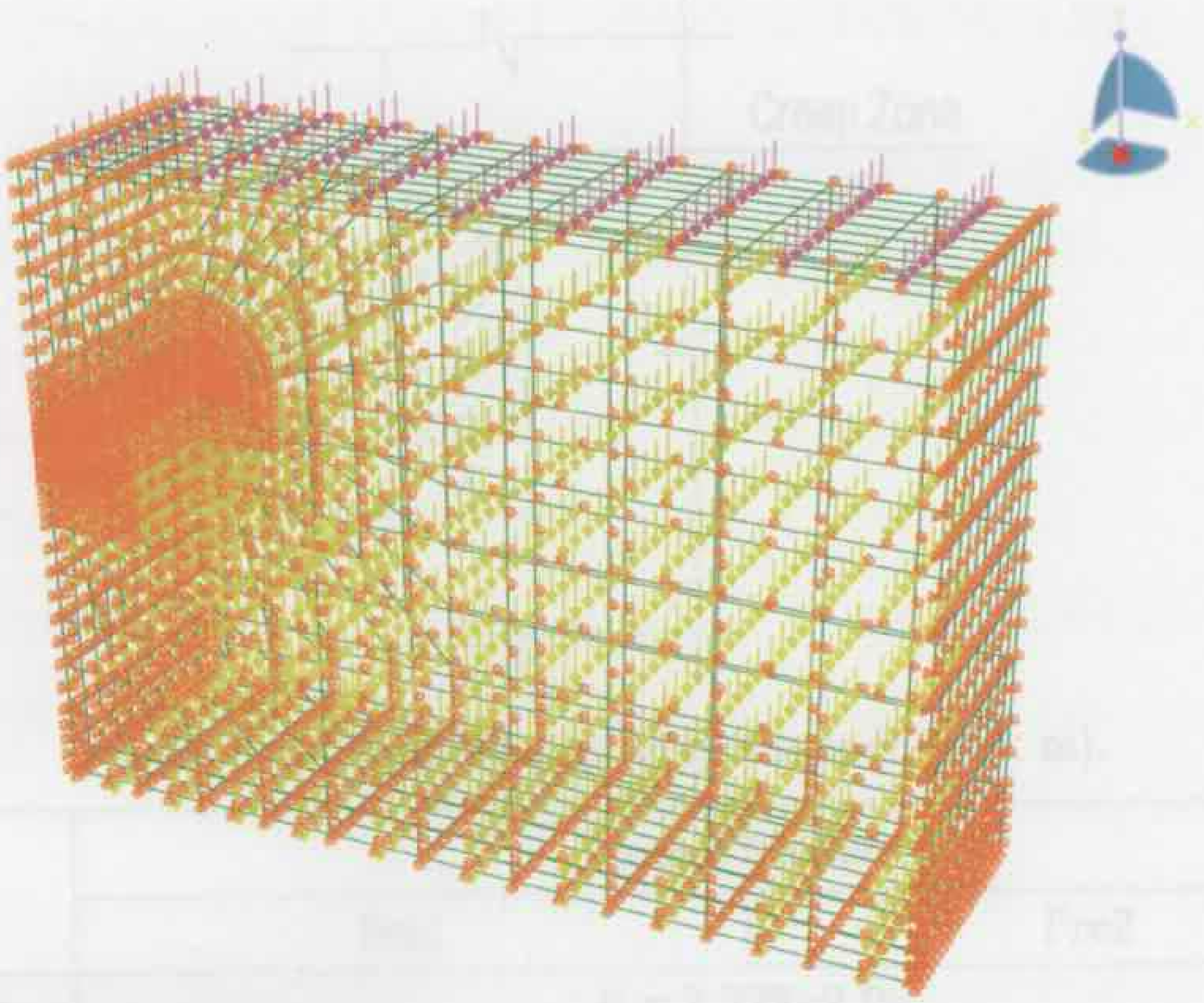

Figure 8.5: Boundary conditions of Frejus tunnel models.

8.2.2 MATERIAL PROPERTIES

In the Frejus tunnel model, the steel rockbolts were treated as elastic i.e. not creeping. Steel fibre reinforced shotcrete is a traditional FRS and was commonly used in tunnel projects for the lining structure. The time-dependent properties of Novotex FRS have been discussed in Chapter 4.3, and the creep parameters of Novotex FRS were selected to represent the creep behaviour of steel FRS lining in the Frejus tunnel models.

During the tunnel excavation process, the generated increment of deviator stress is a maximum in a surrounding region of the tunnel section, and it is assumed that the creep deformation only occurs when the material is under a change in deviator stress, so that a region surrounding the tunnel section as shown in Figure 8.6 is set as the 'creep zone' in the Frejus tunnel models. The Frejus tunnel was excavated in schistose rock, the creep parameters of the schistose rock was extrapolated through the back analysis of the time-recorded tunnel section convergence data. The material properties of the schistose rock, FRS and rockbolts for the Frejus tunnel models are summarized in Table 8.1.

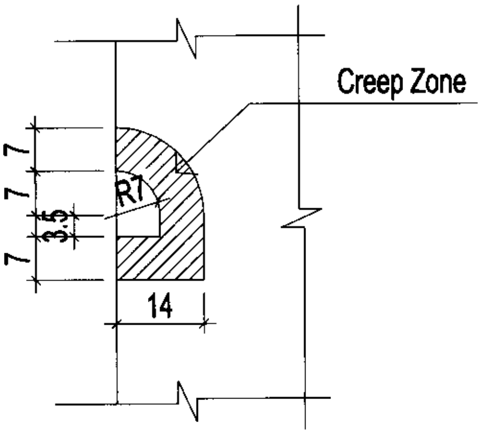

Figure 8.6: Creep Zone of Frejus tunnel (unit: m).

	Tunnel Models	
	Fre1	Fre2
Schistose rock	E = 2.328e9 Pa ν = 0.3	
Creep parameters of schistose rock	F=5.2e-10 n=0.85 m=-0.8 (ABAQUS)	
	σ = 12 MPa A=1 B=-0.067 α=100 (SAFEA)	σ = 25 MPa A=1 B=-0.065 α=100 (SAFEA)
Shotcrete lining	Novotex E = 5.848e9 Pa ν = 0.15 Thickness = 0.2m	
Creep parameters of shotcrete	Compression region F=4.0e-37, n=4.6, m=-0.6 (ABAQUS)	
	σ = 14 MPa A=1 B=-0.097 α=10 (SAFEA)	σ = 16 MPa A=1 B=-0.083 α=100 (SAFEA)
Rockbolts	ϕ35X4000mm E = 2.0e11 Pa ν = 0.3	

Table 8.1: Material properties of Frejus tunnel models.

8.2.3 BACK ANALYSIS OF TUNNEL CREEP DEFORMATION

Frejus tunnel was excavated through the schistose rock and the self weight of the ground is assumed to be 24000N/m^3. The initial ground conditions of the Frejus tunnel were generated using Equation 8.1.

$$\begin{aligned}\sigma_{1,2} &= \sigma_{NS} = \sigma_{WE} = 0.5\sigma_v \quad MPa \\ \sigma_3 &= \sigma_v = 0.024H \quad MPa\end{aligned} \tag{8.1}$$

where H is the depth below the ground surface, σ_v is the vertical stress, σ_{WE} and σ_{NS} are horizontal stress in west-east and north-south direction respectively (the tunnel runs north-south direction). The initial field deformation due to the gravity load of the ground was reset to zero since the initial deformation of the ground under gravity load has already finished before the excavation of the tunnel. The excavation of the ground and establishment of lining and rockbolts were controlled by removing and activating corresponding elements.

The convergence of the tunnel section was measured in the horizontal 1-4 direction as shown in Figure 8.1. During the numerical tunnel excavation process, the instantaneous horizontal deformation of the ground is a maximum in the side walls around the tunnel section. Figure 8.7 shows the deformation of the Frejus tunnel at station 5 (Fre1 at 600m depth), and the deformation scale factor is set as 10 to make the deformation identifiable. It can be seen that the top section is moving down, while the bottom section is moving up, and the side wall is pushed inwards after excavation.

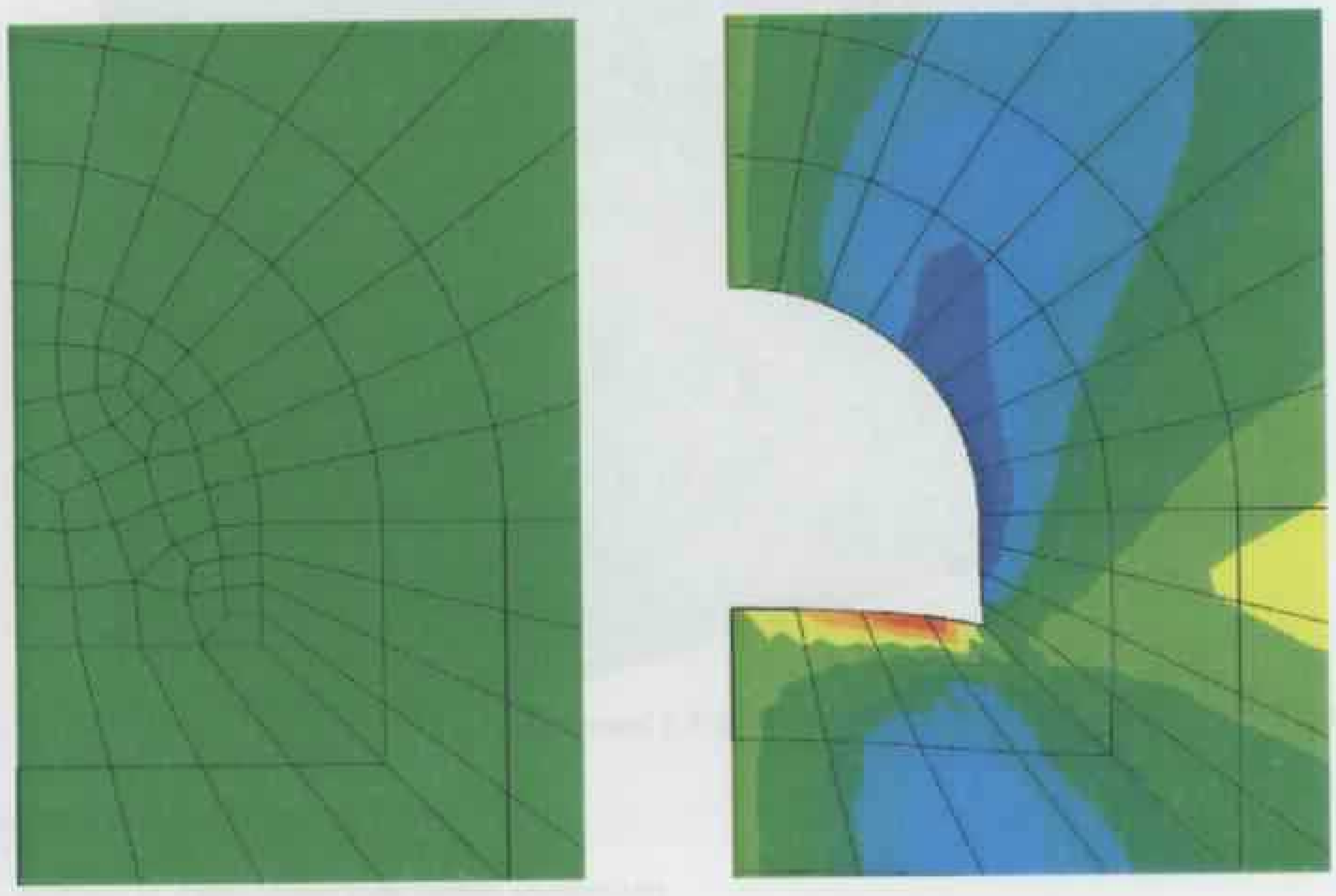

Before Excavation After Excavation

Figure 8.7: Tunnel deformation after excavation.

An example of the horizontal deformation of the Frejus tunnel model at station 5 (Fre1 at 600m depth) are shown in Figures 8.8a&b.

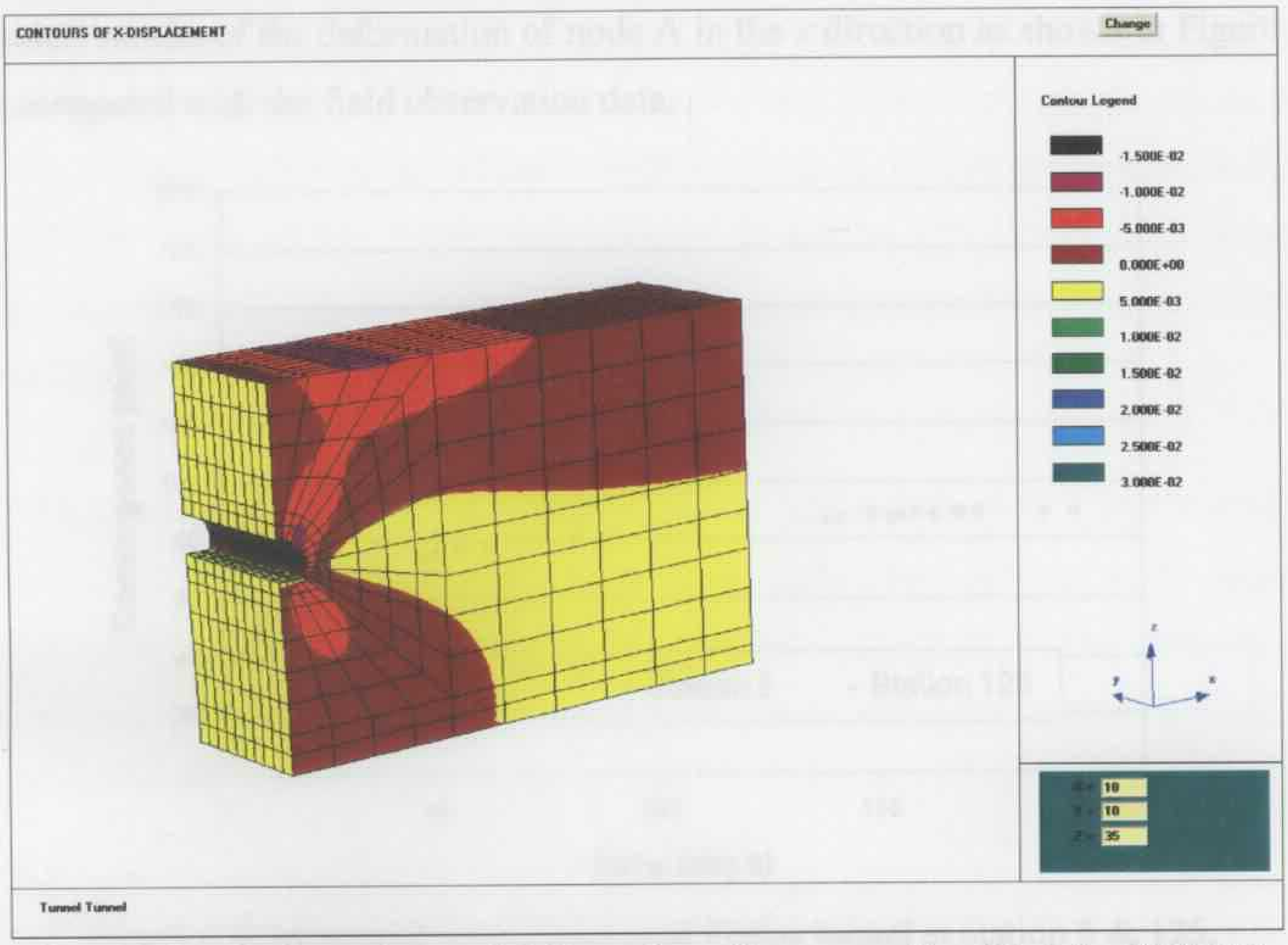

Figure 8.8a: Horizontal tunnel deformation after excavation (Fre1 by SAFEA).

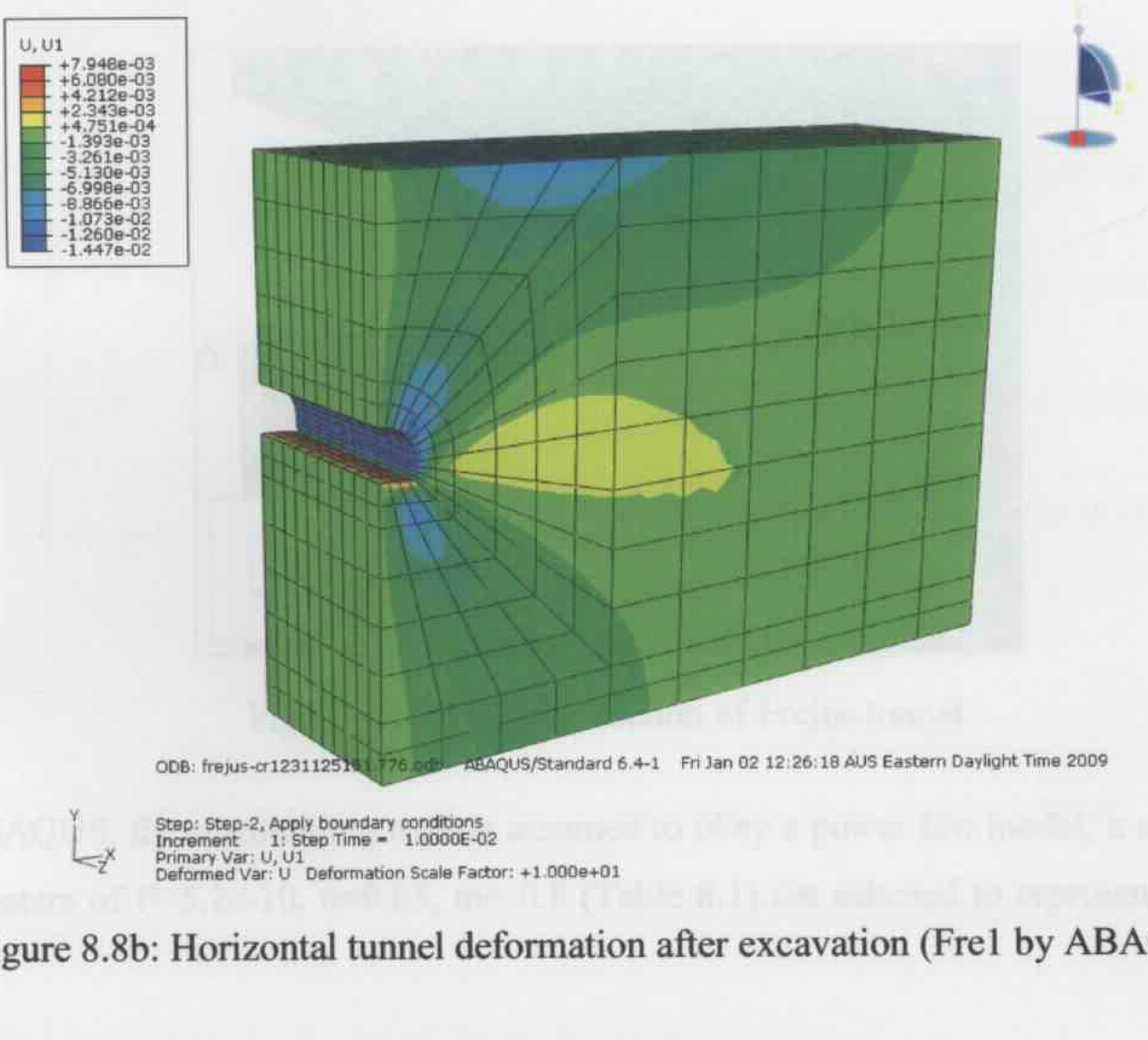

Figure 8.8b: Horizontal tunnel deformation after excavation (Fre1 by ABAQUS).

The horizontal convergence of the Frejus tunnel at station 5 and station 125 were measured with time in the 1-4 direction (Figure 8.1) as shown in Figure 8.9. The numerical results of the deformation of node A in the *x* direction as shown in Figure 8.10 were compared with the field observation data.

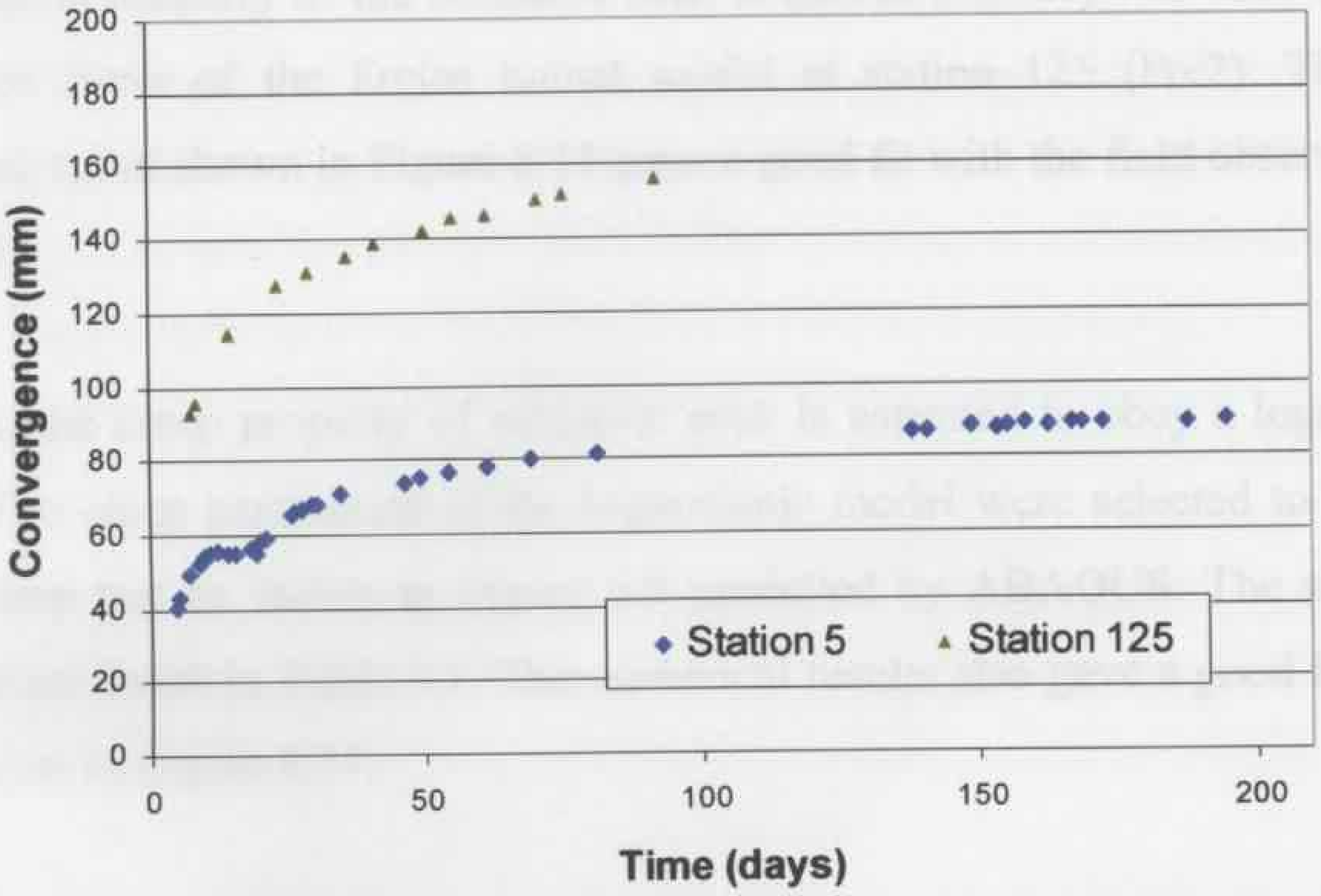

Figure 8.9: Measured convergences of Frejus tunnel at station 5 & 125.

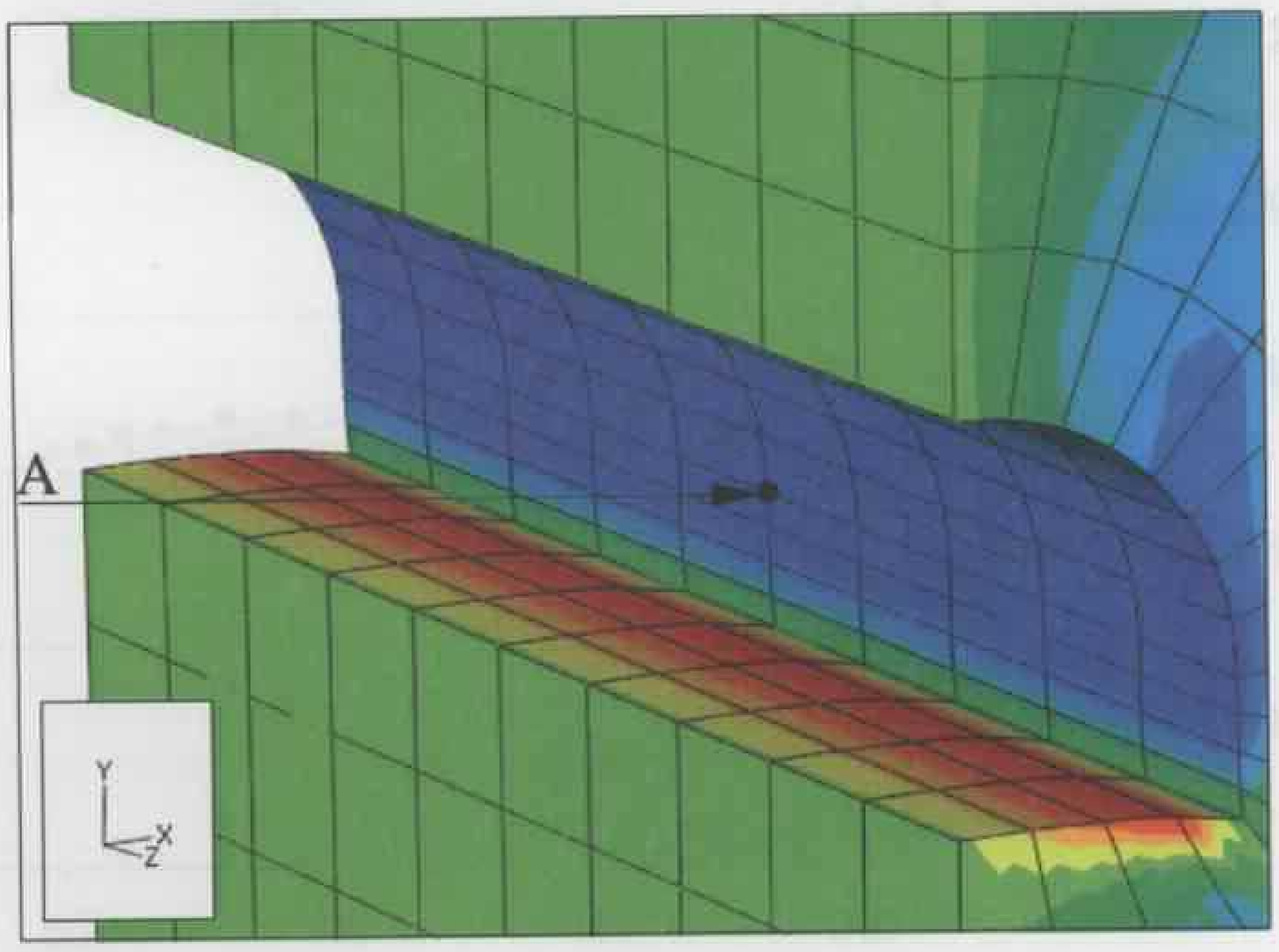

Figure 8.10: Opening section of Frejus tunnel.

In ABAQUS, the surrounding rock is assumed to obey a power law model, a set of creep parameters of F=5.2e-10, n=0.85, m=-0.8 (Table 8.1) are selected to represent the creep properties of the schistose rock. With the selected creep parameters, the numerical convergence curve of the Frejus tunnel model at station 5 can fit the field observation data well as shown in Figure 8.11. At station 125 of the Frejus tunnel, the overburden depth of the tunnel section is 1200 m. The same creep parameters used to represent the time-dependent property of the schistose rock at station 5 (Fre1) was used to predict the convergence curve of the Frejus tunnel model at station 125 (Fre2). The numerical convergence curve shown in Figure 8.11 gave a good fit with the field observation data at station 125.

In SAFEA, the creep property of schistose rock is assumed to obey a logarithmic-time function. The creep parameters of the logarithmic model were selected to fit numerical uniaxial creep test as shown in Figure 6.9 modelled by ABAQUS. The selected creep parameters are listed in Table 8.1. The numerical results also gave a good fit to the field data as shown in Figure 8.11.

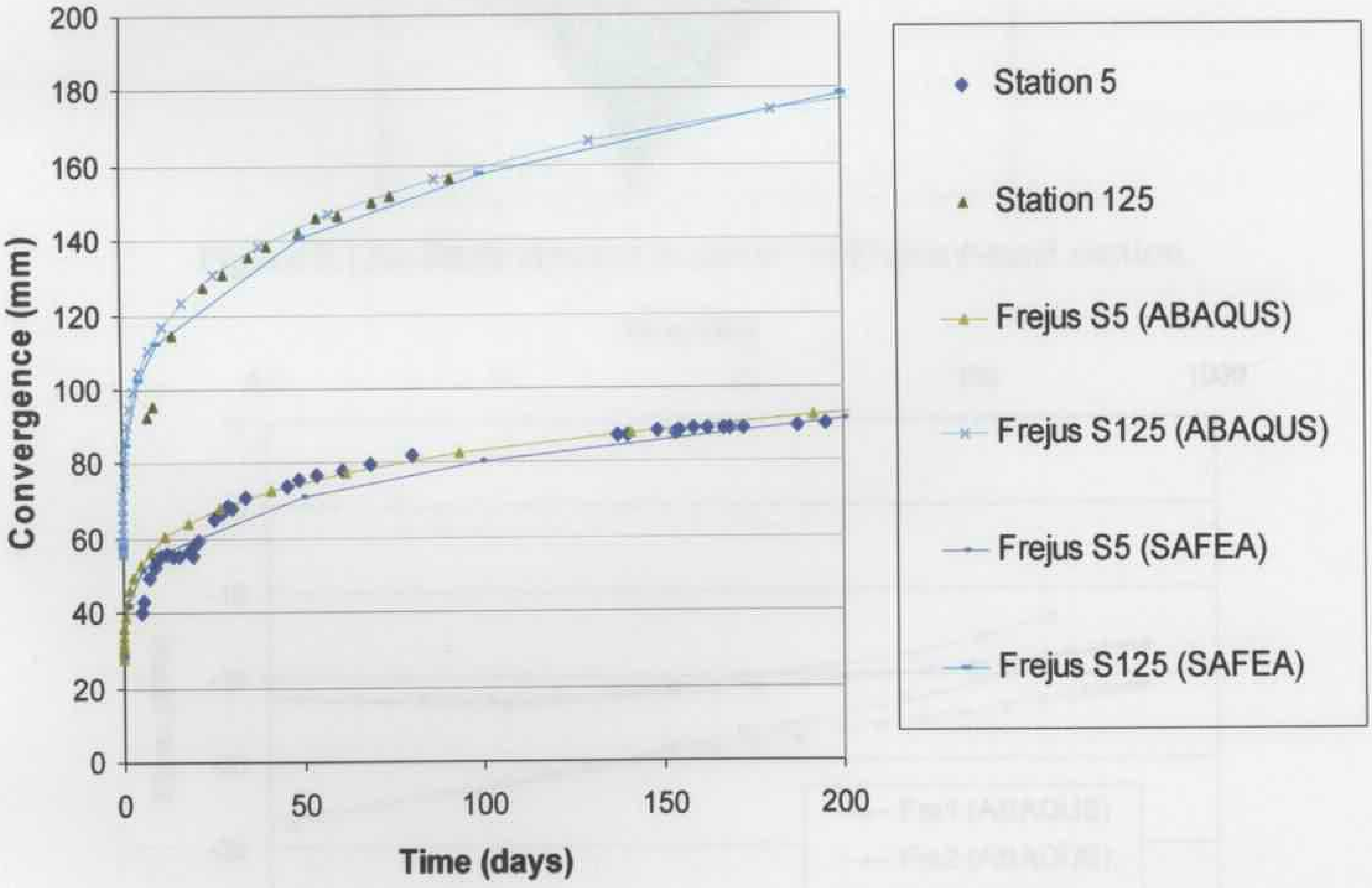

Figure 8.11: Measured and numerical convergence of Frejus tunnel.

Only the convergence of the tunnel was measured in the field, the stress in the lining, rockbolts and surrounding rock were not measured but discussed here based on the numerical results.

Figure 8.12b shows that the tangential stresses in the shell elements on the centre part of the crown of the Frejus tunnel (Shell element No. 75, Figure 8.12a) decrease significantly over time. The initial lining stresses in station 125 (Fre2 at 1200 m depth) are bigger and drop at a faster rate than in station 5 (Fre1 at 600 m depth). It is also seen that after a long time period, the final stresses in the lining drop to within a close range.

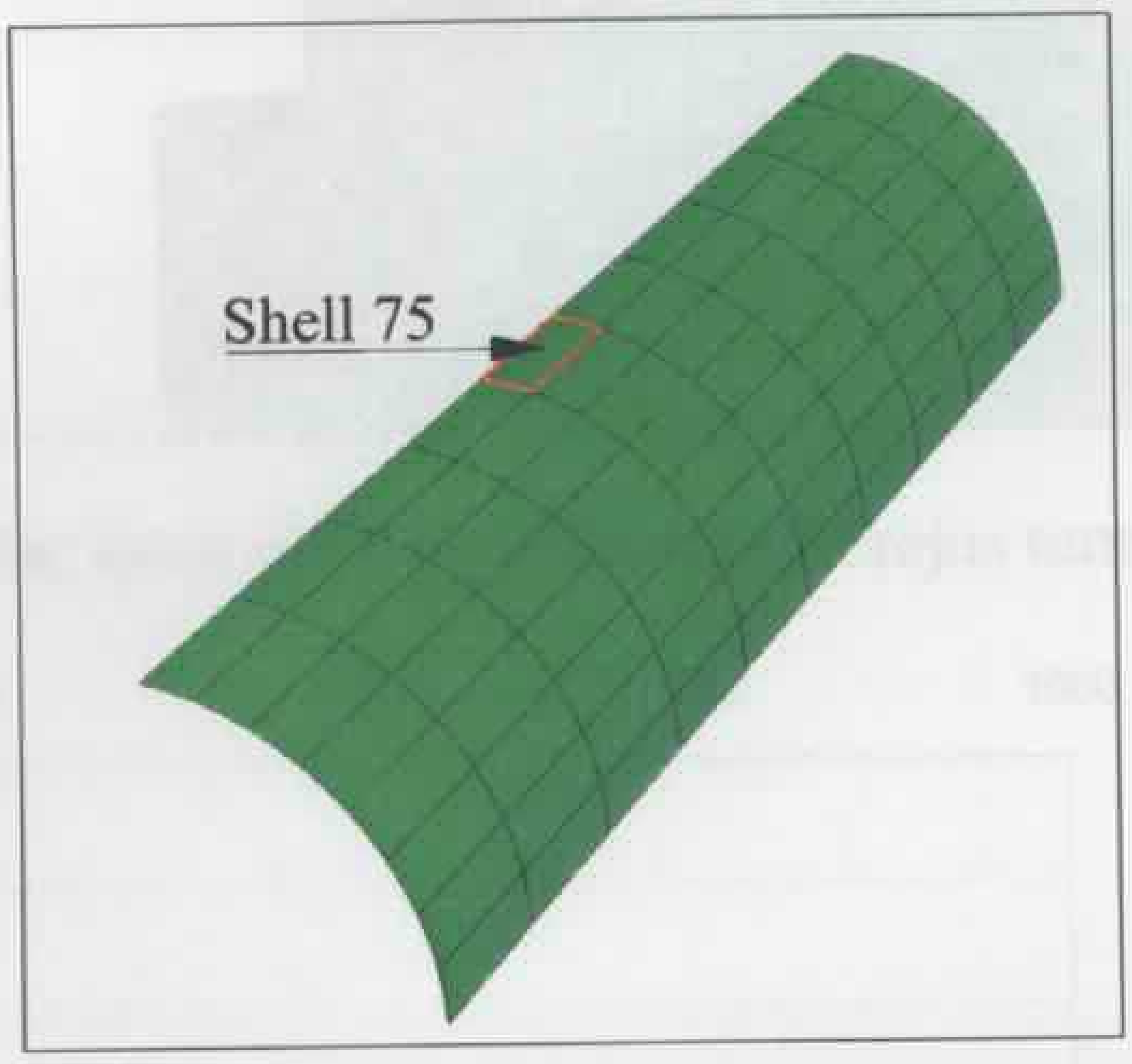

Figure 8.12a: Shell element in crown of Frejus tunnel section.

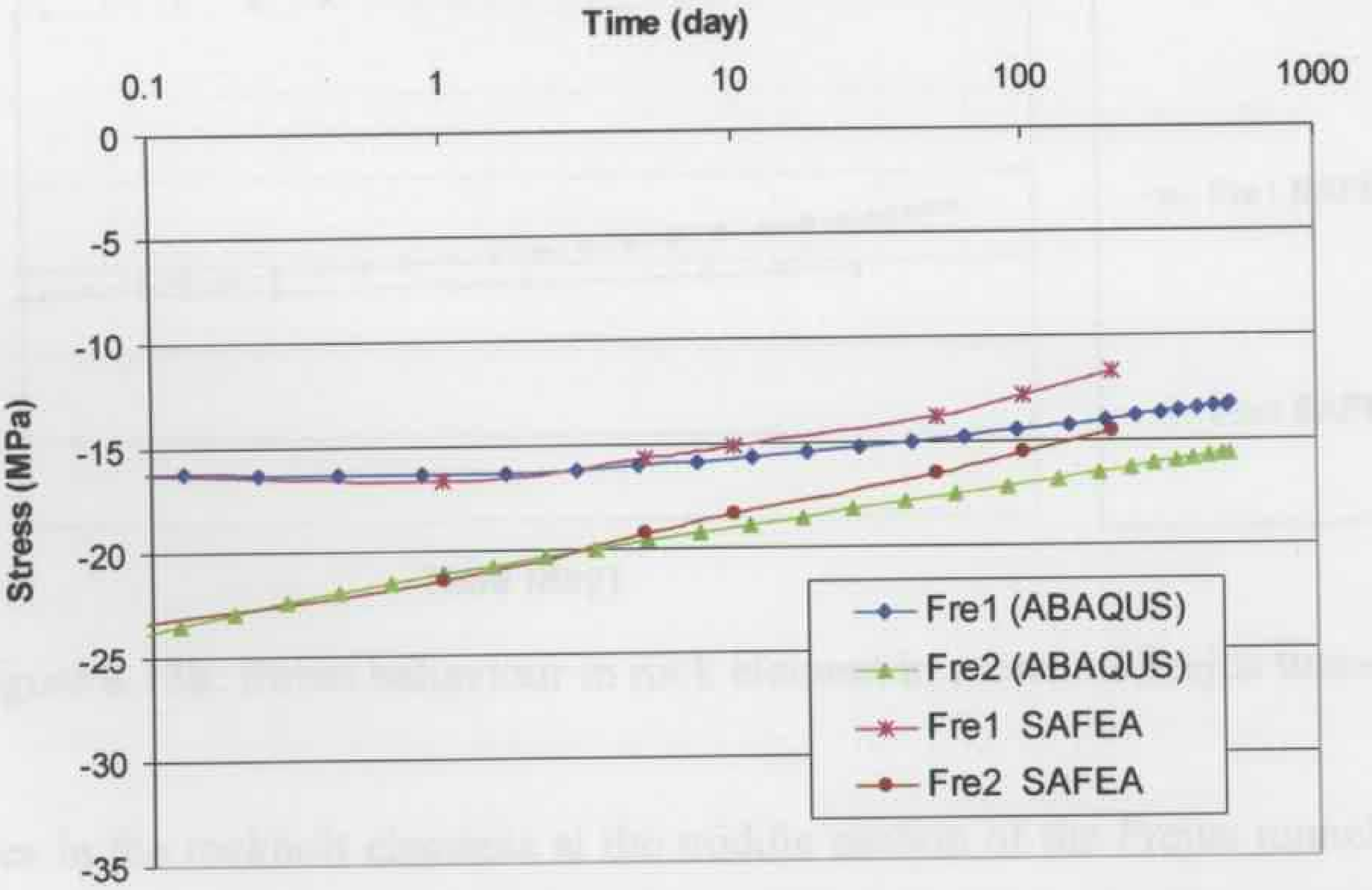

Figure 8.12b: Tangential stress behaviour in lining element in crown of Frejus tunnel.

In the Frejus tunnel, the surrounding rock of the tunnel section is under compression, and the stress in the rock element at the top of the tunnel sections as shown in Figure 8.13a are discussed here. It can be seen in Figure 8.13b that the initial stresses in the rock at station 125 are higher than at station 5, while in all these cases, the stresses in the rock around the tunnels decreases very slowly.

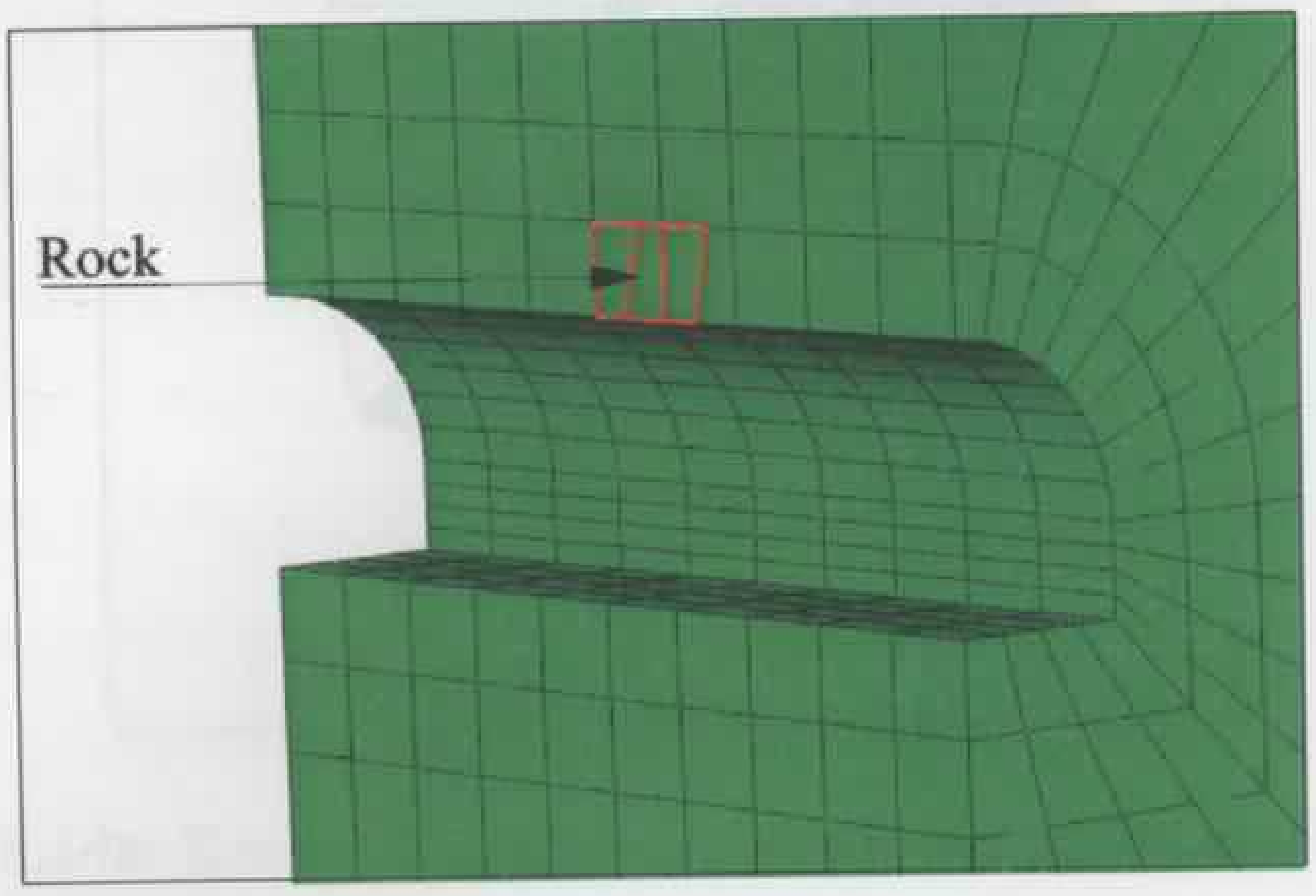

Figure 8.13a: Rock element in crown of Frejus tunnel section.

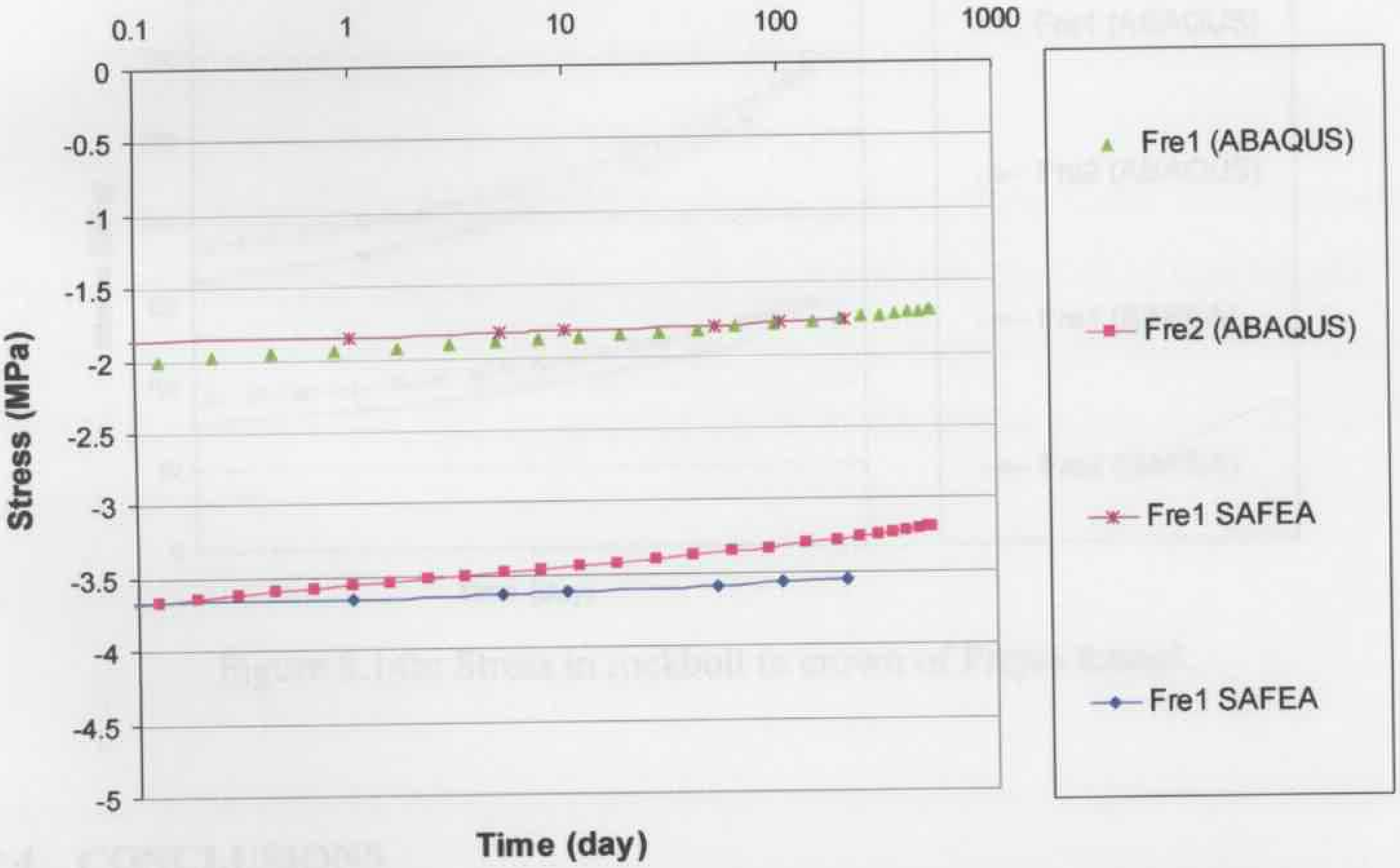

Figure 8.13b: Stress behaviour in rock element in crown of Frejus tunnel.

The stresses in the rockbolt elements at the middle section of the Frejus tunnel as shown in Figure 8.14a will increase with time. The initial tension stresses in the rockbolts at station 125 (Fre2 at 1200 m depth) are bigger and increase at a faster rate than at station 5 (Fre1 at 600 m depth).

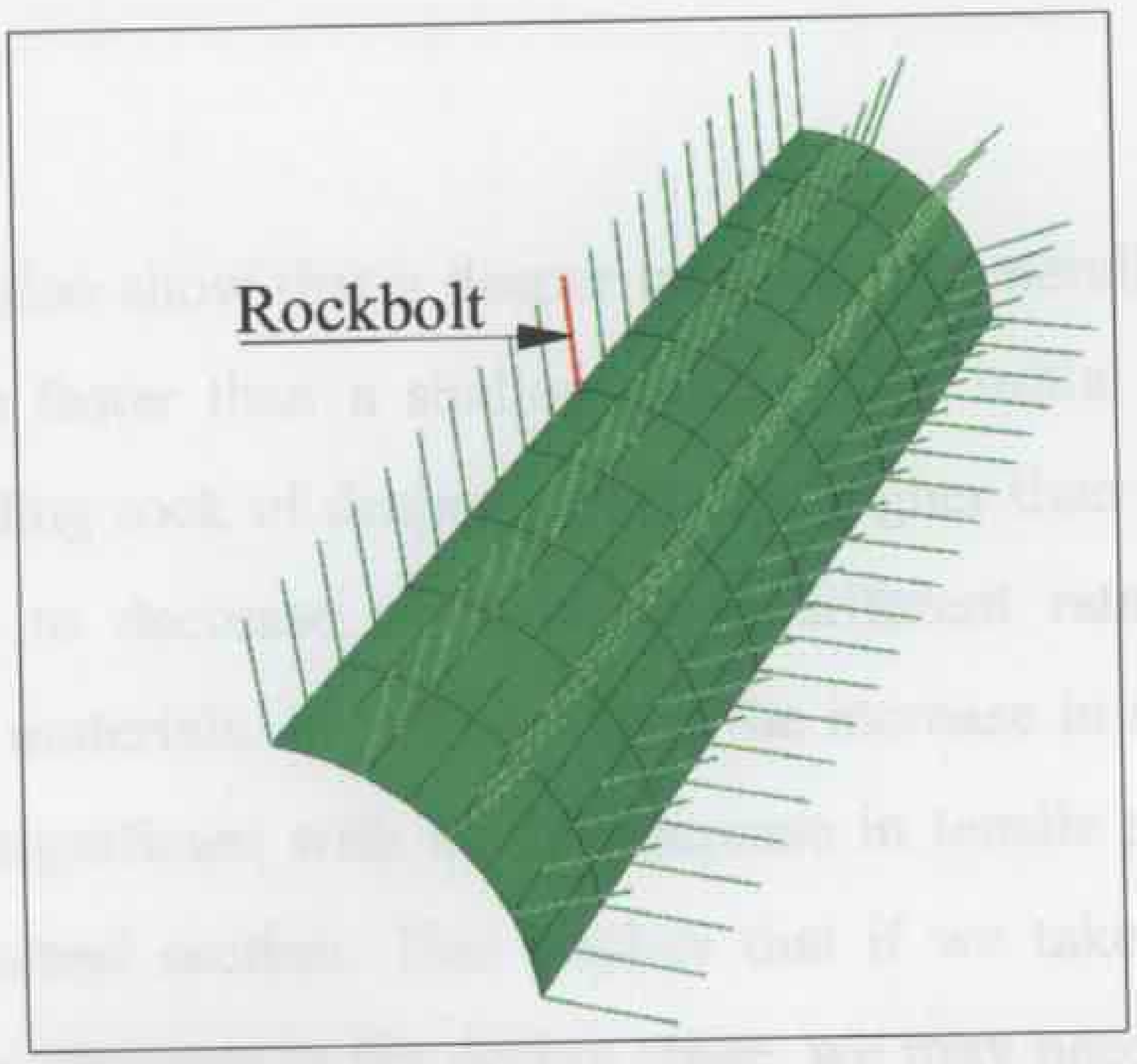

Figure 8.14a: Rockbolt element in crown of Frejus tunnel section.

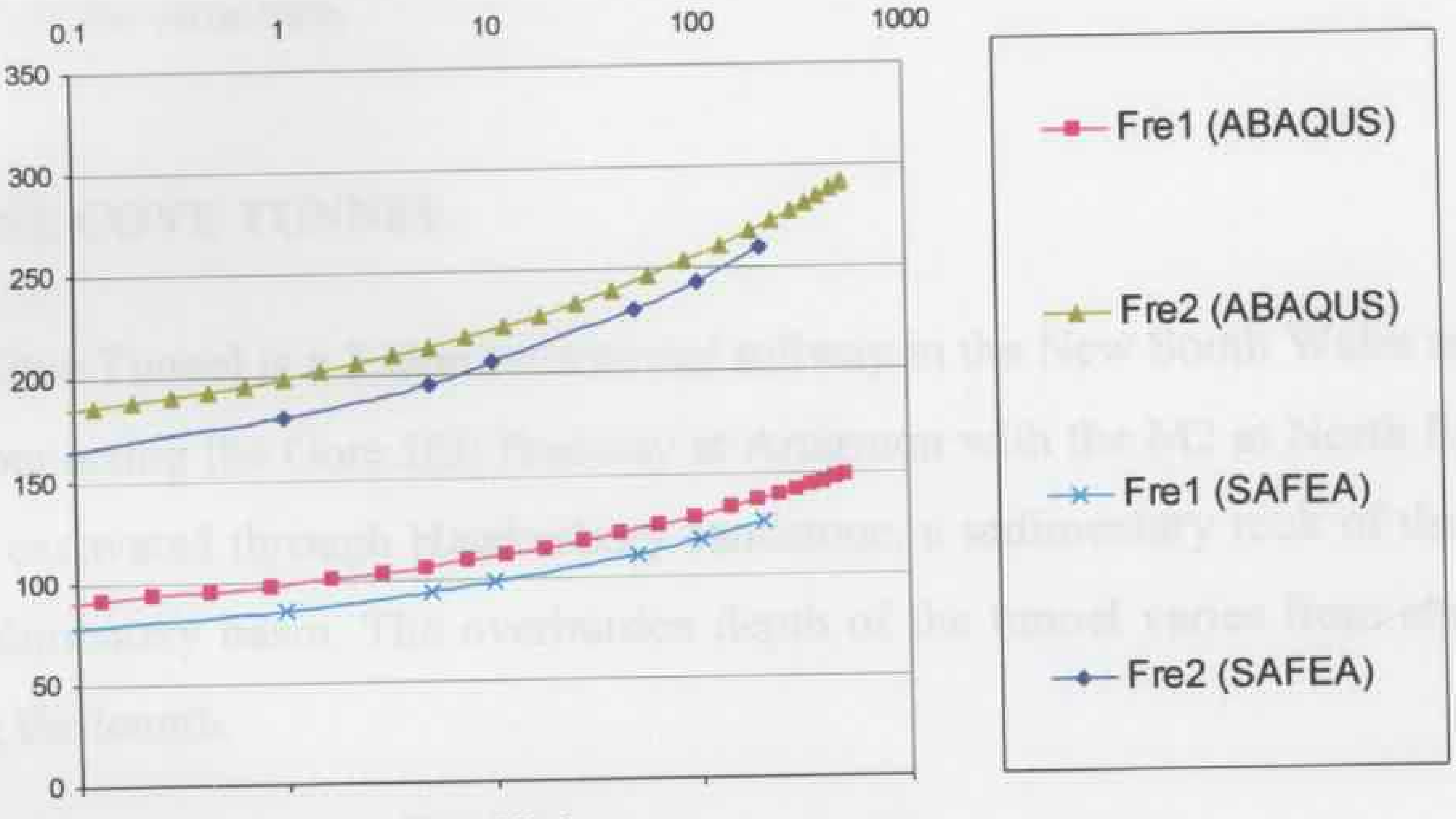

Figure 8.14b: Stress in rockbolt in crown of Frejus tunnel.

8.2.4 CONCLUSIONS

The back analysis of the creep performance of Frejus tunnel indicated that the creep parameters of the ground can be obtained by selecting creep parameters for the rock to fit the time-dependent field observation convergence data of a tunnel section. With the selected creep parameters, the finite element method can be used to predict the time-dependent convergence of the tunnel at other stations under different depths, or it can also be used to predict the time-dependent performance of other tunnels under similar ground conditions.

The numerical results also show that a deeper tunnel will generally have a bigger initial deformation and close faster than a shallow tunnel. The initial stresses in the lining, rockbolts and surrounding rock of deeper tunnels are higher than in the shallow tunnels, and the stresses tend to decrease or increase at different rates based on the creep properties of different materials. In this example, the increase in stress in the rockbolt is predicted to be quite significant with a 62% increase in tensile stress in the bolt at the crest for the deeper tunnel section. This implies that if we take into consideration the creep behaviour of the structure in the design stage, we may need to increase the design safety factor of the FRS lining and/or rockbolts to satisfy the long-term strength requirement of the structure.

8.3 LANE COVE TUNNEL

The Lane Cove Tunnel is a 3.6km twin tunnel tollway in the New South Wales motorway network, connecting the Gore Hill Freeway at Artarmon with the M2 at North Ryde. The tunnel was excavated through Hawkesbury sandstone, a sedimentary rock of the Triassic Sydney Sedimentary basin. The overburden depth of the tunnel varies from about 20 to 50 m along the length.

8.3.1 NUMERICAL TUNNEL MODEL

Field observation data for the surface settlement at Station 850 of Lane Cove tunnel was measured and provided by the Roads and Traffic Authority (RTA, NSW). The tunnel was composed of an eastbound road tunnel, a westbound road tunnel and a ventilation tunnel. At Station 850, the cross section of the tunnel is as shown in Figures 8.15a & b.

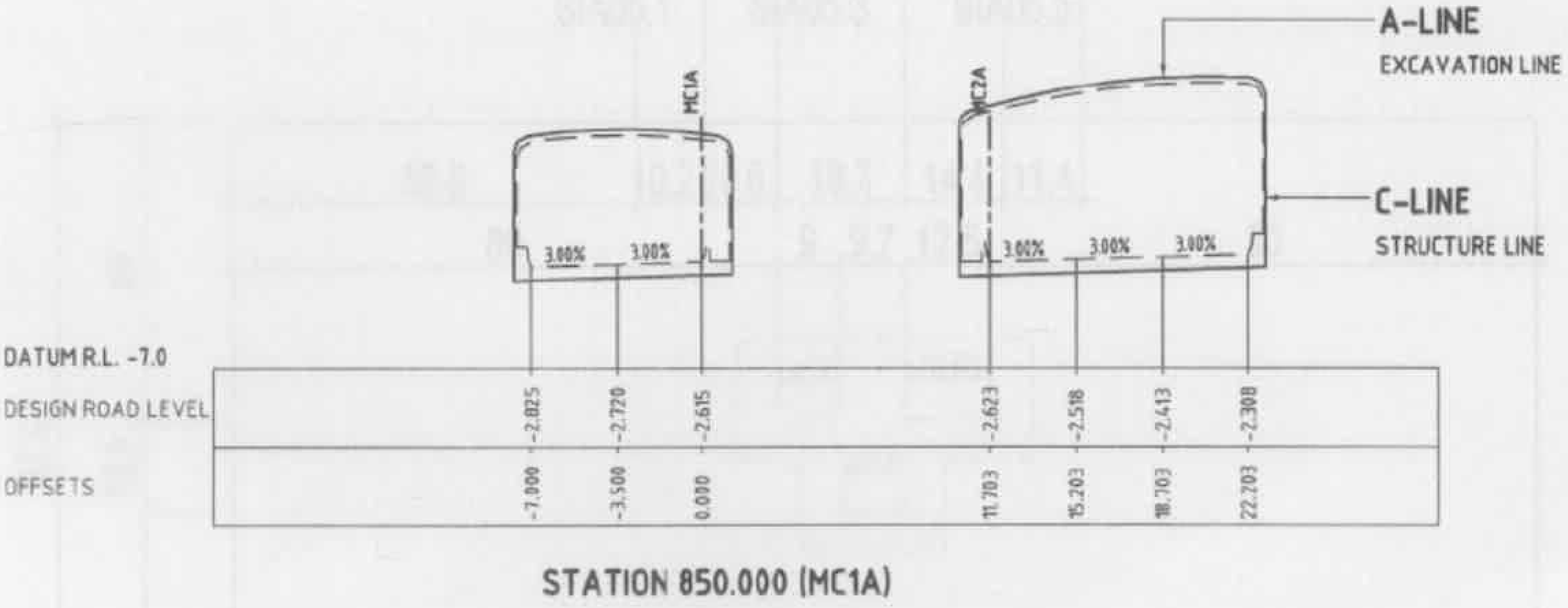

Figure 8.15a: Eastbound and westbound road tunnel cross-sections.

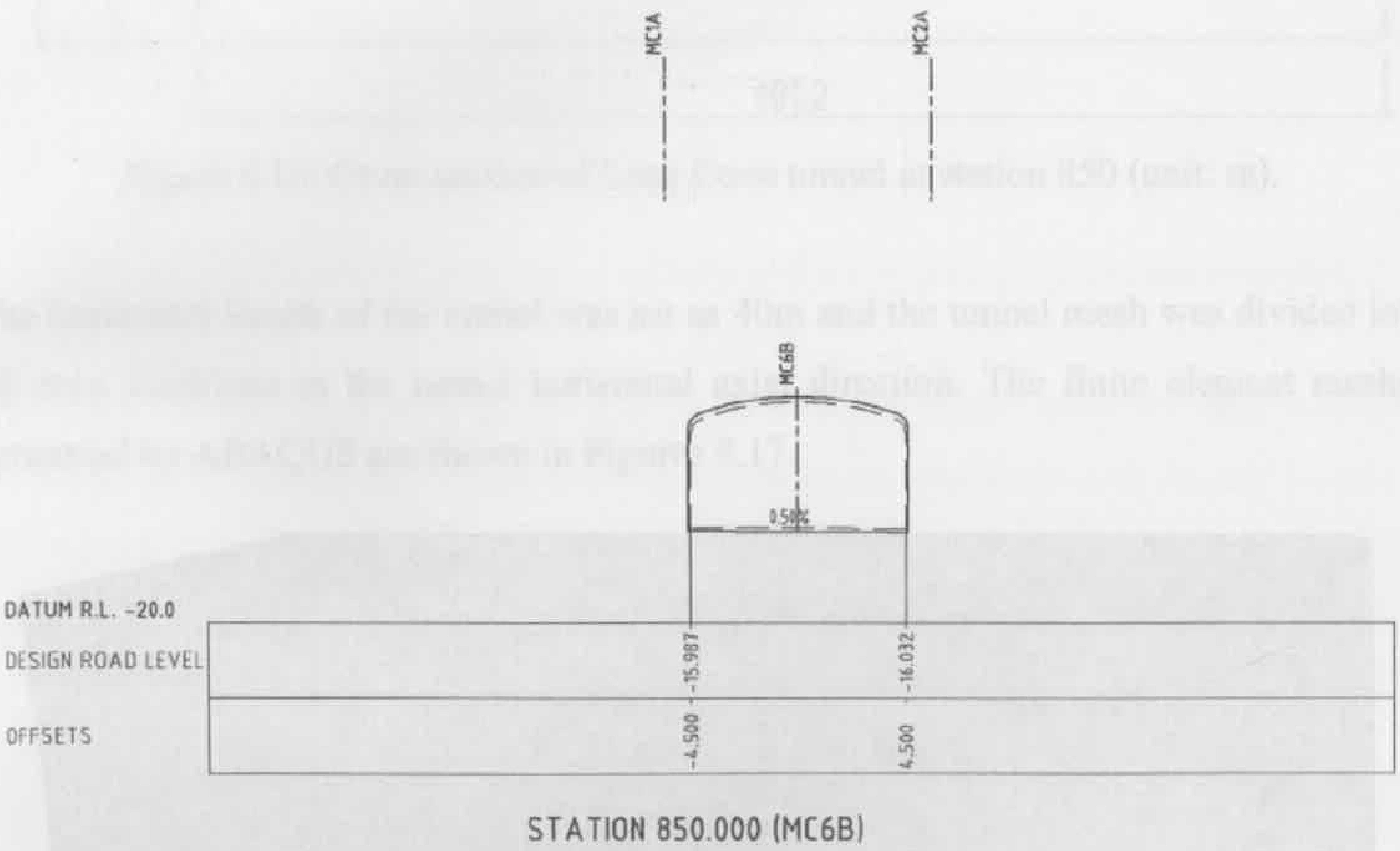

Figure 8.15b: Ventilation tunnel cross-section.

At station 850, the overburden depth of the Lane Cove tunnel was 44 m, the cross section of the numerical model is as shown in Figure 8.16. The surface settlement at the positions SIA05.1~05.6 were recorded with time, while the numerical results of surface settlement are compared with the field data in the following analysis.

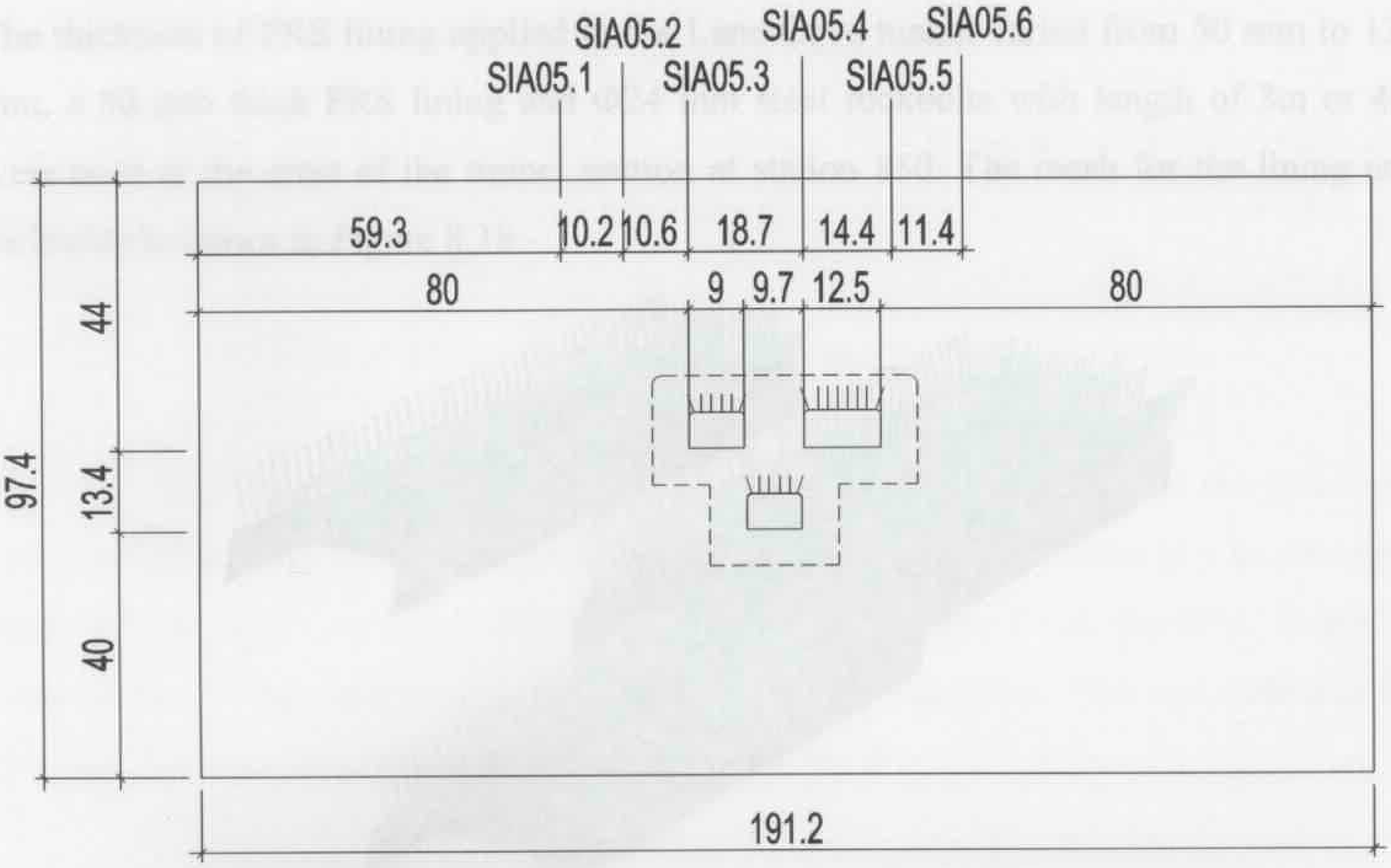

Figure 8.16: Cross section of Lane Cove tunnel at station 850 (unit: m).

The horizontal length of the tunnel was set as 40m and the tunnel mesh was divided into 10 even partitions in the tunnel horizontal axial direction. The finite element meshes generated by ABAQUS are shown in Figures 8.17.

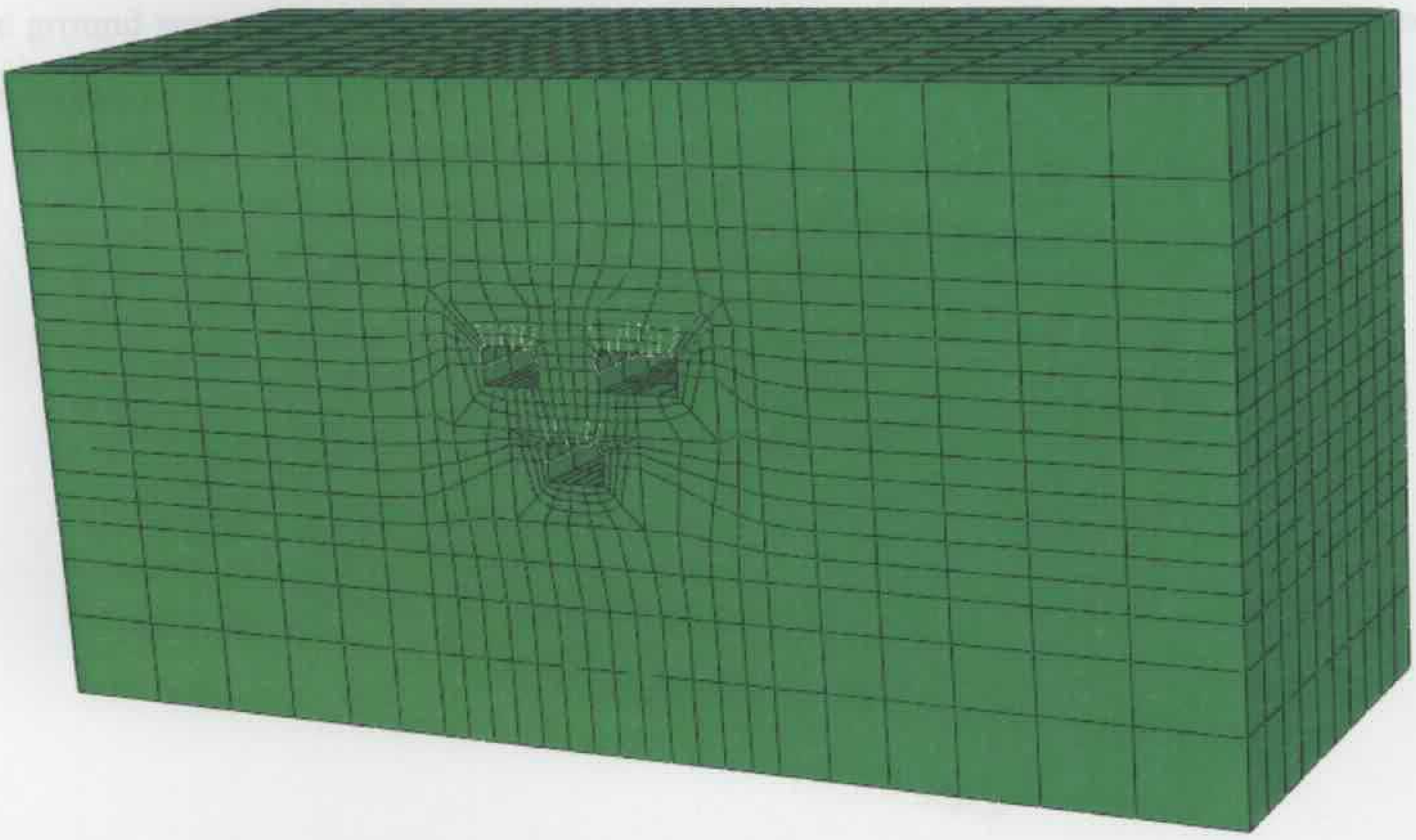

Figure 8.17: Mesh of Lane Cove tunnel model for ABAQUS.

The thickness of FRS lining applied in the Lane Cove tunnel varied from 50 mm to 125 mm, a 50 mm thick FRS lining and Φ24 mm steel rockbolts with length of 3m or 4m were used at the crest of the tunnel section at station 850. The mesh for the lining and rockbolts is shown in Figure 8.18.

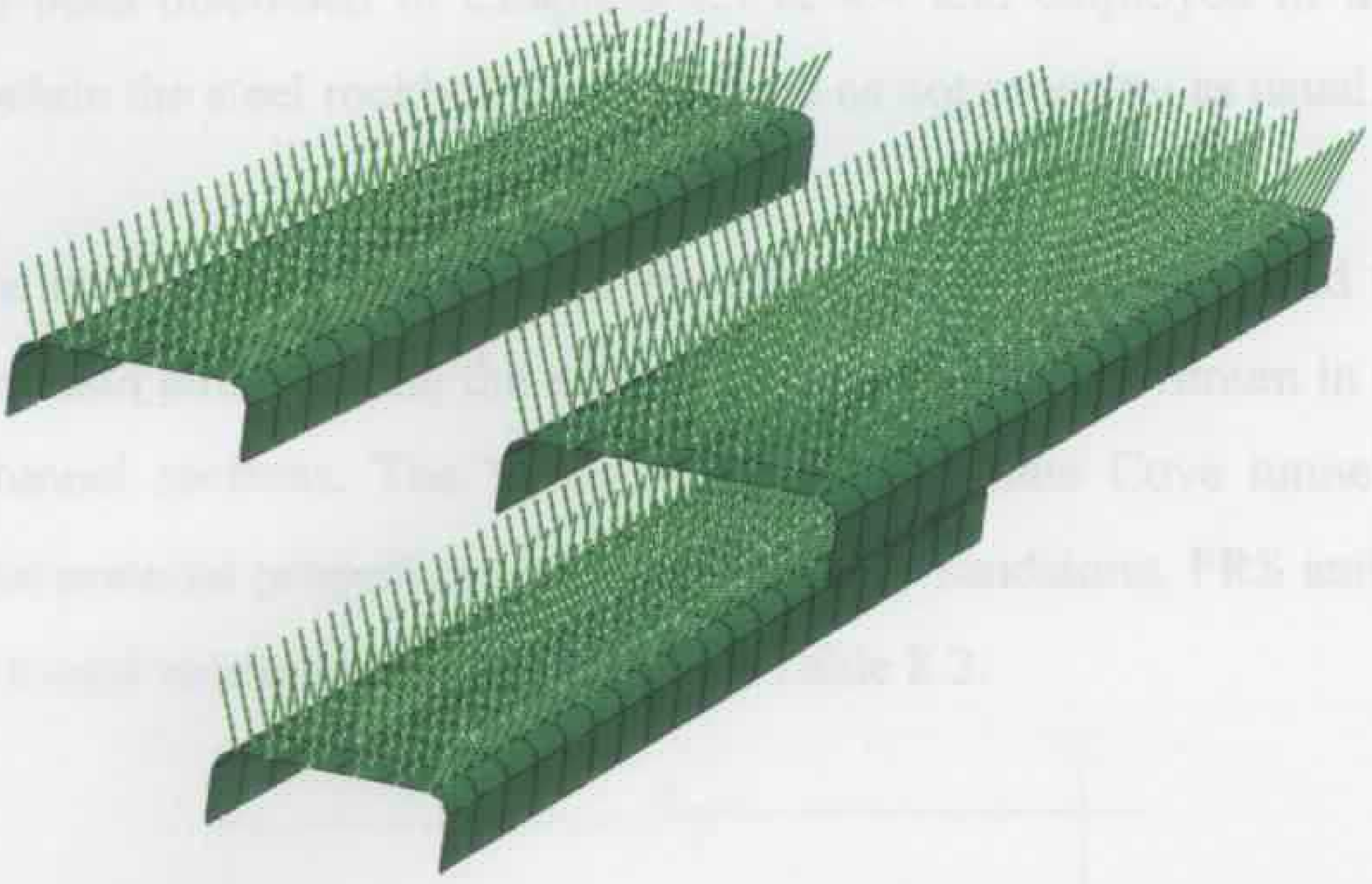

Figure 8.18: Mesh of lining and rockbolts elements in Lane Cove tunnel model.

The top surface of the tunnel model was set to be unrestrained while the base and sides were restrained against movement in both perpendicular directions, and the self weight of the ground was assumed to be 24000N/m^3. The boundary conditions of the tunnel model are shown in Figure 8.19.

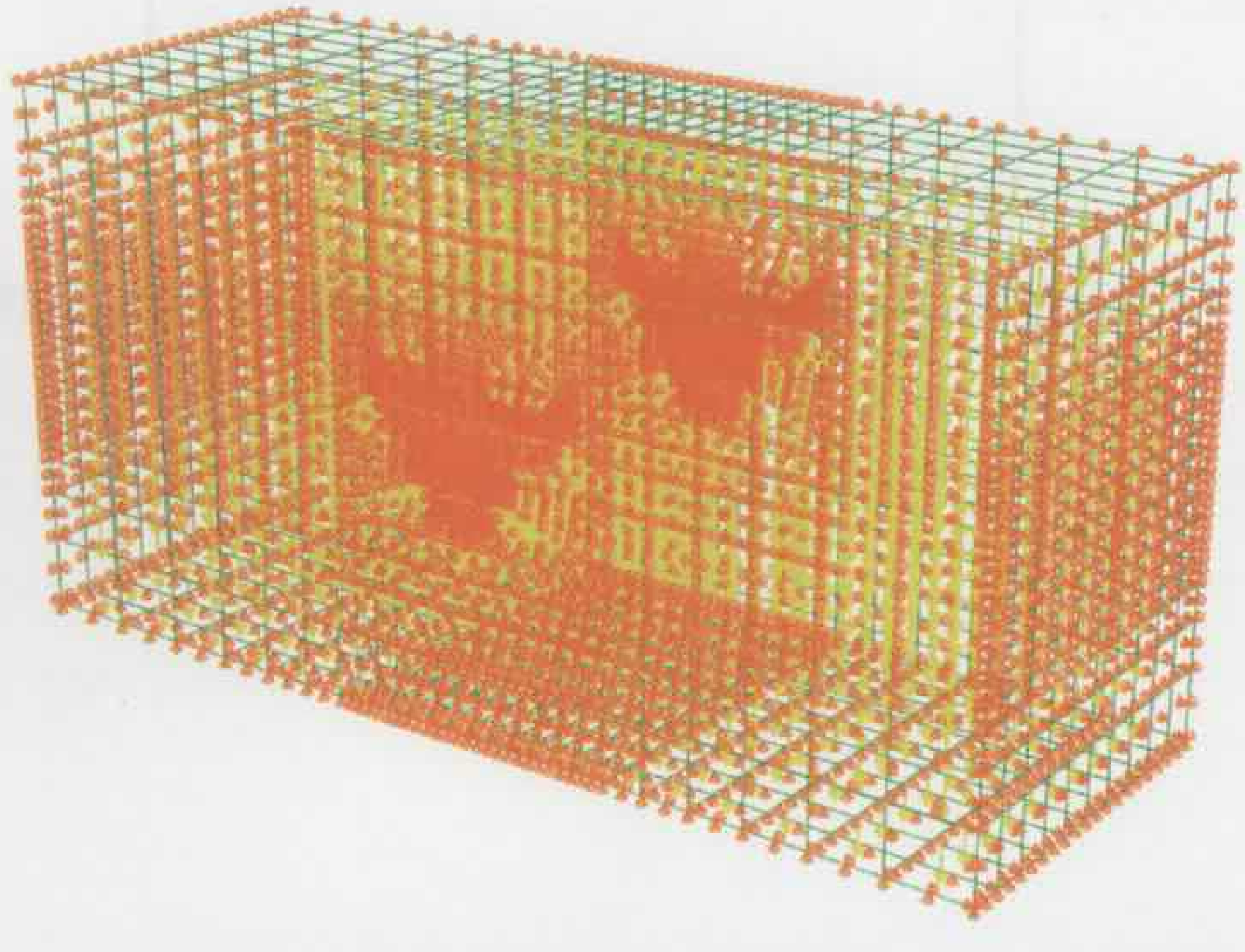

Figure 8.19: Boundary conditions of Lane Cove tunnel models.

8.3.2 MATERIAL PROPERTIES

The Lane Cove tunnel was supported by a combined FRS lining and rockbolt system and constructed in Hawkesbury sandstone. The time-dependent property of Novotex FRS and sandstone have been discussed in Chapters 4.3 & 4.4 and employed in the Lane Cove tunnel model, while the steel rockbolts were treated as not creeping as usual.

The Lane Cove tunnel has three parallel excavated tunnel sections, and the generated increment of deviator stress during the excavation process is a maximum in a surrounding region of the tunnel sections. The 'creep zone' for the Lane Cove tunnel is shown in Figure 8.20. The material properties of the Hawkesbury sandstone, FRS and rockbolts for the Lane Cove tunnel models are summarized in Table 8.2.

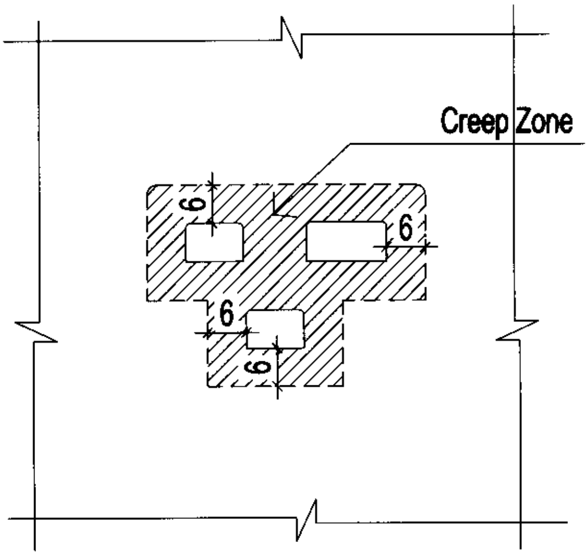

Figure 8.20: Creep Zone of Lane Cove tunnel (unit: m).

	Lane Cove Tunnel Models
Sandstone	E = 3.0e9 Pa v = 0.3
Creep parameters of Sandstone	F=7.0e-20 n=2.19 m=-0.98 (ABAQUS)
Shotcrete lining	Novotex E = 5.848e9 Pa v = 0.15 Thickness = 0.05m
Creep parameters of shotcrete	F=4.0e-37 n=5.0 m=-0.1 (ABAQUS)
Rockbolts	Ø24X3000mm/ Ø24X4000mm E = 2.0e11 Pa v = 0.3

Table 8.2: Material properties of Lane Cove tunnel models.

8.3.3 BACK ANALYSIS OF TUNNEL CREEP DEFORMATION

Lane Cove tunnel was excavated through the Hawkesbury sandstone and the self weight of the ground is assumed to be 24000N/m^3. The initial ground conditions of Lane Cove tunnel were generated using Equation 6.1 as for the circular tunnel models in Chapter 6.

In the excavation analysis, the excavation of the rock and establishment of the lining and rockbolts were controlled by removing and activating the corresponding elements. The instantaneous deformation of the tunnel opening is shown in Figure 8.21, and the deformation scale factor is set as 200 to make the deformation identifiable. It can be seen that the top section is moving down, while the bottom section is moving up at each of the sections, and the bigger section experienced a larger deformation.

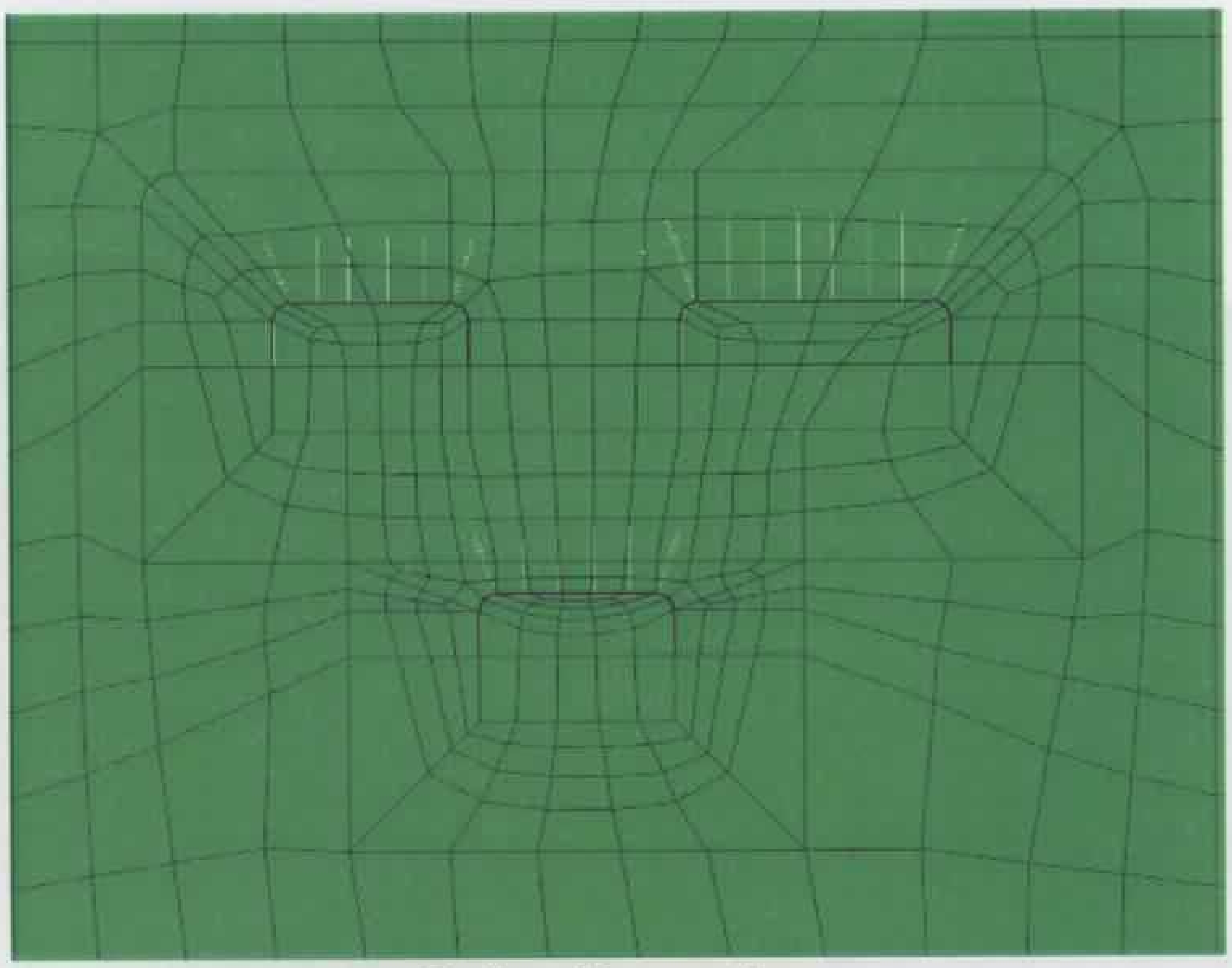

Before Excavation

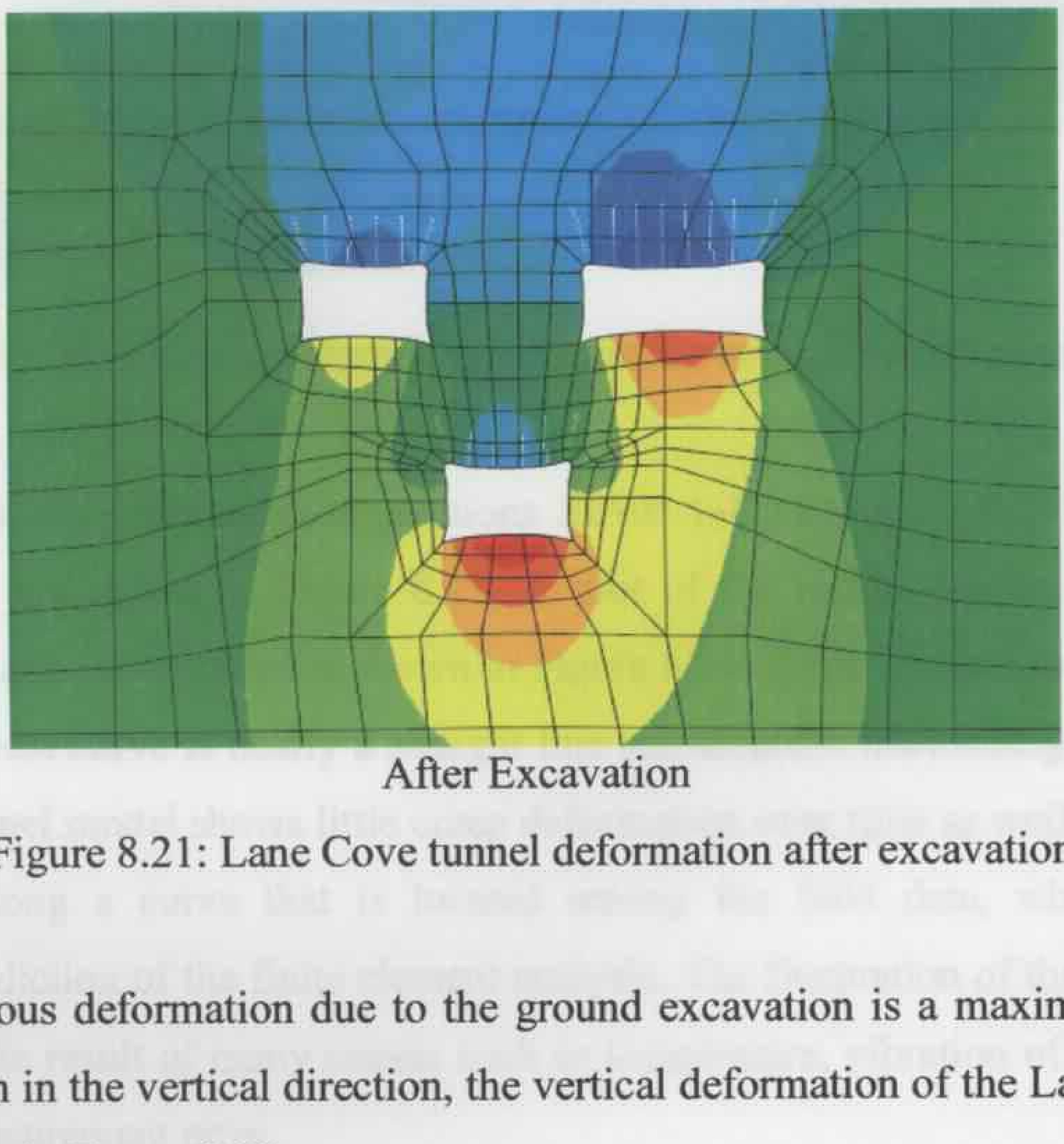

After Excavation

Figure 8.21: Lane Cove tunnel deformation after excavation.

The instantaneous deformation due to the ground excavation is a maximum around the opening section in the vertical direction, the vertical deformation of the Lane Cove tunnel model is shown in Figure 8.22.

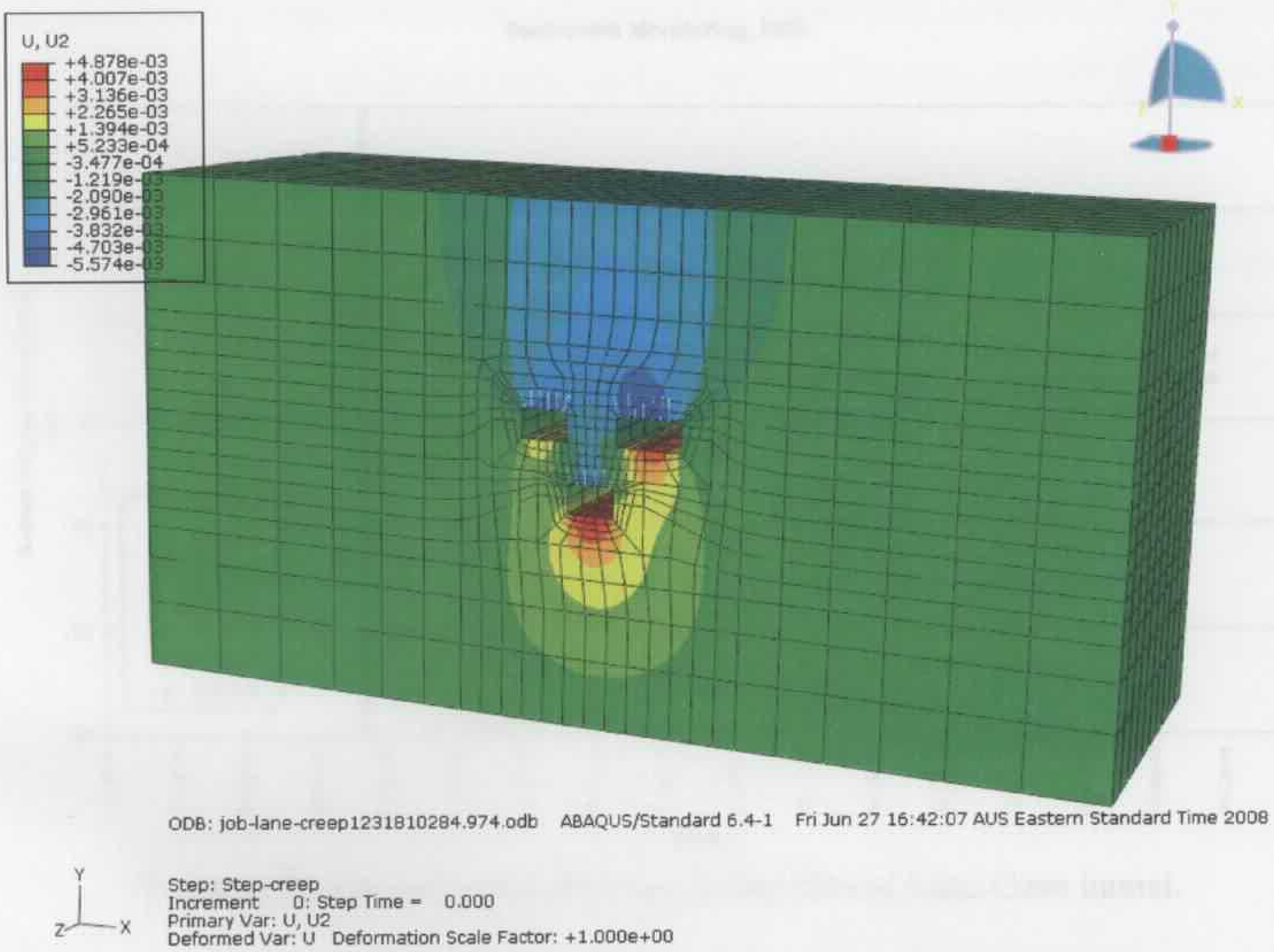

Figure 8.22: Vertical deformation of Lane Cove tunnel after excavation.

The ground surface settlements at positions SIA05.1~05.6 (Figure 8.16) were recorded with time and are shown in Figure 8.23. A plot of the results for the ground surface settlement of Lane Cove tunnel is shown in Figure 8.24. It can be seen that the numerical ground settlement curve is nearly a straight line and displays little change with time; the Lane Cove tunnel model shows little creep deformation over time as well. The numerical results plot along a curve that is located among the field data, which indicates a reasonable prediction of the finite element analysis. The fluctuation of the field data over time may be the result of many causes such as temperature, vibration of heavy vehicles, or random measurement error.

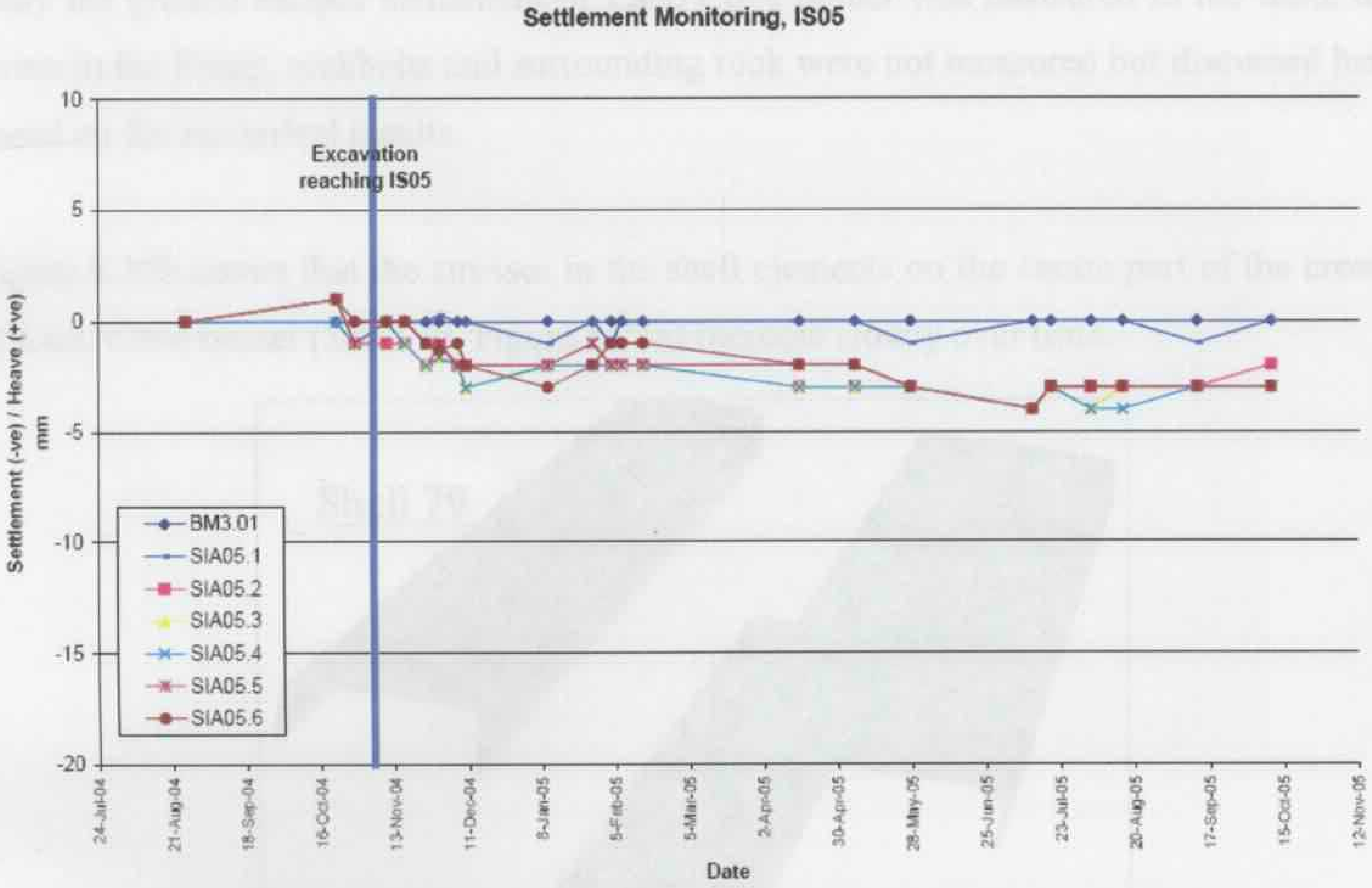

Figure 8.23: Ground settlement monitoring data of Lane Cove tunnel.

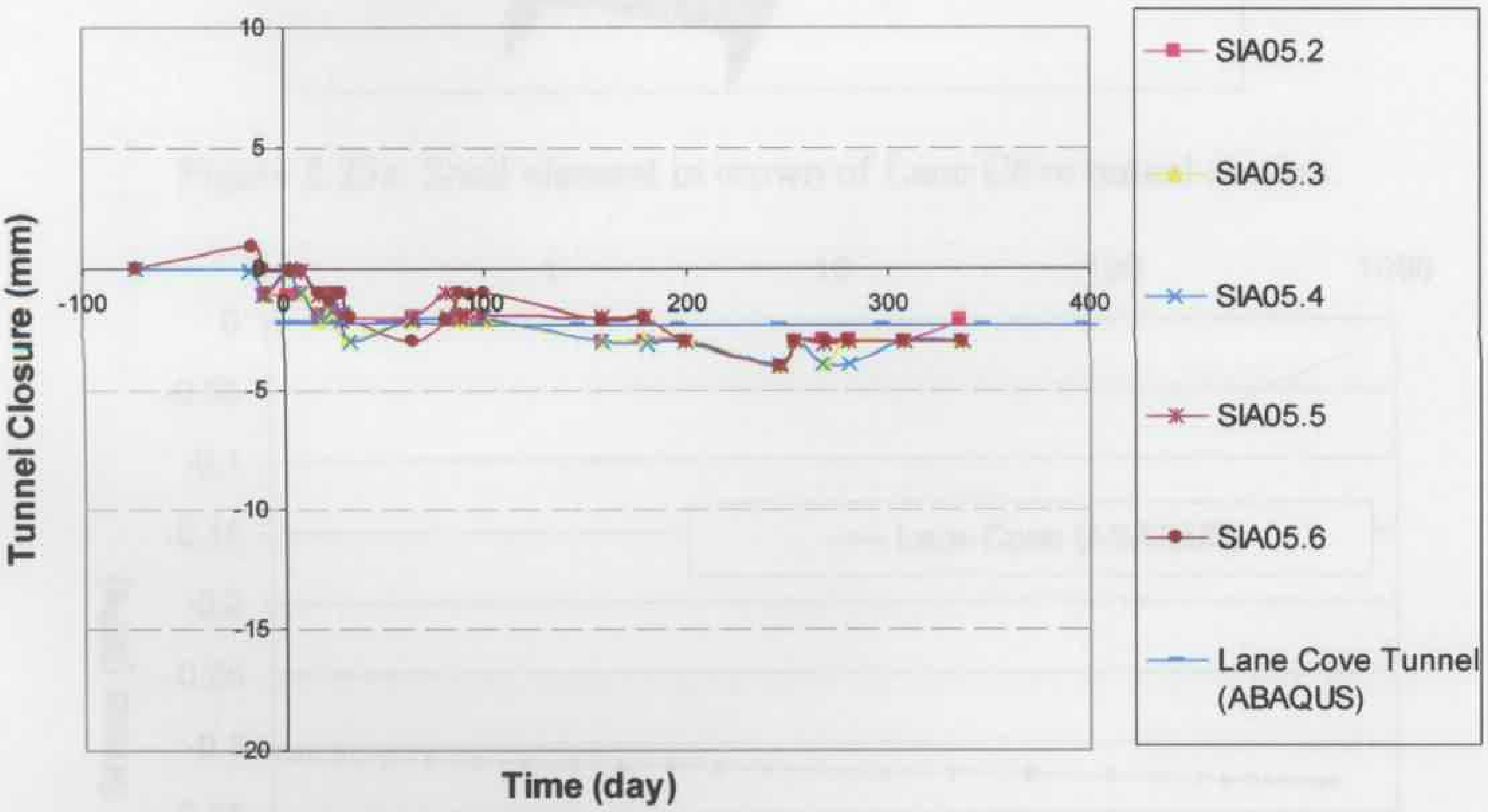

Figure 8.24: Numerical results for ground settlement above Lane Cove tunnel.

Only the ground surface settlement of Lane Cove tunnel was measured in the field, the stress in the lining, rockbolts and surrounding rock were not measured but discussed here based on the numerical results.

Figure 8.25b shows that the stresses in the shell elements on the centre part of the crown of Lane Cove tunnel (Shell 79, Figure 8.25a) increase slowly over time.

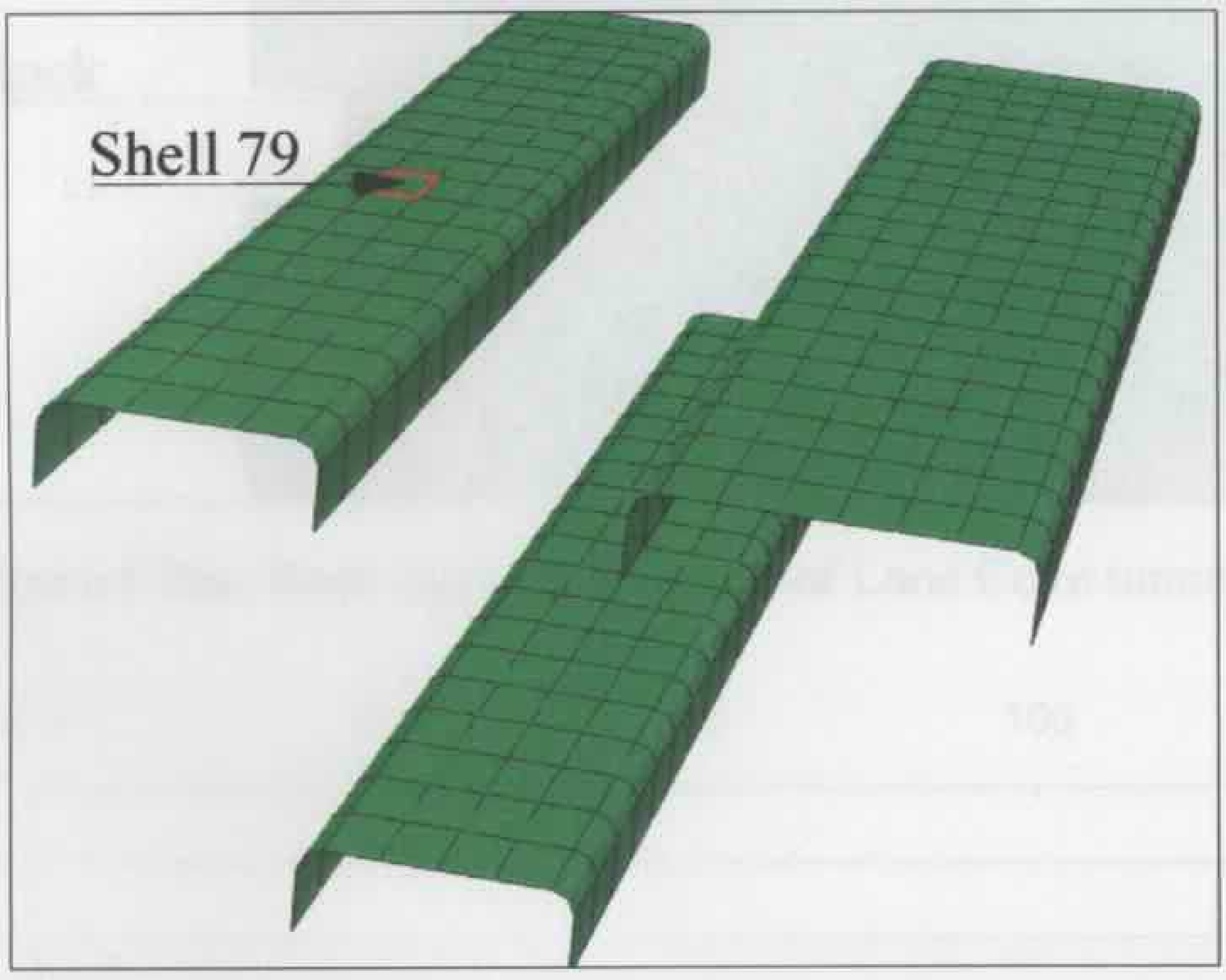

Figure 8.25a: Shell element in crown of Lane Cove tunnel section.

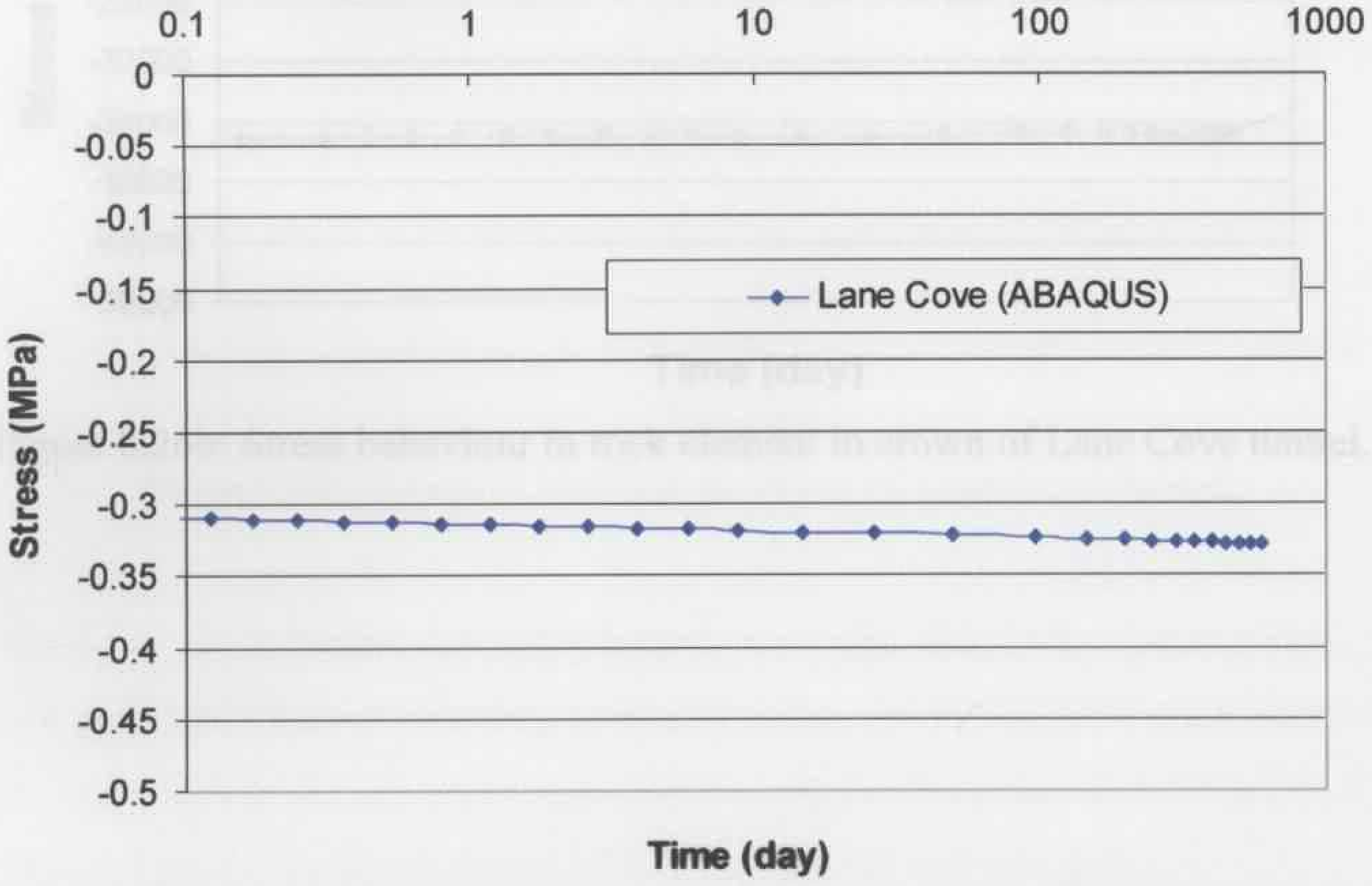

Figure 8.25b: Stress behaviour in lining element in crown of Lane Cove tunnel.

Figure 8.26b shows that the stresses in the element located in the rock at the crown of Lane Cove tunnel (as shown in Figure 8.26a) displays little change with time.

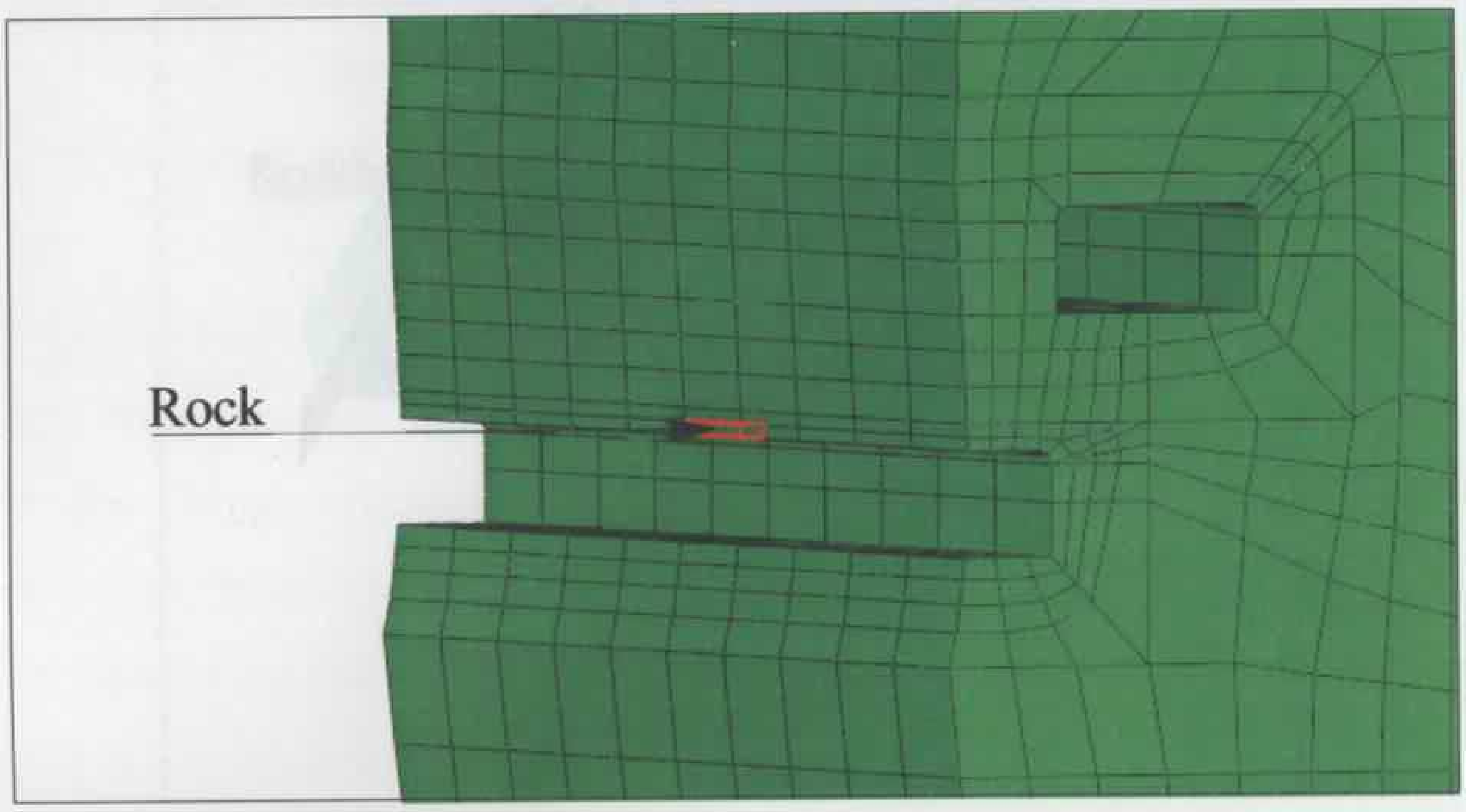

Figure 8.26a: Rock element in crown of Lane Cove tunnel.

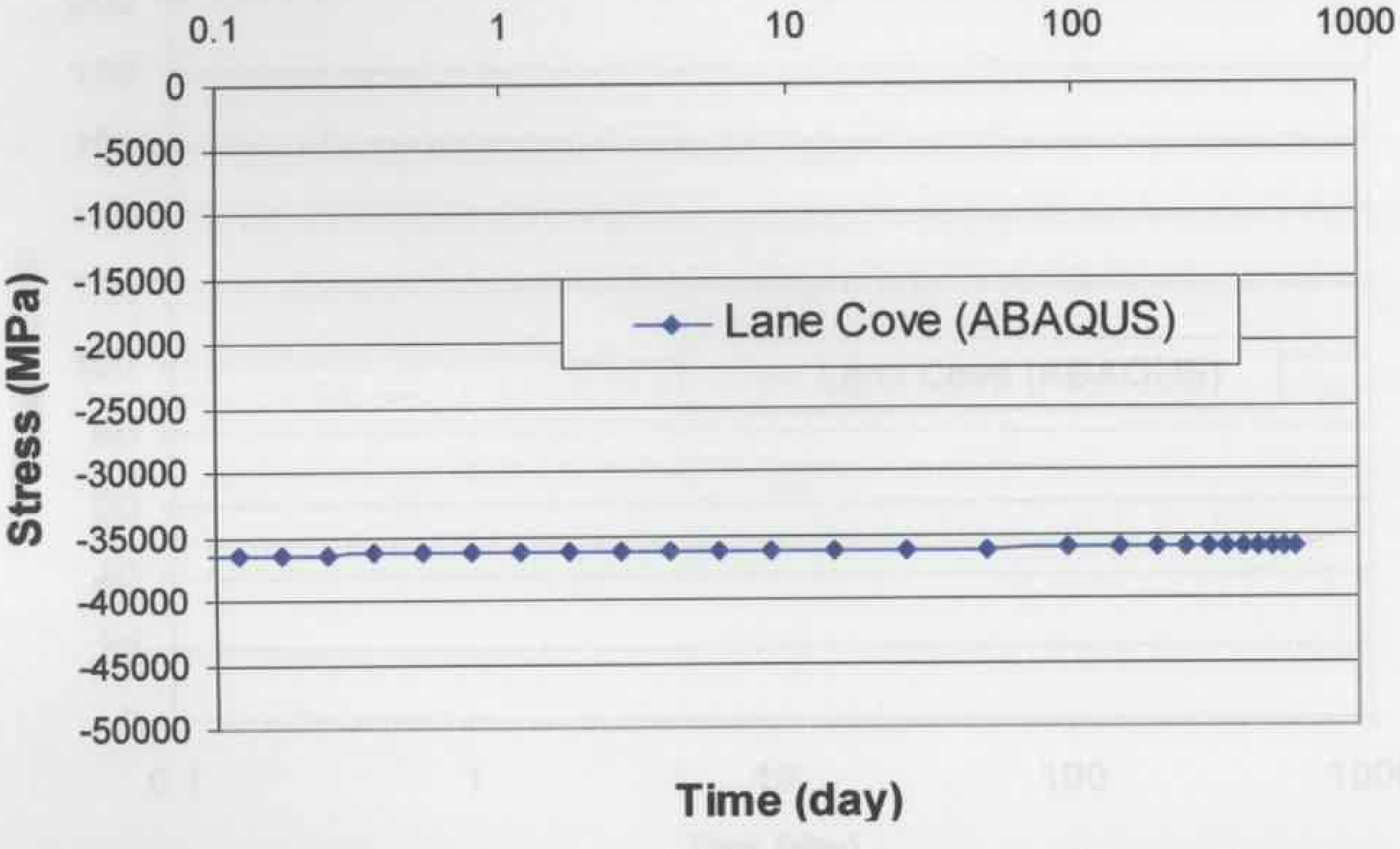

Figure 8.26b: Stress behaviour in rock element in crown of Lane Cove tunnel.

Figure 8.27b shows that the stresses in the rockbolt element at the crown of Lane Cove tunnel (as shown in Figure 8.27a) displays little change with time.

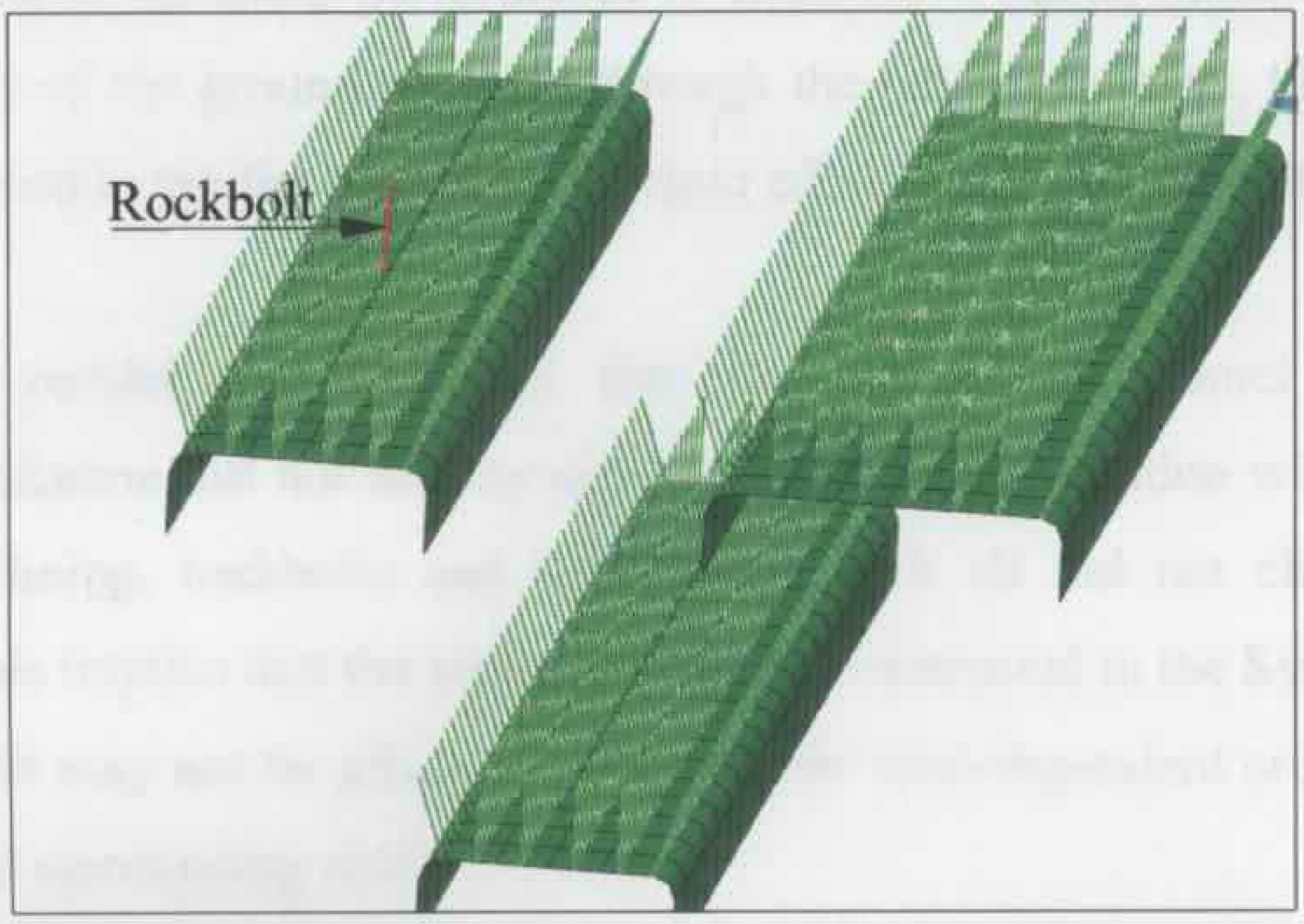

Figure 8.27a: Rockbolt element in crown of Lane Cove tunnel.

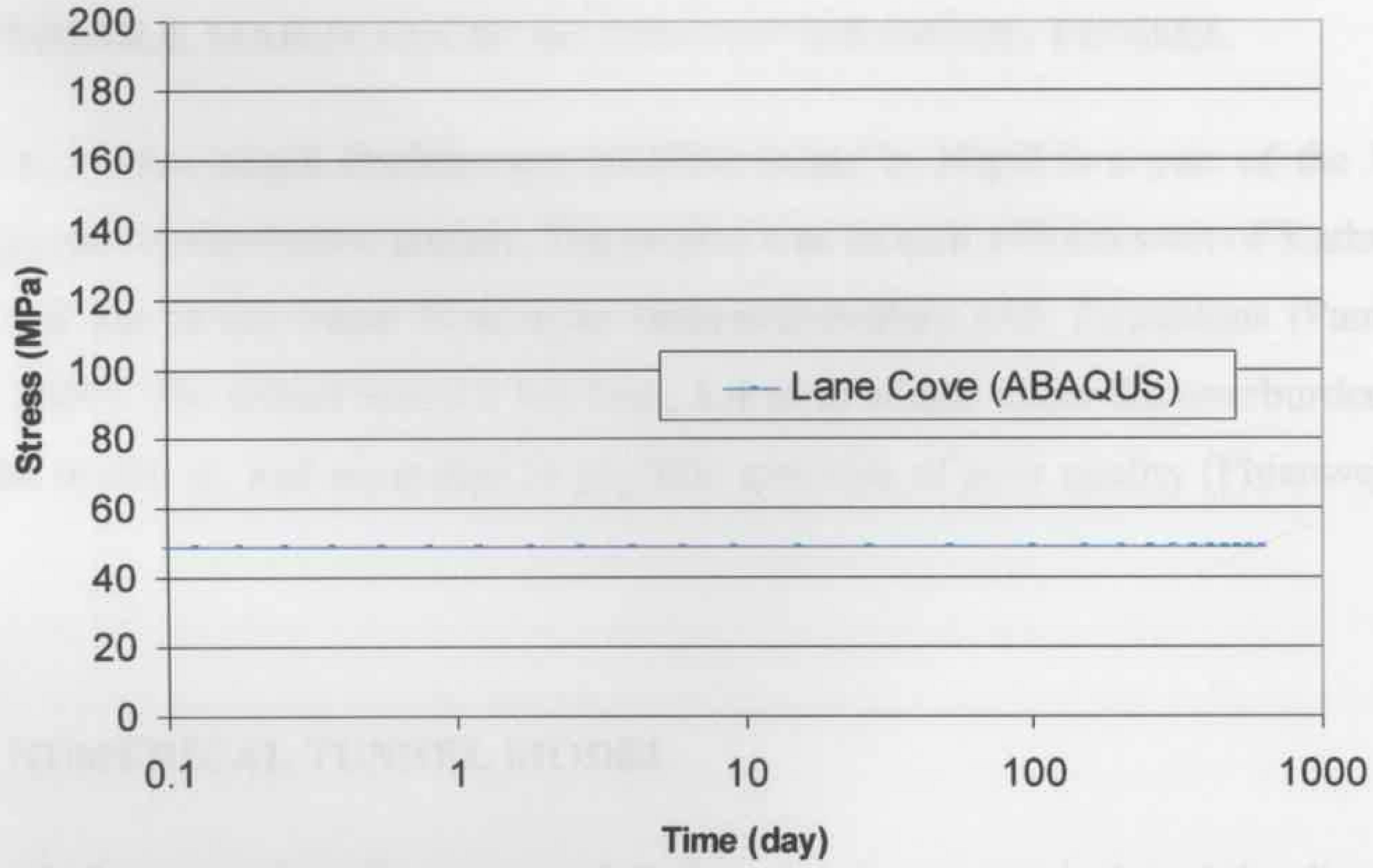

Figure 8.27b: Stress in rockbolt in crown of Lane Cove tunnel.

Since the Lane Cove tunnel has three tunnel openings, the finite element mesh is too complicated and too time-consuming to run by using the FORTRAN code SAFEA, and the Lane Cove tunnel did not show significant creep performance with time, the SAFEA model was not used here and only ABAQUS was used in this research.

8.3.4 CONCLUSIONS

The back analysis of the creep performance of Lane Cove tunnel indicated that with the creep parameters of the ground obtained through the laboratory tests, the finite element method can be used to predict the field behaviour of a tunnel structure with time.

The numerical results also indicated that the Lane Cove tunnel constructed in Hawkesbury sandstone did not display significant creep deformation with time, and the stresses in the lining, rockbolts and surrounding rock all did not change with time significantly. This implies that the transport tunnels constructed in the Sydney area at less than 100 m depth may not be affected greatly by the time-dependent creep properties of the shotcrete and surrounding rock.

8.4 MIDDLE MARSYANGDI HYDROPOWER (MMH) TUNNEL

The Middle Marsyangdi Hydropower (MMH) tunnel in Nepal is a part of the Nepal's second largest hydroelectric project. The project was located 170 km west of Kathmandu, Nepal, and lies in the lesser Himalayan meta-sedimentary rock formations (Panthi and Nilsen, 2007). The tunnel was 5.2 km long, 5.4 m in width, under the overburden depth from 200 to 600 m, and excavated in phyllitic quartzite of poor quality (Phienwej et al., 2007).

8.4.1 NUMERICAL TUNNEL MODEL

Only half of the tunnel section was modelled since it is symmetrical, and the dimensions of the cross section of the tunnel are shown in Figure 8.28. The closure measurements of different tunnel sections at different depths were recorded and investigated in this research. The creep parameters for the phyllitic quartzite was extrapolated through back analysis of the field data at one location, and then employed in the finite element models to predict the time-dependent closure at the other two locations.

Three numerical models were built up, model MMHT1 and MMHT2 refer to the tunnel section 180 and 196 with an overburden depth of 200 m, while model MMHT3 refers to the tunnel section 220 with an overburden depth of 225 m. The self weight of the ground was assumed to be 24000N/m^3. The 150 m depth of rock above was transferred as a pressure load of 3.6 MPa applied on the top surface of model MMHT1 and MMHT2, and again the 175 m depth of rock overburden was transferred as a pressure load of 4.2 MPa applied on the top surface of model MMHT3.

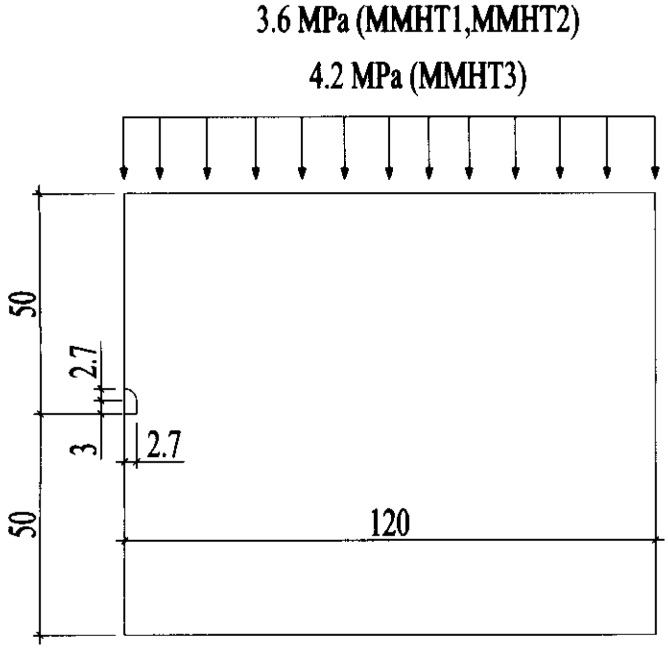

Figure 8.28: Numerical cross section of MMH tunnel model (unit: m).

The horizontal length of the tunnel was set as 30m and the tunnel mesh was divided into 10 even partitions in the tunnel horizontal axial direction so that the deformation in the middle section would not be affected significantly by the face boundary restraints. The finite element mesh is shown in Figure 8.29.

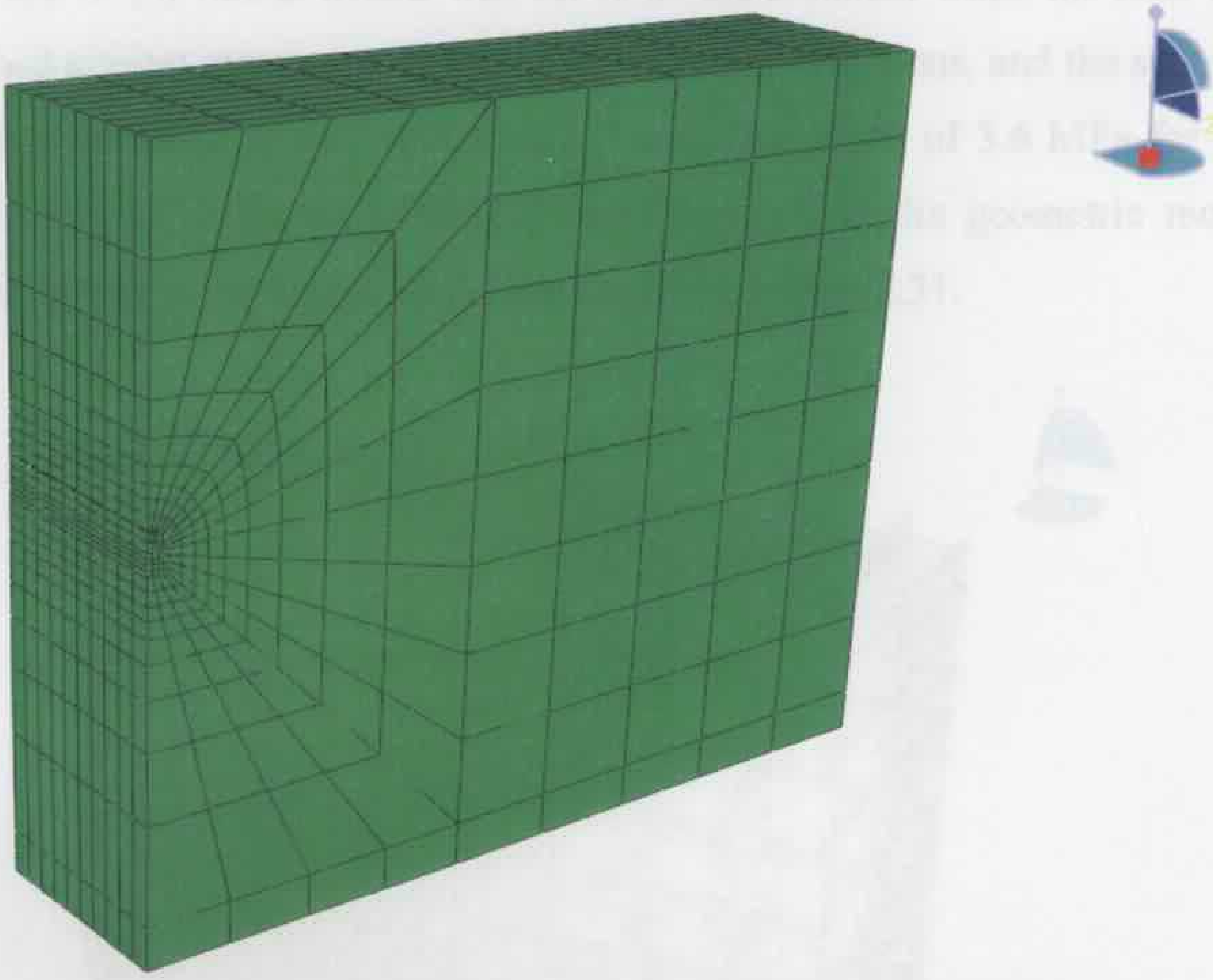

Figure 8.29: Finite element mesh of MMH tunnel model.

A 100mm thick shotcrete lining was applied on the crest of the section, and the mesh of the lining is shown in Figure 8.30.

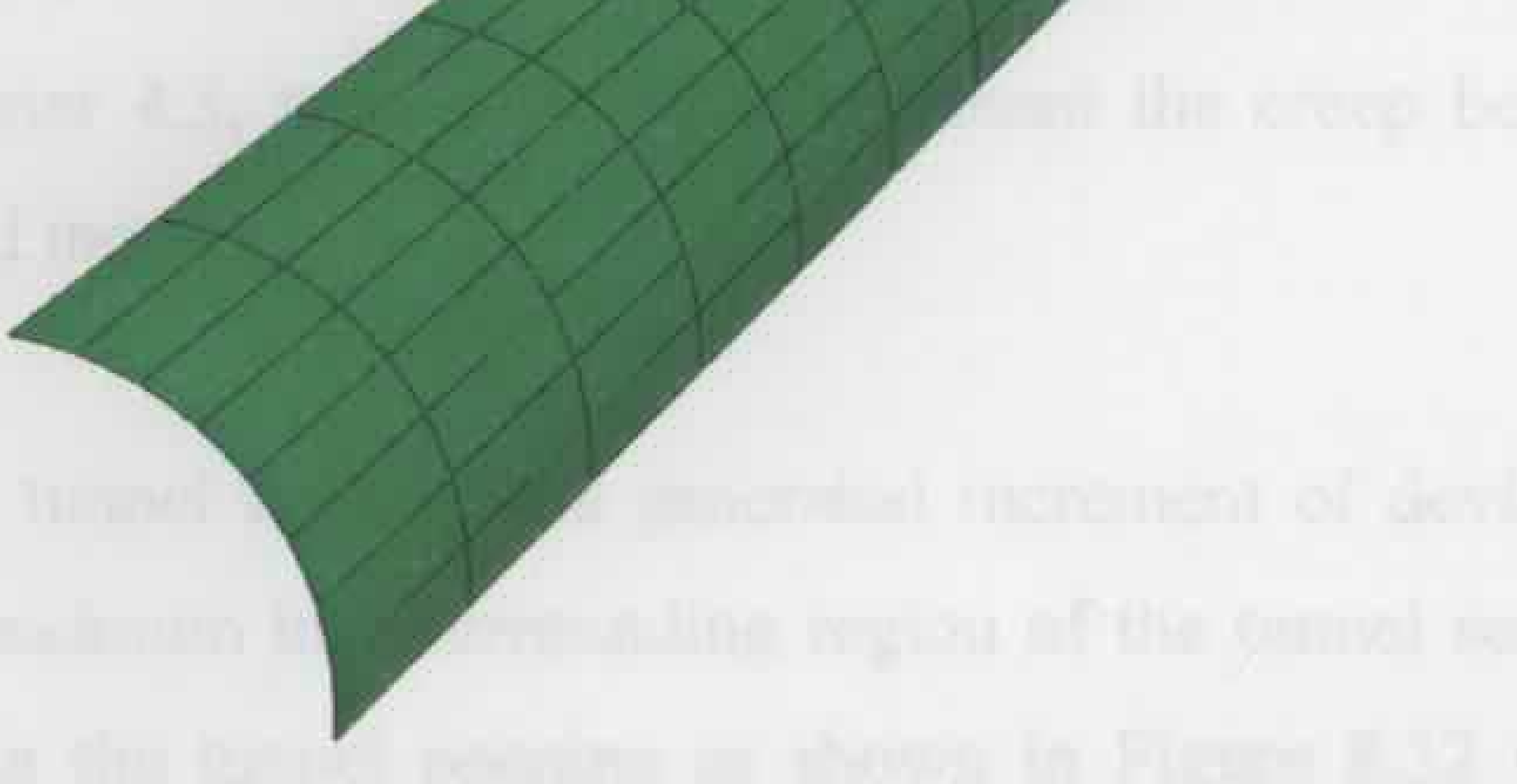

Figure 8.30: Finite element mesh of lining in MMH tunnel model.

The top surface of the tunnel model was set to be unrestrained while the base and sides were restrained against movement in both perpendicular directions, and the self weight of the ground was assumed to be 24000N/m^3. The surface loads of 3.6 MPa for MMHT1 and MMHT2 (or 4.2 MPa for MMHT3) were applied on the geometric model. The boundary conditions of the tunnel model are shown in Figure 8.31.

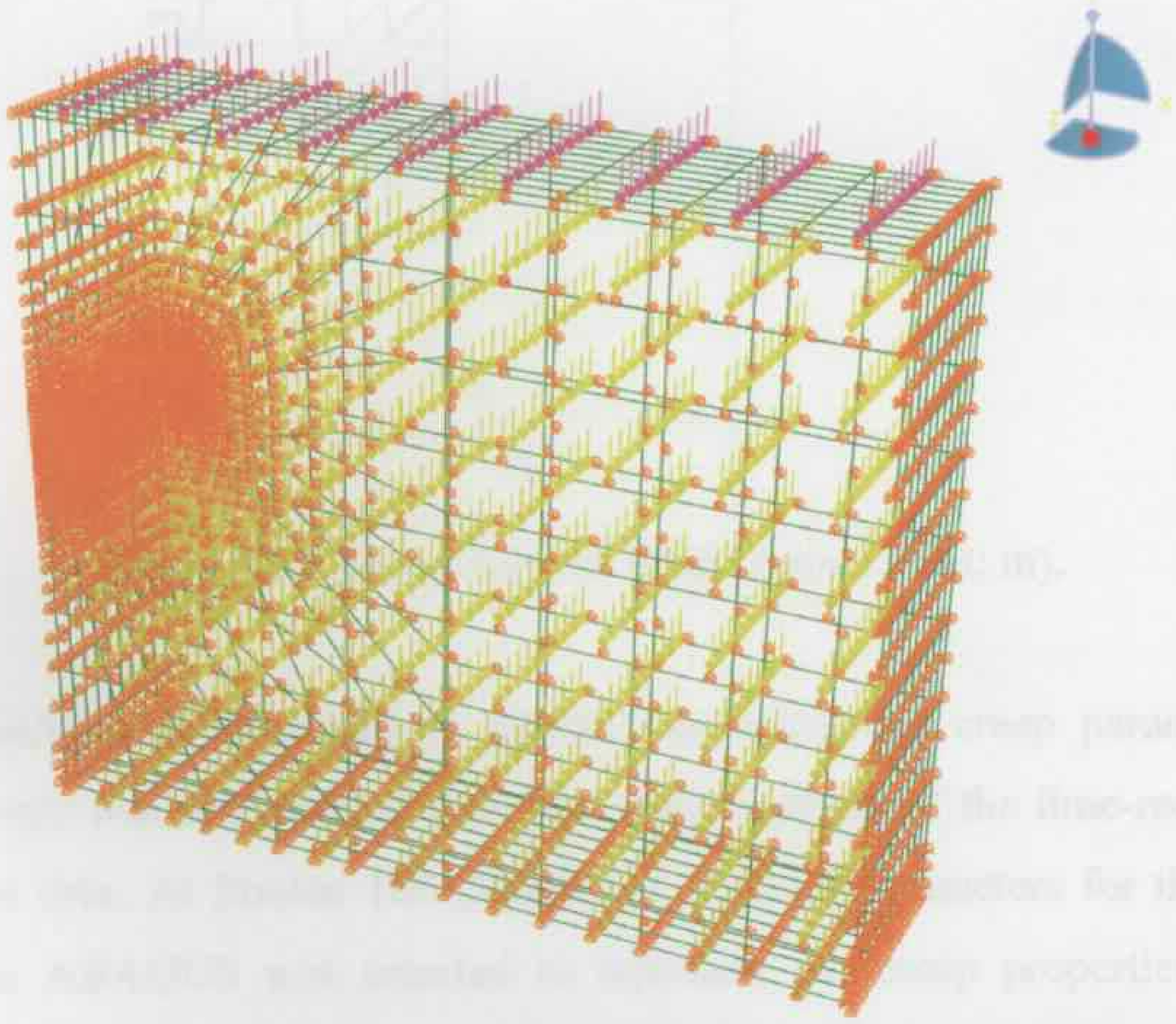

Figure 8.31: Boundary conditions of MMH tunnel model.

8.4.2 MATERIAL PROPERTIES

In the MMH tunnel models, the creep parameters of Novotex FRS, which have been discussed in Chapter 4.3, were selected to represent the creep behaviour of steel FRS lining in the tunnel models.

As for the Frejus tunnel models, the generated increment of deviator stress due to the excavation is a maximum in a surrounding region of the tunnel section, and so that this region surrounding the tunnel opening as shown in Figure 8.32 was set as the 'creep zone'.

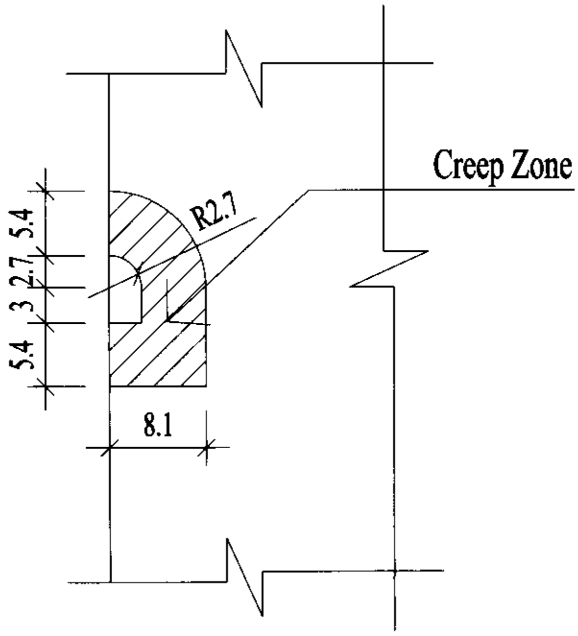

Figure 8.32: Creep Zone of MMH tunnel (unit: m).

The MMH tunnel was excavated in phyllitic quartzite, the creep parameters of the phyllitic quartzite was extrapolated through a back analysis of the time-recorded tunnel section closure data. At Station 180 (MMHT1), a set of parameters for the power law model used in ABAQUS was selected to represent the creep properties of phyllitic quartzite by fitting the numerical tunnel closure curve to the field observation data. The selected creep parameters were later employed in the finite element models to predict the tunnel closure deformation curve at the other two locations. The material properties of the phyllitic quartzite and FRS for the MMH tunnel models are summarized in Table 8.3.

	Tunnel Models		
	MMHT1	MMHT2	MMHT3
Phyllitic quartzite	E = 1.956e9 Pa ν = 0.3	E = 2.054e9 Pa ν = 0.3	E = 1.413e9 Pa ν = 0.3
Creep parameters of Phyllitic quartzite	F=7.5e-7 n=0.45 m=-0.9 (ABAQUS)		
	σ = 3 MPa A=1 B=-0.039 α=10e6 (SAFEA)	σ = 3 MPa A=1 B=-0.039 α=10e6 (SAFEA)	σ = 3.5 MPa A=1 B=-0.036 α=10e6 (SAFEA)
Shotcrete lining	Novotex E = 5.848e9 Pa ν = 0.15 Thickness = 0.1m		
Creep parameters of shotcrete	Compression region F=4.0e-37, n=4.6, m=-0.6 (ABAQUS)		
	σ = 5.5 MPa A=1 B=-0.027 α=0.1 (SAFEA)	σ = 5.5 MPa A=1 B=-0.027 α=0.1 (SAFEA)	σ = 6.5 MPa A=1 B=-0.046 α=0.1 (SAFEA)

Table 8.3: Material properties of MMH tunnel models.

8.4.3 BACK ANALYSIS OF TUNNEL CREEP DEFORMATION

The initial ground conditions of the MMH tunnel were generated using Equation 8.1 as for the Frejus tunnel, and the tunnel was excavated in north-south direction. The excavation of the ground and establishment of lining were controlled by removing and activating corresponding elements. The instantaneous deformation of the ground is a maximum around the tunnel opening, as shown in Figure 8.33 (MMHT1), where the deformation scale factor is set as 30 to make the deformation identifiable. It can be seen that the top section is moving down, while the bottom section is moving up, and the side wall is pushed inwards after excavation.

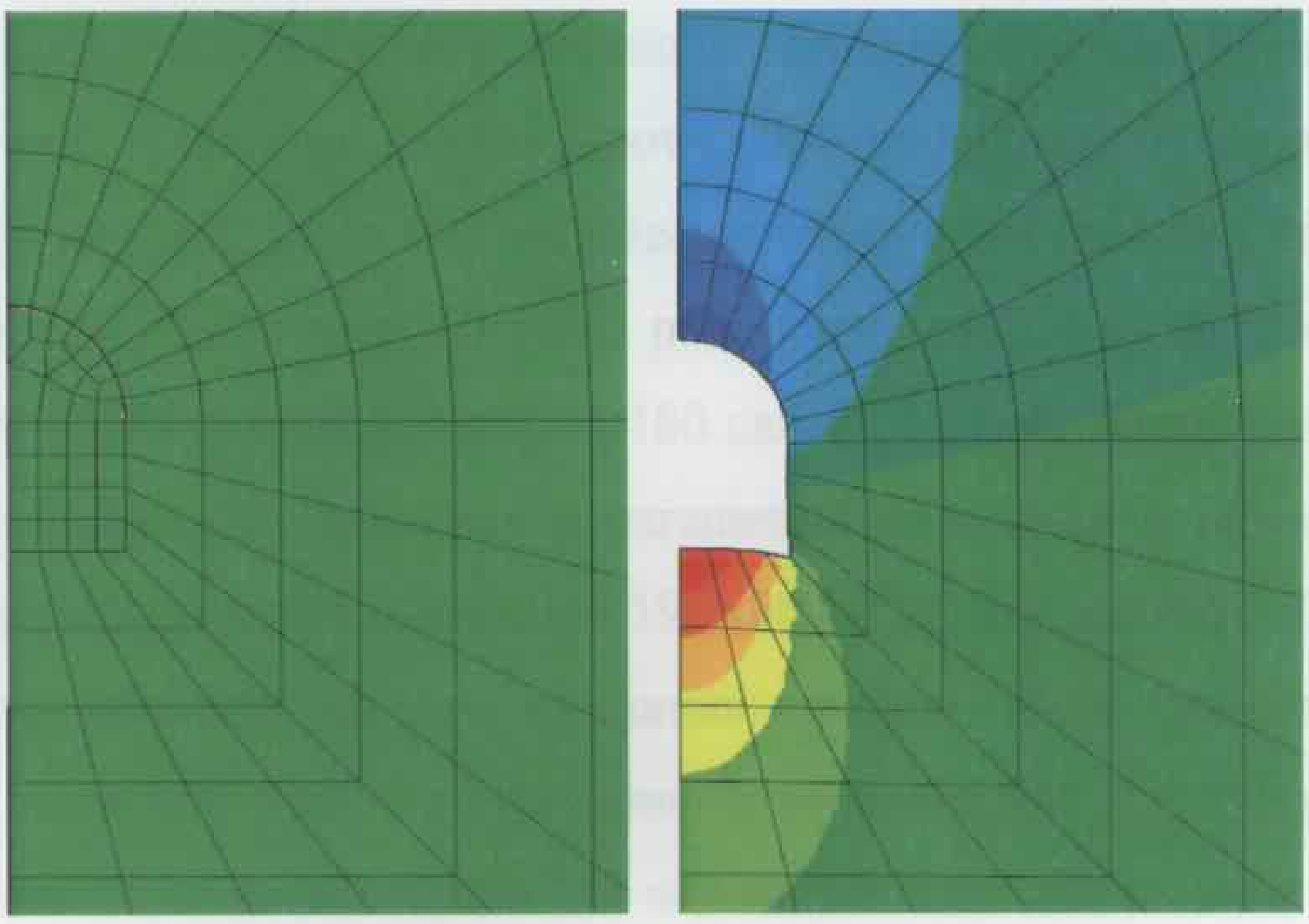

Before Excavation After Excavation

Figure 8.33: Tunnel deformation after excavation.

An example of the vertical deformation of the MMT tunnel model at station 180 (MMHT1 at 200m depth) are shown in Figures 8.34.

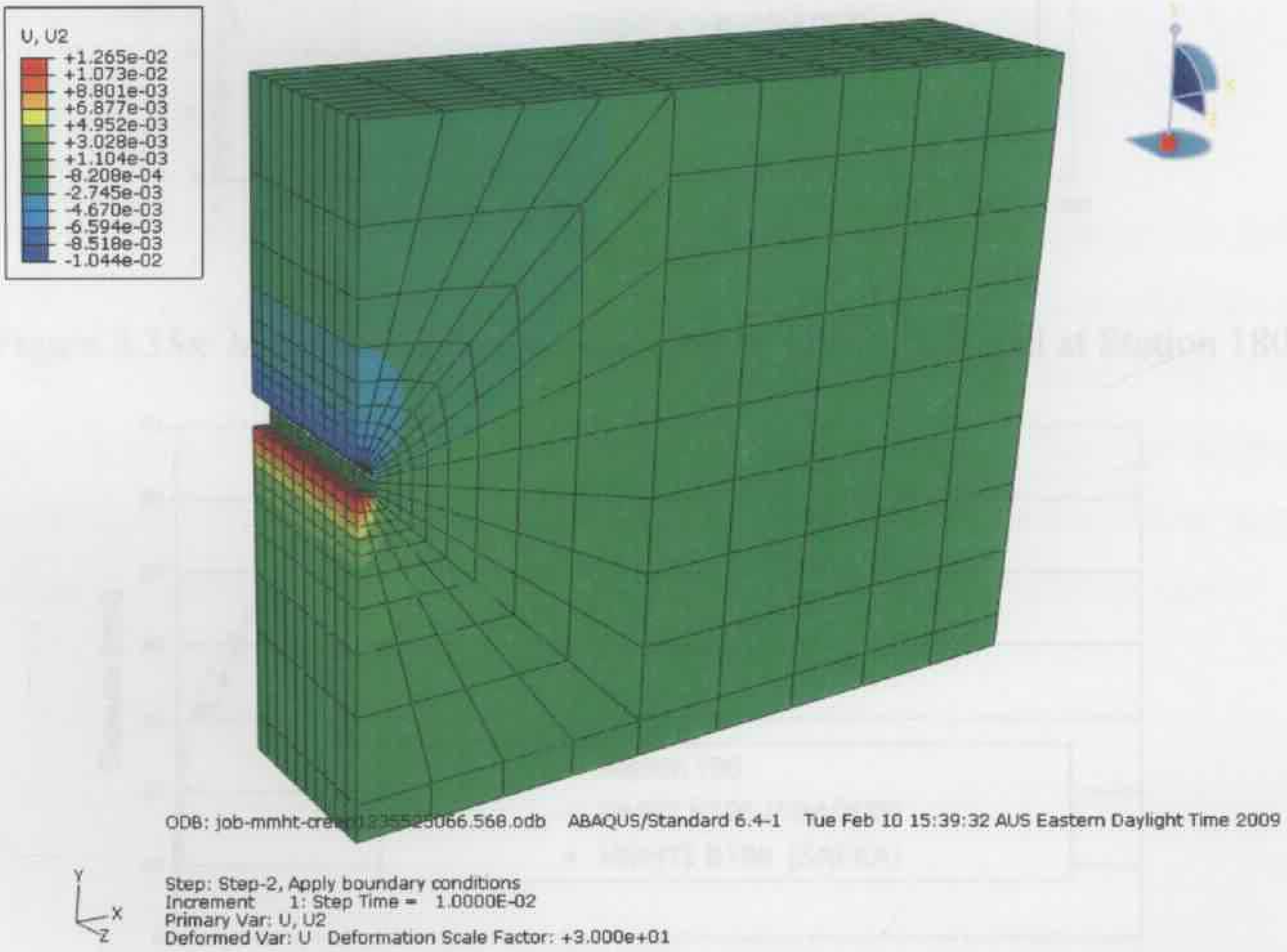

Figure 8.34: Vertical tunnel deformation after excavation (MMHT1).

The increase of tunnel closures at three locations were measured with time. In ABAQUS, the surrounding rock is assumed to obey a power law model, a set of creep parameters of F=7.5e-7, n=0.45, m=-0.9 (Table 8.3) are selected to represent the creep properties of the phyllitic quartzite. With the selected creep parameters, the numerical creeping closure curve of the MMH tunnel model at station 180 can fit the field observation data well as shown in Figure 8.35a. The same creep parameters were used to represent the creep property of the phyllitic quartzite at station 196 (MMHT2) and station 220 (MMHT3) to predict the time-dependent closure of tunnel opening under similar geotechnical conditions. The numerical closure curve shown in Figures 8.35b & 8.35c gave a good fit with the field observation data at station 196 and station 220.

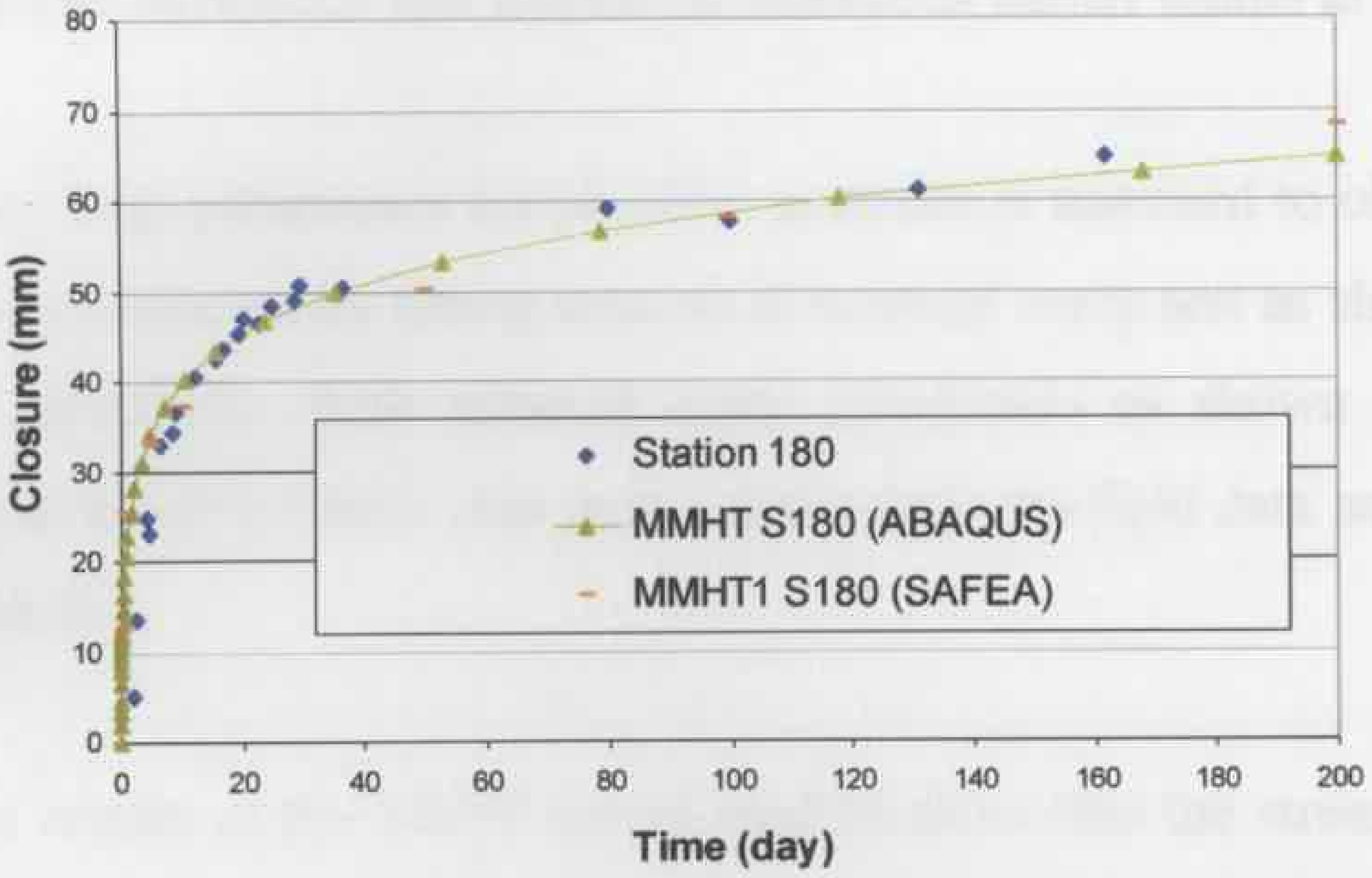

Figure 8.35a: Measured and numerical closure of MMH tunnel at Station 180.

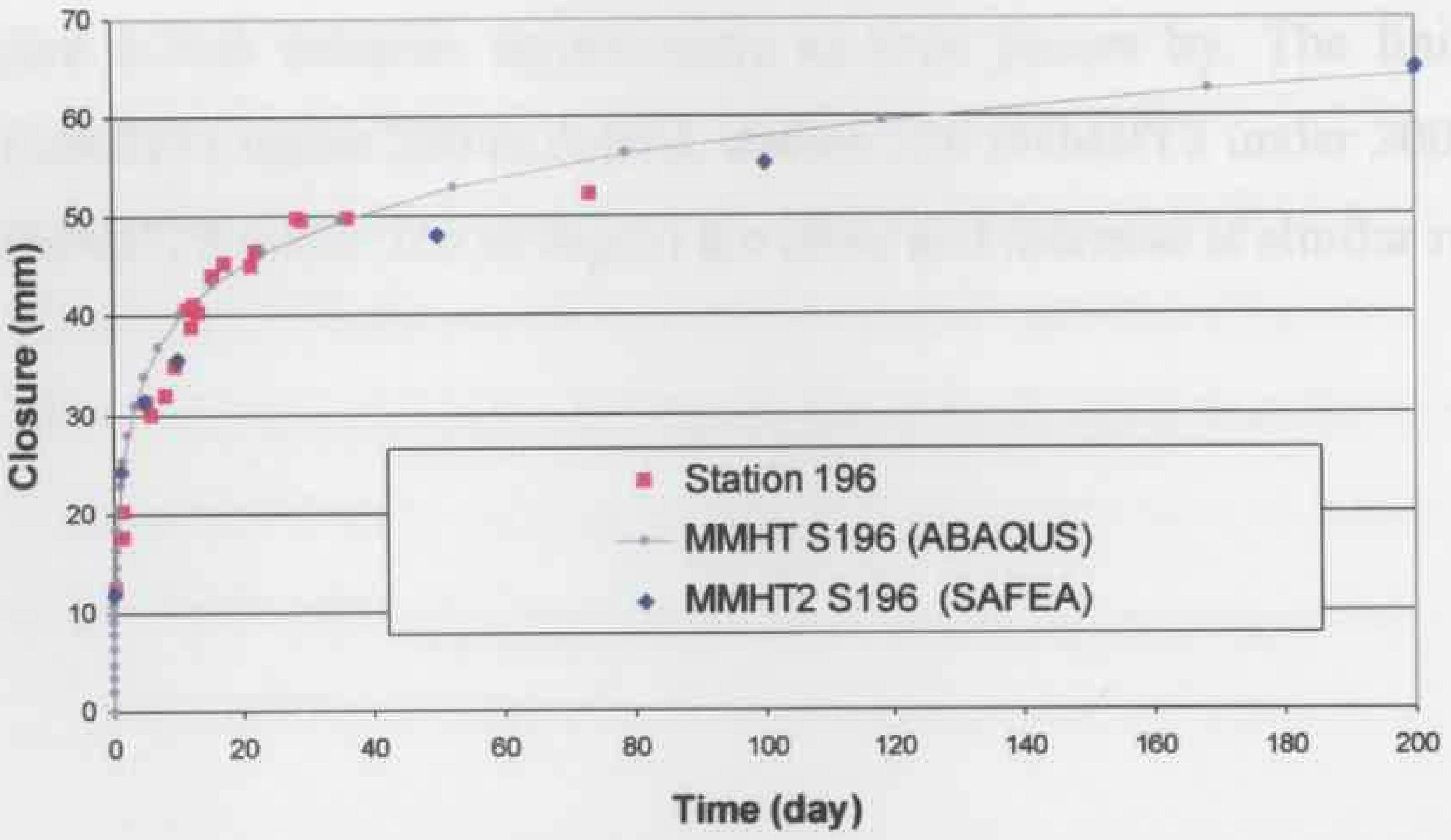

Figure 8.35b: Measured and numerical closure of MMH tunnel at Station 196.

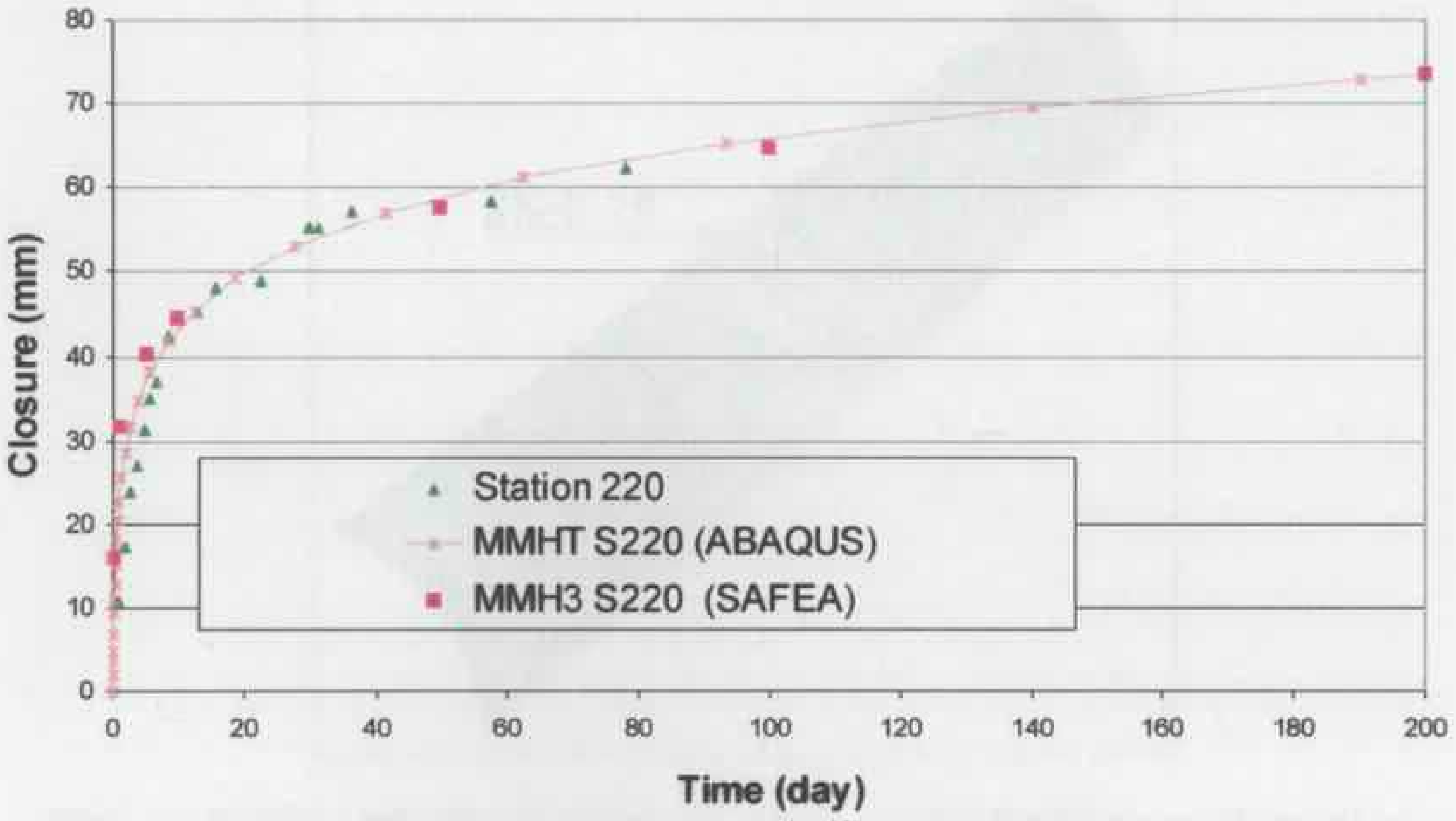

Figure 8.35c: Measured and numerical closure of MMH tunnel at Station 220.

In SAFEA, the creep parameters for phyllitic quartzite is assumed to obey a logarithmic-time function and selected by fitting numerical uniaxial creep test as shown in Figure 6.9 modelled by ABAQUS. With selected creep parameters as shown in Table 8.3, the numerical tunnel closure results also gave a good fit to the field data as shown in Figures 8.35a, 8.35b&8.35c.

The numerical results of the MMH tunnel models show that the stress in the lining and surrounding rock change with time at different rates. Figure 8.36b shows that the stresses in the shell elements on the centre part of the crown of the MMH tunnel (Shell element No. 75, Figure 8.36a) increase significantly as time passes by. The lining stresses at station 180 (MMHT1 under 200 m depth), station 196 (MMHT2 under 200 m depth) and station 220 (MMHT3 under 225 m depth) are close and increase at similar rates.

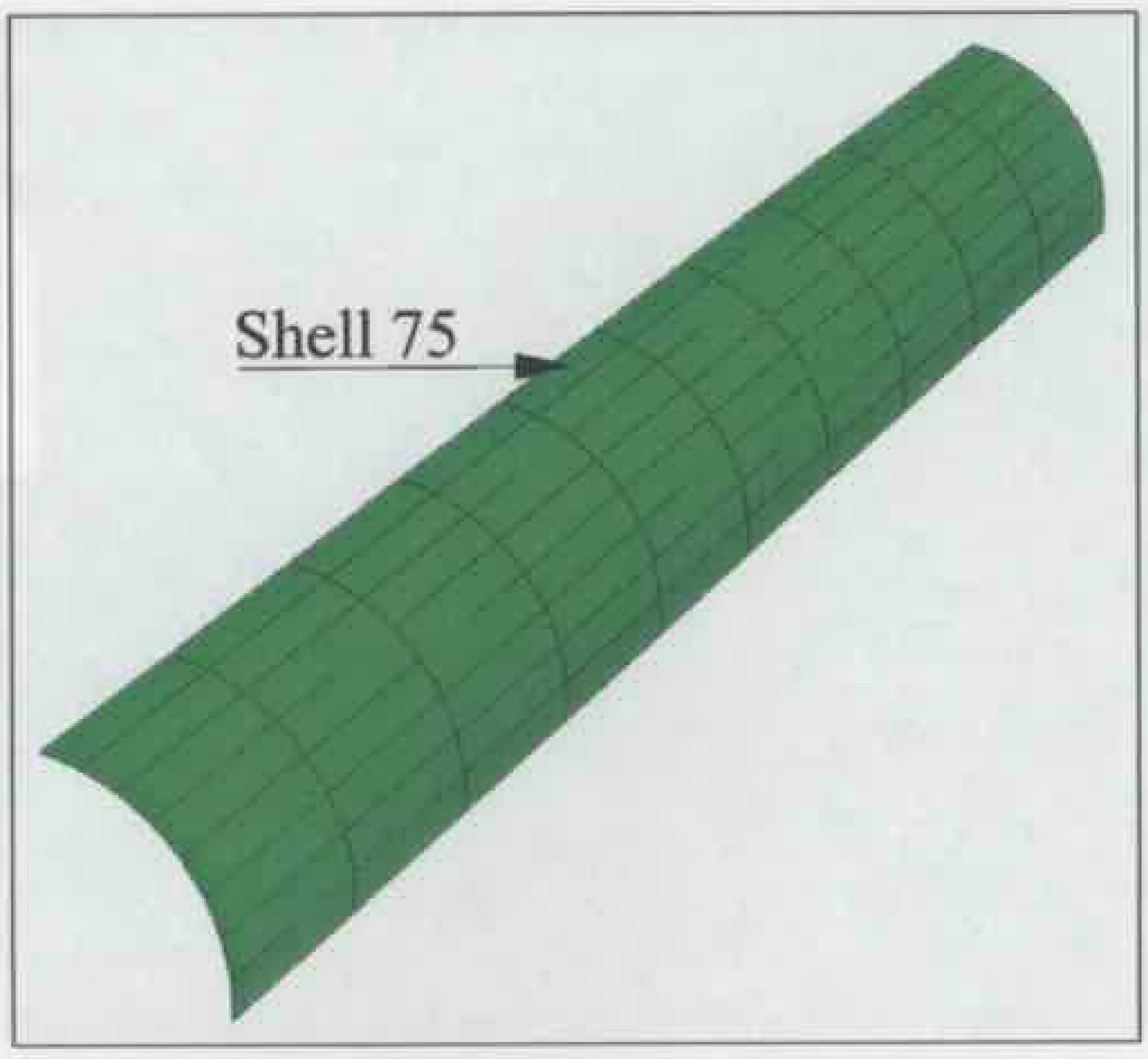

Figure 8.36a: Shell element in crown of MMH tunnel section.

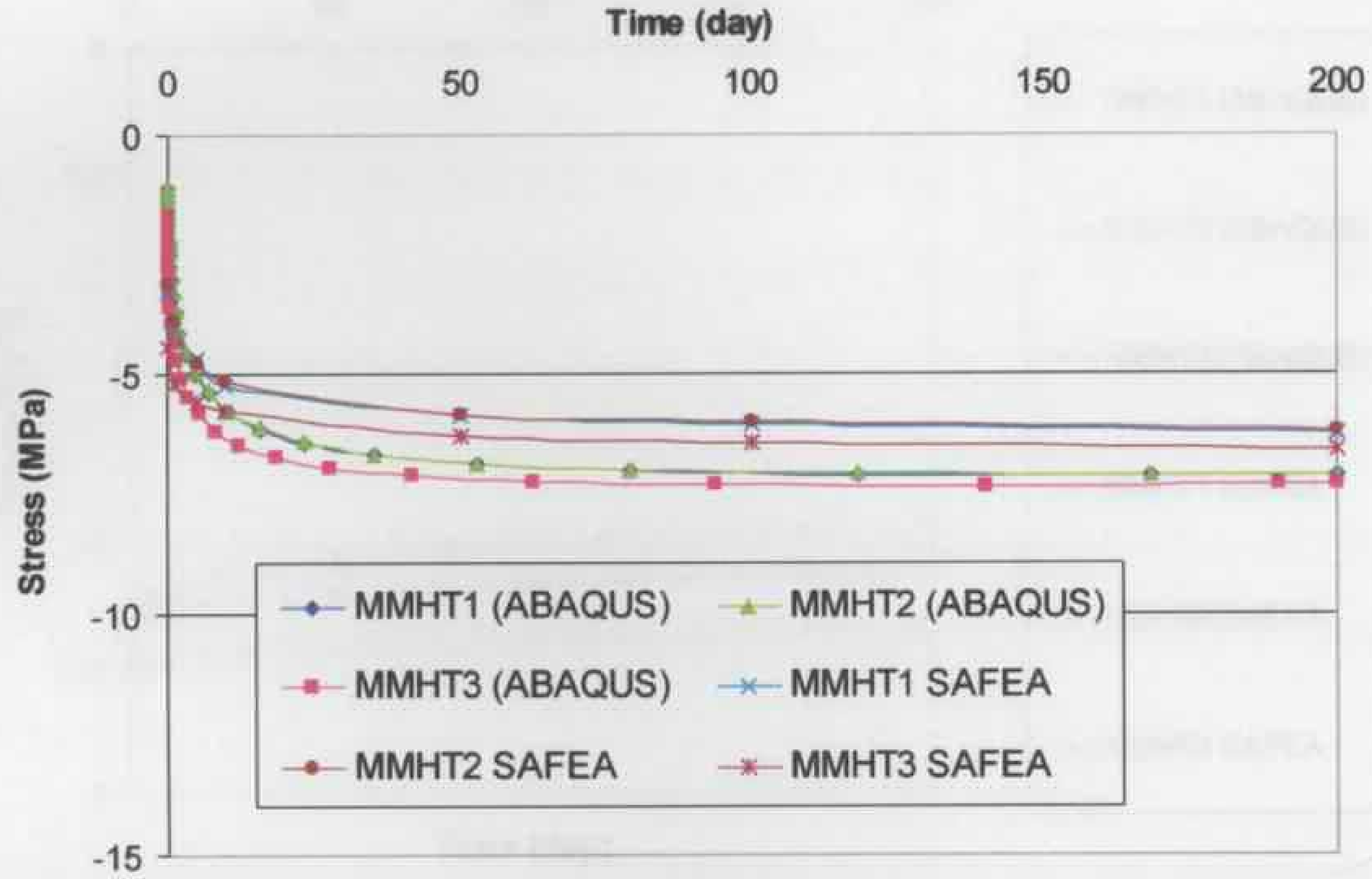

Figure 8.36b: Stress behaviour in lining element in crown of MMH tunnel.

In the MMH tunnel, the surrounding rock of the tunnel section is under compression, and the stress in the rock element at the top of the tunnel sections (Figure 8.37a) decreases slowly at all three locations (Figure 8.37b). It can also be seen that the stress in the rock at station 220 (MMHT3 under 225 m depth) is higher than that at station 180 and 196 (MMHT1 and MMHT2 under 200 m depth).

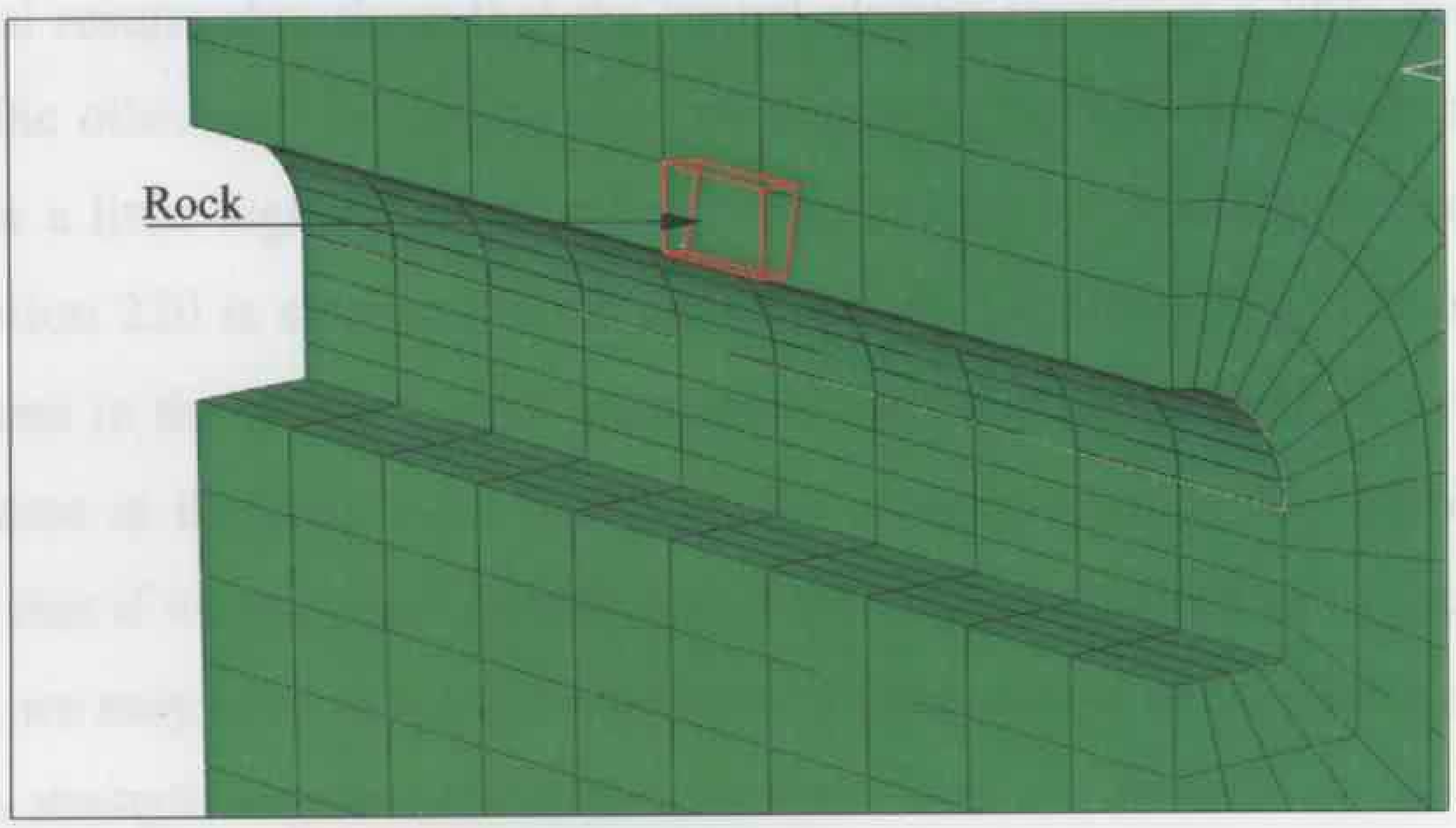

Figure 8.37a: Rock element in crown of MMH tunnel section.

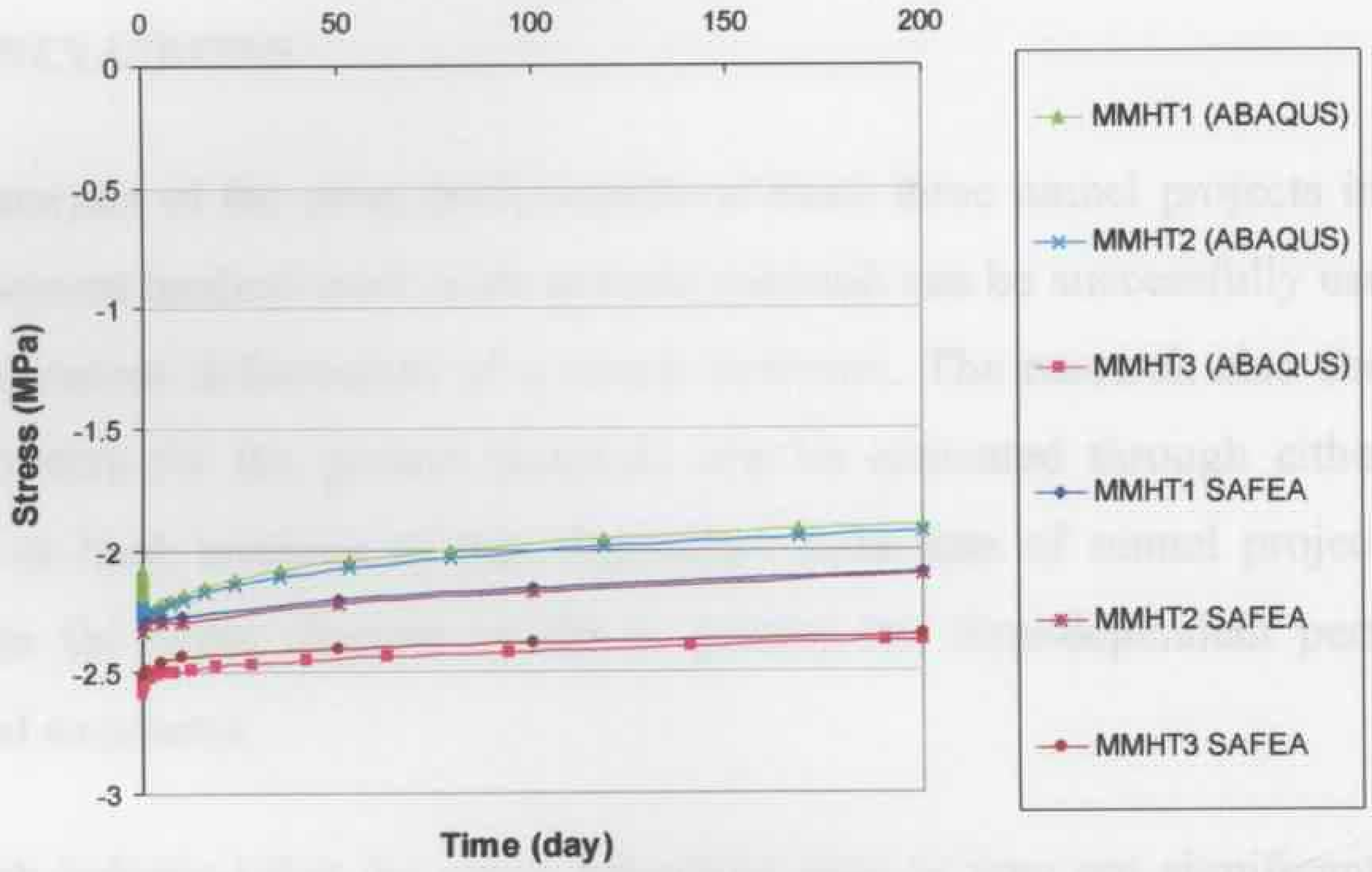

Figure 8.37b: Stress behaviour in rock element in crown of MMH tunnel.

8.4.4 CONCLUSIONS

The back analysis of the creep performance of the MMH tunnel used the same analysis process as in the Frejus tunnel creep analysis case. It proved again that the creep parameters of the ground can be obtained by back analysing the time-dependent field observation data of tunnel closure at one location, and then employed in the finite element tunnel model to predict the time-dependent closure of the tunnel at other locations under similar ground conditions.

The numerical results also show that the tunnel closure increases a little faster at station 220 than at the other two locations, and this might be because the overburden depth at station 220 is a little higher than at other two locations and the elastic modulus of the ground at station 220 is smaller than at the other two locations. It can also be observed that the stresses in the lining tend to increase while the stresses in the surrounding rock tend to decrease at different rates based on the creep properties of different materials. This implies that if we take into consideration the creep behaviour of the structure in the design stage, we may need to increase the design safety factor of the FRS lining to satisfy the long-term strength requirement of the structure.

8.5 CONCLUSIONS

The back analysis of the creep performance of these three tunnel projects indicated that the finite element method used in the present research can be successfully used to predict the time-dependent deformation of a tunnel structure. The research also shows that the creep parameters for the ground materials can be estimated through either laboratory creep tests or back analysis of time-dependent field data of tunnel projects, and then employed in the finite element model to predict the time-dependent performance of underground structures.

The research indicated that the creep behaviour may or may not significantly influence the time-dependent performance of tunnel structures, which depends on many factors, such as the ground conditions, the shape and dimensions of the tunnel, the overburden depth of the tunnel, and the time-dependent properties of the ground and FRS lining. If the creep properties of materials are taken into consideration in the design stage, the time-dependent performance of the support system can be predicted and a safer design of a tunnel structure can be provided.

CHAPTER 9 - SUMMARY AND CONCLUSIONS

9.1 SUMMARY

In this thesis, the time-dependent behaviour of tunnel structures has been investigated, and a theory of the visco-elastic behaviour of materials has been developed by using the finite element method to predict the long term behaviour of tunnel projects.

A literature review has been made in Chapter 2. An overview of historic observations of creep (relaxation) phenomena both for in situ tunnel projects and laboratory tests has been discussed. Many theoretical hypotheses and different viscoelastic or viscoplastic constitutive creep laws which describe the relationship between stress, strain, and time, as well as temperature in the creep process have been proposed and discussed. Different methods including empirical methods, analytical methods and finite element methods used to investigate the time-dependent creep deformation in tunnel projects have also been reviewed.

In Chapter 3, the basic mechanical properties of rock and shotcrete have been discussed, and a constitutive mechanical law which represents the stress-strain-time relationship of the material using a logarithmic function was proposed. The bulk modulus and shear modulus of materials are defined as changing with time obeying a logarithmic function, and the constitutive law is then implemented in the finite element code to calculate the materials' creep deformation by a convolution integral. The integral equation was simplified by employing a Laplace Transform, and then solved by a three-dimensional finite element solver; the solution in real time was finally obtained by a direct numerical Talbot inversion. A simple case study was performed and the results show that the developed code gave accurate numerical results that can be used to solve the finite element equations to a satisfactory precision in the 'tunnel engineering structure scale'.

Chapter 4 introduced the laboratory creep tests used to investigate the time-dependent mechanical properties of shotcrete, sandstone and shale. The ASTM C-1550 round determinate panel tests were used to investigate the creep deformation of FRS samples under bending. The tests were carried out on three different types of FRS, including one steel fibre (Novotex) and two new kinds of macro-synthetic fibre (Strux and HPP). The uniaxial compressive creep tests were performed to measure the deformation of test samples over time under a constant load to investigate the creep property of shotcrete, sandstone and shale under compression. All the experiments were simulated by finite element methods, and the appropriate creep parameters for different materials were estimated by fitting the numerical curves to the experimental deformation curves and later employed in the tunnel models.

Chapter 5 presented the developed the finite element code SAFEA (Semi Analytic Finite Element Analysis) in detail. The program was written in the FORTRAN language and can be used to simulate laboratory creep tests and tunnel excavation and tunnel creep deformation analysis. Different types of element are used in the code to represent different components in the tunnel structure models. Another commercial finite element program ABAQUS used in the present research was also introduced in this Chapter. It uses a power time hardening law to represent the creep behaviour of the materials in the analysis. Some numerical cases were run to verify the accuracy of the program by comparing the results obtained from SAFEA with the results obtained by ABAQUS, and the numerical results of two programs fit each other well.

Chapter 6 illustrated the case study of some numerical circular tunnel models. The tunnels were supported by a macro-synthetic fibre (HPP) reinforced shotcrete lining, and constructed at different depths and under different ground conditions. The numerical results of the instantaneous ground deformation due to tunnel excavation obtained by SAFEA and ABAQUS gave a reasonable fit. The creep parameters of the materials for the power law model used in ABAQUS were estimated from laboratory tests as detailed in Chapter 4, while the creep parameters of materials for the logarithmic creep model used in SAFEA were selected by fitting the deflection curve of uniaxial creep test generated by ABAQUS under a certain stress level. The creep analysis of the two programs all indicated that the overburden depth, mechanical properties and creep parameters of different ground affect the time-dependent behaviours of tunnels significantly.

Chapter 7 used similar numerical analysis processes as those of Chapter 6; some numerical flat roof tunnels supported by a combined shotcrete lining and rockbolts system were modelled. The tunnels were constructed at different depths and under different ground conditions, and three different types of FRS (HPP, Strux and Novotex) were used for the lining, here Novotex is steel fibre while Strux and HPP are macro-synthetic fibres. The numerical results indicated similar conclusions drawn from Chapter 6 that the overburden depth and different ground conditions affect the time-dependent behaviours of tunnels significantly. The results also show that the flat roof tunnels tend to creep faster than the circular tunnels, and the different properties of the FRS do affect the time-dependent performance of a tunnel support structure but not significantly.

Finally, to verify the application of the method to practical problems, numerical back analyses were carried out on some selected practical projects, i.e. the Frejus Tunnel in France, the Lane Cove Tunnel in Australia, and the Middle Marsyangdi Hydropower (MMH) tunnel in Nepal. In the Frejus Tunnel models and the MMH tunnel models, the creep parameters of the rock materials were extrapolated through the back analysis of the time-dependent field observation data of tunnel projects, while in the Lane Cove Tunnel model, the creep parameters of rock materials were obtained through laboratory creep tests on the material specimens. The predicted time-dependent convergences of the tunnel were obtained in all tunnel models, and the numerical results gave a good fit to the field data. The numerical results also indicated that the stresses in the lining, rockbolts and surrounding rock in the tunnel support structure tend to decrease or increase at different rates based on the creep properties of different materials, and imply that if we take into consideration the creep behaviour of the material in the design stage, we may need to increase the design safety factor of the FRS lining and/or rockbolts to satisfy the long-term strength requirement of the structure.

9.2 CONCLUSIONS

The thesis indicated that the two finite element methods that are based upon different creep theories in the present research can adequately perform the creep analysis for a tunnel support structure. The creep parameters of materials can be extrapolated through laboratory creep tests or tunnel field data. With the creep parameters, it is possible to predict the long term performance of a tunnel support structure, and the numerical results can help us to get a better understanding of the time-dependent behaviour of tunnel structure as a whole and every component in the supporting system.

The research indicated that with a defined set of creep parameters, the logarithmic creep function used in SAFEA can be used to represent a material's creep behaviour under a given stress level, while the power law creep model used in ABAQUS can be used to represent a material's creep behaviour under different stress levels.

In SAFEA, a Laplace transform and Talbot inversion are used to simplify the integral equation and get an approximate solution for the problem, while ABAQUS performs an integral calculation by dividing the requested period into many small time steps and assuming that the increment varies linearly with time over a finite increment of time. Both methods give solutions within a satisfied precision range in the tunnel engineering structure scale.

For the uniaxial creep test under a constant load where stress is unique in the specimens, the logarithmic creep function can represent the test very well, while for the ASTM C-1550 round determinate panel tests where a constant load is applied at the centre of the panel, the stress in the panel specimen is not unique and a power law creep model is needed to represent this test.

The first choice to get the creep parameters of a material is through laboratory creep tests, such as a uniaxial creep test, relaxation test or ASTM test, but the laboratory creep tests are normally very time-consuming and costly. Otherwise if the field observation data exists for a tunnel project, it is possible to approximate creep parameters for the surrounding rock through numerical back analysis of the field data and employ these in further tunnel projects in similar ground conditions. With the creep parameters obtained either way, the finite element methods can give a good prediction for the long term performance of a tunnel support structure.

The field observation data and numerical analysis results all indicated that the creep behaviour of materials do affect the long term performance of the shotcrete and rockbolt support. The convergence deformation of tunnel section will increase, while the stress in the lining, rockbolt and surrounding rock tend to decrease or increase at different rates with time based on many factors such as the shape and dimensions of the tunnel section, the overburden depth above the tunnel, the ground condition, the elastic and creep properties of the ground, FRS lining and rockbolt, and the design of the combined FRS lining and rockbolt supporting system. Generally speaking, a shallow tunnel in hard rock may display little creep deformation, while a deep tunnel in soft ground conditions may be influenced by the creep behaviour significantly. The use of different types of FRS lining was predicted not to affect the long term behaviour of the tunnel structure significantly in the present research.

In conclusion, it is necessary and possible to take into consideration the creep behaviour of the materials used in a tunnel design, and we may need to increase the design safety factor of the FRS lining and/or rockbolts to satisfy the long term performance of the tunnel structure.

9.3 SUGGESTIONS FOR FURTHER WORK

This thesis provided a method which considers the visco-elastic properties of materials and can be used to predict the long term behaviour of tunnel and provide a safer design for the tunnel support structure. Further work may be carried out on the following area:

- The creep data for sandstone and shale under different stress levels are not sufficient, more laboratory uniaxial creep tests need be performed on the sandstone and shale specimens under different constant loads.

- Laboratory creep tests need be performed on other types of rock, especially on soft rock to investigate the creep properties of different geo-materials.

- More time-dependent in situ observation data of tunnel support structures can provide valuable information for the investigation of the creep properties of soil and rock and the design of further tunnel projects constructed in similar ground conditions.

- More laboratory creep tests under different temperatures and new creep theory is needed to take into consideration the influence of temperature on the creep performance of different materials.

REFERENCES

ABAQUS Analysis User's Manual, (2003). Version 6.4. © ABAQUS, Inc, USA.

Adachi, T. and Oka, F., (1982). *"Constitutive Equations for Normally Consolidated Clay Based on Elasto-Viscoplasticity"*, Soils and Foundations, Vol. 22, No. 4, p. 57-70.

Akai, K., (1963). *"Study on long-term consolidation of undisturbed saturated clay"*, Soil and Foundation, Vol. 4, No. 1, p. 50-56.

Akagi, T., (1985). *"Application of Rheological Models to Nonlinear Creep Properties of Rock"*, A. A. Balkema, Vol. 1, p. 415-420.

Augustesen, A., Liingaard, M., and Lade, P. V., (2004). *''Evaluation of time-dependent behavior of soils''*, Int. J. Geomech., Vol.4(3), p.137-156.

Baek, W. and Moriwaki, T., (2004). "Internal behavior of clayey ground improved by vertical drains in 3D-consolidation process", Soils and Foundations, Vol. 44, No. 3, p. 25-37.

Barden, L., (1968). "Recent developments in consolidation theory and technique", Civil Engineering (London), Vol. 63, No. 738, p. 52-54.

Barden, L., (1969). *"Time dependent deformation of normally consolidated clays and peats"*, American Society of Civil Engineers, Journal of the Soil Mechanics and Foundations Division, Vol. 95, No. SM1, p. 1-31.

Berre, T. and Iversen, K., (1972). *''Oedometer tests with different specimen heights on a clay exhibiting large secondary compression.''* Geotechnique, Vol. 17(1), p. 53-70.

Bernard, E.S., (2004). "Creep of cracked fibre reinforced shotcrete panels", Shotcrete: More Engineering Developments, Taylor & Francis Group, London, p. 47-57.

Bjerrum, L., (1967). *"Engineering geology of Norwegian normally-consolidated marine clays as related to settlements of buildings"*, Norges Geotekniske Institutt -- Publikasjon, No. Publ 71, 38p.

Boidy, E., Bouvard, A. and Pellet, F., (2002). *"Back analysis of time-dependent behaviour of a test gallery in claystone"*, Tunnelling and Underground Space Technology, Vol. 17, No. 4, p. 415-424.

Bridge, R.Q., (1979). "*Composite Columns Under Sustained Load*", ASCE J Struct Div, Vol. 105, No. 3, p. 563-576.

Buisman, A.S.K., (1936). "*Results of long duration settlements tests*", Proc. 1st International Conference on Soil Mechanics and Foundation Engineering, Harvard University, Cambridge Massachusetts, Vol.1, pp. 103-106.

Busch, W.H. and Keller, G.H., (1982). "*Consolidation characteristics of sediments from the Peru-Chile continental margin and implications for past sediment instability*", Marine Geology, Vol. 45, 1-2, p. 17-39.

Campos de Orellana, A.J., (1996). "*Pressure solution creep and non-associated plasticity in the mechanical behavior of potash mine openings*", International Journal of Rock Mechanics and Mining Sciences, Vol. 33, No. 4, p. 347-370.

Carter, J. P. and Booker, J. R., (1982). "*The analysis of consolidation and creep around a deep circular tunnel in clay*", Numerical methods in geomechanics. Proc. 4th international conference, Edmonton, Vol. 2, p. 537-544.

Carter, J. P. and Booker, J. R., (1983). "*Creep and Consolidation around Circular Openings in Infinite Media*", International Journal of Solids and Structures, Vol. 19, No. 8, p. 663-675.

Chen, W.Z., Zhu, W.S. and Shao, J.F., (2004). "*Damage coupled time dependent model of jointed rockmass and application to large underground cavern exacavation*", Int J Rock Mech Min Sci 41, p. 669-677.

Christian, J. T., (1999). "*What has the finite element method done for (or to) geotechnical engineering?*" Civil Engineering Practice, Vol. 14, No. 2, p. 73-74.

Dalgic, S., (2002). "*Tunneling in squeezing rock, the Bolu tunnel, anatolian motorway, Turkey*", Engineering Geology, Vol. 67, No.1-2, p. 73-96.

Dube, A. K., Singh, B., Mithal, R. S. and Singh, B., (1977). "*Pressure On Tunnel Supports In Squeezing Rocks*", Proceedings - Annual Allerton Conference on Circuit and System Theory, p. 39-44.

Feda, J., (1992). "*Creep of soils and related phenomena, Development in geotechnical engineering*", Elsevier Science, North-Holland, Amsterdam, The Netherlands, Vol. 68.

Fernandez, G., (1994). "*Rock mechanics for underground storage*", In: Presented at the SMRI-fall Meeting, Hannover, Germany.

George, K.P., (1969). "*Cracking in pavements influenced by viscoelastic properties of soil-cement*", Highway Research Record, No. 263, p. 47-59.

Ghaboussi, J. and Gioda, G., (1977). "*On The Time-Dependent Effects In Advancing Tunnels*", International Journal for Numerical and Analytical Methods in Geomechanics, Vol. 1, No. 3, p. 249-269.

Ghaboussi, J., Ranken, R.E. and Hendron, A.J., (1981). "*Time-dependent behavior of solution caverns in salt*", ASCE 107 (GT10), p. 1379 – 1401.

Gioda, G. and Cividini, A., (1979). "*Numerical Study of Non Linear Consolidation Problems Taking Into Account Creep Effects*", SAE Preprints, Vol. 1, p. 149-161.

Grimstad, E., (2001). "*Behaviour of steel fibre reinforced shotcrete during large deformations in squeezing rock*", Shotcrete: Engineering Developments, p.119-122.

Gurung, N. and Iwao, Y., (1998). "*Observations of deformation and engineering geology in the Lam Ta Khong tunnel, Thailand*", Engineering Geology, Vol. 51, No. 1, p. 55-63.

Hellmich, C., Sercombe, J., Ulm, F.J. and Mang, H., (2000). "*Modeling of early-age creep of shotcrete. II: Application to tunneling*", Journal of Engineering Mechanics, Vol. 126, No. 3, p. 292-299.

Hisatake, M., (2003). "*Effects of steel fiber reinforced high-strength shotcrete in a squeezing tunnel*", Tunnelling and Underground Space Technology, Vol. 18, No. 2-3, p. 197-204.

Hoefer, K.H. and Knoll, P., (1971). "*Investigations into the mechanism of creep deformation in carnallite, and practical applications*", Int J Rock Mech Mining Sci, Vol. 8, No. 1, p. 61-73.

Hoek, E., (2001). "*Big tunnels in bad rock*", Journal of Geotechnical and Geoenvironmental Engineering, Vol. 127, No. 9, p. 726-740.

Hunter, G. and Khalili, N., (2000). "*A Simple Criterion for Creep Induced Failure of Over-Consolidated Clays*", Pro. GeoEng 2000 Conference.

Jamiolkowski, M., Ladd, C.C., Germaine, J.T., and Lancellotta, R., (1985). "*New developments in field and laboratory testing of soils*", Proceedings eleventh international conference on soil mechanics and foundation engineering, AA Balkema, p. 57-153.

Jeff, L. B., (1997). *"Characterization of MSC/NASTRAN & MSC/ABAQUS Elements for Turbine Engine Blade Frequency Analysis"*, in Air Force Research, Lab Propulsion Directorate, Turbine Engine Division.

Jong, I.C., (2005). *"Teaching Students Work and Virtual Work Method in Statics: A Guiding Strategy with Illustrative Examples"*, Proceedings of the 2005 American Society for Engineering Education Annual Conference & Exposition

Kaiser, P. K. and Morgenstern, N. R., (1981). *"Time-Dependent Deformation of Small Tunnels - 1. Experimental Facilities"*, International Journal of Rock Mechanics and Mining Sciences & Geomechanics Abstracts, Vol. 18, No. 2, p. 129-140.

Kaiser, K., (1981). *"Time-Dependent Deformation of Small Tunnels - 2. Typical Test Data"*, International Journal of Rock Mechanics and Mining Sciences & Geomechanics Abstracts, Vol. 18, No. 2, p. 141-152.

Komamura, F. and Huang, R.J., (1974). *"New Rheological Model for Soil Behavior"*, American Society of Civil Engineers, Journal of the Geotechnical Engineering Division, Vol. 100, No. GT7, p. 807-824.

Kondner, R.L. and Ho, M.M.K., (1965). *"Energy dissipation of cohesive soil by fourier transformation of stress relaxation response"*, Society of Rheology -- Transactions, Vol. 9, No. Part 1, p. 145-157.

Kontogianni, V., Psimoulis, P. and Stiros, S., (2006). *"What is the contribution of time-dependent deformation in tunnel convergence?"*, Source: Engineering Geology, Vol. 82, No. 4, p. 264-267.

Kontogianni, V., Tzortzis, A. and Stiros, S., (2004). *"Deformation and failure of the Tymfristos tunnel, Greece"*, Journal of Geotechnical and Geoenvironmental Engineering, Vol. 130, No. 10, p. 1004-1013.

Koppejan, A.W., (1948). "A formula combining the Terzaghi load compression relationship and the Buisman secular time effect", Proc. 2nd Int. Conf. Soil Mech. And Found. Eng., Rotterdam, 3, p. 32-38.

Kranz, R.L., (1979). *"Crack growth and development during creep of Barre granite"*, Int J Rock Mech Min Sci 16, p. 22-35.

Lacerda, W. A., and Houston, W. N. (1973). *"Stress relaxation in soils"*, Proc., 8th ICSMFE, 1/34, p. 221-227.

Lackner, R., Macht, J., Hellmich, C. and Mang, H. A., (2002). *"Hybrid method for analysis of segmented shotcrete tunnel linings"*, Journal of Geotechnical and Geoenvironmental Engineering, Vol. 128, No. 4, p. 298-308.

Ladanyi, B. and Melouki, M., (1993). "*Determination of creep properties of frozen soils by means of the borehole stress relaxation test*", Canadian Geotechnical Journal, Vol. 30, No. 1, p. 170-186.

Ladd, C. C., Foott, R., Ishihara, K., Schlosser, F., and Poulos, H. J., (1977). "*Stress-deformation and strength characteristics.*", Proc., 2, 9th ICSMFE, Japan, p. 421-494.

Leroueil, S. and Marques, M.E.S., (1996). "*Importance of strain rate and temperature effects in geotechnical engineering*", Geotechnical Special Publication, No. 61, Measuring and Modeling Time Dependent Soil Behavior, p. 1-60.

Li, Y. and Xia, C., (2000). "*Time-dependent tests on intact rocks in uniaxial compression*", International Journal of Rock Mechanics and Mining Sciences, Vol. 37, No. 3, p. 467-475.

Liingaard, M., Augustesen, A. and Lade, P. V., (2002). "*Observed Time Dependent Behavior of Soils*", 15th ASCE engineering mechanics conference, Columbia University, New York.

Lo, K. Y. and Yuen, Clement M. K., (1981). "*Design Of Tunnel Lining In Rock For Long Term Time Effects*", Canadian Geotechnical Journal, Vol. 18, No. 1, p. 24-39.

Lopes, M.L., Cardoso, A.S. and Yeo, K.C., (1994). "*Modelling Performance of a Sloped Reinforced Soil Wall Using Creep Function*", Geotextiles and Geomembranes, Vol. 13, No. 3, p. 181-197.

Malvern, L.E., (1951). "*The Propagation of Longitudinal Waves of Plastic Deformation in a Bar of Material Exhibiting a Strain-Rate Effect*", J. Appl. Mech., Trans. ASME, Vol. 18, p. 203-208.

Malvern, L.E., (1984). "*Experimental and Theoritical Approaches to Characterization of Material Behavior at High Rates of Deformation*", in Mechanical Properties at High Rates of Strain, Conf. Ser. No. 70, Ed. J. Harding, Institute of Physics, London, 1-20.

Mangat, P. S. and Motamedi, A. M., (1985). "*Theory for the Creep of Steel Fibre Reinforced Cement Matrices under Compression*", Journal of Materials Science, Vol. 20, No. 3, p. 1119-1133.

Matsushita, M., Tatsouka, F., Koseki, J., Cazacliu, B., Benedetto, H. and Yasin, S.J.M., (1999). "*Time effects on the pre-peak deformation properties of* *sands"*, Pre-failure Deformation Characteristics of geomaterials, Jamiolkowski, Lancellotta & Lo Presti (eds.), Balkema, Rotterdam, p. 681-689.

Maxwell, J.C., (1867). *"On the Dynamical Theory of Gases"*, Philosophical Transactions of the Royal Society of London, Vol. 157, p. 49-88.

Mesri, G., (1973). *"Coefficient of Secondary Compression"* J. of the Soil Mech. and Found. Div., ASCE, Vol. 99, No. SM1, p. 123-137.

Mesri, G. and Castro, A., (1987). *" C_α / C_c Concept And K_0 During Secondary Compression"*, Journal of Geotechnical Engineering, Vol. 113, No. 3, p. 230-247.

Mesri, G., Feng, T.W. and Shahien, M., (1999). *"Coefficient of consolidation by inflection point method"*, Journal of Geotechnical and Geoenvironmental Engineering, Vol.125, No. 8, p. 716-718.

Mesri, G. and Godlewski, P.M., (1977). *"Time- and stress-compressibility interrelationship"*, Journal of geotechical engineering, 103(GT5), p. 417-430.

Mott, N.F., (1956a). *"Creep and fracture of metals at high temperatures"*, In: Proceedings of NPL symposium HMSO, London, p. 21-24.

Mott, N.F., (1956b). *"Creep in metal crystals at very low temperature"*, Source: Philosophical Magazine, Vol. 1, 8th Series, No. 6, p. 568-572.

Murayama, S. and Shibata, T., (1958). *"On the rheological characters of clay"*, Disaster Prevention Research Institute, Kyoto University, Bulletins, Bulletin No. 26, p. 1-43.

Murayama, S. and Shibata, T., (1959). *"On the secondary consolidation of clay"*, Second Japan Congress on Testing Materials, p.178-181.

Murayama, S. and Shibata, T., (1964). *"Flow and stress relaxation of clays"*, Proceedings of IUTAM Symposium on Rheology and Soil Mechanics, Kravchenko J, Sirieys PM (eds), Grenoble, Springer: Berlin, p. 99-129.

Murayama, S., (1969). *"Effect of Temperature on Elasticity of Clays"*, Nat Acad Sciences-Nat Research Council- Highway Research Board-Special Report 103, p.194-203.

Oda, Y. and Mitachi, T., (1988). *"Stress relaxation characteristics of saturated clays"*, Soils and Foundations, Vol. 28, No. 4, p. 69-80.

Oida, A., (1984). *"Analysis of Rheological Deformation of Soil By Means of Finite Element Method"*, Journal of Terramechanics, Vol. 21, No. 3, p. 237-251.

Oka, F., Adachi, T. and Yashima, A., (1994). *"Instability of an elasto-viscoplastic constitutive model for clay and strain localization"*, Mechanics of Materials, Vol. 18, No. 2, p. 119-129.

Okubo, S., Nishimatsu, Y. and Fukui, K., (1991). *"Complete creep curves under uniaxial compression"*, Int J Rock Mech Min Sci Geomech Abstr 28, p. 77-82.

Pan, J.Z., (1986). *"General Rheological Model of Paddy Soils in South China"*, Journal of Terramechanics, Vol. 23, No. 2, p. 59-68.

Pan, J.Z., Cai, G.F. and Huang, Y.J., (1990). *"Modified rheological model for paddy soils in South China after remoulding"*, Journal of Terramechanics, Vol. 27, No. 1, p. 1-5.

Pan, Y.-W. and Dong, J.-J., (1991). *"Time-dependent tunnel convergence - I. Formulation of the model* International", Journal of Rock Mechanics and Mining Sciences & Geomechanics Abstracts, Vol. 28, No. 6, p. 469-475.

Pan, Y.-W. and Dong, J.-J., (1991). *"Time-dependent tunnel convergence - II. Advance rate and tunnel-support interaction"*, International Journal of Rock Mechanics and Mining Sciences & Geomechanics Abstracts, Vol. 28, No. 6, p. 477-488.

Panthi, K.K. and Nilsen, B., (2007). *"Uncertainty analysis of tunnel squeezing for two tunnel cases from Nepal Himalaya"*, International Journal of Rock Mechanics and Mining Sciences, Vol. 44, Issue. 1, P. 67-76.

Peck, R. B., (1969). *"Deep excavations and tunneling in soft ground"*, Proc. of the 7th int. Conference on Soil Mechanics and Foundation Engineering, State of the art volume, Sociedad Mexicnan de Mecanica de Suelos, A. C., p. 225-290.

Pellet. F., Sahli. M., Boidy. E. and Boulon. M., (2000). *"Modelling of time-dependent behaviour of sandstones for deep underground openings"*, International Symposium on Civil Engineering in the 21st Century; Beijing China, p. 431-438.

Pells, P.J.N. (2002). *"Developments in the design of tunnels and caverns in the Triassic rocks of the Sydney region"*, International Journal of Rock Mechanics and Mining Sciences, Vol. 39, p. 569 – 587.

Persson, B., (1998). *"Quasi-instantaneous and long-term deformations of high performance concrete with sealed curing"*, Advanced Cement Based Materials, Vol. 8, No. 1, p. 1-16.

Perzyna, P. (1963). *"Constitutive equations for work-hardening and rate sensitive plastic materials"*, Polska Akademiya Nauk - Proceedings of Vibration Problems, Vol. 4, No. 3, p. 281-290.

Perzyna, P. (1966). *"Fundamental problems in viscoplasticity"*, Adv. Appl. Mech., Vol. 9, p. 244-377.

Phienwej, N. and Cording, E.J., (1991). *"Sheared shale response to deep TBM excavation"*, Engineering Geology, Vol. 39, No. 3-4, p. 371-391.

Phienwej, N., Thakur, P. K. and Cording, E.J., (2007). *"Time-dependent response of tunnels considering creep effect"*, International Journal of Geomechanics, Vol. 7, No. 4, p. 296-306.

Poulos, H. G., Davis, E. H., and Ambrosis, L. P. (1976). *''Method of calculating long-term creep settlements.''* J. Geotech. Eng. Div., Am. Soc. Civ. Eng., Vol. 102(7), p. 787-804.

Rabotnov, Y. N. (1969). *"Creep problems in structural members"*, North-Holland, Amsterdam, The Netherlands.

Roscoe, K.H., Schofield, A.N. and Thurairajah, A., (1963). *"Yielding of clays in states wetter than critical"*. Geotechnique, Vol. 13, No. 3, p. 211-240.

Roux, A. J. A. and Denkhaus, H. G., (1954). *"An investigation into the problem of rock bursts-An operational research project"*, J. chem. metall. Min. Soc. S.Afr. 55, p. 103-124.

Sahli, M., Pellet, F., Boidy, E., and Fabre, G. (2001). *"Modeling of viscous behavior of rocks for deep tunnel"*, ISRM regional symposium, Eurock.

Saito, M., (1965). *"Forecasting the time of occurrence of a slope failure"*, Proc. 6th Int. Conf. Soil Mech. Found. Enorg. 2, p. 53-541.

Saito, M., (1969). *"Forecasting time of slope failure by tertiary creep"*, Proc. 7th Int. Conf. Soil Mech. Found. Engr O. Mexico, p. 677-683.

Schiffman, R.L., Ladd, C.C. and Chen, A.T.F., (1964). *"The secondary consolidation of clay"*, Rheology and soil mechanics. International Union of Theoretical and Applied Mechanics: Symposium Grenoble.

Sekiguchi, H. and Toriihara, M., (1976). *"Theory of One-Dimensional Consolidation of Clays with Consideration of Their Rheological Properties"*, Soils and Foundations, Vol. 16, No. 1, p. 27-44.

Semple, R. M., Hendron, A. J. and Mesri, G., (1973). *"Effect Of Time-Dependent Properties Of Altered Rock On Tunnel Support Requirements"*, Report of Investigations - United States, Bureau of Mines, 217p.

Sercombe, J., Hellmich, C., Ulm, F.J. and Mang, H., (2000). *"Modeling of early-age creep of shotcrete. I: Model and model parameters"*, Journal of Engineering Mechanics, Vol. 126, No. 3, p. 284-291.

Shalabi, F.I., (2005). *"FE analysis of time-dependent behaviour of tunneling in squeezing ground using two different creep models"*, Tunnelling and Underground Space Technology, Vol. 20, p. 271–279.

Silvestri, V., Soulie, M., Touchan, Z. and Fay, B., (1988). *"Triaxial Relaxation Tests on a Soft Clay"*, Advanced Triaxial Testing of Soil and Rock, ASTM STP 977, p. 321-337.

Singh, A. and Mitchell, J.K., (1968). "General stress-strain-time function for soils", American Society of Civil Engineers Proceedings, Journal of the Soil Mechanics and Foundations Division, Vol. 94(1), p. 21-46.

Singh, D. P., (1975). *"Study of Creep of Rocks"*, International Journal of Rock Mechanics and Mining Sciences & Geomechanics Abstracts, Vol. 12, No.9, p. 271-275.

Singh, T. N. and Verma, A. K., (2005). *"Prediction of creep characteristic of rock under varying environment"*, in *Environ Geol 48*, p. 559–568.

Skrzypek, J. J. (1993). *"Plasticity and creep-Theory, examples, and problems"*, (English edition) B. H., Richard, ed., CRC Press, London.

Small, J. C. and Booker, J. R., (1984). *"Finite Layer Analysis of Layered Elastic Materials Using a Flexibility Approach. Part 1 - Strip Loadings"*, International Journal for Numerical Methods in Engineering, Vol. 20, No. 6, p. 1025-1037.

Small, J. C. and Booker, J. R., (1986). *"Finite Layer Analysis of Layered Elastic Materials Using a Flexibility Approach. Part 2 - Circular And Rectangular Loadings"*, International Journal for Numerical Methods in Engineering, Vol. 23, No. 5, p. 959-978.

Starfield, A. M. and McClain, W. C., (1973). *"Project Salt Vault: A Case Study in Rock Mechanics"*, International Journal of Rock Mechanics and Mining Sciences, Vol. 10, No. 6, p. 641-657.

Sulem, J., Panet, M. and Guenot, A., (1987a). *"Closure Analysis In Deep Tunnels"*, International Journal of Rock Mechanics and Mining Sciences & Geomechanics Abstracts, Vol. 24, No. 3, p.145-154.

Sulem, J., Panet, M. and Guenot, A., (1987b). *"Analytical Solution for Time-Dependent Displacements in a Circular Tunnel"*, International Journal of Rock Mechanics and Mining Sciences & Geomechanics Abstracts, Vol. 24, No. 3, p. 155-164.

Talbot, A. (1979). *"The Accurate Numerical Inversion of Laplace Transforms"*, J. Inst. Maths Applies, Vol. 23, p. 97-120.

Taylor, D.W., (1942). *"Research on consolidation of clays"*, Tech. rept. Massachusetts Institute of Technology, Serial 82.

Ter-Martirosyan, Z. G., (1979). *"On the Parameters of Secondary Consolidation of Clays"*, Proceedings of the European Conference on Soil Mechanics and Foundation Engineering, Vol. 1, Meas, Sel and Use of Des Parameters in Geotech Eng, p. 297-301.

Ter-Stepanian, G., (1975). *"Creep of a Clay during Shear and Its Rheological Model"*, Geotechnique, Vol. 25, No. 2, p. 299-320.

Terzaghi, K., (1925). *"Erdbaumechanik"*, Franz Deuticke, Vienna.

Terzaghi, K., Peck, R. B. and Mesri, G., (1996). *Soil mechanics in engineering practice*, 3rd Ed., Wiley, New York.

Tian, W.M., Silva, A.J., Veyera, G.E. and Sadd, M.H., (1994). *''Drained creep of undisturbed cohesive marine sediments''*, Can. Geotech. J., Vol. 31, p. 841-855.

Tran, V.N.G., Bernard, E.S. and Beasley, A.J., (2005). *"Constitutive modeling of fiber reinforced shotcrete panels"*, Journal of Engineering Mechanics, 131, 5, p. 512-521.

Wahls, H. E., (1962). *''Analysis of primary and secondary consolidation''*, J. Soil Mech. Found. Div., Vol. 88(SM6), p. 207-231.

Wu, T.H., Resendiz, D. and Neukirchner, R.J., (1966). *"Analysis of consolidation by rate process theory"*, Journal of the soil mechanics and foundations division, American Society of Civil Engineers, Vol. 92(6), p. 229-248.

Yamada, B., (1968). *"On one-dimensional consolidation by three-dimensional dehydration"*, Japan Society of Civil Engineers - Transactions, No. 149, p. 46-63.

Yassaghi, A. and Salari-Rad, H., (2005). *"Squeezing rock conditions at an igneous contact zone in the Taloun tunnels, Tehran-Shomal freeway, Iran: A* *case study"*, International Journal of Rock Mechanics and Mining Sciences, Vol. 42, No. 1, p. 95-108.

Yin, J.H. and Graham, J., (1989). *"Viscous-elastic-plastic modelling of one-dimensional time-dependent behaviour of clays"*, Canadian Geotechnical Journal, Vol. 26, No. 2, p. 199-209.

Yin, J.H. and Graham, J., (1994). *"Equivalent times and one-dimensional elastic viscoplastic modelling of time-dependent stress-strain behaviour of clays"*, Canadian Geotechnical Journal, Vol. 31, No. 1, p. 42-52.

Yin, J.H. and Graham, J., (1996). *"Elastic visco-plastic modelling of one-dimensional consolidation"*, Geotechnique, Vol. 46, No. 3, p. 515-527.

Yin, J.H. and Graham, J., (1999). *"Elastic viscoplastic modelling of the time-dependent stress-strain behaviour of soils"*, Canadian Geotechnical Journal, Vol.36, No.4, p. 736-745.

Zakhariev, G., Khadzhikov, L. and Marinov, P., (1971). *"Rheological Model of Polymers and Glass-Reinforced Plastics"*, Polymer Mechanics (English translation of Mekhanika Polimerov), Vol. 7, No. 5, p. 761-766.

Zienkiewicz, O. C., (1983). *"Generalized Finite Element Method - State Of The Art And Future Directions"*, Journal of Applied Mechanics, Transactions ASME, Vol. 50, No. 4b, p. 1210-1217.

Zhang, J., (2003). *"Modeling of the influence of fibers on creep of fiber reinforced cementitious composite"*, Composites Science and Technology, Vol. 63, No. 13, p. 1877-1884.

Zhu, X. G., Yang, Q. and Luan, M. T., (2006). *"Utilizing ABAQUS modeling new Austrian tunneling method process"*, Yantu Lixue/Rock and Soil Mechanics, Vol. 27, No SUPPL., p. 283-289.

Zhu, X. R. and Wang, J. C., (2004). *"Introduction to partly soil models in ABAQUS Software and their application to the geotechnical engineering"*, Yantu Lixue/Rock and Soil Mechanics, Vol. 25, No SUPPL. 2, p. 144-148.